Universiteit Leiden
The Netherlands

Engineering precision surgery: Design and implementation of surgical guidance technologies

Oosterom, M.N. van

Citation
Oosterom, M. N. van. (2020, April 22). *Engineering precision surgery: Design and implementation of surgical guidance technologies*. Retrieved from https://hdl.handle.net/1887/92363

Version:	Publisher's Version
License:	Licence agreement concerning inclusion of doctoral thesis in the Institutional Repository of the University of Leiden
Downloaded from:	https://hdl.handle.net/1887/92363

Note: To cite this publication please use the final published version (if applicable).

Cover Page

Universiteit Leiden

Leiden University Repository

The handle http://hdl.handle.net/1887/92363 holds various files of this Leiden University dissertation.

Author: Oosterom, M.N. van
Title: Engineering precision surgery: Design and implementation of surgical guidance technologies
Issue Date: 2020-04-22

Engineering precision surgery

Design and implementation of surgical guidance technologies

Matthias N. van Oosterom

Design and lay-out: M.N. van Oosterom
Printed by: Ipskamp Printing B.V., Enschede

The research described in this thesis has received funding from the European Research Council (advanced grant, no. 323105).

Financial support from Crystal Photonics GmbH, Eurorad S.A., Intuitive Surgical Inc., KARL STORZ Endoscopie Nederland B.V., MILabs B.V., PI Medical Diagnostic Equipment B.V., SurgicEye GmbH and Verb Surgical Inc. for printing of this thesis is gratefully acknowledged.

Engineering precision surgery

Design and implementation of surgical guidance technologies

Proefschrift

ter verkrijging van
de graad van Doctor aan de Universiteit Leiden,
op gezag van Rector Magnificus prof. mr. C.J.J.M. Stolker,
volgens besluit van het College voor Promoties
ter verdediging op woensdag 22 april 2020
klokke 15.00 uur

door

Matthias Nathanaël van Oosterom

geboren te Rijswijk
in 1990

Promotors:	Prof. dr. C.J.H. van de Velde Prof. dr. F.W.B. van Leeuwen
Thesis committee:	Prof. dr. J.A. van der Hage Dr. R.A. Valdés Olmos Prof. dr. F.J. Beekman (Delft University of Technology) Prof. dr. J. Dankelman (Delft University of Technology) Prof. dr. N. Navab (Technical University of Munich)

TABLE OF CONTENTS

Chapter 1	General introduction and outline of this thesis	7
	PART ONE: ENGINEERING NOVEL NAVIGATION MODALITIES FOR FLUORESCENCE GUIDED SURGERY	
Chapter 2	Surgical Navigation: An Overview of the State-of-the-Art Clinical Applications	15
Chapter 3	Navigation of a robot-integrated fluorescence laparoscope in preoperative SPECT/CT and intraoperative freehand SPECT imaging data: a phantom study	39
Chapter 4	Navigation of Fluorescence Cameras during Soft Tissue Surgery – Is it Possible to Use a Single Navigation Setup for Various Open and Laparoscopic Urological Surgery Applications?	57
Chapter 5	Navigating surgical fluorescence cameras using near-infrared optical tracking	81
	PART TWO: ENGINEERING NOVEL DETECTION MODALITIES FOR TRACER-BASED SURGICAL GUIDANCE	
Chapter 6	U-SPECT-BioFluo: an integrated radionuclide, bioluminescence, and fluorescence imaging platform	103
Chapter 7	Extending the hybrid surgical guidance concept with freehand fluorescence tomography	123
Chapter 8	Revolutionizing (robot-assisted) laparoscopic gamma tracing using a DROP-IN gamma probe technology	145
	OUTLOOK	
Chapter 9	Computer-assisted surgery: virtual- and augmented-reality displays for navigation during urological interventions	171
Chapter 10	Summary Samenvatting Curriculum Vitae List of Publications	187

CHAPTER 1

GENERAL INTRODUCTION AND OUTLINE OF THIS THESIS

GENERAL INTRODUCTION

Surgery is still one of the main forms of treatment in the management of primary tumors and initial metastatic spread. Accurate surgical resection of cancer-related tissue requires a balance to be struck between radical excision, increasing the chance of a good oncological outcome, and minimal damage to healthy tissues, decreasing the chance of surgery related side effects [1-3]. We and others have reasoned that resection of all diseased tissue while sparring healthy tissue, can be achieved when technologies become available that advance the surgical precision. It is of much importance, both during preoperative diagnosis and intraoperative guidance, that technologies become available that are able to specifically define and localize which tissues are tumor infected and which are not. When tracers are available that can specifically stain the disease-related tissue, a need is created for detection modalities able to carefully localize these tracers. Intraoperatively, such detection modalities can aid tracer localization via a combination of acoustical, numerical or image-based feedback, providing a so-called 'image guided surgery' setup.

Radioactive tracers, also called nuclear tracers, are the clinical standard for molecular imaging due to their sensitivity and high tissue penetration [4]. Radiotracers are used for both preoperative diagnosis and intraoperative radioguidance. Fluorescent tracers offer complementary features such as high resolution, real-time and visual guidance within the surgical field [5]. Unfortunately, tissue attenuation limits the value of fluorescence tracers to superficial indications [6]. Consequently, hybrid tracers, being both radioactive and fluorescent, have been investigated [7, 8]. These tracers provide a best-of-both-worlds scenario for lesion localization. To optimally benefit from these complementary tracer signatures, the development of dedicated hybrid surgical detection modalities has been proposed [9-11]. Surgical navigation takes the concept of image guided surgery even a step further. Analogues to how we use the global positioning system (GPS) based navigation on our smartphones to guide ourselves through traffic in every-day-life, surgical navigation systems specifically guide the surgeon's tool towards the targeted tissue in the patient [12, 13].

In this thesis, the engineering of a number of novel tracing, imaging and navigation modalities is introduced and their potential within image guided surgery has been evaluated.

OUTLINE OF THIS THESIS

Part one of this thesis is focused towards the concept of surgical navigation and investigates the application specifically in combination with fluorescence guided surgery. **Chapter 2** starts off with an introduction in to the general concept of using navigation in the operating room. The first part of this chapter focusses on providing a technical background of the basic concepts needed for a surgical navigation workflow. The second part provides a short overview of the clinical applications, specifically looking at the fields of needle-based interventions, surgical resections and orthopedic surgery.

My research efforts specifically focused on hybrid surgical guidance concepts that make use of both nuclear and fluorescence imaging. In particular, navigation was used to position the fluorescence camera, thereby facilitating the execution of fluorescence guided surgery for applications were lesions are located deep within the patient anatomy. **Chapter 3** introduces the navigation of a fluorescence laparoscope in the robot-assisted surgery setting, a field rapidly emerging for a lot of different surgical indications (e.g. prostatectomy). In **Chapter 4**, the same navigation concept was translated to a fluorescence laparoscope and exoscope, making the hybrid navigation concept applicable to both open surgery (evaluation in penile cancer patients) and laparoscopic surgery (evaluation in prostate cancer patients). From the different proof-of-concept evaluations reported in this thesis and the study by KleinJan et al. [14], it turned out that near-infrared optical tracking, used in the current navigation setup, in some cases obstructed fluorescence imaging. **Chapter 5** investigates this limiting phenomenon in detail, suggesting several engineering solutions that could be used to overcome this obstruction.

Part two introduces the engineering of new (hybrid) detection modalities. **Chapter 6** describes the creation of a preclinical animal imaging modality able to optimally support preclinical hybrid tracer development. **Chapter 7** introduces the concept of freehand Fluorescence imaging, allowing for (pseudo-) 3D imaging and navigation using fluorescent tracer signatures in the operating room. When combined with freehand SPECT this provides a singular hybrid modality, able to benefit from the advantages of nuclear and fluorescence imaging to supply tracer imaging, navigation and augmented reality display. **Chapter 8** specifically focusses on optimizing detection of radioactive tracer signatures during robot-assisted laparoscopic surgery, introducing a tethered and highly flexible DROP-IN gamma probe.

Chapter 9, the future outlook of this thesis, places all the introduced concepts, including surgical navigation, hybrid surgical guidance and DROP-IN modalities, in the perspective of computer-assisted surgery. This chapter provides a review of the recent clinical evaluations in this field, connecting the evaluated technologies and recommending future directions of research. A summary of the thesis is provided in **Chapter 10**.

REFERENCES

1. *KleinJan, G., et al., A prediction model relating the extent of intraoperative fascia preservation to erectile dysfunction after nerve-sparing robot-assisted radical prostatectomy. Journal of Robotic Surgery, 2018: p. 1-8.*
2. *Kraima, A.C., et al., Careful Dissection of the Distal Ureter Is Highly Important in Nerve-sparing Radical Pelvic Surgery: A 3D Reconstruction and Immunohistochemical Characterization of the Vesical Plexus. International Journal of Gynecological Cancer, 2016. 26(5): p. 959-966.*
3. *Weng, H., et al., Intrafascial versus interfascial nerve sparing in radical prostatectomy for localized prostate cancer: a systematic review and meta-analysis. Scientific reports, 2017. 7(1): p. 11454.*
4. *Herrmann, K., O. Nieweg, and S.P. Povoski, Radioguided Surgery: Current Applications and Innovative Directions in Clinical Practice. 2016: Springer.*
5. *van Leeuwen, F.W., J.C. Hardwick, and A.R. van Erkel, Luminescence-based Imaging Approaches in the Field of Interventional Molecular Imaging. Radiology, 2015. 276(1): p. 12-29.*
6. *Stoffels, I., et al., Intraoperative fluorescence imaging for sentinel lymph node detection: prospective clinical trial to compare the usefulness of indocyanine green vs technetium Tc 99m for identification of sentinel lymph nodes. JAMA Surg, 2015. 150(7): p. 617-623.*
7. *Hekman, M.C., et al., Tumor-targeted Dual-modality Imaging to Improve Intraoperative Visualization of Clear Cell Renal Cell Carcinoma: A First in Man Study. Theranostics, 2018. 8(8): p. 2161.*
8. *van Leeuwen, F.W., et al., Hybrid surgical guidance based on the integration of radionuclear and optical technologies. The British journal of radiology, 2016. 89(1062): p. 20150797.*
9. *Bugby, S.L., J. Lees, and A. Perkins, Hybrid intraoperative imaging techniques in radioguided surgery: present clinical applications and future outlook. Clinical and translational imaging, 2017. 5(4): p. 323-341.*
10. *Gambini, J.P. and T.P. Quinn, Hybrid tracers and devices for intraoperative imaging: the future for radioguided surgery? Clinical and Translational Imaging, 2016. 4(5): p. 343-351.*
11. *KleinJan, G.H., et al., Hybrid surgical guidance: Does hardware integration of gamma-and fluorescence-imaging modalities make sense? J Nucl Med, 2017. 58: p. 646-650.*
12. *Bernhardt, S., et al., The status of augmented reality in laparoscopic surgery as of 2016. Medical image analysis, 2017. 37: p. 66-90.*
13. *Rassweiler, J., et al., Surgical navigation in urology: European perspective. Curr Opin Urol, 2014. 24(1): p. 81-97.*
14. *KleinJan, G.H., et al., Toward (Hybrid) Navigation of a Fluorescence Camera in an Open Surgery Setting. J Nucl Med, 2016. 57(10): p. 1650-1653.*

PART ONE

Engineering novel navigation modalities for fluorescence guided surgery

CHAPTER 2

SURGICAL NAVIGATION:
AN OVERVIEW OF THE STATE-OF-THE-ART CLINICAL APPLICATIONS

Adapted from: Waelkens P, van Oosterom MN, van den Berg NS, Navab N, van Leeuwen FWB

In: Radioguided Surgery; Edited by Herrmann K, Nieweg OE and Povoski SP; Cham, Switzerland: Springer International Publishing, 2016, Chapter 4, pp. 57-73

ABSTRACT

Anatomical and/or functional imaging modalities like computed tomography (CT), magnetic resonance imaging (MRI) and ultrasound, often combined with contrast agents, and molecular imaging modalities like single-photon emission computed tomography (SPECT) and positron emission tomography (PET) have become standard tools to aid in the diagnosis, monitoring and treatment of disease or injury. Yet, translating this wealth of detailed preoperative imaging information into better surgical treatment and clinical outcome is an ongoing challenge. Patient scans usually provide a 3D map of the disease, often placed in the context of the patient's anatomy, that surgeons can use as a reference to guide them during an intervention. It would be very convenient for the surgeon to know exactly where surgical tools are on this map relative to the target location or, even better, to be provided with an optimal path from the tools towards the target.

INTRODUCTION

An analogy can be made between surgical navigation and global positioning system (GPS)-based navigation apps available on smartphones and similar devices, as illustrated in Figure 1. Smartphone navigation shows a map of our surroundings, analogous to a patient scan (Figure 1a). It shows our current location on this map (using GPS tracking), analogous to showing where surgical tools are in the image of the patient (Figure 1b). The user can mark the objective on the map, analogous to marking the location of the surgical target (e.g. tumor, lymph node; Figure 1c). Subsequently, the navigation app then suggests an optimal route between our current location and the objective, analogous to suggesting an optimal trajectory of the surgical tools to the target (Figure 1d).

Navigation is a collective term that describes any workflow where patient scans, real-time tracking, and, occasionally, computer-aided planning are combined into real-time spatial information that provides orientation (Figure 1b, c) and sometimes even guidance to reach the target location (Figure 1d) during an intervention. The main benefit of this technology is the possibility to precisely indicate where structures of interest are located relative to the surgical tools in

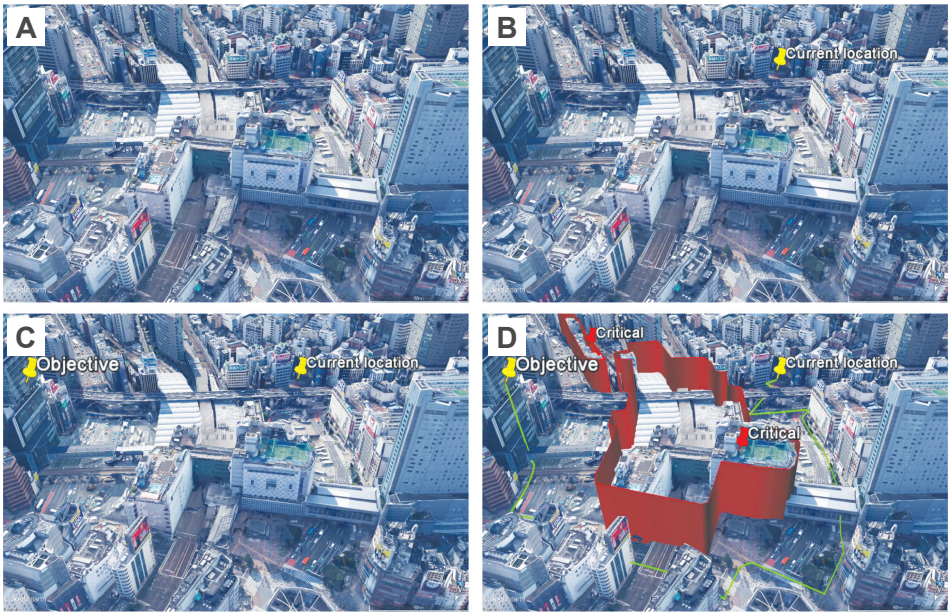

Figure 1. Analogy between surgical navigation and smartphone navigation apps. (a) *Raw 3D map of the region of interest (Depicted: Shibuya Station, Tokyo).* ***(b)*** *Current location of the surgical tools on the map, analogous to GPS localization.* ***(c)*** *The target location for navigation, i.e. the objective, can be marked on the map.* ***(d)*** *Guidance of surgical tools to the target along optimal path (in green), whilst avoiding damage to nearby critical structures. Images generated with Google Earth, satellite images provided by USGS/NASA Landsat.*

3D. This is possible even when the structures of interest are covered by tissue and cannot be seen during surgery. Although surgical navigation technologies have not yet reached full maturity, clinical evidence already suggests it is of benefit to many clinical applications. Navigation promises to bring machine precision to clinical interventions, and will likely contribute to the emergence of more precise, less invasive and, hopefully, more effective procedures.

This chapter starts with the presentation of a typical navigation workflow and the methodologies behind this approach. Subsequently a broad overview of navigation in various clinical fields, including radioguided surgery, is provided. We close the chapter with a short discussion on the presented applications and the general developments we may expect in the upcoming years.

NAVIGATION WORKFLOW

The tracking systems (Figure 2.5) are an essential component in all navigation workflows as they define the intraoperative coordinate system during an intervention. They are used to estimate the position and orientation of specially marked objects (Figure 2.7,8). These estimates, combined with registrations, enable the placement of tracked tools, patient scans and, if available, (computer-aided) planning in the same coordinate system. For object tracking, there are a number of different techniques available, e.g. near-infrared (NIR) optical tracking, electromagnetic (EM) tracking, mechanical tracking and acoustic tracking [1–4]. Of these techniques, NIR optical tracking and EM tracking are by far the most commonly used in clinical practice and will therefore be of main focus for this book chapter. With NIR optical tracking systems (Figure 2a.5), the emission and detection of NIR light is used to determine the position of trackers in space. To obtain stereo-vision, thus depth optical perception, this NIR light has to be captured by at least two cameras in a known spatial configuration. NIR optical tracking can only work when enough fiducial markers (small objects that each approximate a point and jointly representing three noncollinear points of a tracker; see next section) are in the line of sight of these NIR cameras. Marker occlusion, e.g. by surgical staff standing between the tracking system and the fiducials, is a limitation of this tracking technique and of optical tracking in general.

EM tracking systems (Figure 2b.5), on the other hand, rely on variations in the magnetic field generated by a dedicated field generator to determine the position of sensor coils present on the tracker relative to the generator. The varying magnetic field induces current and potential in the coils. Usually, multiple coils are combined into a single tracker, and the combined readings from these coils provide enough information to estimate the position and orientation of the tracker in space. Unlike NIR tracking, EM tracking systems do not require a direct line of sight to the trackers, but they have different limitations:

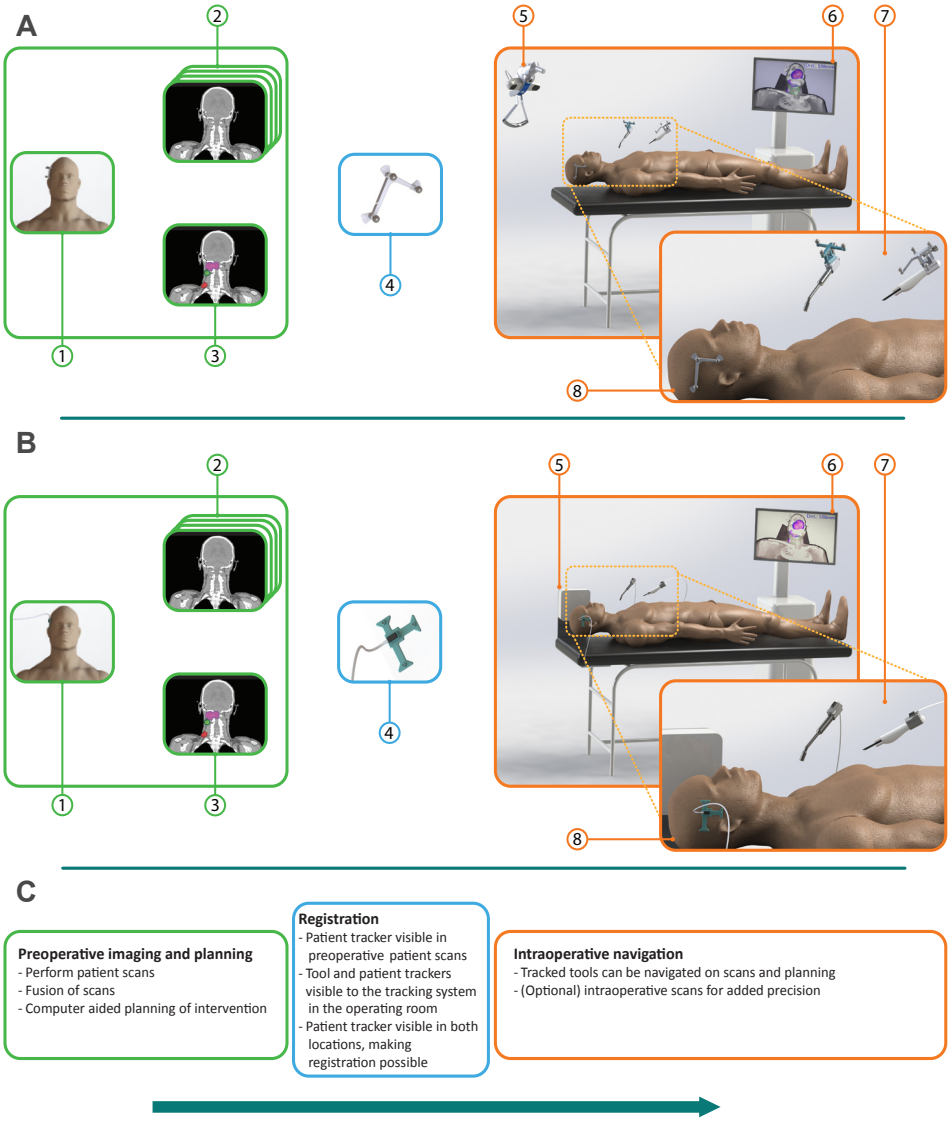

Figure 2. Overview of a typical navigation workflow. (a) *Uses optical tracking and* ***(b)*** *Uses electromagnetic tracking.* ***(c)*** *Describes the sequence of steps in a typical workflow.* ***1*** *patient with tracker,* ***2*** *multiple patient scans,* ***3*** *computer-aided planning,* ***4*** *tracker visible in preoperative and intraoperative coordinate systems,* ***5*** *tracking system,* ***6*** *navigation platform,* ***7*** *tracked tools,* ***8*** *patient with tracker on OR table. CAD models of dummy human male (by LeonMaryasin) and hospital bed (by Felipe Ospina Ochoa) found in the community library of grabcad.com.*

(1) Nearby metal objects can distort the magnetic field, leading to incorrect position and orientation estimations, and (2) the working volume of current EM tracking systems is usually smaller than that of NIR optical tracking systems.

Tracking

Patient Tracking

In most navigation workflows, the purpose of tracking surgical tools is to determine their position relative to the patient's anatomy and the diseased tissue therein (as in Figure 1b) as such to better guide the surgeon during the procedure. The typical navigation workflow will make use of preoperative imaging, meaning that the preoperative imaging data set (Figure 2.1-3) has to be coupled to the interventional intraoperative coordinate system (Figure 2.5-8). The trick used to achieve this preoperative and intraoperative co-registration is to place a special tracker (Figure 2.4) at the same position on the patient during preoperative imaging and during the intervention. This tracker is, by design, both visible to the tracking system and easily segmented from the preoperative scan. Once segmented, the position of the tracker relative to the patient can be calculated, leading to a registration between the coordinates of the patient and the tracker.

To use the patient scan as a 3D map that is accurately positioned in the intraoperative coordinate system, the patient-to-tracker registration has to be coupled to the tracked position of the tracker in the intervention room. Essential requirements for precise registration are the identical placement of the tracker during preoperative imaging and during the intervention, and as little tissue deformation as possible between imaging and the intervention.

A tracker is an object that is visible to the tracking system and holds enough information for the tracking system to unambiguously establish all six degrees of freedom of the tracker in 3D space (three degrees of freedom for the position and three for the orientation). Trackers can be attached to surgical tools or to portions of the patient's anatomy, enabling their tracking (Figure 2.7,8). To accomplish tracking, the position of at least three noncollinear points must be monitored, as we illustrate in Figure 3. Most trackers are designed to be clearly visible to the tracking system and easy to segment from patient scans, as seen in Figure 2.4. Such trackers are visible both in the preoperative and in the intraoperative coordinate systems, providing the link between them and making registrations possible. The composition of a tracker is dependent on the tracking technology that will be used during the procedure. For example, NIR optical trackers (Figures 2a.4 and 3) consist of a rigid frame holding multiple (usually three noncollinear, sometimes more) fiducial markers. A fiducial marker is a small object that approximates a point. Most NIR fiducial markers are both clearly visible in preoperative scans and clearly visible to the tracking system. On the other hand, a modern EM tracker usually consists of a bundle of sensor coils inside a small case (around 0.5 cm^3) attached to a cable (wireless variants exist [5], but are uncommon) (as an example, the small black box attached to the surgical tools on Figure 2b.7 is an EM tracker). An EM tracker variant that is visible in patient scans (see Figure 2b.4) consists of a standard EM tracker attached to a frame that is large enough to be easily segmented in the patient scans.

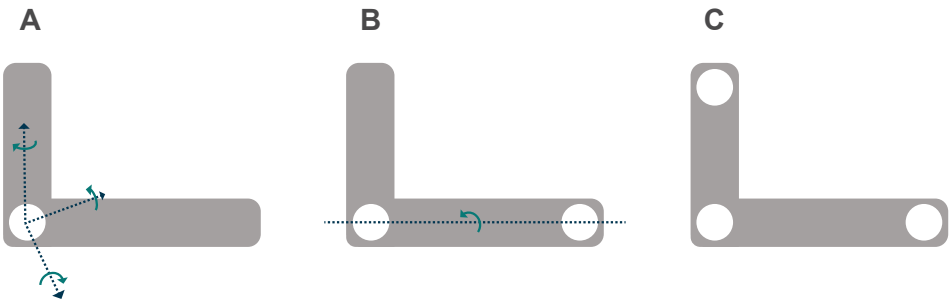

Figure 3. Fiducial markers on a rigid tracker. (a) *One fiducial, no orientation information* ***(b)*** *Two fiducials, orientation around dotted line unknown* ***(c)*** *Three noncollinear fiducials, unambiguous position and orientation*

The (EM and NIR optical) trackers described above provide a simple way to perform tracking and registration to the patient scans; of course, more complicated alternatives exist. For example, instead of a tracker, multiple loose fiducial markers can also be used to track the position and orientation of an object, provided at least three fiducials are noncollinear. This is equivalent to using a tracker, since both approaches provide enough measurements to cover the six degrees of freedom. Some authors report the use of fiducials which are visible in the patient scans, but not to the tracking system. For example, Krücker et al. [6] reported placing such fiducials on the patient's skin. During the intervention, the position of the fiducials then had to be marked by a tracked pointer, thus providing the connection between patient scans and tracking system.

Tracking of Surgical Tools

A similar, but simpler, approach is used to determine the position of the surgical tools in the intraoperative coordinate system. For this, a tracker is attached to the surgical tool that needs to be navigated. Here it is crucial that this tracker is placed at a predefined position on the surgical tool (see Figure 2.7), and that the tool is calibrated relative to the navigation platform. This calibration, in combination with the tracking information of the surgical tool tracker, allows tracking of the tip of the tool (or of any other part of the tool that is relevant during the intervention) thereby providing navigation from the perspective of the tip of the surgical tool. Tools like needles are routinely tracked using the methods described above. Some authors even report tracking tools to aid in implant placement [7–9]. Aside from surgical tools, it is also possible to track (handheld) imaging systems (e.g. ultrasound probes, gamma probes, portable gamma cameras and portable fluorescence imaging systems) as will be discussed later. A tracked scanning procedure performed with a handheld imaging system is referred to as "tracked freehand imaging".

Limitations and Implicit Assumptions of Tracking

Most navigation workflows make an implicit assumption about the body that is being tracked, namely, that it is a rigid body, i.e. that it has exactly the same shape any time during preoperative imaging and during surgery. If a body does not deform, it is sufficient to track the position and orientation of a tiny portion of it to know where the rest is. This is the justification for only placing a single tracker and/or a minimal amount of fiducial markers on a patient to track his or her position and orientation. Of course, the rigid body assumption may sometimes be unrealistic and can lead to mistakes. If the object being tracked is not a rigid body, the tracking approaches described in this text are, in general, inadequate. For example, a patient may change pose between preoperative imaging and the intervention without affecting the relative positions of the fiducial markers; in this case, the change in shape would not be detected by the tracking system. Surgeons must be aware of the implicit rigid body assumption of tracking systems and of the entailing limitations. In particular, it is always sensible to verify the precision of any registration between preoperative and intraoperative coordinates prior to and during an intervention, especially if a change in the shape of the patient is likely.

Current tracking systems work by tracking a relatively small number of points in 3D; in general, this is not sufficient to deal with arbitrary deformations. Some authors, e.g. Krücker et al. [6] for thoracic and abdominal cavity interventions and Matziolis et al. [10] for navigated total knee arthroplasty, report the use of a redundant amount of fiducials/trackers, providing more information than necessary to obtain the six degrees of freedom of a rigid body. As a consequence, more than one rigid body could be tracked in such a workflow. This can accommodate some kinds of movement, e.g. the movement of the tibia relative to the femur. Still, these multi-rigid, landmark-based, arrangements also make implicit rigidity assumptions on the patient's shape, like the single rigid body case, and cannot accommodate arbitrary deformations particularly well. This said, redundant fiducials/trackers can be used to measure body deformation; if the spatial configuration changes during tracking, this information can be useful to correct, or at least explain, tracking errors during navigation. In addition, such findings may allow for elastic registrations which are a promising approach to handle body deformation (briefly discussed later in this chapter). Another reason for a redundant amount of fiducials, specific to optical tracking techniques, is that some fiducials may not lie in the direct line of sight of the tracking system; a large amount of fiducials reduces the chance that less than three noncollinear fiducials are visible.

On the other hand, images acquired with tracked freehand imaging are, due to tracking, automatically located in the intraoperative coordinate system; this means such images are already in the same coordinate system as the tracked surgical tools, rendering a registration between preoperative and intraoperative coordinates unnecessary. As a consequence, navigating tools in tracked

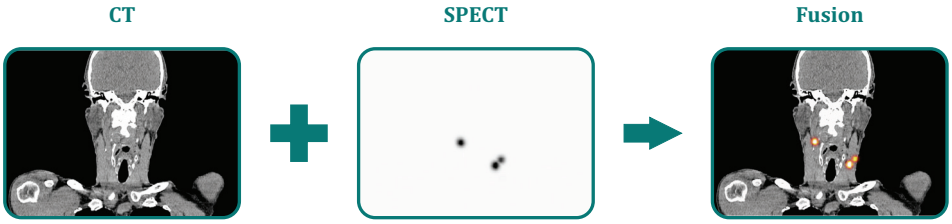

Figure 4. Image fusion. *CT and SPECT are registered, which enables a fused visualization*

freehand imaging scans is fairly straightforward. Such workflows are already reported in literature [11–13]. In the absence of specialized (and expensive) operating rooms with integrated MRI or CT scanners, tracked freehand imaging is often the only kind of 3D imaging that can be made available in the operation room. Intraoperative imaging can also be used to help verify the progress of a procedure, to cope with patient movement and sometimes even to quickly perform 3D intraoperative scans of the region of interest [11–14]. Tracked freehand ultrasound [15] is already available. An interesting novelty, especially for radioguided surgery, is tracked freehand SPECT, a SPECT generated from a tracked portable gamma camera [12, 13, 16–18].

Registration and Fusion

In the previous section, we explained how two coordinate systems (preoperative with patient scans and intraoperative with tracking information) can be connected via tracking of trackers, allowing objects from both coordinate systems to be shown in a single coordinate system. This connection between coordinate systems is called a registration. Since combining the complementary information of different patient scans allows for a more complete model of the patient, e.g. in the form of PET and MRI data, the registration concept described in the previous section should be expanded to more than two coordinate systems. This is readily possible using image registration. In fact, it is possible to register an arbitrary number of coordinate systems in a chain of registrations.

In a typical navigation workflow, all preoperative scans (Figure 2.2) are registered to each other. In at least one of these preoperative scans, the patient has to be outfitted with a tracker (Figure 2.1); this scan is then used to register the preoperative and intraoperative coordinate systems. With this registration, all other preoperative scans are also (indirectly) registered to the intraoperative coordinate system and can be navigated on. Registered patient scans are sometimes shown in composite views, where information from multiple scans is condensed into a single “fused” visualization, as illustrated in Figure 4. Note that registering multiple patient scans (i.e. performing image registrations) is often a complex and error-prone task, especially when there is deformation in the patient’s anatomy between scans. For this reason, image registrations should always be critically evaluated for errors and imprecisions prior to their use for navigation (or planning).

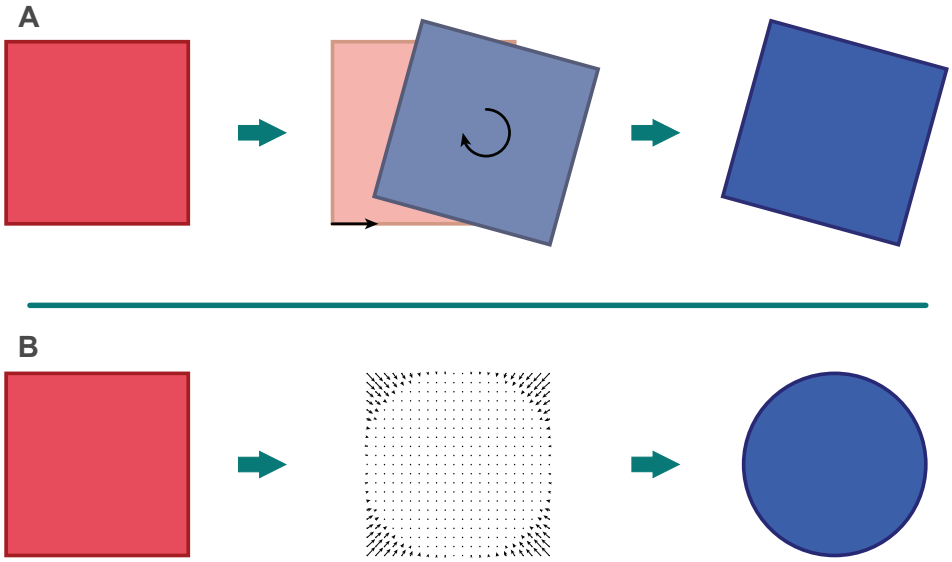

Figure 5. Types of registration. *(a) Rigid registration, a composition of rotation and translation. (b) Elastic registration, a deformation field is applied to warp the square into a circle.*

Registration methods can be separated into two types: rigid and elastic. A registration that consists exclusively of a composition of rotation and translation is called a rigid registration (see Figure 5a). Rigid registrations can always be described by a transformation matrix. The vast majority of registrations currently performed in clinical practice, including most registrations using trackers or fiducials, are rigid. Rigid registrations are relatively easy to understand, fairly simple to verify, correct, and often precise enough for the intended application. But rigid registrations are, by definition, limited in the degrees of freedom that they can accommodate.

A very common example of rigid registrations is a SPECT and CT registration (see Figure 4). Here a hybrid imaging device combines a measure of the distribution of a radiotracer (SPECT) with a scan of (CT) the patient's anatomy in a single imaging session; no significant patient movement is assumed during imaging, so the transformation matrix for this rigid registration is the identity matrix. Since many clinical applications only require a good alignment inside a small region of interest, rigid registrations will often be sufficient, even if a correct rigid alignment of the whole scans is not possible. In the cases where rigid registrations are not adequate to align scans as a result of extensive tissue movement, e.g. breast MRI scans [19] or preoperative to intraoperative brain scan alignment [20, 21], other types of registration are required.

Registrations that can handle arbitrary deformations, meaning random tissue movements, are called elastic or deformable registrations (see Figure 5b). Elastic registrations cannot be described by a transformation matrix, due to their complexity. Instead, they are described by deformation fields. Elastic registrations

are the topic of image analysis papers for decades already, but their use in clinical practice has been very limited thus far. The main reason for this is that there is a trade-off between flexibility, the ability to handle arbitrary deformations, and robustness, the ability to consistently yield reasonably precise registrations. There is not one sweet spot between flexibility and robustness that works for all clinical applications, meaning an elastic registration algorithm has to be fine-tuned for each specific application. This, combined with the difficulty of finding an elastic registration method that works for the target application in the first place, greatly lowers the appeal of this technology, compared to the more generally applicable rigid registrations.

Computer-Aided Planning

Tracking and registration enable us to see the position of the tracked surgical tools overlaid on patient scans. The distance or the preferred route towards the target cannot be established with this information alone. Computer-aided planning software provides the navigation platform with the additional information needed to achieve both distance and route (Figure 1c) estimates. To enable such planning, it is necessary to segment (i.e. define the boundaries of) the target structure in the patient scans and provide this segmentation to the navigation platform. For some surgeries, damage to critical structures must be avoided at all costs; in such cases, navigation from point A to B in a straight line does not suffice (Figure 1c).

Here navigation can be further improved to navigation along a path that avoids damage to nearby critical structures, as schematically shown in Figure 1d. In order to provide such a "smart" route towards the target structure, it is also necessary to segment all critical structures that need to be avoided. To further clarify this approach, we illustrate how computer-aided planning fits into a navigation workflow by considering the resection of a kidney lesion (see Figure 6). The starting point is the patient scan shown in Figure 6a. If computer-aided planning is used, the kidney lesion and nearby critical structures are segmented (Figure 6b). This segmentation can then be used to compute an optimal trajectory to the target (Figure 6c). This plan is transferred to the navigation platform and can be used to position the surgical tools along the computed optimal path.

In computer-aided planning, manual and semi-automatic segmentations are currently the tools of choice in clinical practice. Manual segmentations, as their name implies, require manual drawings of the contours and interior of all structures that have to be segmented. The main advantage of manual segmentations is that the user has complete control over what label each voxel in the 3D preoperative scan gets. However, manual segmentations can be extremely time consuming, especially for high-resolution 3D scans. Among all segmentation methods, manual segmentations, unsurprisingly, also suffer from the highest interobserver variability. A semi-automatic segmentation is a manual segmentation with some automatic assistance. For example, a drawing tool that

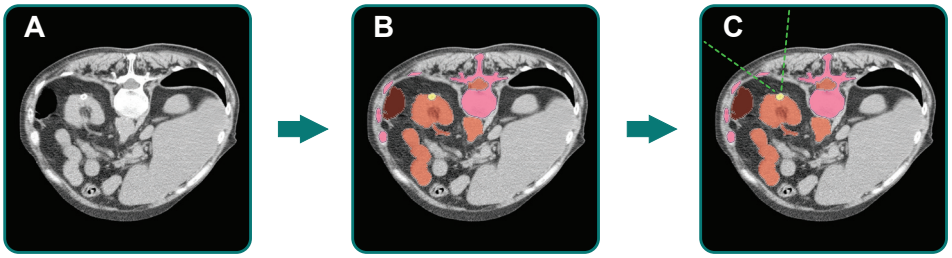

Figure 6. Computer-aided planning in the treatment of a kidney lesion. (a) *Raw patient scans* ***(b)*** *Segmentation of kidney lesion (yellow), nearby critical structures (orange) and nearby bones (pink)* ***(c)*** *Optimal paths to lesion (green dotted lines); as short as possible whilst avoiding damage to critical structures.*

automatically fills surrounding voxels of a similar color, or, for example, a tool for vessel segmentation, where only the start and endpoint of the segment have to be defined manually. Semi-automatic segmentations require far less user input and can be performed significantly faster and with higher reproducibility than manual segmentations. On the other hand, the user partially surrenders the segmentation process over to the computer, thereby reducing his or her personal touch. Automatic segmentations, and in particular atlas-based segmentations [22], have improved a lot in recent years and are slowly gaining more acceptance.

A fully automatic segmentation is a segmentation that requires no user interaction. The obvious advantage of automatic segmentations is that they neither need to be performed nor supervised by a trained medical specialist. Experienced human operators, whilst usually superior to automatic methods, are subject to time constraints and susceptible to boredom, unlike machines. These time and boredom constraints are not limiting when a single segmentation of a target structure has to be performed, but can become an issue when repetitive or more extensive segmentations are required. For example, segmenting all bones in thousands of full-body scans for an anatomy experiment would certainly yield interesting insights, but very few experts would volunteer for such a tedious task. Computers do not get bored; as a consequence, they can provide much more extensive segmentations than could reasonably be expected from a human expert. It goes without saying that automatic segmentations always have to be critically evaluated by an expert.

CLINICAL APPLICATIONS OF NAVIGATION

Attempts at surgical navigation have already been reported as early as the year 1889 [23]; these involved stereotactic frames combined with generic atlases (i.e. maps) of the anatomy, used as reference during the procedure. Due to the anatomical variation found in humans, generic atlases cannot be correct for all anatomical regions of all patients; hence, they are often not reliable for precise

guidance. Patient-specific approaches to navigation, where patient scans are used instead of generic atlases, only became realistic with the development of 3D imaging technologies like CT and MRI, that became commercially available in the 1970s [24] and 1980s, respectively. We focus on patient-specific navigation approaches in this chapter and do not delve further into publications from before the time of 3D imaging.

Neurosurgery is one of the pioneering fields in surgical navigation; 3D navigation experiments are reported as early as 1986 [4]. Additional neuronavigation systems and studies are reported in the 1990s, e.g. by Germano et al. [25] and Gumprecht et al. [26], among many others. The navigation workflow described in these works corresponds to the "typical" navigation workflow seen in clinical practice today, namely, navigation of the surgical tools in preoperative patient scans. The most important limitation of this approach can be seen when the intraoperative reality significantly deviates from the anatomy depicted in the preoperative scans. In this case the estimated position of the tracked tools relative to the patient's anatomy can be off by many centimeters, negating the precision benefits navigation is supposed to bring. Outside its application in neurosurgery and in external beam radiation therapy (not discussed in this chapter; see Khan et al. [27] for a review on radiation therapy), navigation is not very widespread in clinical practice thus far, even though many other clinical applications could greatly benefit from a well-thought-out navigation workflow. Mounting evidence of navigation's benefits for particular types of treatment, ideally combined with a greater awareness of what is technically feasible, should slowly change this state of affairs. To grant the reader a short overview of how navigation can be applied in various clinical fields and what the current limitations are, the remainder of this section presents selected research on needle placement, navigated resections, and navigation in orthopedic surgeries.

Needle Placement

The objective of a needle placement procedure is to insert a needle into the patient so that the tip of the needle is as close as possible to the target location. Needles can be used to obtain biopsy samples, radio-frequency (RF) ablations, micro-wave ablations and electrode placement, among many other clinical applications. Some of these applications require a very precise needle placement, and it is expected that these will benefit most from navigation. The main challenge encountered during needle placement is that both the target location defined on imaging and, once the insertion begins, the needle tip are not visible to the physician. To compound these difficulties, the tissue (or needle) may deform during or as a result of the needle placement.

Needle navigation workflows combine patient scans with needle tracking. With tracking (and registration of the tracking system to the patient scans), the estimated (3D) position of the needle tip in the anatomy can be shown in real-time on all patient scans. In most needle navigation workflows, the target

location is marked on one of the registered patient scans, as in Figure 1c; this way the navigation platform can indicate the current needle trajectory or estimate the shortest route from the needle tip to the target location. A more sophisticated workflow could also incorporate the segmentation of critical structures along the possible paths of the needle, allowing for the selection of an optimal path towards the target location whilst avoiding damage to critical structures, as shown in Figure 6c.

Stereotactic needle navigation is already used for decades to aid in the placement of electrodes for deep brain stimulation [28]. For more sophisticated navigation procedures, needles are usually tracked with the NIR optical or EM tracking systems. NIR optical tracking requires the tracker to be in direct line of sight of the cameras, meaning the tracker must be attached to a portion of the needle that is not inserted into the patient. Depending on the precision of the tracking system, and the distance from the tracker to the needle tip, aggravated by the possibility of needle bending, estimates of the needle tip position using NIR optical tracking may be somewhat imprecise. EM tracking does not possess the direct line of sight limitation, and trackers could be attached anywhere on or inside the needle. A particularly interesting recent development are miniaturized EM trackers with less than 1 mm in diameter, i.e. narrow enough to be placed inside needles. As a consequence, EM tracking can now be used to directly track the tip of a needle [29]. Additionally, multiple EM trackers can be used to monitor the bending of needles [30].

Müller et al. [31] investigated needle navigation for soft tissue biopsies, using NIR optical tracking. Navigated and conventional CT-guided liver needle biopsies were compared in five pigs, with a total of 20 tumors biopsied. The authors report that the navigated biopsies, on average, involved significantly fewer CT scans ($p = .01$) and lower dose length products ($p = .001$) compared to the conventional biopsies. Krücker et al. [6] describe the navigation of needles for biopsies and RF ablations, mostly targeted at liver and kidney lesions. Their trial involved 51 navigated needle placements in 40 procedures with a workflow consisting of segmenting the needle target location in preoperative CT scans, sometimes combined with PET scans. During the intervention, navigation of the (EM) tracked needle was combined with conventional ultrasound and 1–5 intraoperative CT scans, to make a correct placement more likely. Both during registration and needle placement, the patient needed to hold his or her breath, to minimize registration errors. The authors compared the precision of conventional image guidance with that of navigation for 19 targets (liver, kidney, neck and paracardiac mediastinum). The authors report a significantly ($p = .0006$) better precision using navigation: range [0.4–12.1 mm] with median 2.5 mm, against range [3.3–81.9 mm] with median 14.8 mm. Additionally one interventional radiologist assessed the utility of all 51 placements: 22 of the placements (43 %) would be very difficult or impossible to perform without navigation and an additional 24 placements (47 %) were facilitated by navigation. This study puts needle

navigation in a very positive light, though the authors point out that the number of patients was relatively small and that a statistically meaningful comparison of outcomes with a control group was not performed.

Ungi et al. [11] propose a radiation-free, ultrasound-only workflow for navigated facet joint injections. The assumption is that this workflow yields the same clinical outcome as alternatives using fluoroscopy or CT imaging, whilst minimizing radiation exposure of the patient and surgical crew. The suggested method would work as follows: (1) a tracked freehand ultrasound scan of the spine segment to be treated is performed prior to needle insertion; (2) after imaging, the target location is segmented in the reconstructed 3D ultrasound volume; and (3) the tracked needle is then navigated to the target. Recall that both tracked tools and images acquired with tracked freehand imaging are in the intraoperative coordinate system, so, in this case, no registration step is required prior to navigation. A particular problem in conventional ultrasound-guided needle placement is that the ideal needle path is often blocked by the transducer during insertion. Hence, separating the imaging and needle insertion steps is a sensible approach. The authors performed 100 facet joint injections in cadaveric lamb models, 50 using the conventional ultrasound-guided method and 50 with the suggested (navigated) method. This increased the insertion success rate 94 % vs. 44 % and significantly shortened insertion times.

Navigated Resections

The surgical removal of all, or part, of an organ, tissue or structure is often performed to treat diseases like cancer. To avoid recurrences, it is important to remove all tumorous tissue during surgery. Ideally the tumor should not be pierced during surgery, to avoid the spillage and possible spread of tumor cells. To accomplish both a thorough tumor removal and minimize spillage, surgeons usually define a safety margin surrounding the tumor and perform the resection around this margin; all tissue inside the safety margin is removed. The resected specimen is then sent to pathology to check for positive margins, i.e. the presence of tumor cells in the edges of the excised specimen. Ideally, pathology should confirm negative specimen margins in all tumor resections. Unfortunately, this is not always the case; for example, Jacobs [32] cites reports of positive margin findings ranging from 20 % to as high as 70 % for partial mastectomies. Identification of the boundary between the diseased and healthy tissues can be addressed by the use of tracers, especially radionuclides, as described in detail in other chapters of this book. Imprecise surgical resection, can probably be improved by navigation. For example, navigation is widely used to resect brain tumors; some of the first navigation systems were designed for neurosurgery applications [2, 25, 26]. On the one hand, the brain is quite susceptible to damage, so surgical interventions should be as precise and minimally invasive as possible, yielding good disease treatment whilst minimizing the chance of permanent neurological damage. Moreover, the brain is embedded in a rigid bone case (the neurocranium),

meaning it does not deform significantly between imaging and surgery. This strong need for precision combined with the favorable rigidity of the target anatomy led to the development of clinically and commercially successful neuronavigation systems (using NIR optical tracking), which make use of preoperative CT or MRI scans. Over the years, attempts to integrate many neurosurgery specific tools, like pointer tools or even entire surgical microscopes [3, 26], have been reported.

Many resections, including brain tumor resections, involve significant tissue deformation during surgery, making traditional preoperative scan-based navigation progressively more imprecise. To counter this, intraoperative CT and MRI systems have been suggested [33, 34]. Due to their relatively high price, complicated logistics, large volume, and relatively long acquisition times, it is questionable if these imaging systems will find widespread adoption in clinical settings. Tracked freehand imaging may prove to be a more viable intraoperative imaging solution. Unsgaard et al. [14] describe a modern neuronavigation workflow for brain tumor resections with preoperative MRI for initial planning and multiple intraoperative tracked ultrasound scans to monitor the progress of the resection and to cope with brain shift [20]. The system used by the authors simultaneously shows the position of the tracked instruments side-by-side on the preoperative MRI and on the latest ultrasound volume. Whenever significant tissue changes occurred, a new ultrasound scan was performed and the navigation procedure was adapted. In addition to more accurate navigation, the authors report that intraoperative ultrasound was very useful in detecting residual tumor after the planned resection was performed. In their subjective experience, in over half of the 91 procedures investigated, residual tumor was discovered in resections that were otherwise considered to be complete. The system described by the authors used NIR optical tracking.

Radioguided interventions are interventions that make use of tracers, especially radioactive tracers that allow for SPECT and PET imaging; fluorescent and hybrid fluorescent-radioactive tracers are also used for some applications [35–37]. Tracers mainly aid in the detection of target structures (like tumors or lymph nodes) and in more precise refinement of their borders. Tracers can be of use both preoperatively, enabling SPECT/CT (Figure 5) and PET/CT scans, and intraoperatively, providing real-time acoustic or visual feedback from radiation or fluorescence readings [38–41].

SPECT, and to a lesser extent PET, scans are generally used to preoperatively identify the lesions that should be taken out during surgery using specialized imaging devices, like gamma probes (1D) or gamma/fluorescence cameras (2D) [42, 43]. A logical evolution of this is to track the intraoperative devices, allowing navigation of them on the preoperative images, possibly reducing the time needed and increasing the accuracy of the intraoperative radioactive hotspot localization. Brouwer et al. [44] successfully navigated a tracked gamma probe in preoperative SPECT/CT images towards sentinel lymph nodes in ten

patients with penile carcinoma. Here preoperative SPECT/CT-based navigation was combined with the intraoperative acoustic feedback produced by the tracked gamma probe. Tracked gamma probes can be used even more extensively in navigation workflows, for the generation of freehand SPECT [16] scans, that can be created during both the pre- and intraoperative process. Freehand SPECT scans have a smaller field of view and may have lower resolution than traditional SPECT scans, but they can be performed with cheaper and significantly less bulky devices. A particular advantage of freehand SPECT is that multiple scans can be performed during surgery if necessary, allowing the surgeon to double-check his or her work thereby decreasing the chance of incomplete resections. Rahbar et al. [45] performed navigated parathyroidectomy combining both preoperative SPECT/CT and freehand SPECT. Other authors report performing navigated sentinel lymph node biopsies on freehand SPECT scans in, for example, breast [12] and head and neck cancer [13, 46]. Recently, Engelen et al. [47] reported on the use of the freehand SPECT technology in combination with a mobile gamma camera. Compared to the gamma probe-based procedure, the use of a mobile camera could speed up the generation of the freehand SPECT, and the sensitivity of the camera might help improve lesion resolvability. All freehand SPECT works cited here used NIR optical tracking to track the gamma probes.

With the introduction of hybrid tracers, that contain both a radioactive and a fluorescent label (e.g. indocyanine green (ICG)-^{99m}Tc-nanocolloid [38, 39, 48]), the field of radioguided surgery further expanded. These tracers can extend navigation workflows based on SPECT/CT and freehand SPECT with intraoperative fluorescence image guidance. Brouwer et al. [49] presented a proof of concept via navigation of a tracked fluorescence laparoscope towards the hybrid tracer-containing sentinel lymph node seen on preoperative SPECT/CT. Here, as soon as the fluorescence laparoscope was near enough to the sentinel lymph node, fluorescence imaging could be performed to complement the navigation. A requirement for a successful hybrid workflow is that navigation leads the laparoscope to less than 1 cm from the target location, since fluorescence signal depth penetration is only around 1 cm in human soft tissue [50]. The benefit provided by the fluorescence imaging is that a real-time visual feedback of the tracer with respect to the local anatomy is provided. This real-time feedback can be used to better cope with potential inaccuracies in the SPECT/CT-based navigation, e.g. due to patient movement and tissue deformation.

Navigated Orthopedic Surgeries

Orthopedic surgeries are performed to treat fractures and congenital musculoskeletal malformations and to replace worn out joints with implants, among many other applications. Many orthopedic surgeries, especially procedures involving implant placement, are focused on bones, making them particularly promising candidates for navigation. Bones, unlike soft tissue, usually do not deform. This rigidity should, therefore, lead to precise registrations and, as a

consequence, precise navigations. The assumption is that the machine precision provided by navigation leads to a faster and more precise implant placement. This increased implant placement accuracy may lead to a better clinical outcome, e.g. increased range of motion, better joint stability, increased implant longevity and later onset of arthritis.

Rambani et al. [51] reviewed numerous applications of navigation in orthopedic surgery, with an emphasis on navigated total knee arthroplasty (TKA) and total hip arthroplasty (THA). The authors pointed out that both for TKA and THA, correct implant alignment is essential to increase implant longevity and to achieve a good functional outcome. It was assumed that navigation may improve implant alignment compared to conventional TKA and THA. However, a recent meta-analysis involving 3423 patients (33 studies) concluded that navigated TKA brings no clear benefits in clinical outcome compared to conventional TKA, whilst at the same time, the mean duration of surgery was increased by 23 % [52]. On the other hand, a meta-analysis of three THA studies (n = 250) concluded that navigation in THA improves the precision of acetabular cup placement [53]. Taking both these studies into account, the authors conclude that the potential benefits of navigation both for TKA and THA are not yet clearly proven or disproven and suggest multicenter randomized controlled trials with long-term follow-up for these procedures.

Larson et al. [7] described the navigated placement of pedicle screws in pediatric patients with congenital spine deformity. Their workflow consisted of an initial planning of the screw placement performed on preoperative CT scans. Then, during surgery, one or more intraoperative CT scans of the spine, with an optical tracker screwed onto the patient, were used for surgical navigation (as in Figure 1b). This form of navigation allowed the authors to measure the width and depth of each screw tract, allowing screw dimensions to be custom fit to each pedicle. Results of 14 patients were presented (four cases of isolated hemivertebra and ten cases of complex spinal deformations), with a total of 142 screws placed. In this study, a 99.3 % success rate was achieved, even though the majority of screws was placed in vertebrae with congenital deformities. The authors report that comparable precision for pedicle screw placement without navigation was obtained in other studies [54], albeit for patients without congenital spine deformity.

Both Rana et al. [9] and Gander et al. [8] describe the reconstruction of unilateral orbital fractures combining the use of selective laser-melted patient-specific implants (PSIs) and navigated implant placement. Gander et al. point out that inadequate implant shape and imprecise implant placement may lead to visual disturbance and aesthetically poor results. It is assumed that PSIs have a shape that better fits to the fractured anatomy and that navigation improves the precision of the implant placement. The workflow starts with a CT scan of the patient, depicting both the fractured and the uninjured orbits, followed by a computer-aided planning step to determine the desired shape of the

implant. PSIs are outfitted with ridges and landmarks, which enable navigated placement. The implants are not tracked directly; instead a tracked pointer is manually placed along the implant's ridges and landmarks during navigated insertion. Once the implant is in place, the tracked pointer can be used to verify that the implant placement is precise enough, potentially avoiding the need of additional scans to verify the implant placement after surgery. The navigation is performed on the preoperative CT scan. Both groups proceed to analyze if the proposed workflow is superior to the more traditional (manually) pre-bent titanium mesh (PBTM) implants. Based on their experiments, both groups suggest PSIs are superior to PBTM implants. Unfortunately, none of the groups directly measured the impact navigation had on the procedure or on the clinical outcome; navigation was simply used in all procedures, presumably under the assumption that this would lead to more precise (or equally precise, but faster) implant placement.

DISCUSSION

In this chapter we described surgical navigation methods and their clinical applications over a broad range of medical fields. Navigation promises to bring machine precision to the operating room. Most authors reported a positive opinion of navigation, usually backed by experimental results from (small) clinical studies. Additionally, many authors expressed the subjective opinion that navigation was beneficial or helpful for their respective application; Krücker et al. [6] go as far as stating that "procedures were facilitated that would have otherwise been difficult or impossible to perform without this technology". These results place navigation in a good light, but there are some issues that still need to be considered.

We identified three navigation workflow variants in clinical practice. The first variant is navigation on preoperative scans alone, which is usually seen in interventions with no significant tissue deformation during surgery, for example, the navigated reconstruction of unilateral orbital fractures [8, 9]. The same type of navigation can also be used to bring surgical instruments close to the target location in (laparoscopic) surgeries, as reported by Brouwer et al. [49]. Navigation on preoperative scans is the most straightforward and probably most widely used navigation variant. In some cases, however, the navigation based on preoperative scans alone can become quite imprecise, especially in the later stages of an intervention, where significant tissue deformation and patient movement may have taken place. To date tissue deformation and patient movement between imaging and surgery present significant challenges to navigation on preoperative scans. Fortunately, many creative solutions to detect and deal with deformation are already reported in literature. Krücker et al. [6], who investigated navigation in the thoracic and abdominal cavities, mentioned breath holding and respiratory gating to minimize deformations. Using a redundant

amount of fiducials, non-rigid movement could be detected. A second navigation variant combines navigation on preoperative scans with intraoperative scans. In this variant, the navigation on preoperative scans only provides rough guidance, and, whenever more precision is needed, intraoperative scans are taken. Such workflows are described in [6, 7, 14]. Navigation workflows using preoperative scans alone are unsuitable for many clinical applications. With the integration of intraoperative imaging into a workflow, such navigation can, however, be applied in a much broader range of settings. The final navigation variant is navigation on intraoperative scans alone. This variant has become practical with the recent emergence of tracked freehand imaging. Recall that both tracked tools and images from tracked freehand imaging are in the same coordinate system, meaning no registration between patient scans and surgical tools is required, thus leading to a simpler navigation workflow. This navigation variant is already reported by a few groups [11–13], and we expect this list to grow significantly with the more widespread adoption of tracked freehand imaging systems.

Regarding tracking technologies, both EM and NIR optical tracking are widely used both for freehand imaging and navigation. Both technologies work well most of the time. Tracker occlusion is the main drawback of NIR optical tracking; distortion of the magnetic field due to metallic objects and small working volume are the drawbacks of EM tracking. It is not yet clear which technology will become dominant. However, with the advent of miniaturized EM trackers, that fit inside needles and can directly track the tip [29], it seems EM tracking has an advantage, at least, in needle placement interventions.

Most navigation workflows presented in this chapter compared favorably to their conventional, non-navigated alternatives. This, however, is not sufficient evidence to make blanket statements about the usefulness of navigation in general. In fact, there also is evidence suggesting that navigation provides no tangible benefits during some types of surgery; for example, Bauwens et al. [52] pointed out that navigation seems to bring no benefits to TKA surgeries. Another important issue is the amount of evidence presented to back up the claims of the benefits of a navigation workflow. Randomized controlled trials (RCT) involving large numbers of patients, the current gold standard for clinical trials, have not been performed for any of the reported methods. An open question is how much and what kind of evidence is considered sufficient to prove the benefits (or lack thereof) of a navigation workflow. It is unclear how the alleged benefits of a particular navigation workflow compared to an equivalent non-navigated alternative should be measured. Perhaps precision should be measured directly, as reported by Krücker et al. in [6], where the needle angle insertion is measured both for the navigated and non-navigated workflows; based on these measurements, estimates of the procedures' precision can be calculated and compared. Or perhaps the clinical outcome after a number of years should be evaluated instead, as in the meta- analysis of TKA and THA clinical studies reported by Rambani et al. in [51]. Alternatively, the subjective opinion of an expert [6, 14]

may also provide a relevant measure. Should the experience of a surgeon also influence the measure? If so, how should one combine results from multiple surgeons with different skill sets? The lack of a consensus on how to measure the benefits of a navigation workflow surely stands in the way of large clinical trials. It is unclear when, or even if, a consensus on this measure will emerge. Even if a consensus measure emerges, one should consider if RCTs are the ideal type of trial for navigation workflows. Can clinical equipoise, i.e. the existence of a general uncertainty in the expert medical community over whether a technique is beneficial or not, be assumed for all navigation workflows? If a surgical team strongly believes a navigation workflow is superior to the alternative for a specific type of surgery, is it acceptable to perform non-navigated surgery just for the sake of a more statistically sound trial? Given all these questions, chances are RCTs will not be performed for many current and future navigation workflows. Alternative ways of gathering convincing evidence should probably be investigated. It should be pointed out that convincing evidence of the clinical benefits of a technique is a precondition for reimbursement by health insurance companies in many countries, so providing such evidence for navigated workflows is essential for them to become mainstream.

Whilst navigation is not (yet) the ultimate solution to improve surgical outcomes across the board, it does seem to be genuinely beneficial in various types of surgery. Evidence suggesting better clinical outcomes in these cases combined with ever lower barriers to its adoption leads us to believe that the use of navigation will be much more widespread in the near future, hopefully contributing to better clinical outcomes for ever more patients.

REFERENCES

1. *Rassweiler J, et al. Surgical navigation in urology: European perspective. Curr Opin Urol. 2014;24(1): 81–97.*
2. *Willems P, et al. Neuronavigation and surgery of intra- cerebral tumours. J Neurol. 2006;253(9):1123–36.*
3. *Watanabe E, et al. Three-dimensional digitizer (neuro- navigator): new equipment for computed tomography-guided stereotaxic surgery. Surg Neurol. 1987;27(6): 543–7.*
4. *Roberts DW, et al. A frameless stereotaxic integration of computerized tomographic imaging and the operating microscope. J Neurosurg. 1986;65(4):545–9.*
5. *Balter JM, et al. Accuracy of a wireless localization system for radiotherapy. Int J Radiat Oncol Biol Phys. 2005;61(3):933–7.*
6. *Krücker J, et al. Clinical utility of real-time fusion guidance for biopsy and ablation. J Vasc Interv Radiol. 2011;22(4):515–24.*
7. *Larson AN, et al. The accuracy of navigation and 3D image-guided placement for the placement of pedicle screws in congenital spine deformity. J Pediatr Orthop. 2012;32(6):e23–9.*
8. *Gander T, et al. Patient specific implants (PSI) in reconstruction of orbital floor and wall fractures. J Craniomaxillofac Surg. 2015;43(1):126–30.*
9. *Rana M, et al. Increasing the accuracy of orbital reconstruction with selective laser melted patient-specific implants combined with intraoperative navigation. J Oral Maxillofac Surg. 2015;73(6):1113–8.*

10. *Matziolis G, et al. A prospective, randomized study of computer-assisted and conventional total knee arthroplasty. J Bone Joint Surg Am. 2007;89(2):236–43.*
11. *Ungi T, Lasso A, Fichtinger G. Tracked ultrasound in navigated spine interventions. In: Spinal imaging and image analysis. Cham: Springer; 2015. p. 469–94.*
12. *Bluemel C, et al. Freehand SPECT for image-guided sentinel lymph node biopsy in breast cancer. Eur J Nucl Med Mol Imaging. 2013;40(11):1656–61.*
13. *Heuveling DA. Evaluation of the use of freehand SPECT for sentinel node biopsy in early stage oral carcinoma. Oral Oncol. 2015;51(3):287–90.*
14. *Unsgaard G, et al. Neuronavigation by intraoperative three-dimensional ultrasound: initial experience during brain tumor resection. Neurosurgery. 2002;50(4):804–12.*
15. *Fenster A, Downey DB, Cardinal HN. Three-dimensional ultrasound imaging. Phys Med Biol. 2001;46(5):R67.*
16. *Wendler T, et al. First demonstration of 3-D lymphatic mapping in breast cancer using freehand SPECT. Eur J Nucl Med Mol Imaging. 2010;37(8):1452–61.*
17. *Bluemel C, et al. Freehand SPECT-guided sentinel lymph node biopsy in early oral squamous cell carcinoma. Head Neck. 2014;36(11):E112–6.*
18. *Navab N, et al. First deployments of augmented reality in operating rooms. Computer. 2012;7:48–55.*
19. *Rueckert D, et al. Nonrigid registration using free- form deformations: application to breast MR images. IEEE Trans Med Imaging. 1999;18(8):712–21.*
20. *Roberts DW, et al. Intraoperative brain shift and deformation: a quantitative analysis of cortical dis- placement in 28 cases. Neurosurgery. 1998;43(4): 749–58.*
21. *Ferrant M, et al. Registration of 3-D intraoperative MR images of the brain using a finite-element biomechanical model. IEEE Trans Med Imaging. 2001;20(12):1384–97.*
22. *van Rikxoort EM, et al. Adaptive local multi-atlas segmentation: application to heart segmentation in chest CT scans. Proc. SPIE 6914, Medical Imaging 2008: Image Processing, 691407. DOI:10.1117/12.772301.*
23. *Kandel EI, Schavinsky YV. Stereotaxic apparatus and operations in Russia in the 19th century. J Neurosurg. 1972;37(4):407–11.*
24. *Beckmann E. CT scanning the early days. BJR. 2005;79(937):5–8.*
25. *Germano IM. The NeuroStation system for imageguided, frameless stereotaxy. Neurosurgery. 1995; 37(2):348–50.*
26. *Gumprecht HK, Widenka DC, Lumenta CB. BrainLab VectorVision Neuronavigation System: technology and clinical experiences in 131 cases. Neurosurgery. 1999;44(1):97–104.*
27. *Khan FM, Gibbons JP. Khan's the physics of radiation therapy. Philadelphia: Lippincott Williams & Wilkins; 2014.*
28. *Holl EM, et al. Improving targeting in image-guided frame-based deep brain stimulation. Neurosurgery. 2010;67:ons437–47.*
29. *Hakime A, et al. Electromagnetic-tracked biopsy under ultrasound guidance: preliminary results. Cardiovasc Intervent Radiol. 2012;35(4):898–905.*
30. *Lei P, et al. Real-time tracking of liver motion and deformation using a flexible needle. Int J Comput Assist Radiol Surg. 2011;6(3):435–46.*
31. *Müller SA, et al. Navigated liver biopsy using a novel soft tissue navigation system versus CT-guided liver biopsy in a porcine model: a prospective randomized trial. Acad Radiol. 2010;17(10):1282–7.*
32. *Jacobs L. Positive margins: the challenge continues for breast surgeons. Ann Surg Oncol. 2008;15(5):1271–2.*
33. *Maesawa S, et al. Clinical indications for high-field 1.5 T intraoperative magnetic resonance imaging and neuro-navigation for neurosurgical procedures-review of initial 100 cases. Neurol Med Chir. 2009;49(8): 340–50.*
34. *Grunert P, et al. Basic principles and clinical applications of neuronavigation and intraoperative computed tomography. Comput Aided Surg. 1998;3(4):166–73.*

35. *Mariani G, et al. A review on the clinical uses of SPECT/CT. Eur J Nucl Med Mol Imaging. 2010; 37(10):1959–85.*
36. *van den Berg N, et al. Hybrid tracers for sentinel node biopsy. Q J Nucl Med Mol Imaging. 2014;58: 193–206.*
37. *Histed SN, et al. Review of functional/anatomic imaging in oncology. Nucl Med Commun. 2012;33(4):349.*
38. *van den Berg NS, et al. Multimodal surgical guidance during sentinel node biopsy for melanoma: combined gamma tracing and fluorescence imaging of the sentinel node through use of the hybrid tracer indocyanine green-(99m)Tc-nanocolloid. Radiology. 2015;275(2):521–9.*
39. *Brouwer OR, et al. A hybrid radioactive and fluorescent tracer for sentinel node biopsy in penile carcinoma as a potential replacement for blue dye. Eur Urol. 2014;65(3):600–9.*
40. *KleinJan GH, et al. Optimisation of fluorescence guidance during robot-assisted laparoscopic sentinel node biopsy for prostate cancer. Eur Urol. 2014;66(6):991–8.*
41. *Eiber M, et al. Evaluation of hybrid 68Ga-PSMA- ligand PET/CT in 248 patients with biochemical recurrence after radical prostatectomy. J Nucl Med. 2015;56(5):668–74.*
42. *Povoski SP, et al. A comprehensive overview of radioguided surgery using gamma detection probe technology. World J Surg Oncol. 2009;7(1):11.*
43. *Heller S, Zanzonico P. Nuclear probes and intraoperative gamma cameras. Semin Nucl Med. 2011;41(3): 166–81.*
44. *Brouwer OR, et al. Feasibility of intraoperative navigation to the sentinel node in the groin using preoperatively acquired single photon emission computerized tomography data: transferring functional imaging to the operating room. J Urol. 2014; 192(6):1810–6.*
45. *Rahbar K, et al. Intraoperative 3-D mapping of parathyroid adenoma using freehand SPECT. EJNMMI Res. 2012;2(1):51.*
46. *Mandapathil M, et al. Freehand SPECT for sentinel lymph node detection in patients with head and neck cancer: first experiences. Acta Otolaryngol. 2014; 134(1):100–4.*
47. *Engelen T, et al. The next evolution in radioguided surgery: breast cancer related sentinel node localization using a freehandSPECT-mobile gamma camera combination. Am J Nucl Med Mol Imaging. 2015;5(3):233–45.*
48. *Brouwer OR, et al. Comparing the hybrid fluorescent–radioactive tracer indocyanine green–99mTc-nanocolloid with 99mTc-nanocolloid for sentinel node identification: a validation study using lymphoscintigraphy and SPECT/CT. J Nucl Med. 2012;53(7): 1034–40.*
49. *Brouwer OR, et al. Image navigation as a means to expand the boundaries of fluorescence-guided surgery. Phys Med Biol. 2012;57(10):3123.*
50. *Chin PT, et al. Multispectral visualization of surgical safety-margins using fluorescent marker seeds. Am J Nucl Med Mol Imaging. 2012;2(2):151.*
51. *Rambani R, Varghese M. Computer assisted navigation in orthopaedics and trauma surgery. Orthop Trauma. 2014;28(1):50–7.*
52. *Bauwens K, et al. Navigated total knee replacement. J Bone Joint Surg Am. 2007;89(2):261–9.*
53. *Gandhi R, et al. Computer navigation in total hip replacement: a meta-analysis. Int Orthop. 2009;33(3): 593–7.*
54. *Ledonio CGT, et al. Pediatric pedicle screws: comparative effectiveness and safety. J Bone Joint Surg Am. 2011;93(13):1227–34.*

CHAPTER 3

NAVIGATION OF A ROBOT-INTEGRATED FLUORESCENCE LAPAROSCOPE IN PREOPERATIVE SPECT/CT AND INTRAOPERATIVE FREEHAND SPECT IMAGING DATA: A PHANTOM STUDY

Adapted from: van Oosterom MN, Engelen MA, van den Berg NS, KleinJan GH, van der Poel HG, Wendler T, van de Velde CJH, Navab N., van Leeuwen FWB

The Journal of Biomedical Optics, 2016, 21(8): 086008

ABSTRACT

Robot-assisted laparoscopic surgery is becoming an established technique for prostatectomy and is increasingly being explored for other types of cancer. Linking intraoperative imaging techniques, such as fluorescence guidance, with the three-dimensional insights provided by preoperative imaging remains a challenge. Navigation technologies may provide a solution, especially when directly linked to both the robotic setup and the fluorescence laparoscope. We evaluated the feasibility of such a setup. Preoperative single-photon emission computed tomography/X-ray computed tomography (SPECT/CT) or intraoperative freehand SPECT (fhSPECT) scans were used to navigate an optically tracked robot-integrated fluorescence laparoscope via an augmented reality overlay in the laparoscopic video feed. The navigation accuracy was evaluated in soft tissue phantoms, followed by studies in a human-like torso phantom. Navigation accuracies found for SPECT/CT-based navigation were 2.25 mm (coronal) and 2.08 mm (sagittal). For fhSPECT-based navigation, these were 1.92 mm (coronal) and 2.83 mm (sagittal). All errors remained below the <1-cm detection limit for fluorescence imaging, allowing refinement of the navigation process using fluorescence findings. The phantom experiments performed suggest that SPECT-based navigation of the robot-integrated fluorescence laparoscope is feasible and may aid fluorescence-guided surgery procedures.

INTRODUCTION

Despite the fact that robot-assisted laparoscopic surgery can provide value in many surgical applications (e.g., gynecologic [1], liver [2], and rectal [3] surgery), it is still most commonly used for the surgical management of prostate cancer [4]. In addition to the removal of the primary prostate cancer (prostatectomy), such procedures are often accompanied by a form of lymph node dissection focused on the removal of lymphatic metastases, e.g., a (extended) lymphadenectomy, a sentinel node (SN) procedure [5], or, in the future, a prostate-specific membrane antigen targeted nodal dissection [6].

It is widely accepted that image guidance toward the (possible) location of prostate cancer metastases may help improve surgical accuracy and therefore reduce the procedure-associated side effects [7]. It is for this reason that the da Vinci robotic platform (Intuitive Surgical Inc., Sunnyvale, California) is now routinely equipped with a near-infrared (NIR) fluorescence laparoscope (Firefly, Intuitive Surgical Inc.). The concept here is that fully integrated visual identification of the target, using fluorescence guidance, helps the urologist to interpret the surgical field and, as such, improves surgical guidance. Unfortunately, fluorescence guidance has a very limited in-depth signal penetration due to absorption and scatter of the fluorescence excitation and emission light by tissue (roughly <1 cm) [8,9]. This makes the technology lose value when lesions are located at unknown locations hidden deep within the patient's anatomy. We underlined this shortcoming during robot-assisted SN biopsy procedures that made use of a tracer that is both radio- and fluorescence-labeled indocyanine green (ICG)-^{99m}Tc-nanocolloid [10,11]. These studies illustrated that, dependent on the camera system, up to 19.6% of the SNs were missed during the urologist's fluorescence-based inspection of the surgical field. Here, insight with regard to the tracer location, provided by the preoperative single-photon emission computed tomography/X-ray computed tomography (SPECT/CT) images, enabled the urologist to also resect the SNs not directly visible using fluorescence imaging. Ex vivo fluorescence imaging then confirmed the presence of the fluorescence signal in the resected SNs.

Based on the preoperatively acquired imaging information, surgeons can cognitively plan their route toward target structures [e.g., tumorous tissue or (tumor positive) lymph nodes] and around delicate structures (e.g., blood vessels, nerves, and/or ureters). Unfortunately, applying this information in the operating room (OR) remains challenging. The link between using pre- and intraoperative imaging methods may be strengthened using surgical navigation (via e.g., optical patient tracking), allowing a technological integration of pre- and intraoperative findings. Applying this technology to soft tissue environments is challenging due to tissue shift and deformation. Here, movement after acquisition of the patient scan(s) poses the biggest problem [12-15]. Such deformations can only be corrected using intraoperative imaging findings and/or reference

marker points placed at the tissue of interest. For example, a radioactive readout can be used to confirm the navigation accuracy or even provide an intraoperative freehand SPECT (fhSPECT) scan that allows for navigation in a three-dimensional (3-D) "snapshot" map generated in the OR setting [16-19]. Alternative to (or in conjunction with) using a radioactive signature for intraoperative confirmation of the navigation accuracy, validation in the form of fluorescence imaging can be used [20,21]. In this study, we describe the integration of the above features in a robotic setup using (human-like) phantoms. For this, we used both SPECT/CT and fhSPECT findings as the basis for the navigation process. Additionally, we have integrated these data sets into the laparoscopic video feed using an augmented reality overlay. Such a "hybrid navigator" concept also means that in the future, different pre- and intraoperative imaging sources can be integrated in an interactive augmented reality view that can be fed into the console of the operating urologist.

METHODS

Navigated Fluorescence Laparoscope Setup

The complete navigation setup consisted of a combination of the Firefly laparoscope, integrated with the da Vinci® Si surgical robot, and the declipseSPECT navigation system (SurgicEye GmbH, Munich, Germany; Figure 1a) with integrated NIR optical tracking system (OTS; Polaris Vicra, Northern Digital Inc., Waterloo, Canada), which provides a tracking accuracy <0.5 mm (95% confidence interval; 0.25 mm root mean square (RMS) [22]). Different reference targets were used to optically track the 3-D position and orientation (3-D pose) of objects, such as the laparoscope, gamma probes, and the different phantom setups. All reference targets contained a unique asymmetric geometry of at least three fiducials visible to the OTS.

To allow for the navigation device to describe all the different objects (e.g., surgical target and laparoscope) in the surgical workflow, all objects had to be connected by placing them in a common coordinate system provided by the OTS [23]. Transforming a 3-D object pose from one coordinate system to another was achieved using 4 × 4 transformation matrices. An overview of the different transformations needed in this setup is illustrated in Figure 1. Estimation of these transformations is described in more detail throughout the text below.

Single-Photon Emission Computed Tomography/X-Ray Computed Tomography

Before acquisition of the SPECT/CT scan, a three-fiducial phantom reference target (PRT) was fitted to the exterior of the phantom setups, allowing for optical tracking by the OTS. It remained at a fixed position with respect to the phantom throughout the experiments. Next to its visibility to the OTS, this PRT is also

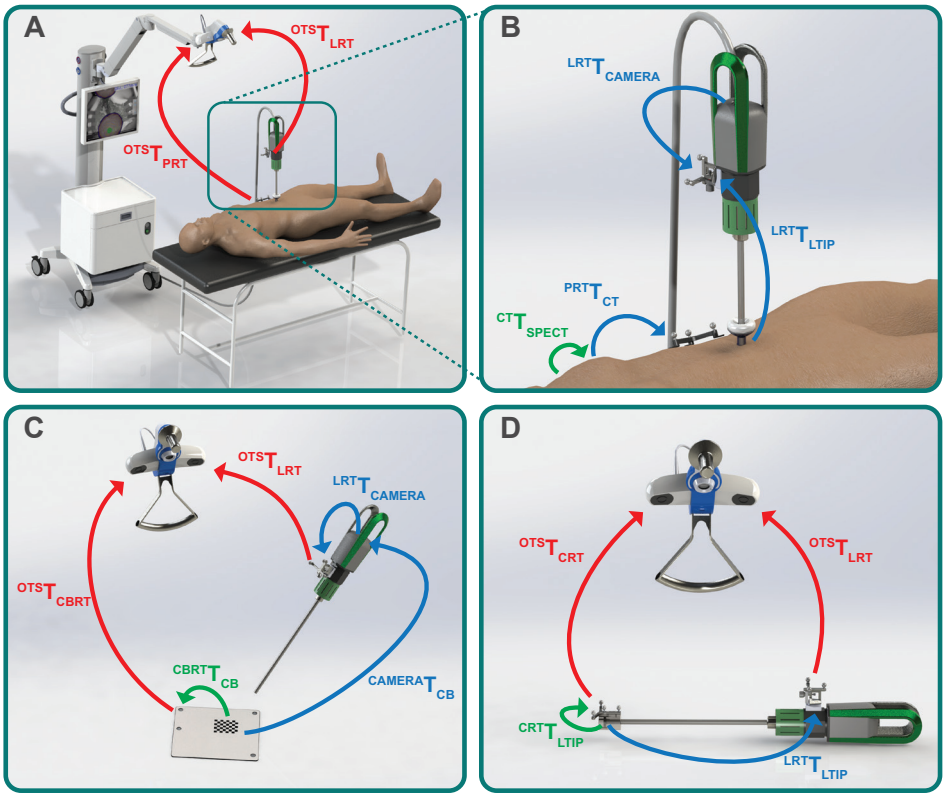

Figure 1. Overview navigation setup and underlying coordinate transformations. (a) *Schematic overview of the navigation setup showing the navigation system with the overhead camera and OTS positioned above the patient. Both patient and fluorescence laparoscope are tracked with a unique reference target. Transformations from both the PRT and LRT coordinate systems to the OTS coordinate system are displayed with the red arrows.* ***(b)*** *Zoom-in of the PRT and LRT fixed to the patient and laparoscope, respectively. The green and blue arrows in the lower left corner are figurative and describe the transformation from the SPECT data coordinate system to that of the CT data and from the CT data to the PRT, respectively. The blue* ${}^{LRT}T_{CAMERA}$ *transformation arrow is calculated in the calibration shown in* ***(c)*** *and the blue* ${}^{LRT}T_{LTIP}$ *transformation arrow is calculated in the calibration shown in* ***(d)****, with LTIP indicating the laparoscope's tip.* ***(c)*** *Schematic overview of the coordinate transformations in the checkerboard calibration step. Both of the blue transformation matrices shown here are found in this calibration step. The green transformation is given to the navigation system (here, CB stands for checkerboard and CBRT stands for checkerboard reference target).* ***(d)*** *Schematic overview of the coordinate transformations in the tip calibration step. This calibration step determines the blue transformation matrix* ${}^{LRT}T_{LTIP}$*. Similar as stated above, the green transformation is given to the navigation (here, CRT stands for calibrator reference target). 3-D models of dummy human male (by user Areshero) and hospital bed (by user Felipe Ospina Ochoa) come from the community library of grabcad.com.*

clearly distinguishable in the CT imaging data, allowing the navigation system to segment it from the CT imaging data and calculate the transformation ${}^{PRT}T_{CT}$ from the CT coordinate system to the PRT coordinate system (Figure 1b) [20]. Since the SPECT/CT imaging system (Dual Head Symbia TruePoint SPECT/CT, Siemens

Healthcare GmbH, Erlangen, Germany) was a combined apparatus, the registration between the CT and SPECT imaging data itself is provided in the digital imaging and communications in medicine tags of the 3-D images. This allows for the connection between the SPECT imaging data and the CT coordinate system provided by the transformation matrix ${}^{CT}T_{SPECT}$.

Freehand Single-Photon Emission Computed Tomography

Multiple fhSPECT scans were acquired using either an SOE 311 gamma probe with a Europrobe 3 control unit (Eurorad S.A., Eckbolsheim, France) or a HiSens gamma probe with a, SG03 control unit (Crystal Photonics GmbH, Berlin, Germany). A four-fiducial gamma probe reference target (GPRT) was fitted to allow tracking of these modalities by the navigation system. Scanning times varied between 2 and 3 min. Placement of the PRT was the same as for SPECT/CT-based navigation. Using both the PRT and the GPRT during the fhSPECT acquisition, the 3-D fhSPECT scanning data can be placed in the navigation workflow by linking it to the PRT via the 4 × 4 transformation matrix ${}^{PRT}T_{fhSPECT}$, provided by the navigation system itself.

Fluorescence Laparoscope

During the navigation experiments, both the standard laparoscope white-light setting and the fluorescence light setting were used. To connect the laparoscope video feed to the navigation system, an Epiphan frame grabber (DVI2PCIe, Epiphan Systems Inc., Ottawa, Ontario, Canada) was integrated into the navigation cart. Either the laparoscope processed video feed was connected directly from the digital visual interface (DVI) output at the back of the surgical robot vision cart or the laparoscope raw video feed was connected from the component output on the back of the camera console. To track the 3-D pose of the laparoscope with the navigation system, a three-fiducial reference target was attached to the camera housing (laparoscope reference target (LRT); see Figure 1b). The optical wavelengths used for object tracking and fluorescence emission partly overlapped, being both in the 800- to 900-nm range. Nevertheless, interference issues were not expected during intra-abdominal use of the laparoscope.

An adapted version of the declipseSPECT 6.0 (SurgicEye GmbH) software was used to incorporate the laparoscope video feed in both calibration and navigation workflows. Two steps of calibrations were performed with the fluorescence laparoscope to allow proper use in the navigation workflow:

1. Calibration of intrinsic and extrinsic camera-system parameters using a “checkerboard” calibration and the Open Source Computer Vision (OpenCV) camera calibration library [24]. The intrinsic camera parameters were the focal length and principal point while the extrinsic camera parameters described the translation and rotation with respect to the LRT coordinate system represented by the transformation matrix ${}^{LRT}T_{CAMERA}$ (see Figure 1b-c).

The calibration of these camera parameters was performed to enable an augmented reality projection of the processed pre- or intraoperative imaging data on top of the fluorescence laparoscope video feed; thus providing the augmented projection of navigation targets (with SPECT) and anatomical reference (with CT) in both the whitelight and fluorescence light camera options.

2. Calibration of the 3-D pose transformation from the coordinate system of the laparoscope tip to that of the LRT was defined as transformation matrix ${}^{LRT}T_{LTIP}$ (see Figure 1d). The laparoscope tip calibration was performed with a cylindrical construction (a calibrator), tracked with a four-fiducial calibrator reference target (CRT). Because of the known geometry of the calibrator, it was possible to determine the relation between the CRT and the center of the tip of the laparoscope, represented by the transformation matrix ${}^{CRT}T_{LTIP}$. During the navigated procedure, this tip calibration allows the navigation system to display the relative distance from the laparoscope tip to one of the selected navigation targets.

Soft Tissue Phantom

The soft tissue phantom setup (Figure 2a) consisted of a tray with the PRT placed on a stand and a silicone half sphere with four Eppendorf tubes (Eppendorf AG, Hamburg, Germany) placed inside. The silicone half sphere structure, with a diameter of ~15 cm at its base and a height of ~5 cm, was cast from Dragon Skin® FX-Pro silicone rubber (Smooth-On Inc., Macungie, Pennsylvania), with addition of Thi-Vex® Silicone Thickener (Smooth-On Inc.) for the skin part and Slacker® Tactile Mutator (Smooth-On Inc.) for the softer fat part. SilTone pigments (FormX, Amsterdam, The Netherlands) were used to color the rubber.

Two 260-µL Eppendorf tubes served as the navigation targets, to be scanned with (fh)SPECT imaging, and were placed at roughly 5 cm apart. With a volume of 260 µL, the Eppendorf tubes should resemble a typical lymph node size found in lymph node dissection for prostate cancer; KleinJan et al. [25] reported a range of 80 to 860 µL, with a median of 170 µL. These tubes were filled with a mixture of ICG and ^{99m}Tc: 253 µL of an ICG solution and 7 µL of a ^{99m}Tc solution (~5 MBq). The ICG solutions used, in this study, consisted of 31.25 µg/mL ICG (ICG-Pulsion, Pulsion Medical Systems, Munich, Germany) dissolved in human serum albumin (Albuman 200 g/l, Sanquin, Amsterdam, The Netherlands). With this as stock solution, the effective ICG solutions used in the phantom experiments range from 9.62 to 31.03 µg/mL. This quantity was chosen based on both clinical relevance (0 to 18.10 µg/mL typically found in lymph nodes during prostatectomy [25]) and best visibility during fluorescence guidance (best visibility found between 2.44 and 78.27 µg/mL [26]). The ^{99m}Tc solutions used, in this study, were obtained from a ^{99m}Tc-sodium pertechnetate solution (750 MBq/mL saline, Technekow, Mallinckrodt Medical BV, Petten, The Netherlands). Two

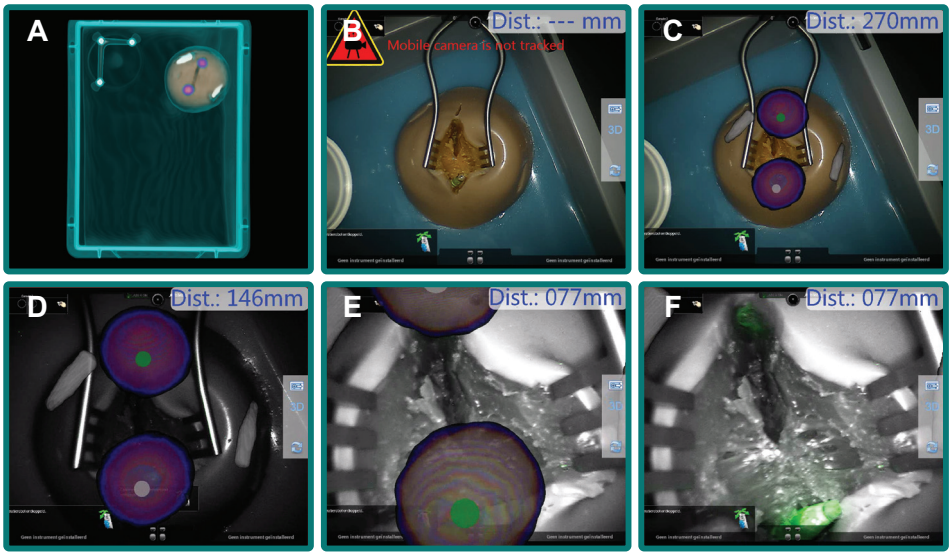

Figure 2. Navigation of the fluorescence laparoscope based on preoperative SPECT/CT imaging and intraoperative fluorescence guidance as performed on the tissue-mimicking phantom set-up. (a) *Volume rendering of the fused SPECT/CT scan of the tissue-mimicking phantom setup. The SPECT hotspots are shown in purple/blue.* ***(b–f)*** *Augmented reality video feed from the perspective of the fluorescence laparoscope as seen on the navigation device, when navigating to the navigation targets. These targets are indicated as gray and green circles and are defined by the SPECT signal (displayed purple/blue). The distance shown is the distance from the tip of the camera to the selected (green) target. The CT overlay is shown in white/gray.* ***(b)*** *The phantom shown by white-light modus, without augmented SPECT/CT overlay. (An error states that the mobile camera is not tracked due to the LRT being just at the border of the tracking volume.)* ***(c)*** *White-light modus with augmented SPECT/CT overlay.* ***(d, e)*** *Fluorescence light modus with augmented SPECT/CT overlay. In this mode, the background video is shown in gray.* ***(f)*** *Fluorescence light modus without augmented SPECT/CT overlay. Fluorescence is displayed in green.*

additional 500-µL Eppendorf tubes were hidden on the sides of the tissue mimicking structure to serve as "anatomical reference" in the CT images. These tubes were filled with CT contrast agent [Ultravist 300 mg/mL (Bayer AG, Leverkusen, Germany) 50% diluted with demineralized water]. To constrain movement of all the objects in the phantom setup, and therefore constrain the navigation error, the silicone structure and the PRT stand were glued to a silicone bottom layer in the tray. The PRT itself was taped to the stand. Note however, to allow easy access to the target sources, the precut phantoms were opened with a wound spreader during navigation, a manipulation that could have possibly introduced a (minor) deformation error to the navigation setup.

Laparoscopic Torso Phantom

The human-like laparoscopic torso phantom was made out of a standard life-sized anatomical model of the human skeleton, generally used for educational

purposes. A transparent plastic mannequin was split in two parts over the coronal plane and the skeleton was cut to fit inside. The skeleton was fixed after which a silicone model of the prostate and three lymph nodes were incorporated, thereby simulating the SN biopsy procedure during robot-assisted laparoscopic prostatectomy [10,11,27]. Both the prostate model and the lymph node models were cast from Dragon Skin® FX-Pro silicone rubber and Slacker® Tactile Mutator using the color pigments for different colors. Mixtures of ICG and ^{99m}Tc were then inserted into the prostate and SN models. For the prostate model, a 1.5-mL Eppendorf tube was incorporated in the cast and was used to store a 260-µL tube filled with 80 µL of the ICG solution and 180 µL of the ^{99m}Tc solution (~200 MBq). The lymph node phantoms contained a 260-µL tube with a mixture of 258 µL of the ICG solution and 1.8 µL of the ^{99m}Tc solution (~2 MBq). This resulted in a 100:1 ratio in radioactivity for the prostate model with respect to each of the individual lymph nodes, which should be a reasonable ratio in SN mapping [28-31].

Four 12-mm trocars were placed in the transparent shell of the torso phantom to allow docking of the da Vinci robot, including the fluorescence laparoscope. A PRT was fixed at the sternum location of the phantom.

Evaluation Navigation Accuracy

The total navigational accuracy was evaluated in the soft tissue phantom setups and divided in both coronal and sagittal errors. The laparoscope was placed in a stand vertically with respect to the navigation target at a distance of roughly 5 cm. The navigation accuracy determination was then performed manually by comparing the target distance as given by the navigation system to the distance found with a ruler (measurement precision of ~1 mm), in a manner similar to that described by Brouwer et al. [16]. For the sagittal plane, the distance from laparoscope tip to target was indicated by the navigation system in numbers (precision of 1 mm). The coronal distance was indicated with the augmented reality overlay over the laparoscopic video feed, consisting of a green target point and a scalable purple/blue cloud of activity around it. The green target point provided a clear reference for the accuracy determination and was compared to the actual target as seen on the video. Since the navigation targets consisted of small Eppendorf tubes, the midpoint of the fluid was used for the measurements. For each navigation setup (SPECT/CT and fhSPECT), three different soft tissue phantoms were used with each their own scans, each containing two distinct targets (n = 6 over three phantoms). Each individual measurement was performed by two different observers, resulting in 24 measurements in total. IBM SPSS statistics 22 software (International Business Machines Corp., New York, USA) was used to compare if the accuracy of SPECT/CT- and fhSPECT-based navigation was significantly different using an unpaired t-test (95% confidence interval).

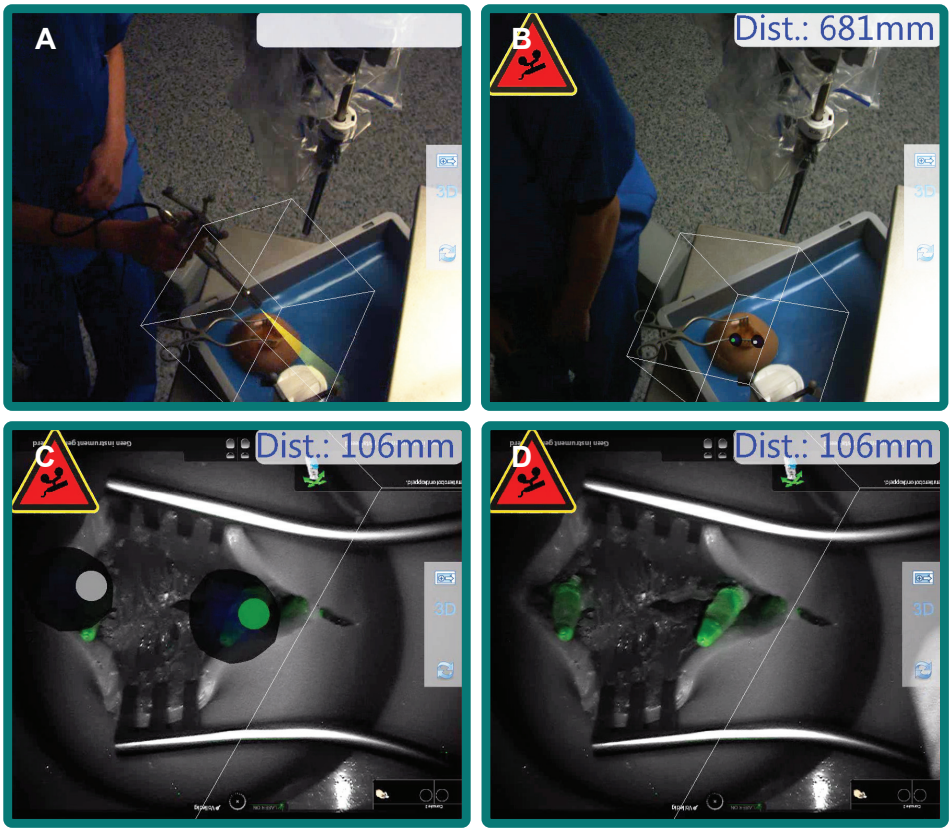

Figure 3. Navigation of the fluorescence laparoscope based on intraoperative fhSPECT imaging and intraoperative fluorescence guidance as performed on the tissue-mimicking phantom set-up. (a) *Acquisition of the fhSPECT scan with a tracked gamma probe from the perspective of the overhead navigation system camera.* ***(b)*** *Acquired fhSPECT scan (shown in purple/blue) displayed as an augmented reality projection over the phantom setup. The distance shown is the distance from the tip of the laparoscope to the selected (green) navigation target, defined by the fhSPECT signal hotspots. (A red sign in the upper left corner indicates that the gamma probe is no longer in the tracking volume, since it is no longer in use after the scan acquisition.)* ***(c)*** *Video feed from the perspective of the fluorescence laparoscope in fluorescence light modus, with augmented fhSPECT overlay.* ***(d)*** *Video feed from the perspective of the fluorescence laparoscope in fluorescence light modus, without augmented fhSPECT overlay.*

Overview of Coordinate Frames and Calibration Steps

An overview of the different coordinate transformations applied for the navigation workflow is provided in Figure 1. All transformations are divided in three different colors (red, blue, and green) to distinguish how they are found. The transformations determined by the OTS in real time are shown in red, the ones calculated during registration or calibration procedures are shown in blue, and all transformations deduced from known geometries are shown in green.

RESULTS

Figure 2 shows an example of the navigation process performed using preoperative SPECT/CT; Figure 2b-f show snapshots of the Firefly video feed combining the laparoscopic view (in white-light and fluorescence modus) and an augmented overlay of the SPECT/CT data. The navigation targets, displayed as dots, are defined by the signal hotspots found in the SPECT imaging data and the two white Eppendorf-shaped signals in the CT view (Figure 2a, c and d) function as anatomical markers. In a similar manner, we could also use "intraoperative" fhSPECT data sets for navigation (see Figure 3).

In the laparoscopic navigation view, the CT and/or (fh)SPECT overlay could be turned on and off independent of each other and the size of the SPECT hotspots (threshold on the SPECT signal) could be scaled according to preference. Qualitatively, navigation to the different targets (depicted as green colored dots) in the soft tissue phantoms appeared accurate using both scan modalities; during the navigation process, the augmented hotspots in the video feed and the distance to the targets seemed well registered to the fluorescent findings. As mentioned in the 'Methods and Materials' section, optical wavelengths of the OTS and fluorescence emission overlapped. However, other than in previous studies [21], the NIR light of the OTS did not interfere with the fluorescence detection of the Firefly.

The navigation accuracy for the SPECT/CT- and fhSPECT-based navigation procedures was quantified (see Table 1). Average errors for the SPECT/CT-based navigation were 2.25 mm (median 2 mm) and 2.08 mm (median 2 mm) in the coronal and sagittal plane, respectively. For the fhSPECT-based navigation, these were quite similar: 1.92 mm (median 2 mm) and 2.83 mm (median 3 mm). These results underline that the navigation accuracy, in the setup studied, stays well below the 1-cm tissue limit needed for successful fluorescence detection [8,9]. Comparison of the errors found for both scan modalities did not result in a significant difference (p values of 0.764 and 0.282 for the coronal and sagittal plane, respectively).

Table 1. Overview of the accuracy measurements in the tissue-mimicking phantom setups for navigation based on both SPECT/CT and fhSPECT.

Navigation based on	Anatomical plane	Mean (mm)	Standard deviation (mm)	Range (mm)
SPECT/CT	Coronal	2.25	1.86	0 to 5
	Sagittal	2.08	1.02	0.5 to 3.5
fhSPECT	Coronal	1.92	1.88	0 to 4.5
	Sagittal	2.83	1.25	1 to 4

Evaluation of the navigation setup using a torso phantom (Figure 4) illustrates the clinical setup to which the navigation should be translated. In addition, it demonstrates the setup remained effective when the robot is fully docked.

DISCUSSION

We have integrated surgical navigation, made possible via optical tracking, with (robot-assisted) laparoscopic fluorescence-guided surgery. Hereby, a robot-docked fluorescence laparoscope could be successfully navigated to target structures located in two different phantom setups with an accuracy of ~2 mm. All different imaging modalities used (fluorescence, SPECT/CT, and fhSPECT) could be available during navigation, thereby allowing compensation for the weaknesses of the individual modalities (e.g., the limited tissue penetration of fluorescent signals or the inaccuracies of surgical navigation due to soft tissue deformations). The presented soft tissue navigation setup suggests a next step in providing surgeons with more precise orientation and localization during robot-assisted procedures.

Theoretically, a preoperatively acquired SPECT/CT scan can be considered more precise than an intraoperatively acquired fhSPECT; with SPECT/CT, a lot more information is collected for the 3-D image reconstruction due to larger gamma cameras and longer scan times [18]. Therefore, for a rigid phantom setup, one would expect the navigation errors found when navigation was based on SPECT/CT to be smaller than when navigation was based on fhSPECT. In our measurements, performed on the semi-rigid soft tissue phantoms, navigational accuracy was similar for both the two scan methods. This suggests that navigation based on fhSPECT may serve as a valuable and cost-effective alternative for navigation based on SPECT/CT.

Moreover, due to the intraoperative nature of fhSPECT imaging (e.g., using a DROP-IN gamma probe [31,32]), the technique should suffer much less from tissue deformations that result from patient movement. In fact, due to the short acquisition time (roughly between 2 and 3 min), one could easily acquire a new scan after any expected tissue deformation or displacement (e.g., removal of the primary tumor site). In addition, intraoperative real-time visualization of fluorescence can be used to compensate for navigational errors below ~1 cm.

Translation of the proposed navigation setup to clinical use should be straightforward, as the robotic setup remains identical. We do see two questions that require attention, depending on the specific clinical application chosen: (1) Will NIR optical tracking be sufficient for a dynamic robotic intervention? (2) What will be the range of tissue deformation found in patients and how does this relate to the fluorescence detection limit?

Regarding the first point, in this study, optical tracking was used to define the 3-D pose of the phantom setup, laparoscope, and gamma probe using three different reference targets containing at least three fiducials each. As shown,

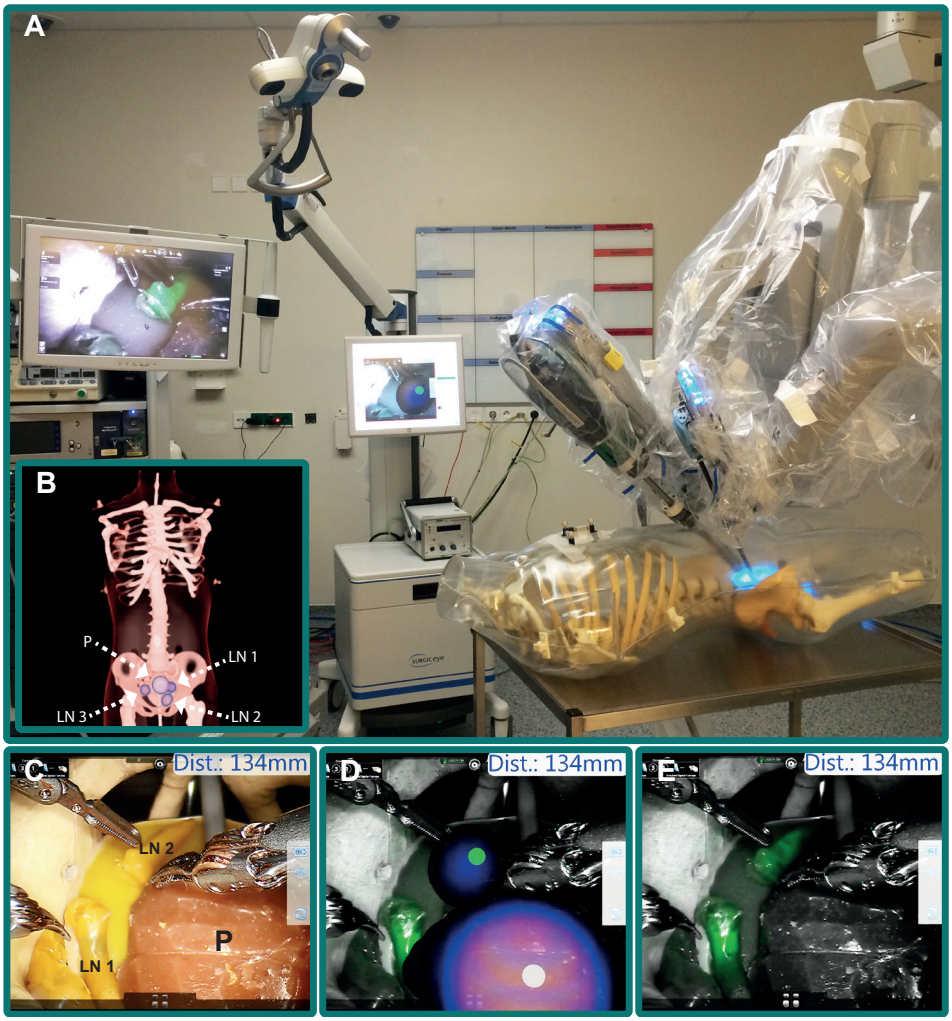

Figure 4. Evaluation of the combined fluorescence navigation system based on preoperative SPECT/CT. (a) *Operation room setup with the navigation system, fluorescence laparoscope, the surgical robot, and the torso phantom. On both the torso phantom and the fluorescence laparoscope, a reference target is attached.* ***(b)*** *Volume rendering of the fused SPECT/CT scan of the torso phantom setup. The SPECT hotspots are shown in pink/blue. The arrows indicate the prostate (P) and 3 lymph nodes (LN).* ***(c–e)*** *Augmented reality video feed from the perspective of the fluorescence laparoscope as seen on the navigation device when navigating to the navigation targets. These targets are indicated as gray and green circles and are defined by the SPECT signal (displayed purple/blue). The distance shown is the distance from the tip of the laparoscope to the selected (green) target.* ***(c)*** *White-light modus; letters indicating the specific lymph nodes (LN 1 and LN 2) and the prostate (P) in the anatomy of the phantom.* ***(d)*** *Fluorescence light modus with augmented SPECT overlay.* ***(e)*** *Fluorescence light modus without the augmented SPECT overlay. Lymph node LN 1 is located too close to the highly active prostate P (1:100 ratio in radioactivity) to resolve it as a separate navigation target by the used rendering.*

this was feasible, but a general limiting factor was that the OTS has to maintain a direct line-of-sight to at least three of the reference target fiducials to allow for 3-D pose determination of the tracked object [23]. A feature that limits the OR layout and logistics. This may be overcome by increasing the number of fiducials per reference target or by using multiple OTS cameras on different sides of the OR [33]. A possible drawback of using NIR optical tracking in combination with NIR fluorescence imaging is the overlap in spectra used for object tracking and fluorescence imaging. In previous work, we found that this could be a considerable issue when using an open surgery fluorescence camera [21]. To our surprise, we did not detect such an extensive interference when the Firefly laparoscope was applied outside of the phantom body. This finding could provide a basis for solving the issues previously reported. This said, in a laparoscopic setting, the tracking light is not likely to interfere with the fluorescence detection, since fluorescence imaging is conducted inside the patient's body.

Alternative to NIR optical tracking, electromagnetic (EM) tracking or mechanical tracking could also provide outcome. With an intrinsic accuracy up to ~0.5 mm (RMS) for EM tracking versus ~0.25 mm (RMS) for optical tracking [22,34], EM tracking still seems quite promising. However, a major disadvantage with this technique is the susceptibility to distortions of the EM tracking field by nearby metal objects or EM interferences, rendering it much less accurate [35]. Although inaccurate, mechanical tracking of the robotic arms is possible by using forward kinematics to calculate the 3-D pose of the end effector such as the laparoscope or the surgical instrument [36]. Fuerst et al. greatly improve this accuracy to an approximate error of 0.2 mm by combining the mechanical tracking with visual-based tracking via the stereoscopic laparoscope video feed [32].

In the presented navigation workflow, the navigation targets are displayed as a two-dimensional augmented reality overlay superimposed in the laparoscopic video feed while the distance from the laparoscope tip to target is shown in numbers. When implemented in clinical use, it might be hard to get a good idea of how deep the target structures really lie. Therefore, the augmented reality visualization may in the future be enhanced by dynamic augmented cues (e.g., small arrows indicating both direction and distance) or more depth perception cues (e.g., as shown by Bichlmeier et al. [37] and Kutter et al. [38]).

CONCLUSION

In a phantom setup, both pre- and intraoperative SPECT data sets can be used to accurately navigate the da Vinci robot-integrated fluorescence laparoscope toward surgical targets. Hereby, a basis is generated for future robot-assisted navigation toward fluorescent lesions.

REFERENCES

1. *E. E. Medlin, D. M. Kushner, and L. Barroilhet, "Robotic surgery for early stage cervical cancer: evolution and current trends," J. Surg. Oncol. 112(7), 772–781 (2015).*
2. *R. Montalti et al., "Outcomes of robotic vs laparoscopic hepatectomy: a systematic review and meta-analysis," World J. Gastroenterol. 21(27), 8441–8451 (2015).*
3. *R. Biffi et al., "Dealing with robot-assisted surgery for rectal cancer: current status and perspectives," World J. Gastroenterol. 22(2), 546–556 (2016).*
4. *G. Novara et al., "Systematic review and meta-analysis of studies reporting oncologic outcome after robot-assisted radical prostatectomy," Eur. Urol. 62(3), 382–404 (2012).*
5. *N. S. van den Berg et al., "Sentinel lymph node biopsy for prostate cancer: a hybrid approach," J. Nucl. Med. 54(4), 493–496 (2013).*
6. *T. Maurer et al., "Prostate-specific membrane antigen-radioguided surgery for metastatic lymph nodes in prostate cancer," Eur. Urol. 68, 530–534 (2015).*
7. *F. Greco et al., "Current perspectives in the use of molecular imaging to target surgical treatments for genitourinary cancers," Eur. Urol. 65(5), 947–964 (2014).*
8. *P. T. Chin et al., "Multispectral visualization of surgical safety-margins using fluorescent marker seeds," Am. J. Nucl. Med. Mol. Imaging 2(2), 151–162 (2012).*
9. *F. W. van Leeuwen, J. C. Hardwick, and A. R. van Erkel, "Luminescence-based imaging approaches in the field of interventional molecular imaging," Radiology 276(1), 12–29 (2015).*
10. *G. H. KleinJan et al., "Optimisation of fluorescence guidance during robot-assisted laparoscopic sentinel node biopsy for prostate cancer," Eur. Urol. 66(6), 991–998 (2014).*
11. *G. H. KleinJan et al., "Multimodal hybrid imaging agents for sentinel node mapping as a means to (re)connect nuclear medicine to advances made in robot-assisted surgery," Eur. J. Nucl. Med. Mol. Imaging 43(7), 1278–1287 (2016).*
12. *M. Baumhauer et al., "Navigation in endoscopic soft tissue surgery: perspectives and limitations," J. Endourol. 22(4), 751–766 (2008).*
13. *J. Rassweiler et al., "Surgical navigation in urology: European perspective," Curr. Opin. Urol. 24(1), 81–97 (2014).*
14. *F. Nickel et al., "Navigation system for minimally invasive esophagectomy: experimental study in a porcine model," Surg. Endosc. 27(10), 3663–3670 (2013).*
15. *N. C. Buchs et al., "Augmented environments for the targeting of hepatic lesions during image-guided robotic liver surgery," J. Surg. Res. 184(2), 825–831 (2013).*
16. *O. R. Brouwer et al., "Feasibility of intraoperative navigation to the sentinel node in the groin using preoperatively acquired single photon emission computerized tomography data: transferring functional imaging to the operating room," J. Urol. 192(6), 1810–1816 (2014).*
17. *T. Wendler et al., "First demonstration of 3-D lymphatic mapping in breast cancer using freehand SPECT," Eur. J. Nucl. Med. Mol. Imaging 37(8), 1452–1461 (2010).*
18. *T. Engelen et al., "The next evolution in radioguided surgery: breast cancer related sentinel node localization using a freehandSPECT-mobile gamma camera combination," Am. J. Nucl. Med. Mol. Imaging 5(3), 233–245 (2015).*
19. *C. Bluemel et al., "Intraoperative 3-D imaging improves sentinel lymph node biopsy in oral cancer," Eur. J. Nucl. Med. Mol. Imaging 41(12), 2257–2264 (2014).*
20. *O. R. Brouwer et al., "Image navigation as a means to expand the boundaries of fluorescence-guided surgery," Phys. Med. Biol. 57(10), 3123–3136 (2012).*
21. *G. H. KleinJan, "Towards (hybrid) navigation of a fluorescence camera in an open surgery setting," J. Nucl. Med. (2016).*
22. *Northern Digital Inc., "Northern digital, polaris optical tracking systems," 2016, http://www.ndigital.com/medical/products/polaris-family/ (5 August 2016).*
23. *P. Waelkens et al., "Surgical navigation: an overview of the state-of-the art clinical applications," in Radioguided Surgery, K. Herrmann, O. E. Nieweg, and S. P. Povoski, Eds., pp. 57–73, Springer (2016).*

24. *Z. Zhang, "A flexible new technique for camera calibration," IEEE Trans. Pattern Anal. Mach. Intell. 22(11), 1330–1334 (2000).*
25. *G. H. KleinJan et al., "Fluorescence guided surgery and tracer-dose, fact or fiction?" Eur. J. Nucl. Med. Mol. Imaging 43(10), 1857–1867 (2016).*
26. *N. S. van den Berg et al., "(Near-infrared) fluorescence-guided surgery under ambient light conditions: a next step to embedment of the technology in clinical routine," Ann. Surg. Oncol. 23(8), 2586–2595 (2016).*
27. *H. G. van der Poel et al., "Intraoperative laparoscopic fluorescence guidance to the sentinel lymph node in prostate cancer patients: clinical proof of concept of an integrated functional imaging approach using a multimodal tracer," Eur. Urol. 60(4), 826–833 (2011).*
28. *L. Bergqvist, S. E. Strand, and B. R. Persson, "Particle sizing and biokinetics of interstitial lymphoscintigraphic agents," Sem. Nucl. Med. 13(1), 9–19 (1983).*
29. *B. A. Kapteijn et al., "Validation of gamma probe detection of the sentinel node in melanoma," J. Nucl. Med. 38(3), 362–366 (1997).*
30. *L. Jansen et al., "Improved staging of breast cancer through lymphatic mapping and sentinel node biopsy," Eur. J. Surg. Oncol. 24(5), 445–446 (1998).*
31. *M. N. van Oosterom et al., "Revolutionizing (robot-assisted) laparoscopic gamma tracing using a DROP-IN gamma probe technology," Am. J. Nucl. Med. Mol. Imaging 6(1), 1 (2016).*
32. *B. Fuerst et al., "First robotic SPECT for minimally invasive sentinel lymph node mapping," IEEE Trans. Med. Imaging 35(3), 830–838 (2015).*
33. *T. Sielhorst et al., "Online estimation of the target registration error for n-ocular optical tracking systems," in Medical Image Computing and Computer-Assisted Intervention (MICCAI 2007), pp. 652–659, Springer (2007).*
34. *Northern Digital Inc.,, "Northern digital, aurora electromagnetic tracking systems," http://www.ndigital.com/medical/products/aurora/ (5 August 2016).*
35. *H. Kenngott et al., "Magnetic tracking in the operation room using the da Vinci® telemanipulator is feasible," J. Rob. Surg. 7(1), 59–64 (2013).*
36. *A. Reiter, P. K. Allen, and T. Zhao, "Appearance learning for 3D tracking of robotic surgical tools," Int. J. Rob. Res. 33(2), 342–356 (2014).*
37. *C. Bichlmeier et al., "Contextual anatomic mimesis hybrid in-situ visualization method for improving multi-sensory depth perception in medical augmented reality," in 6th IEEE and ACM Int. Symp. on Mixed and Augmented Reality (ISMAR 2007), pp. 129–138 (2007).*
38. *O. Kutter et al., "Real-time volume rendering for high quality visualization in augmented reality," in Int. Workshop on Augmented Environments for Medical Imaging Including Augmented Reality in Computer-Aided Surgery (AMI-ARCS) (2008).*

CHAPTER 4

NAVIGATION OF FLUORESCENCE CAMERAS DURING SOFT TISSUE SURGERY

Is It Possible To Use A Single Navigation Setup For Various Open And Laparoscopic Urological Surgery Applications?

Adapted from: van Oosterom MN, Meershoek P, KleinJan GH, Hendricksen K, Navab N, van de Velde CJH, van der Poel HG, van Leeuwen FWB

The Journal of Urology, 2018, 199(4): 1061–1068

ABSTRACT

Real-time visualization of fluorescence imaging can guide surgeons during tissue resection. Unfortunately tissue induced signal attenuation limits the value of this technique to superficial applications. By positioning the fluorescence camera via a dedicated navigation setup we reasoned that the technology could be made compatible with deeper lesions, increasing its impact on clinical care. Such an impact would benefit from the ability to implement the navigation technology in different surgical settings. For that reason we evaluated whether a single fluorescence camera could be navigated toward targeted lesions during open and laparoscopic surgery. A fluorescence camera with scopes available for open and laparoscopic procedures was integrated with a navigation platform. Lymph nodes identified on SPECT/CT (single photon emission computerized tomography/computerized tomography) or freehand single photon emission computerized tomography acted as navigation targets and were displayed as augmented overlays in the fluorescence camera video feed. The accuracy of this setup was evaluated in a phantom study of 4 scans per single photon emission computerized tomography imaging modality. This was followed by 4 first in human translations into sentinel lymph node biopsy procedures for penile (open surgery) and prostate (laparoscopic surgery) cancer. Overall the phantom studies revealed a tool-target distance accuracy of 2.1 mm for SPECT/CT and 3.2 mm for freehand single photon emission computerized tomography, and an augmented reality registration accuracy of 1.1 and 2.2 mm, respectively. Subsequently open and laparoscopic navigation efforts were accurate enough to localize the fluorescence signals of the targeted tissues in vivo. The phantom and human studies performed suggested that the single navigation setup is applicable in various open and laparoscopic urological surgery applications. Further evaluation in larger patient groups with a greater variety of malignancies is recommended to strengthen these results.

INTRODUCTION

Due to its real-time intraoperative visualization capabilities fluorescence guided surgery is increasingly gaining popularity as a surgical guidance technology [1,2] that is applicable during open and laparoscopic surgery [3,4]. Despite its clear benefits, tissue induced signal attenuation [5] limits the technology to superficial applications (less than 1 cm deep) at known locations [6]. This means that lesions embedded in tissue, e.g. fat, are more difficult to detect [7]. Perhaps even more importantly, this superficial nature prohibits surgical planning, meaning that prior to the start of the procedure the surgeon is blind to the location of the lesion as well as the targeting capabilities of the tracer.

In contrast to fluorescence imaging, nuclear medicine allows for highly sensitive in-depth and noninvasive imaging. For that reason technologies such as SPECT/CT and positron emission tomography/CT are considered the standard for total body molecular imaging. These 3D scans, which display targeted tissues in the anatomical context, are ideal to provide virtual road maps for in-depth surgical planning [8].

In an attempt to connect surgical guidance with preoperative planning the tracer ICG-^{99m}Tc-nanocolloid was introduced in SN biopsy procedures for prostate cancer, among other conditions [9]. Incorporating a radioactive label (^{99m}Tc) and a fluorescent label (ICG), this hybrid tracer enables preoperative SN localization with SPECT/CT and intraoperative guidance with fluorescence imaging. Analogous to global positioning system navigation devices in traffic, surgical navigation in preoperatively acquired patient scans can effectively be used to position surgical tools intraoperatively [10]. Unfortunately tissue displacement and deformation between scan acquisition and the navigation process can deteriorate the precision of the navigation procedure [11,12]. This can be overcome using intraoperative imaging modalities such as fhSPECT to generate a virtual map of the patient [13].

In the past we proposed and found that the in-depth shortcomings of fluorescence guidance could be compensated for when a dedicated navigation setup was used to position the fluorescence camera within a 10 mm vicinity of the fluorescent target. Subsequently fluorescence imaging could detect the lesion in real time and correct for minor navigation inaccuracies. This concept was demonstrated for open surgery using a m-PDE fluorescence camera (Hamamatsu, Hamamatsu City, Japan) [14], laparoscopic surgery using a laparoscopic Tricam SLII fluorescence setup [15] and robot-assisted laparoscopic surgery using a Firefly fluorescence camera (da Vinci Surgery) [16].

Since different clinical indications as well as different hospital standards may demand open or laparoscopic surgery, we reasoned that it would be beneficial to allow for the navigation of a clinical grade fluorescence camera that is applicable during open and laparoscopic surgery. Enabling navigation in different surgical settings could also benefit the dissemination of this novel fluorescence

guided surgery concept.

The Image1 S™ H3-Z FI fluorescence camera can be equipped with different scopes and thereby serve in different surgical settings as an exoscope for open surgery and a laparoscope for laparoscopic surgery [9,17]. The navigation accuracy of this setup was thoroughly evaluated in a phantom study followed by, which is to our knowledge, a first in human translation to open (penile cancer) and laparoscopic (prostate cancer) SN procedures.

METHODS

Navigation Hardware

Figure 1 shows the navigated fluorescence guided surgery setup, consisting of a declipseSPECT navigation system and a IMAGE1 S H3-Z FI fluorescence camera [9] with 3 fluorescence scopes, including a VITOM II 0-degree exoscope, and 0-degree and 30-degree HOPKINS II 10 mm laparoscopes. To allow for position and orientation tracking all tracked objects (e.g. patient, fluorescence camera and gamma probe) were fitted with optical reference targets which were visible to the navigation system near infrared OTS (Figure 1) [10]. To ensure object tracking during navigation a line of sight must be maintained between the OTS and the individual reference targets.

SPECT/CT and fhSPECT Acquisition

Navigation of the fluorescence camera was based on targets defined in SPECT/CT or fhSPECT imaging data. SPECT/CT was performed with a Symbia™ TruePoint SPECT/CT system. FhSPECT was performed with a SOE 311 gamma probe (Eurorad, Eckbolsheim, France) for phantom and open surgical scans while a CXS-OP-SZL-45 laparoscopic gamma probe (Crystal Photonics, Berlin, Germany) was used for laparoscopic scans [18].

Integration of Fluorescence and Navigation Systems

After integration with the navigation system 2 types of real-time guidance were provided in the fluorescence camera video feed. 1) A 2D AR overlay of the SPECT based targets for navigation (e.g. SNs), which is a visual overlay in the camera video feed, could be switched on and off. It helped position the fluorescence camera and establish possible discrepancies between SPECT based navigation and fluorescence based identification of the lesions. 2) A 3D numerical value depicting the distance from the calibrated instrument tip (i.e. the laparoscope or the gamma probe) to the middle of the targeted tissue supporting the identification of lesions positioned beyond the in-depth detection limits of the fluorescent signal.

The navigation workflow for the exoscope was somewhat different than for the laparoscopes. While the laparoscopes were dynamically positioned on top of the area of interest, the exoscope was fixed in an arm. This difference

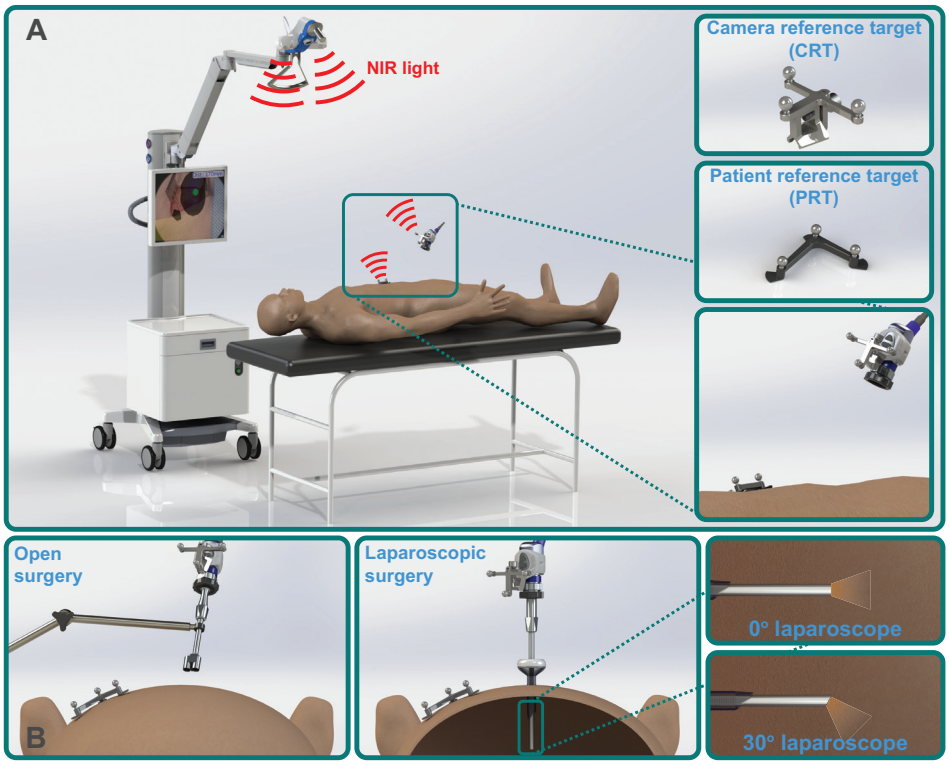

Figure 1. Schematic overview of navigation setup. (a) *Typical setup implementation with OTS directed toward patient and optical reference target attached to patient and fluorescence camera with latter shown without scope.* ***(b)*** *Implementation in exoscopic or laparoscopic application. (NIR = near infrared).*

means that in the laparoscopic setup the distance to the navigation targets was measured with respect to the laparoscope tip. However, for the static exoscope setup this distance was related to a gamma probe used to pinpoint the area of interest.

Evaluations

Navigation Accuracy

The accuracy of the proposed navigation setup was evaluated in a rigid phantom setup for the 2 types of guidance provided, including 1) 3D tool distance accuracy and 2) 2D AR registration accuracy. By comparing the geometrical target location (i.e. the center of the radioactive source) with respect to the navigational targeted location we determined the accuracy of SPECT/CT and fhSPECT based navigation using all 3 camera-scope combinations with 4 examples for each scanning modality. The supplementary material describes the measurement setup in more detail.

Table. Overview of patient characteristics by clinical indication

	Prostate Ca		Penile Ca	
	Pt 1	Pt 2	Pt 3	Pt 4
Age	73	63	70	72
Body mass index (kg/m^2)	33	30	31	22
Tumor stage	cT3aN0MxR0, pN0	cT2cN0M0R0, pN0	pT2N0 R1, verrucous Ca degree 1	pT1aN0Mx, verrucous Ca degree 1
Preop prostate specific antigen (ng/ml)	12.3	59.0	-	-
Biopsy Gleason sum score	7	9	-	-
Injected dose (MBq)	196.30	205.70	78.55	149.87 + 92.22*
No. preop mapped sentinel nodes:				
Left	0	3	2	0
Right	0	3	0	1
Procedure	Laparoscopic surgery (extended lymph node dissection)	Laparoscopic surgery sentinel node biopsy	Open surgery sentinel node biopsy + penile amputation	Open surgery sentinel node biopsy + penile amputation
Injection-surgery interval (hrs)	7	5	6	20 + 17*
Navigation toward	Prostate	Sentinel node, left obturator region	Sentinel node, left inguinal region	Sentinel node, left inguinal region
Location:				
Pt reference target	Right superior anterior iliac spine	Pubic bone	Left knee	Right femur
Optical tracking system	Right side, feet	Right side, feet	Left hip	Right hip

In all patients navigation was successful, fluorescence was confirmed and pathological evaluation revealed no malignancy in excised lymph nodes.
** Repeat injection to ensure no further tumor draining sentinel lymph nodes.*

In Vivo

A proof of concept evaluation of the navigation setup was performed in 4 patients scheduled for SN biopsy. These procedures included 2 laparoscopic prostate cancer related procedures using the 30-degree laparoscope and 2 open surgery penile cancer related procedures using the exoscope (see Table).

ICG-^{99m}Tc-nanocolloid administration and subsequent preoperative SN mapping were done as previously described [9,19].In prostate cases tracer was deposited in the peripheral zone of the prostate and in penile cancer cases tracer was administered peritumorally. Intraoperatively conventional guidance to the SNs was performed using a combination of typical radio and fluorescence tracing [9,19]. The fhSPECT scans served as input for the navigation setup. The OTS was positioned next to the patient and the PRT was attached to the patient with sterile tape (see Table).

Validation of navigation in vivo was waived by the institutional review board at our institution. All involved patients provided signed informed consent.

RESULTS

Phantom Accuracy Measurements

Tool Distance

Figure 2 shows the measurements obtained for tool distance accuracy. Supplementary Table 1 shows the numerical values. For SPECT/CT based navigation the total 3D mean accuracy was 1.50, 2.59 and 2.33 mm for the 0-degree laparoscope, the 30-degree laparoscope and the gamma probe/exoscope work flow, respectively. When navigation was based on fhSPECT, mean accuracy was reduced for all scopes used, including 2.28 mm for the 0-degree laparoscope, 3.50 mm for the 30-degree laparoscope and 3.74 mm for the gamma probe/exoscope work flow. However, the unpaired samples t-test did not reveal a significant difference in any of these settings (p = 0.172, 0.113 and 0.0548, respectively).

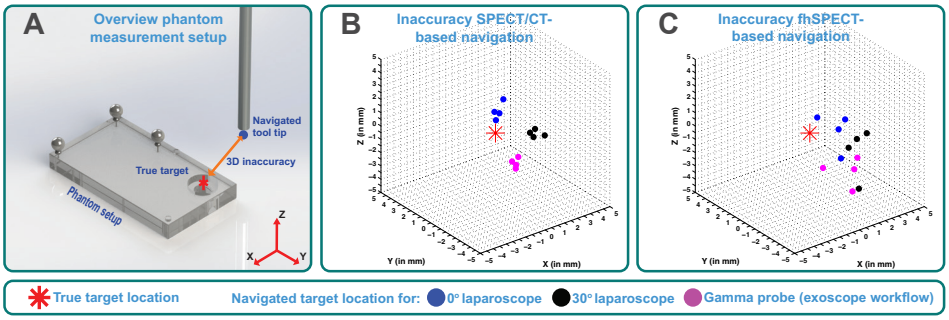

Figure 2. Overview of 3D tool distance accuracy measurements. (a) *Phantom measurement setup with integrated PRT and space to fit radioactive sources.* ***(b-c)*** *Distance measured between true target location and navigated locations visualized by 0-degree and 30-degree laparoscopes, and gamma probe, which is used in exoscope work flow.*

Augmented Reality Registration

Figure 3 shows the findings of AR registration accuracy. Supplementary Table 2 shows the numerical values. In this case the total 2D mean accuracy for navigation based on SPECT/CT was 1.39, 0.67 and 1.20 mm for the 0-degree laparoscope, the 30-degree laparoscope and the exoscope, respectively. For fhSPECT based navigation the mean accuracy was 2.57 mm for the 0-degree laparoscope, 2.00 mm for the 30-degree laparoscope and 1.96 mm for the exoscope. Unlike the tool distance accuracy results these findings for SPECT/CT and fhSPECT significantly differed in all 3 groups ($p = 0.028$, 0.020 and 0.032, respectively). Since camera settings tend to vary during procedures, we studied how altering the distance to the target and the focus of the camera influenced this AR registration accuracy. The supplementary material provides these results.

In Vivo Measurements

Figure 4 shows an overview of the application of the navigation setup for laparoscopic surgery. Patient 1 was scheduled for SN biopsy of the prostate prior to radiotherapy [20]. Unfortunately no tracer drainage was noted in the lymphatics, possibly due to poorly executed tracer administration. Therefore, extended LN dissection was performed. In the absence of radioactive LNs the fhSPECT based navigation was directed toward the prostate. Patient 2 underwent a diagnostic SN procedure prior to radiotherapy [20]. In this patient prostate draining SNs were found, of which 1 was chosen as a target for the navigation process. No tracking problems were encountered. Navigation was successful in each case, including the fluorescence signal confirmation as detected by the laparoscope (see Table).

Figure 5 shows the application of the exoscope navigation setup for open surgery. Patient 3 underwent SN biopsy combined with penile amputation. Two SNs in close proximity to each other were mapped preoperatively and excised as 1 specimen intraoperatively. Navigation to these SNs, which was based on fhSPECT, was considered successful (see Table). Patient 4 was treated with SN biopsy combined with partial penile amputation. Navigation was pursued for the marked SN. Navigation was considered successful, showing well registered AR overlay of fhSPECT and an appropriate distance estimation from the gamma probe to the target (Figure 5). Fluorescence imaging confirmed the location of the SN (see Table). During each open surgery application, operating room lights had to be turned off temporarily to achieve successful fluorescence imaging.

After pathological investigation, no malignancies were found in the excised LNs of all patients included in this study.

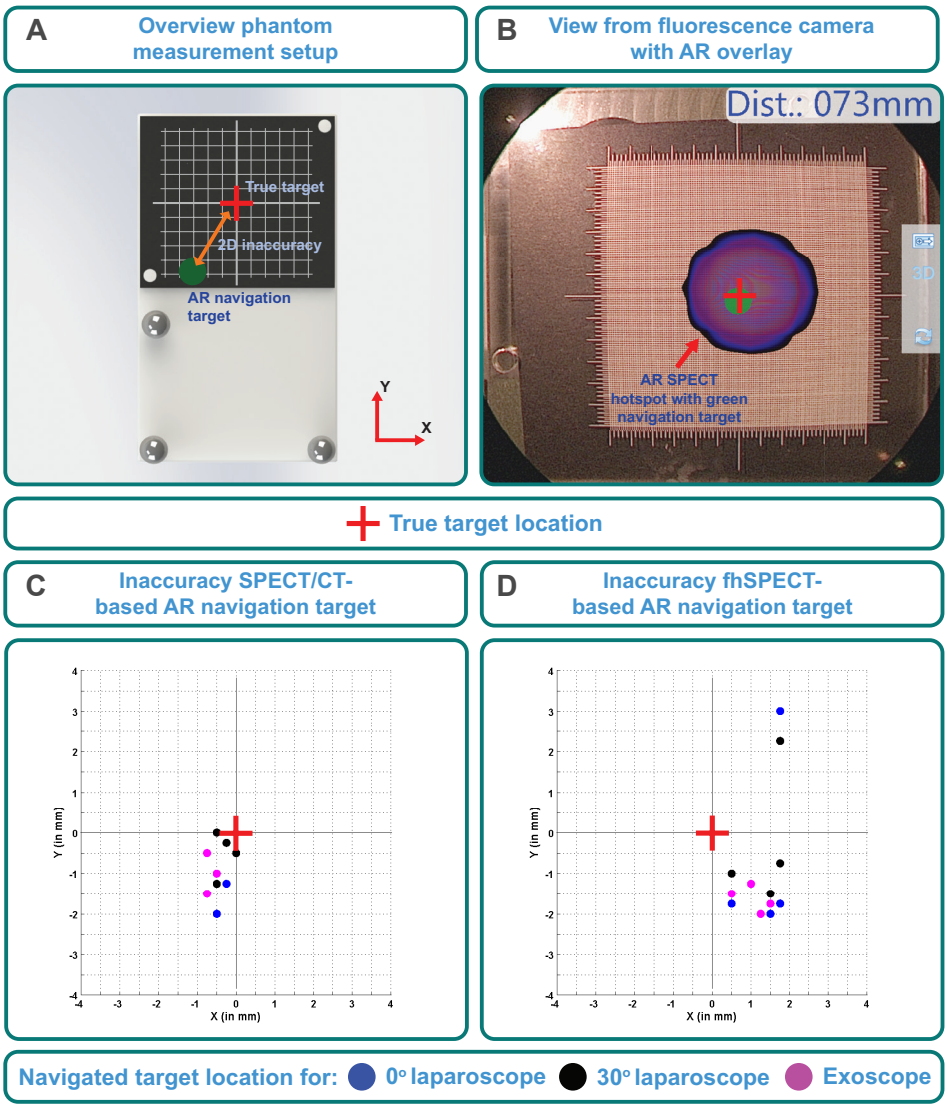

Figure 3. Overview of 2D AR registration accuracy measurements. (a) *Phantom measurement setup with integrated PRT and 2D measurement grid. True target location represents center to place radioactive sources. AR navigation target (green dot) is generated by navigation system.* ***(b)*** *Example of measurement with AR SPECT hotspot overlay (blue and purple shape with green dot at weighted center) in fluorescence camera video feed.* ***(c-d)*** *Visualization of distances measured between AR navigation targets and true target location for 0-degree and 30-degree laparoscopes, and exoscope.*

DISCUSSION

In this proof of concept study we evaluated a navigation setup that facilitates the translation from preoperative planning (SPECT/CT) to intraoperative guidance (fhSPECT, navigation and fluorescence based lesion identification). By directly linking nuclear medicine based, in-depth imaging with superficial fluorescence guidance the weaknesses of the individual techniques could be overcome. Navigation of a single camera setup for open and laparoscopic surgery allowed for an in-depth (greater than 10 mm) extension of applications for which fluorescence guided surgery may be beneficial. The presented generic setup should also benefit operating room logistics, device operating experiences and purchase costs.

Overall the phantom navigation studies showed a tool distance accuracy of 2.1 in SPECT/CT based studies and 3.2 mm in fhSPECT based studies, and AR registration accuracy of 1.1 and 2.2 mm, respectively. Considering the typical size of the targeted lesion, e.g. a SN with a typical diameter of 5 to 10 mm [21], the size of the instrument tip, including the 11 mm diameter of the gamma probe and the 10 mm diameter of the laparoscope, and the fluorescence signal penetration of about 10 mm [6], accuracy was considered sufficient for clinical translation. Contributors to these inaccuracies included OTS imprecisions, optical and geometrical system calibrations, and SPECT scan resolution and fidelity.

Although neither SPECT modality resulted in significant differences in tool distance accuracy measurements, a significant difference was observed for AR registration accuracy measurements. As described by van Oosterom et al, theoretically the quality of SPECT/CT should be higher than that of fhSPECT. Due to its intraoperative nature and short acquisition time, fhSPECT should be better for soft tissue induced deformations [16].

The clinical relevance of the phantom studies was confirmed by implementing the technology in open and laparoscopic urological surgery. While tissue movement influenced navigation accuracy, it was high enough to localize the fluorescence signals of the targeted tissues in vivo. The exoscope was fixed in an arm, making camera positioning less flexible but maintaining a focused and steady video image. In this setting we noted that the distance between the exoscope and the targeted tissue required a balance between a minimum focus distance (approximately 15 cm), the preferred tissue magnification (i.e. surgical context) and the achieved fluorescence imaging sensitivity (supplementary materials).

In addition, the exoscope experienced slight imaging interference caused by the near infrared OTS light, a feature that was reported earlier for the m-PDE fluorescence camera [14]. However, in our study this interference did not negatively influence the exoscopic procedures and it did not influence the laparoscopic procedures at all since the intra-abdominal placement of the camera shielded it from extra-abdominal light sources. While it was successful in the studies that were performed, maintaining a line of sight between the OTS and

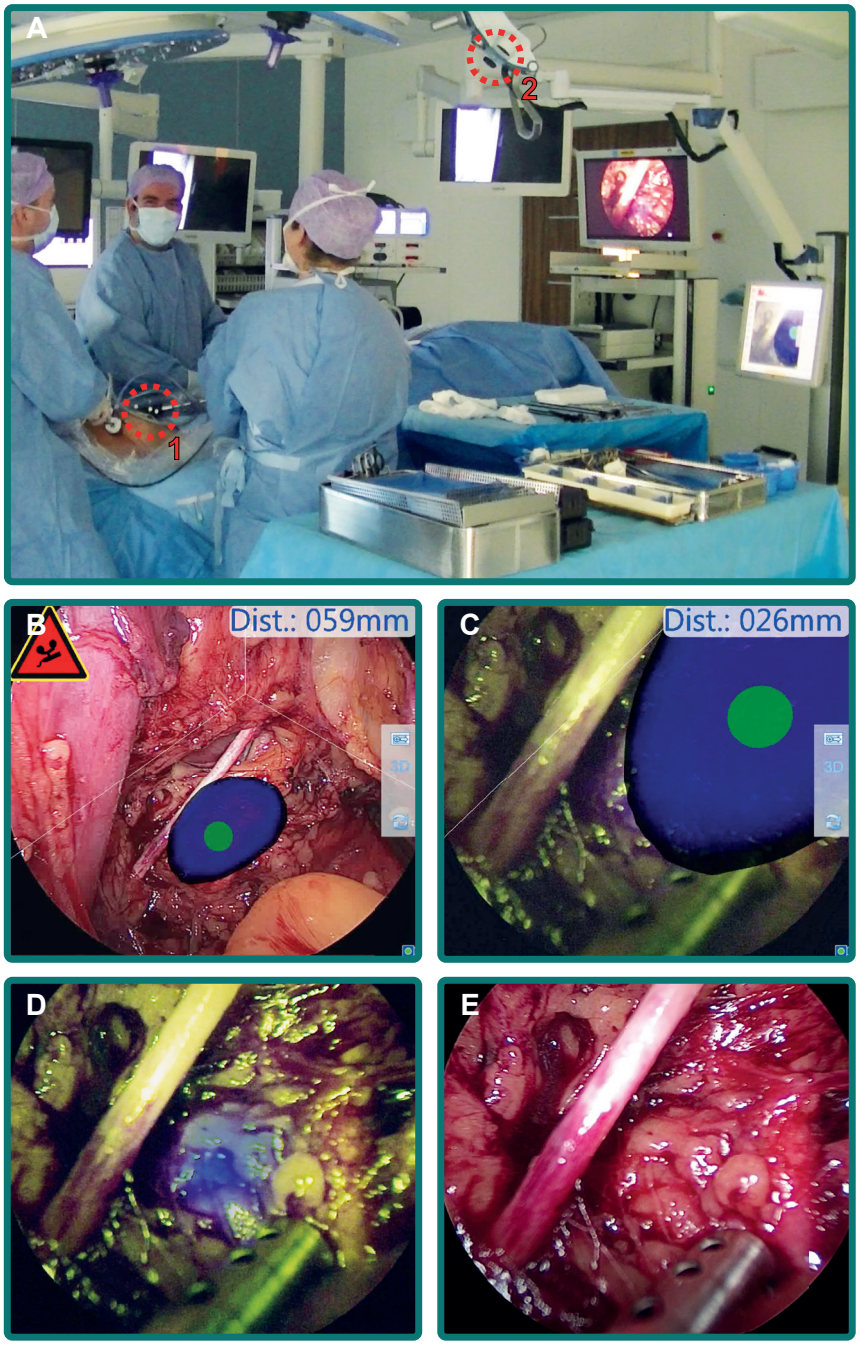

Figure 4. In vivo laparoscopic evaluation of navigation setup for prostate cancer. (a) *Overview of operating room layout with PRT (1) and OTS (2).* ***(b)*** *Freehand SPECT based 2D AR navigation target and 3D tool-target distance in fluorescence camera video feed with fluorescence laparoscope in white light imaging mode.* ***(c)*** *Laparoscope is brought closer to target and switched to fluorescence imaging mode.* ***(d)*** *AR navigation overlay is turned off, showing clear view of fluorescence signal (blue areas) from sentinel lymph node.* ***(e)*** *White light image of lesion location.*

the individual reference targets can be complex in a robotic setting and/or in a crowded operating room. Future engineering will hopefully limit dependence on an OTS for object tracking by using vision based machine learning methods such as deep learning, for example [22].

A larger patient study including different surgical indications and randomized blinding to different features of the surgical guidance process should be performed to identify features with the strongest influence on surgeon performance (e.g. surgery time or the number of otherwise missed lesions). These features could include the different forms of preoperative mapping, navigation guidance, gamma guidance and fluorescence guidance. Such a trial would also demonstrate how often navigation inaccuracies exceed the less than 10 mm tissue penetration of fluorescence signals.

Since the navigation target was determined based on SPECT and fluorescence imaging results showing the same lesion, the current navigation technology depends on using hybrid tracers. In this study navigation was directed toward SNs or the primary tumor site using the hybrid tracer ICG-^{99m}Tc-nanocolloid in experimental studies performed in prostate [9] and penile cancer [19] cases. Translation to other SN procedures performed with the same tracer should be trivial, for example for head and neck cancer [23,24], breast cancer [25] and cervical cancer [26]. At the same time the identical tracer and navigation concept could be applied in hybrid radio guided occult lesion localization procedures [27].

In addition, in light of recent developments toward tumor-receptor targeted hybrid tracers [28,29] an interesting future application includes the application of this navigation concept for intraoperative localization of the primary tumor and metastases, e.g. in renal cancer [30]. In these cases the in-depth tracking capability could help ensure negative surgical margins during resection and could be connected with, for example, CT based navigation approaches [12].

CONCLUSIONS

In this study we investigated a single navigation setup applicable to various open and laparoscopic urological procedures. Phantom experiments were performed to determine the accuracy of navigation while first in human evaluations underlined the translational efficacy of the setup. By combining the complementary imaging information from nuclear and fluorescence imaging the setup allowed for successful in vivo localization of the targeted tissues during penile and prostate cancer related surgery. To strengthen these preliminary results, further evaluation is recommended in larger patient groups with a greater variety of malignancies.

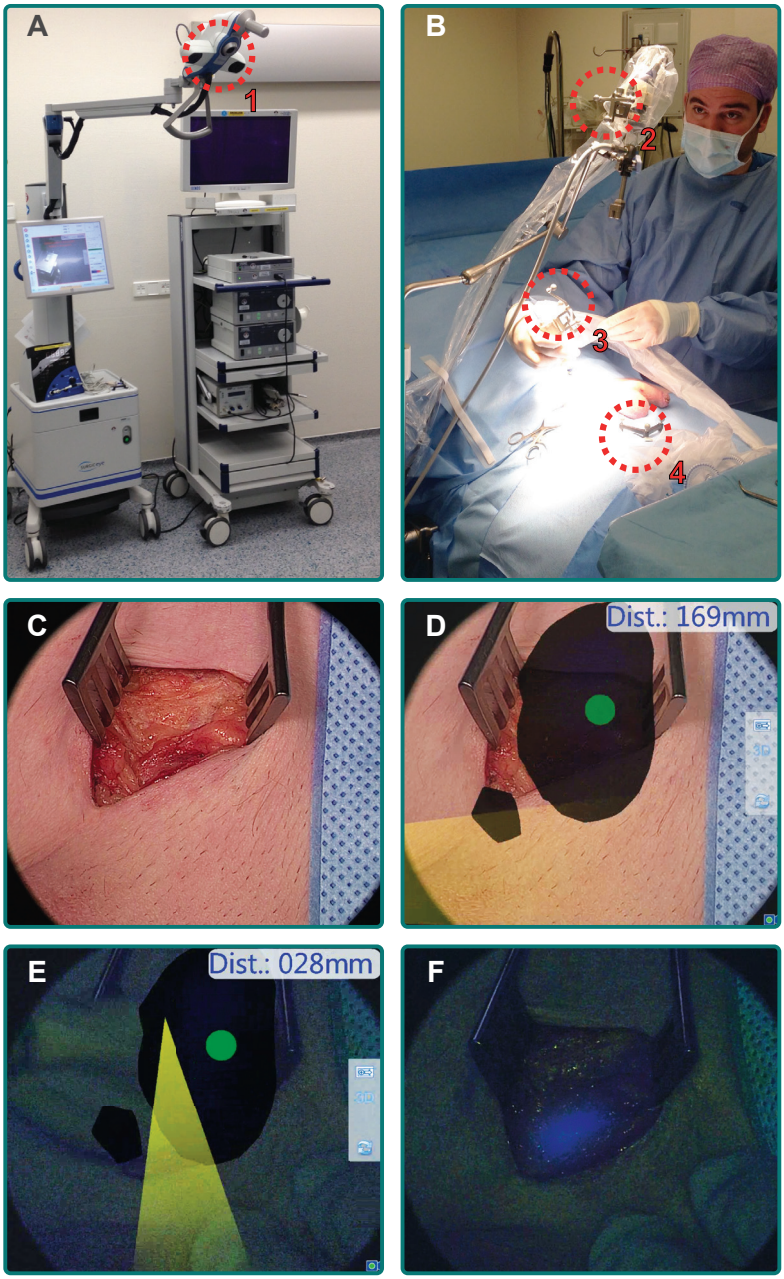

Figure 5. In vivo open surgery evaluation of navigation setup for penile cancer. (a) *Navigation system with OTS (1) and the fluorescence camera imaging tower located at right of operating table.* ***(b)*** *Overview of operating table with camera reference target (2), gamma probe reference target (3) and PRT (4).* ***(c)*** *Surgical site from perspective of fluorescence camera in white light mode.* ***(d)*** *2D AR overlay and 3D tool-target distance shown in fluorescence camera video feed.* ***(e)*** *Gamma probe is moved closer to sentinel lymph node and camera is switched to fluorescence imaging mode.* ***(f)*** *AR navigation overlay is turned off, showing clear view of fluorescence signal (blue areas) from sentinel lymph node.*

REFERENCES

1. *Nguyen QT and Tsien RY: Fluorescence-guided surgery with live molecular navigationda new cutting edge. Nat Rev Cancer 2013; 13: 653.*
2. *van Leeuwen FW, Hardwick JC and van Erkel AR: Luminescence-based imaging approaches in the field of interventional molecular imaging. Radiology 2015; 276: 12.*
3. *DSouza AV, Lin H, Henderson ER et al: Review of fluorescence guided surgery systems: identification of key performance capabilities beyond indocyanine green imaging. J Biomed Opt 2016; 21: 080901.*
4. *Zhu B and Sevick-Muraca E: A review of performance of near-infrared fluorescence imaging devices used in clinical studies. Br J Radiol 2015; 88: 20140547.*
5. *Chin PTK, Welling MM, Meskers SCJ et al: Optical imaging as an expansion of nuclear medicine: Cerenkov-based luminescence vs fluorescence-based luminescence. Eur J Nucl Med Mol Imaging 2013; 40: 1283.*
6. *Stoffels I, Dissemond J, P€oppel T et al: Intraoperative fluorescence imaging for sentinel lymph node detection: prospective clinical trial to compare the usefulness of indocyanine green vs technetium Tc 99m for identification of sentinel lymph nodes. JAMA Surg 2015; 150: 617.*
7. *Crane LM, Themelis G, Pleijhuis RG et al: Intraoperative multispectral fluorescence imaging for the detection of the sentinel lymph node in cervical cancer: a novel concept. Mol Imaging Biol 2011; 13: 1043.*
8. *Olmos RAV, Rietbergen DD and Vidal-Sicart S: SPECT/CT and sentinel node lymphoscintigraphy. Clin Transl Imaging 2014; 2: 491.*
9. *KleinJan GH, van den Berg NS, Brouwer OR et al: Optimisation of fluorescence guidance during robot-assisted laparoscopic sentinel node biopsy for prostate cancer. Eur Urol 2014; 66: 991.*
10. *Waelkens P, van Oosterom MN, van den Berg NS et al: Surgical navigation: an overview of the state-of-the-art clinical applications. In: Radioguided Surgery. Edited by K Herrmann, OE Nieweg and SP Povoski. Cham, Switzerland: Springer International Publishing 2016; chapt 4, pp 57-73.*
11. *Baumhauer M, Feuerstein M, Meinzer HP et al: Navigation in endoscopic soft tissue surgery: perspectives and limitations. J Endourol 2008; 22: 751.*
12. *Rassweiler J, Rassweiler MC, Muller M et al: Surgical navigation in urology: European perspective. Curr Opin Urol 2014; 24: 81.*
13. *Bluemel C, Matthies P, Herrmann K et al: 3D scintigraphic imaging and navigation in radioguided surgery: freehand SPECT technology and its clinical applications. Expert Rev Med Devices 2016; 13: 339.*
14. *KleinJan GH, van den Berg NS, van Oosterom MN et al: Toward (hybrid) navigation of a fluorescence camera in an open surgery setting. J Nucl Med 2016; 57: 1650.*
15. *Brouwer OR, Buckle T, Bunschoten A et al: Image navigation as a means to expand the boundaries of fluorescence-guided surgery. Phys Med Biol 2012; 57: 3123.*
16. *van Oosterom MN, Engelen MA, van den Berg NS et al: Navigation of a robot-integrated fluorescence laparoscope in preoperative SPECT/CT and intraoperative freehand SPECT imaging data: a phantom study. J Biomed Opt 2016; 21: 086008.*
17. *Buda A, Dell'Anna T, Vecchione F et al: Nearinfrared sentinel lymph node mapping with indocyanine green using the VITOM II ICG exoscope for open surgery for gynecologic malignancies. J Minim Invasive Gynecol 2016; 23: 628.*
18. *Müller J, Putora PM, Schneider T et al: Handheld single photon emission computed tomography (handheld SPECT) navigated video-assisted thoracoscopic surgery of computer tomographyguided radioactively marked pulmonary lesions. Interact Cardiovasc Thorac Surg 2016; 23: 345.*
19. *Brouwer OR, van den Berg NS, Matheron HM et al: A hybrid radioactive and fluorescent tracer for sentinel node biopsy in penile carcinoma as a potential replacement for blue dye. Eur Urol 2014; 65: 600.*

20. *Grivas N, Wit E, Pos F et al: Sentinel lymph node dissection to select clinically node-negative prostate cancer patients for pelvic radiation therapy: effect on biochemical recurrence and systemic progression. Int J Radiat Oncol Biol Phys 2017; 97: 347.*
21. *KleinJan GH, Bunschoten A, van den Berg NS et al: Fluorescence guided surgery and tracer-dose, fact or fiction? Eur J Nucl Med Mol Imaging 2016; 43: 1857.*
22. *Laina I, Rieke N, Rupprecht C et al: Concurrent segmentation and localization for tracking of surgical instruments. Presented at Medical Image Computing and Computer-Assisted Intervention (MICCAI) 2017, International Conference, Proceedings, Part II, Quebec City, Quebec, Canada, September 11-13, 2017.*
23. *Christensen A, Juhl K, Charabi B et al: Feasibility of real-time near-infrared fluorescence tracer imaging in sentinel node biopsy for oral cavity cancer patients. Ann Surg Oncol 2016; 23: 565.*
24. *Stoffels I, Leyh J, P€oppel T et al: Evaluation of a radioactive and fluorescent hybrid tracer for sentinel lymph node biopsy in head and neck malignancies: prospective randomized clinical trial to compare ICG-99mTc-nanocolloid hybrid tracer versus 99mTc-nanocolloid. Eur J Nucl Med Mol Imaging 2015; 42: 1631.*
25. *Schaafsma BE, Verbeek FP, Rietbergen DD et al: Clinical trial of combined radio-and fluorescenceguided sentinel lymph node biopsy in breast cancer. Br J Surg 2013; 100: 1037.*
26. *Paredes P, Vidal-Sicart S, Campos F et al: Role of ICG-99mTc-nanocolloid for sentinel lymph node detection in cervical cancer, a pilot study. Eur J Nucl Med Mol Imaging 2017; 44: 1853.*
27. *KleinJan G, Brouwer O, Matheron H et al: Hybrid radioguided occult lesion localization (hybrid ROLL) of 18 F-FDG-avid lesions using the hybrid tracer indocyanine green-99m Tc-nanocolloid. Rev Esp Med Nucl Imagen Mol 2016; 35: 292.*
28. *Azhdarinia A, Ghosh P, Ghosh S et al: Duallabeling strategies for nuclear and fluorescence molecular imaging: a review and analysis. Mol Imaging Biol 2012; 14: 261.*
29. *Banerjee SR, Pullambhatla M, Byun Y et al: Sequential SPECT and optical imaging of experimental models of prostate cancer with a dual modality inhibitor of the prostate-specific membrane antigen. Angew Chem Int Ed Engl 2011; 50: 9167.*
30. *Hekman MC, Boerman OC, de Weijert M et al: Targeted dual-modality imaging in renal cell carcinoma: an ex vivo kidney perfusion study. Clin Cancer Res 2016; 22: 4634.*

SUPPLEMENTARY METHODS

Integration of fluorescence camera and navigation system

The fluorescence camera setup included an IMAGE1 S H3-Z FI Three-Chip FULL HD camera head, an IMAGE 1 S CONNECT module, an IMAGE 1 S H3-LINK link module and a prototype D-LIGHT P light source [1]. The fixation arm used for the VITOM exoscope setup was a VITOM mechanical holding system (KARL STORZ Endoskope).The video output of the fluorescence setup was fed into the navigation system using an approach that makes use of the digital visual interface (DVI) output of the fluorescence camera read-out unit and the DVI input of an Epiphan frame grabber (DVI2PCIe, Epiphan Systems, Ottawa, Ontario, Canada) integrated inside the navigation system [2,3]. This video feed was then integrated in a custom version of the declipseSPECT 6.0 (SurgicEye) software [2,3], that was specifically tailored towards the requirements of this study. First of all, a number of calibration steps were performed to map all relevant features per camera-scope combination. To allow for visualization of the distance from the scope- or gamma probe-tip to the navigation target, the relative geometry of the instrument tip to instrument reference target was calibrated. For this step, geometrically fitting calibrators were designed using computer-aided design software (SolidWorks, Dassault Systèmes, Vélizy-Villacoublay, France). Subsequently, these were 3D printed in acrylonitrile butadiene styrene (ABS) plastics using a Dimension Elite 3D printer (Stratasys, Eden Prairie, MN, USA), with accompanying CatalystEX 4.4 slicer software (Stratasys). To allow for an AR overlay of the SPECT-based navigation targets in the original camera video feed, two optical checkerboard calibrations were performed to map the camera system parameters, similar as described before [3].

To prevent any sterilization issues and to minimize the time needed during surgery, all system calibrations were performed at least one day prior to the procedure. During the procedure, sterile versions of the PRT (patient/phantom reference target), the CRT (camera reference target) and GPRT (gamma probe reference target) were used. The PRT was attached with sterile tape, choosing an available and relatively rigid anatomical location of the patient.

Evaluation of navigation accuracy

Evaluation of the tool distance accuracy

The 3D tool distance accuracy was evaluated using a rigid phantom setup as shown in Figure 2. The base of the phantom was fabricated out of an acrylic plate harboring three integrated metal fiducials with OTS-visible retroreflective plastic spheres on top, resembling a PRT. Next to the PRT, the phantom provided space to allow for insertion of radioactive ^{57}Co disk sources. Four SPECT/CT scans and four fhSPECT scans were acquired of this setup using one ^{57}Co disk source (Eckert & Ziegler Strahlen- und Medizintechnik, Berlin, Germany) of ~1.7 MBq, resembling a reasonable activity for a SN during a SN biopsy procedure [3]. A ^{57}Co

disk source was chosen due to the relatively long half-life of ^{57}Co (271.7 days) and the fixed and known geometry of the disk, while providing gamma rays close to the energy of ^{99m}Tc gamma rays (main energy peaks of 122 keV versus 140 keV respectively). After scan acquisition, the ^{57}Co source was removed and the specific instrument or scope tip was fitted to match the geometrical 'true target location' (i.e. the exact center of the radioactive source) using a custom designed acrylic spacer for the chosen tool. Using the custom navigation software, the 3D distance between the tip and virtual navigational target was recorded, providing a measure for the 3D tool distance accuracy during navigation. The mean of 600 measurements was acquired per tool tip for every individual SPECT/CT and fhSPECT scan.

Evaluation of the augmented reality registration accuracy

The 2D AR registration accuracy was evaluated using the same rigid phantom as for the tool distance accuracy measurements (Figure 3). However, instead of using the custom spacers to fit tool tips to the geometrical target location, a grid pattern plate was placed with its origin at the geometrical 'true target location' (Figure 3a). The grid pattern consisted of a 60 x 60 mm 2D grid, spanning a measurement scale from -30 to +30 mm, in two coronal directions, with a scale interval of 0.5 mm. Consequently, the accuracy of the AR navigational target overlay in the fluorescence camera video feed could be determined by simply directing the camera to the grid pattern, while discerning the distance from the AR target to the grid origin. Depending on the scope used, the total camera setup was positioned straight above the geometric target location with a chosen working distance of 70 cm for the exoscope, 7.5 cm for the 0° laparoscope and 7.5 cm for the 30° laparoscope. Prior to the phantom measurements, these respective distances were also used to focus and calibrate the specific camera-scope combinations. For every measurement, a screenshot was taken, allowing for accuracy measurements in the recorded images. Since the threshold of the AR target overlay can be adapted to preference, the center of the 5-6 mm diameter green navigation target circle was chosen for the error measurements (Figure 3a-b).

Evaluation of 2D augmented reality registration accuracy for changing optical parameters

As mentioned above, the optical characteristics of the scope-camera setups were calibrated at a chosen working distance during for the AR registration accuracy measurements. To analyze how alteration of this working distance and the corresponding adjustment of the camera focus influenced the AR registration accuracy, an additional evaluation was performed. The 2D AR registration measurements, as described in the section above, were repeated at two different distances: for every camera-scope combination, the accuracy was measured at the original calibrated and focused distance and at a closer distance. Measurements at this closer distance were acquired with both a fixed-focus setting and

a refocused setting. For the VITOM exoscope however, a fixed-focus setting was not possible at the closer distance, since the measurement image was too unfocused to use. Both the 0 and 30° laparoscopes were moved from 7.5 cm tot 2.0 cm and the exoscope was moved from 70 to 14 cm.

Exoscope fluorescence detection sensitivity

To provide a steady and focused image of the operating field, the VITOM exoscope camera combination was fitted in the Storz holding mechanism and placed at a chosen distance to the targeted tissue. Typically, this working distance ranges roughly from 10 – 75 cm [4-7]. To investigate the influence of the working distance chosen with respect to the fluorescence imaging capabilities, the fluorescence sensitivity was evaluated between 15 and 85 cm. For this purpose, a black 96-wells well plate was used (Cellstar, Greiner Bio-One, Frickenhausen, Germany), containing a 1 to 1 dilution series ranging from 5.0 mg/mL (6.45 × 10−3 M) to 9.31 ng/mL (1.20 × 10−11 M) ICG (Pulsion Medical Systems, Munich, Germany) dissolved in human serum albumin (Albuman 200 g/L; Sanquin, Amsterdam, The Netherlands). A total of 30 wells was used. All measurements were taken with the operating room lights switched off.

SUPPLEMENTARY RESULTS

Evaluation of navigation accuracy

Evaluation of the tool distance accuracy

A graphical representation of the 3D tool distance accuracy measurements is shown in Figure 2 and supplemental Figure S1, while the mean accuracy values are shown in Supplemental Table S1.

Evaluation of the augmented reality registration accuracy

The results of the 2D AR registration accuracy measurements are visualized in Figure 3b-c, while the mean values are found in supplemental Table S2.

Evaluation of 2D augmented reality registration accuracy for changing optical parameters

The acquired results of the 2D AR registration accuracy for changing optical parameters are given in Supplemental Table S3. Displacement and refocus of both 0° and 30° laparoscopes yielded only a minor difference in 2D AR accuracy. These differences were so small that they would probably not be noticed in clinical practice. For the exoscope setup, however, the distance and focus adaptations were quite severe and the changes in accuracy were more substantial going from 1.20 to 17.40 mm (p-value 0.000) and from 1.96 to 18.22 mm (p-value 0.000) for SPECT/CT- and fhSPECT-based navigation respectively (see Supplemental Table S3).

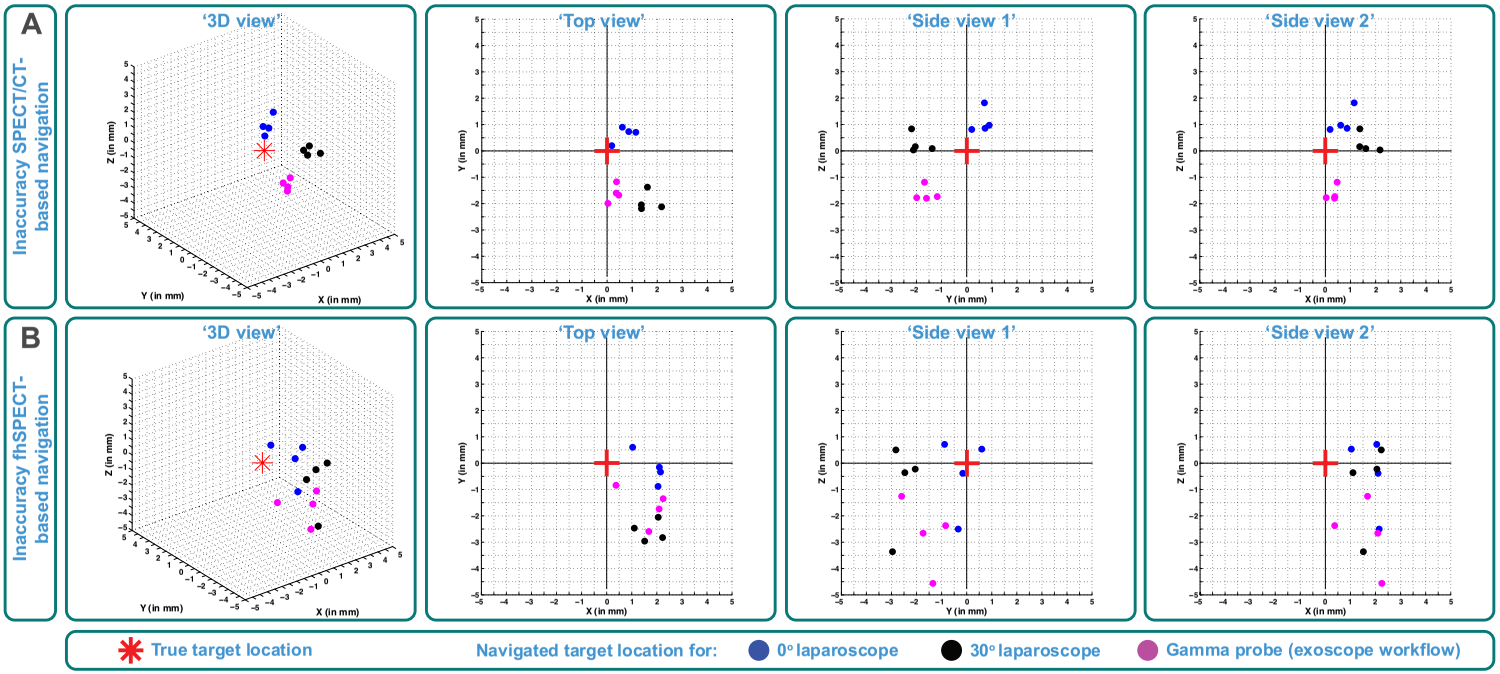

Supplemental Figure S1. Detailed overview of the 3D tool distance accuracy measurements.
*This figure visualizes the accuracy measurements for navigation based on both SPECT/CT **(a)** and fhSPECT **(b)**. Both the total 3D overview and the individual side projections are shown.*

Exoscope fluorescence detection sensitivity

As expected, the exoscope fluorescence imaging sensitivity dropped when applied at larger distances with respect to the fluorescence object of interest. Supplemental Figure S2 shows a clear difference between the number of wells still detected with fluorescence at distances ranging from 15-85 cm. One should note that the Storz system seems to use an automatic image brightness, scaling the overall image brightness to the brightest signal found within the image, including strong reflections or strong fluorescence sources; hence visuals of the wells are not always consistent. Subjectively, we believe fluorescence is still visible at well 17 (distance 15 cm) and well 11 (distance 85 cm). These wells contain 9.84 x 10^{-8} and 6.30 x 10^{-6} M ICG solutions respectively. Using the normalized fluorescence intensity for such an ICG dilution range, as found by Van den Berg et al. [8], gives roughly a 10 fold difference in fluorescence intensity between a working distance of 15 and 85 cm.

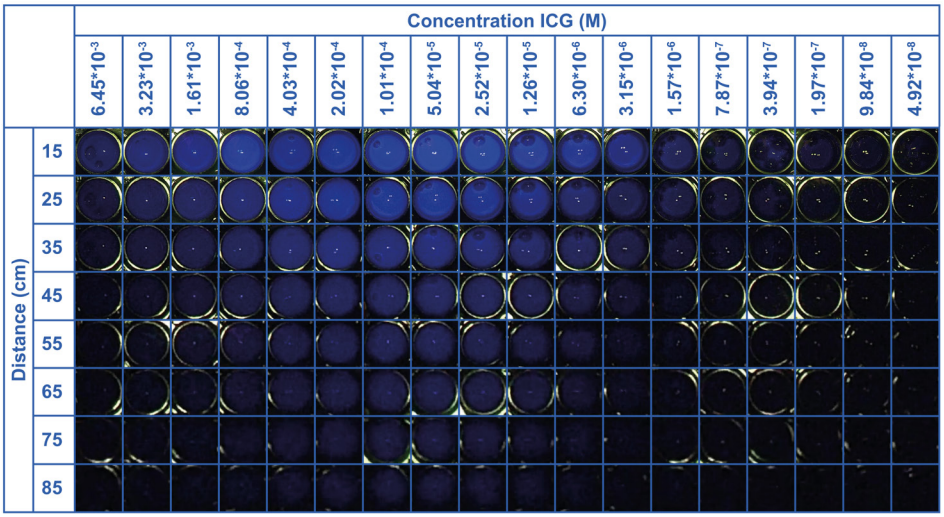

Supplemental Figure S2. Overview of well-plate images captured at different target distances using the exoscope fluorescence imaging mode. *Every well visualizes the fluorescence signal seen at the different ICG concentrations and different exoscope-to-well-plate distance.*

Supplemental Table S1. 3D mean accuracy results for the tool distance accuracy measurements.
These results are based on four individual SPECT/CT scans and four individual fhSPECT scans.

	SPECT/CT-based navigation			fhSPECT-based navigation			Statistical significant difference between mean of both methods(p-values)*
	Separate directions - mean (mm)	Total mean (mm)	Standard deviation (mm)	Separate directions - mean (mm)	Total mean (mm)	Standard deviation (mm)	
0° laparoscope	x: -0.70 y: 0.63 z: -1.11	1.50	0.58	x: -1.83 y: -0.19 z: 0.41	2.28	0.82	No (0.172)
30° laparoscope	x: -1.63 y: -1.93 z: -0.28	2.59	0.39	x: -1.73 y: -2.58 z: 0.86	3.50	0.91	No (0.113)
Gamma probe (exoscope workflow)	x: -0.31 y: -1.61 z: 1.62	2.33	0.27	x: -1.60 y: -1.63 z: 2.71	3.74	1.14	No (0.054)

** Unpaired samples t-test with 95% confidence interval*

Supplemental Table S2. Mean results for the 2D AR registration accuracy measurements.
These results are based on four individual SPECT/CT scans and four individual fhSPECT scans.

	SPECT/CT-based navigation			fhSPECT-based navigation			Statistical significant difference between mean of both methods(p-values)*
	Separate directions - mean (mm)	Total mean (mm)	Standard deviation (mm)	Separate directions - mean (mm)	Total mean (mm)	Standard deviation (mm)	
0° laparoscope	x: -0.44 y: -1.31	1.39	0.45	x: 1.38 y: -0.63	2.57	0.68	Yes (0.028)
30° laparoscope	x: -0.31 y: -0.50	0.67	0.45	x: 1.83 y: -0.25	2.00	0.71	Yes (0.020)
Exoscope	x: -0.63 y: -1.00	1.20	0.33	x: 1.06 y: -1.63	1.96	0.43	Yes (0.032)

** Unpaired samples t-test with 95% confidence interval*

Supplemental Table S3. Total mean results for the AR registration accuracy measurements with changing optical parameters. *These results are based on four individual SPECT/CT scans and four individual fhSPECT scans.*

	Setup	Original distance and focus			Changed distance and fixed focus				Changed distance and changed focus			
		Distance to target (mm)	Total mean (mm)	Standard deviation (mm)	Distance to target (mm)	Total mean (mm)	Standard deviation (mm)	Statistical significance with respect to original (p-values)*	Distance to target (mm)	Total mean (mm)	Standard deviation (mm)	Statistical significance with respect to original (p-values)*
SPECT/CT	0° laparoscope	75	1.39	0.45	20	1.39	0.35	No (0.907)	20	1.45	0.31	No (0.732)
	30° laparoscope	75	0.67	0.45	20	1.17	0.39	Yes (0.005)	20	1.27	0.22	Yes (0.018)
	Exoscope	700	1.20	0.33	140	-‡	-‡	-‡	140	17.40	0.34	Yes (0.000)
fhSPECT	0° laparoscope	75	2.57	0.68	20	2.08	0.56	Yes (0.022)	20	2.11	0.58	Yes (0.047)
	30° laparoscope	75	2.00	0.71	20	2.47	0.64	Yes (0.031)	20	2.46	0.47	Yes (0.047)
	Exoscope	700	1.96	0.43	140	-‡	-‡	-‡	140	18.22	0.61	Yes (0.000)

** Paired samples t-test with 95% confidence interval, ‡ Measurement not possible without changing camera focus*

SUPPLEMENTARY REFERENCES

1. *KleinJan, G. H., van den Berg, N. S., Brouwer, O. R. et al.: Optimisation of Fluorescence Guidance During Robot-assisted Laparoscopic Sentinel Node Biopsy for Prostate Cancer. Eur Urol, 66: 991, 2014*
2. *KleinJan, G. H., van den Berg, N. S., van Oosterom, M. N. et al.: Toward (Hybrid) Navigation of a Fluorescence Camera in an Open Surgery Setting. J Nucl Med, 57: 1650, 2016*
3. *van Oosterom, M. N., Engelen, M. A., van den Berg, N. S. et al.: Navigation of a robot-integrated fluorescence laparoscope in preoperative SPECT/CT and intraoperative freehand SPECT imaging data: a phantom study. J Biomed Opt, 21: 086008, 2016*
4. *Buda, A., Dell'Anna, T., Vecchione, F. et al.: Near-infrared sentinel lymph node mapping with indocyanine green using the VITOM II ICG exoscope for open surgery for gynecologic malignancies. J Minim Invasive Gynecol, 23: 628, 2016*
5. *KleinJan, G. H., Hellingman, D., van den Berg, N. S. et al.: Hybrid surgical guidance: Does hardware integration of gamma-and fluorescence-imaging modalities make sense? J Nucl Med, 58: 646, 2017*
6. *Mamelak, A. N., Drazin, D., Shirzadi, A. et al.: Infratentorial supracerebellar resection of a pineal tumor using a high definition video exoscope (VITOM®). J Clin Neurosci, 19: 306, 2012*
7. *Vercellino, G., Chiantera, V., Gaßmann, J. et al.: Prospective comparison of loop excision under colposcopic guidance versus vitom guidance. Geburtshilfe Frauenheilkd, 72: 945, 2012*
8. *van den Berg, N. S., Miwa, M., KleinJan, G. H. et al.: (Near-infrared) fluorescence-guided surgery under ambient light conditions: a next step to embedment of the technology in clinical routine. Ann Surg Oncol, 23: 2586, 2016*

CHAPTER 5

NAVIGATING SURGICAL FLUORESCENCE CAMERAS USING NEAR-INFRARED OPTICAL TRACKING

Adapted from: van Oosterom MN, den Houting DA, van de Velde CJH, van Leeuwen FWB

The Journal of Biomedical Optics, 2018, 23(5): 056003

ABSTRACT

Fluorescence guidance facilitates real-time intraoperative visualization of the tissue of interest. However, due to attenuation, the application of fluorescence guidance is restricted to superficial lesions. To overcome this shortcoming, we have previously applied three-dimensional surgical navigation to position the fluorescence camera in reach of the superficial fluorescent signal. Unfortunately, in open surgery, the near-infrared (NIR) optical tracking system (OTS) used for navigation also induced an interference during NIR fluorescence imaging. In an attempt to support future implementation of navigated fluorescence cameras, different aspects of this interference were characterized and solutions were sought after. Two commercial fluorescence cameras for open surgery were studied in (surgical) phantom and human tissue setups using two different NIR OTSs and one OTS simulating light-emitting diode setup. Following the outcome of these measurements, OTS settings were optimized. Measurements indicated the OTS interference was caused by: (1) spectral overlap between the OTS light and camera, (2) OTS light intensity, (3) OTS duty cycle, (4) OTS frequency, (5) fluorescence camera frequency, and (6) fluorescence camera sensitivity. By optimizing points 2 to 4, navigation of fluorescence cameras during open surgery could be facilitated. Optimization of the OTS and camera compatibility can be used to support navigated fluorescence guidance concepts.

INTRODUCTION

Fluorescence guidance has demonstrated value in the field of oncologic surgery where it helps provide real-time visualization of the lesion of interest [1]. Due to its depth restrictions, however, the utility of fluorescence guidance is currently limited to superficial lesions [2]. To compensate for this shortcoming, we have previously introduced the clinical use of dual-modality or rather hybrid tracers [3]. These tracers directly link preoperative identification of radioactive lesions at the department of nuclear medicine (e.g., using three-dimensional (3-D) single-photon emission computed tomography/x-ray computed tomography (SPECT/CT) or positron emission tomography/CT (PET/CT) data sets) to the intraoperative detection of fluorescent lesions. Through this connection, it has become possible to create surgical navigation setups that realize positional tracking of fluorescence cameras in pre- or intraoperative 3-D imaging data sets (4-6). Combined with futuristic virtual and augmented reality-based computer-assisted surgery techniques, these approaches extend the use of fluorescence guidance toward lesions that lie beyond the depth-related fluorescence detection limits (i.e., >1 cm deep).

Initial studies, using a near-infrared (NIR) optical tracking system (OTS) and tracking fiducials placed on both the fluorescence camera and the patient, helped to demonstrate the potential of this navigated fluorescence camera concept in a variety of settings [4,5,7,8]. Unfortunately, in some of the open surgical procedures, the OTS caused an interfering flickering signal that prevented fluorescence imaging (see Figures 1–3) [4]. Intriguingly, we observed that this OTS interference differed substantially between the two open surgery cameras we have studied [4,5]; while the interference completely obstructed fluorescence imaging with one system, the effect was only minor for navigation of the other system. Therefore, the aim of this study was to investigate, which features influenced the interference and to identify possible engineering solutions to support further implementation of the navigation concept with fluorescence cameras.

METHODS

Navigation and Tracking Systems

Our “standard” navigation setup was based on the declipse SPECT navigation device (SurgicEye GmbH, Munich, Germany; see Figure 1). This navigation system incorporates a Polaris Vicra OTS (OTS^{vicra}; Northern Digital Inc.,Waterloo, Canada) to allow for object position and orientation tracking of geometrically unique reference targets using a fixed pulsed NIR light source (20 Hz; center wavelength (CWL) of 863 nm; full-width-at-halfmaximum (FWHM) of 49 nm) [4,9]. The pulse on-time per period was about 1.8 ms, resulting in a duty cycle of roughly 4% (see Appendix A).

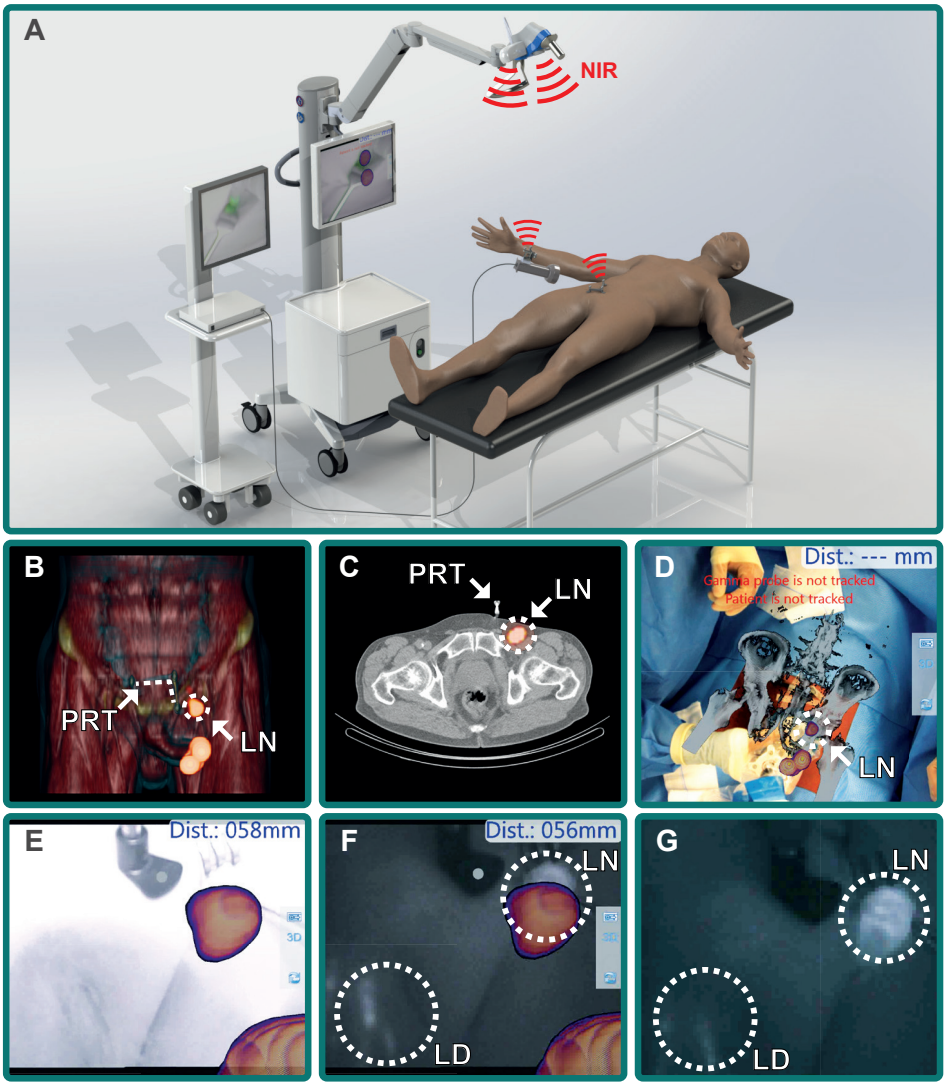

Figure 1. Illustration of in vivo navigated fluorescence camera during penile cancer-related sentinel lymph node biopsy. (a) *Overview of navigated setup in the operating room.* ***(b)*** *3-D rendering of SPECT/CT patient scan, with patient tracking fiducials (PRT) and lymph node targeted for navigation (LN) visible.* ***(c)*** *Two-dimensional slice showing the navigated LN.* ***(d)*** *Augmented reality overlay of the patient scan in the operating room.* ***(e)*** *Augmented reality overlay of the patient scan in the fluorescence camera video feed, displaying the LN location (purple) and the estimated distance toward it. Due to the OTS interference, fluorescence imaging is obstructed, predominantly showing white background in the video feed.* ***(f)*** *Same navigated fluorescence camera image without interference, displaying the LN and lymph ducts (LD).* ***(g)*** *Fluorescence imaging only, without interference.*

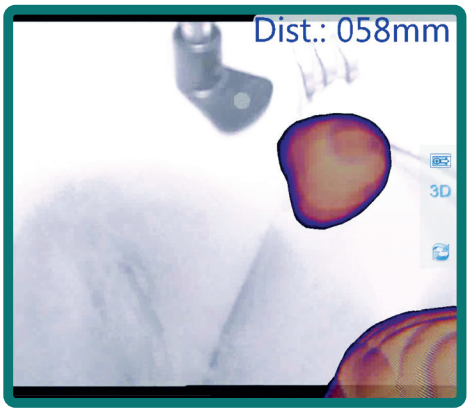

Figure 2. Video example of OTS-induced interference during in vivo navigation of fluorescence camera for penile cancer-related sentinel lymph node biopsy. *With this fluorescence camera, interference completely obstructs fluorescence imaging. Fluorescence and interference signals are both in white (Video 1 [URL: https://doi.org/10.1117/1.JBO.23.5.056003.1]).*

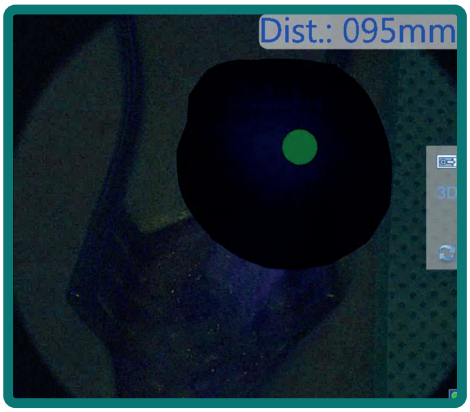

Figure 3. Video example of OTS-induced interference during in vivo navigation of fluorescence camera for penile cancer-related sentinel lymph node biopsy. *With this fluorescence camera, interference is clearly visible when low fluorescence intensities are observed. However, fluorescence imaging is still possible. Fluorescence and interference signals are both in blue (Video 2 [URL: https://doi.org/10.1117/1.JBO.23.5.056003.2]).*

Next to the declipseSPECT integrated OTS^{vicra}, a prototype OTS (OTS^{orthos}; Orthos prototype, Advanced Real-time Tracking GmbH, Weilheim i.OB, Germany) was used. This system allows for manual customization of the pulse frequencies in the 10 to 60 Hz range (CWL: 885 nm, FWHM: 108 nm). The pulse-on time per period was about 0.4 ms, which results in a duty cycle of 0.8% at 20 Hz. To allow for automatic triggering of the pulse frequency, either an analog video signal or digital transistor-transistor-logic signal could be connected via the Bayonet Neill–Concelman (BNC) input connector.

In addition to both these OTSs, a light-emitting diode (LED)-based illumination setup was created, simulating the light source of an OTS. This allowed for controlled variations to be made in both the tracking pulse frequency and duty cycle during the experiments. This configuration consisted of three 850 nm LEDs (CWL: 845 nm, FWHM: 33 nm; HE1-220AC, Harvatek Corp., Hsinchu City, Taiwan) connected to a multichannel universal LED controller (Mightex Systems, Pleasanton, California).

Fluorescence Camera Systems

Two open surgery conformité européenne (CE) marked fluorescence cameras were used for this study. First, a PDE camera (Hamamatsu Photonics K.K., Hamamatsu, Japan; European specifications) using a ring of LEDs (CWL: 755 nm, FWHM: 10 nm) to excite the NIR fluorescent dye indocyanine green (ICG). The light detected by this charge-coupled device (CCD) camera is filtered by a >820

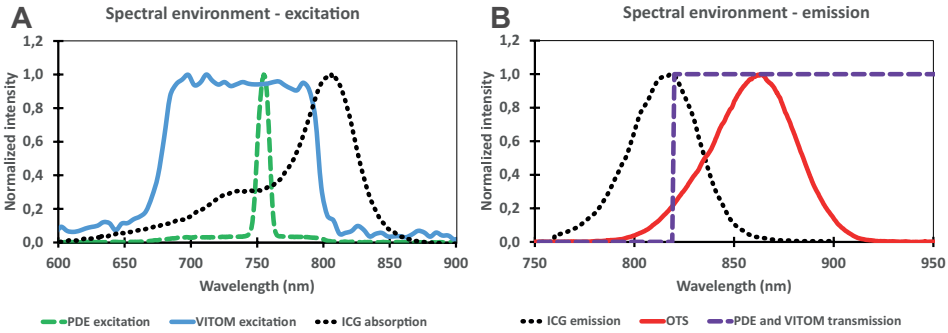

Figure 4. Spectral environment. (a) *The excitation light used by the PDE and VITOM camera and the ICG absorption spectrum.* ***(b)*** *The ICG spectrum and the light spectrum employed by the OTS^{vi-cra}. Spectral transmission window of the PDE and VITOM is estimated from the literature [10,12].*

nm long pass filter [10]. The resulting video-feed was delivered as an analog 50 Hz interlaced video signal. Second, a VITOM exoscopic camera setup (IMAGE1 S H3-Z FI Three-Chip FULL HD camera head and VITOM® II NIR/ICG Telescope 0 deg; KARL STORZ Endoskope GmbH & Co. KG, Tuttlingen, Germany; European specifications). In this setup, fluorescence excitation occurs using a prototype D-LIGHT P filtered Xenon light source (CWL: ~740 nm, FWHM: 120 nm).11 The light collected by the CCD camera was filtered to allow light in the 390 to 670 nm and > 800 nm range to be collected.12 The resulting video-feed was delivered as a digital 50 Hz progressive video signal. A summary of the fluorescence camera and tracking system characteristics is shown in Table 1 and Figure 4.

Surgical Fluorescence Phantom and Human Tissue

A surgical fluorescence phantom was fabricated for the experiments. This setup consisted of a previously described, siliconebased phantom [8] with two fluorescent beads incorporated (see Appendix B). In addition, surgically excised human tissue was used. ICG-nanocolloid (dissolved in saline) was prepared as previously described [13]. Four 0.1 mL injections, with effectively 40 µg/mL ICG, where used for the injection site, where 0.1 mL with 1% of the injected dose was used for the sentinel lymph node [13].

Characterization of the Tracking Interference

All fluorescence camera recordings were performed using an Epiphan frame grabber (DVI2PCIe, Epiphan Systems Inc., Ottawa, Ontario, Canada) integrated within the declipseSPECT navigation system. To quantify the OTS-induced interference, the acquired recordings were analyzed using MATLAB® (The MathWorks Inc., Natick, Massachusetts). To evaluate the intensity of the interference signals in the fluorescence imaging recordings, the mean pixel intensity (MPI) per video frame was calculated with formula (1):

Table 1. Characteristics of the fluorescent dye and devices used.

Light source	Emission spectrum	Frequency	Pulse-on-time		
ICG (in albumin)	CWL: 818 nm FWHM: 40 nm	Continuous[a]	-[a]		
OTS[vicra]	CWL: 863 nm FWHM: 49 nm	20 Hz	~1.8 ms		
OTS[orthos]	885 nm FWHM 108 nm	Modular: 10 - 60 Hz	~0.4 ms		
LED setup	CWL: 845 nm FWHM: 33 nm	Modular	Modular		
Camera	**Excitation light source**	**ICG emission filter**	**Camera frame rate**	**Measured camera recording frequency**	**Sensor type**
PDE (EU version)	LED CWL: 755 nm FWHM: 10 nm	>820 nm	50 Hz interlaced	25 Hz	CCD-based
VITOM (EU version)	Xenon light bulb (D-light P version) CWL: 740 nm FWHM: 120 nm	<670 nm and >820 nm	50 Hz progressive	25 Hz	CCD-based

[a]Is depended on the excitation source used, which is mainly continuous.

$$MPI(t) = \frac{1}{N}\sum_{i=1}^{N} p_i(t) \quad (1)$$

With MPI in counts, t is the video frame number, p_i is the individual pixel value, and N is the total number of pixels in one frame. To quantify the dynamic character of these interference patterns, a "severity of dynamic interference value" (SDIV) was proposed. To include rapid changes in intensity, while excluding gradual changes, this SDIV was formulated as the standard deviation (σ) of the first derivative of MPI; i.e., a stable video illumination would result in a low SDIV while a highly dynamic flickering in the video would result in a high SDIV:

$$SDIV = \sigma_{MPI'} = \sqrt{\frac{1}{J}\sum_{t=1}^{J}(MPI'(t) - \overline{MPI'})^2} \quad (2)$$

With SDIV in counts/frame or counts/s, J is the total number of video frames, MPI' is the first derivative of MPI, and $\overline{MPI'}$ is the average thereof.

Interference Effect for a Modular Tracking Frequency and Duty Cycle

To quantitatively measure the effect that a variable OTS pulse frequency and duty cycle have on the observed interference during fluorescence imaging, the LEDs were used. To generate light reflection, the LED setup was pointed at a flat surface using a 15 cm distance and the camera systems were placed at a 17 cm distance (Figure 5). These distances were chosen to maximize the captive nature of the most sensitive setup while preventing saturation of the camera CCD chips. At each LED setting (frequencies: 5 to 100 Hz, duty cycles: 1% to 90%), 2 s video recordings were generated and analyzed (i.e., MPI and SDIV values) for both fluorescence cameras. These experiments were performed in duplicate.

Interference in a Surgical Phantom and Human Tissue

To simulate surgical application, the two navigated fluorescence camera systems were sequentially positioned right above the surgical phantom using a distance of 15 cm. Subsequently, either the OTS^{vicra} or OTS^{orthos} was also placed above the surgical phantom using a distance of 130 or 30 cm. To illustrate the difference in interference in the "standard" navigation setup, video recordings were produced and analyzed (i.e., MPI and SDIV values) with the OTS^{vicra} turned off and on. Furthermore, using the BNC synchronization input of the OTS^{orthos}, the video signal of the PDE was sampled, allowing for synchronization of the tracking frequency with the PDE acquisition frequency. To illustrate the effect of synchronized NIR optical tracking during surgery, video recordings were acquired with the OTS^{orthos} turned off and on, using a tracking frequency of 20 (unsynchronized) and 25 Hz (synchronized). These recordings were also analyzed for the above-mentioned MPI and SDIV values. Furthermore, the most important measurements, i.e., PDE fluorescence imaging with "no tracking," "OTS^{vicra} tracking at 130 cm" and

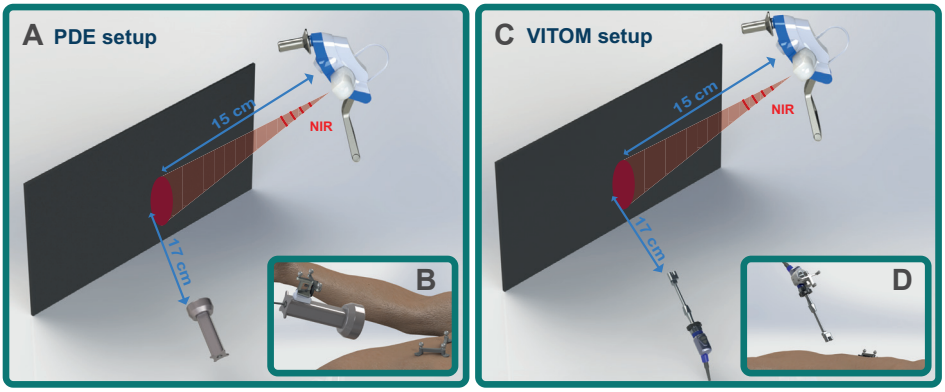

Figure 5. Schematic overview of the measurements with the LED setup. (a) *Setup for the PDE camera and LED setup, both pointed at a black surface.* ***(b)*** *Analogy of the clinical usage of the navigated PDE.* ***(c)*** *Setup for the VITOM and LED setup, both pointed at the black surface.* ***(d)*** *Analogy of the clinical usage of the navigated VITOM.*

"synchronized OTS^{orthos} tracking at 130 cm," were also recorded using the human tissue setting.

Gated Tracking Pulse and Fluorescence Imaging for PDE

To create an alternating gated setup, a tracking pulse should only be sent whenever there is no fluorescence image capture (Figure 6). We assumed the PDE camera would have a "dead-imaging-moment" long enough to send out this tracking pulse, without it being detected by the camera. This was investigated by building and programming a small electronic circuit to sample the frequency timing of the PDE video signal and trigger the OTS^{orthos} tracking pulse. This circuit was built around an LM1881N video processing chip and an Arduino Uno microcontroller (Arduino AG, Italy).

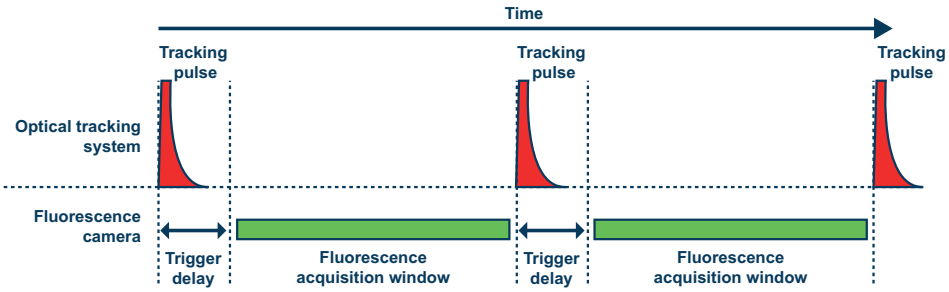

Figure 6. Gated tracking pulse and fluorescence imaging. *In a sequential fashion, optical tracking pulses are only emitted when the fluorescence camera is not acquiring a fluorescence image.*

RESULTS

Interference in a Surgical Phantom Setup

Table 2 and Appendix C demonstrate the interference the 20 Hz OTS^{vicra} induces for the different fluorescence cameras. This interference is the result of the light emitted from the OTS, overlapping with the spectral detection window for which NIR fluorescence cameras are traditionally designed (>800 nm). More specifically, the spectral emission of the OTS overlaps with the fluorescence emission of the clinically approved NIR dye ICG (emission max at 820 nm) and more experimental Cy7-analogs (emission max between 795 and 825 nm) (Figure 4) [4,14,15]. For both systems, the MPI and SDIV values rose when the OTS^{vicra} was turned on (Table 2); a rise of 142.6 counts (PDE) versus 18.5 counts (VITOM) for the mean MPI values and 1757.5 counts/s (PDE) versus 410.0 counts/s (VITOM) for the SDIV values was recorded. As illustrated in Appendix C, the interference in the PDE setup was so severe that it inhibited the differentiation of the fluorescent beads with respect to their surroundings. Using the VITOM setup, the dynamic OTS^{vicra} light was also clearly visible; however, it did not limit the delineation of the fluorescent beads.

Interference Effect for a Modular Tracking Frequency and Duty Cycle

Next to the spectral overlap between the light emitted by the OTS and the spectral detection window of the surgical fluorescence cameras, exposure to the variations in LED light pulse frequencies and duty cycles influenced the

Table 2. Quantitative analysis of the surgical fluorescence phantom measurements with the OTS-^{vicra} and OTS^{orthos}. *Mean MPI and SDIV values calculated for the PDE and VITOM, with and without the OTS turned on at different settings and distances.*

Condition	OTS frequency (Hz)	OTS distance (cm)	Mean MPI (counts)	SDIV (counts/ frame)	SDIV (counts/s)
OTS^{vicra}					
PDE without OTS	-	-	38.7	0.2	5.0
PDE with OTS	20	130	181.3	70.5	1762.5
VITOM without OTS	-	-	27.5	0.2	0.5
VITOM with OTS	20	130	46.0	16.6	415.0
OTS^{orthos}					
PDE without OTS	-	-	32.6	0.2	5.0
PDE with OTS	20	130	42.2	2.6	65.0
PDE with OTS	25	130	54.8	0.1	2.5
PDE with OTS	20	30	88.0	40.7	1017.5
PDE with OTS	25	30	147	0.3	7.5

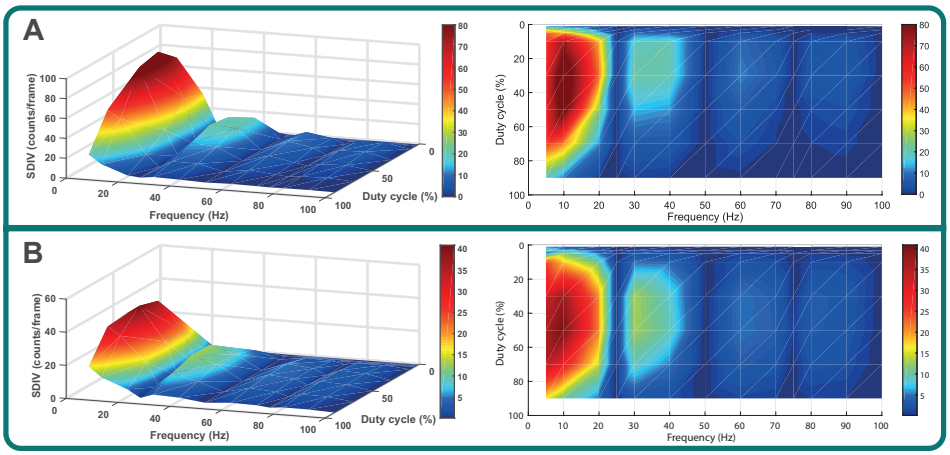

Figure 7. Visualization of the severity of dynamic interference for the fluorescence cameras using the LED setup. (a) *The SDIV results for the PDE in 3-D-view (left) or top-view (right).* ***(b)*** *The SDIV results for the VITOM in 3-D-view (left) or top-view (right).*

interferences (Figure 5). Plotting of the MPI and SDIV revealed the LED settings affected the two cameras differently (Figure 7 and Appendix D). Of both cameras, the PDE proved most sensitive to the NIR LED light, yielding substantially higher MPI values at identical settings; e.g., a mean MPI of 59.3 counts for the PDE and 26.9 counts for the VITOM at a frequency of 20 Hz and duty cycle of 3.2%. As can be seen in Appendix D, the intensity of the MPI decreased with decreasing duty cycles (i.e., duty cycles approaching 0%). Figure 7 reveals the duty cycle settings also influenced the SDIV values, showing a decrease in the intensity of the dynamic interference when duty cycle values approached either 0% or 100%. For both cameras, minimal dynamic interference (i.e., low SDIV value) was observed at tracking pulse frequencies of 25, 50, and 75 Hz, which is in line with recording frame rates of 25 frames per second. Unfortunately, a stable interfering background illumination remained (i.e., stable nonzero MPI values). These results indicate that the mismatch between the frequency of the camera recording frame rate and the OTS tracking light pulse cause the dynamic character (i.e. flickering) of the interference.

Synchronized Tracking Frequency for the PDE in Both Phantom and Human Tissue

Given the above-reported findings, we reasoned that using an alternative OTS with controllable tracking frequency could help solve or reduce the severe flickering effects. Using the surgical phantom setup, Table 2 and Appendix C illustrate that a 20-Hz OTS^{orthos} already reduced the interference intensity fourfold compared to what was observed for the OTS^{vicra}: mean MPI values of 42.2 counts versus 181.3 counts, respectively. This improvement is most likely a combination of a shorter pulse-on time (i.e., a lower duty cycle) and a lower light intensity.

Figure 8. Evaluation of optical tracking during fluorescence imaging for human tissue. (a) *Excised human tissue with the PDE camera situated 15 cm above the tissue.* ***(b)*** *Fluorescence imaging without any tracking. Both injection site (IS) and sentinel lymph node (LN) are visible.* ***(c, d)*** *Example video frames for fluorescence imaging during tracking with the* ***(c)*** *OTS^{vicra} and* ***(d)*** *synchronized OTS^{orthos}.*

When the OTS^{orthos} pulse frequency was matched with the PDE recording frequency (at 25 Hz), SDIV values approached zero and the dynamic character of the interference was completely eliminated (Table 2 and Appendix C), thus providing comparable SDIV values with the OTS^{orthos} turned on and off. However, mean MPI values differed between 54.8 counts with the OTS^{orthos} turned on and 32.6 counts with the OTS^{orthos} turned off (distance of 130 cm). Despite this stable

background, differentiation between fluorescent beads and background in the phantom setup was possible. Figure 8 clearly shows that similar results are found when this concept is applied to human tissue; where fluorescence imaging was rendered unfeasible during tracking with the OTS^{vicra} while fluorescence imaging became possible during tracking with the synchronized OTS^{orthos}.

Gated Tracking Pulse and Fluorescence Imaging for PDE

In an attempt to completely remove the interference during fluorescence imaging, including the background illumination, an alternating gated tracking and fluorescence imaging setup was pursued. Unfortunately, it was not possible to identify a "dead-imaging-moment" capable of harboring the OTS^{orthos} tracking pulse. Consequently, we were not able to get rid of the stable background illumination.

DISCUSSION

In this study we have investigated possible solutions to solve the interference issues found during the navigation of clinical fluorescence cameras using NIR optical tracking in open surgery. The interference was caused by a number of features: (1) the spectral overlap between the ICG emission light and the NIR OTS light, (2) the OTS light intensity, (3) the OTS duty cycle, (4) the OTS frequency, (5) the fluorescence camera recording frequency, and (6) the camera sensitivity. As we have also observed during our previous studies [4,5,8], this combination of features means that the severity of interference varied between the type of fluorescence camera used. More specifically, the observed interference with the OTS^{vicra} completely obstructed fluorescence imaging with the PDE camera while its influence on the imaging output of the VITOM camera was only minor.

Matching the tracking light pulse frequency with the specific camera imaging frequency, or a multiplication thereof, supported a drastic decrease in the dynamic character of the OTS interference. This approach did not solve the stable background signal. Further reduction of this background signal could be realized by minimizing the OTS pulse intensity and duty cycle. It appears that gating of the OTS tracking pulse and fluorescence image capture will provide outcome. For this to work, a fluorescence camera with a (controllable) long enough "dead-imaging-moment" is needed. As shown in Figure 4 and Table 1, there is little room to decrease the spectral overlap by separating the current OTS spectrum from the emission of dyes that fluoresce in the NIR spectrum. This said, successful use of non-NIR dyes for surgical guidance has been reported, e.g., for fluorescein (emission maximum at 530 nm), 5-aminolevulinate/protoporphyrin IX (emission maximum at 635 nm), and Cy5 (emission maximum at 670 nm) [12,16–18]. When such dyes are used in combination with clinically available far-red fluorescence camera systems [12,19], no overlap with the OTS will occur, allowing navigated camera positioning during open surgery.

Instead of changing the fluorescent dye used to create surgical guidance, one could also opt for using an alternative OTS with a light spectrum that does not overlap with the surgical fluorescence cameras. Unfortunately, most (clinical grade) systems use the NIR spectrum to prevent disturbance of the visible operating room lighting [20]. Research grade OTS systems are already available that employ, e.g., CWL 940 nm NIR wavelengths [20], which is higher than the OTS spectra used in this study. Next to NIR optical tracking, other tracking techniques might also provide outcome for the navigation of fluorescence cameras (e.g., electromagnetic tracking, mechanical tracking, and vision-based tracking) [6,9,21,22]. Of these methods, vision-based tracking seems to be optimally suited for fluorescence cameras when combined with (fluorescent) skin fiducials, detectable with the camera [23]. Most realistically a combination of tracking technologies will provide outcome [24,25].

Next to the fluorescence cameras that are currently available in the clinic, this research also supports the navigation of future surgical fluorescence imaging devices; e.g., fluorescence goggles and head-mounted displays [26].

CONCLUSION

We have characterized the different aspects underlying the OTS interference during the navigation of NIR fluorescence cameras and have identified engineering routes that help solve these issues. With that a basis has been created to engineer OTSs specifically tailored toward the navigation of fluorescence cameras during open surgery.

APPENDIX A: SPECTRAL AND TEMPORAL CHARACTERIZATION

A Horiba Jobin Yvon VS140 linear array fiber spectrometer (Horiba Ltd., Kyoto, Japan) with a 1-m optical fiber (M15L01, Thorlabs Inc., Newton, New Jersey) was used to spectrally characterize the excitation light of the different fluorescence cameras and the OTSs used.

To determine both the OTS pulse frequency and its duty cycle, a light-to-voltage setup was used. This setup consisted of an optical light-to-voltage sensor (TSL 250R, TAOS Inc., Plano, Texas), an analog 50 MHz oscilloscope (no. 2225, Tektronix Inc., Beaverton, Oregon), and a direct current power supply (PS613 HQ POWER, Velleman NV, Gavere, Belgium). An example for the OTS^{vicra} is shown in Figure 9.

APPENDIX B: SURGICAL FLUORESCENCE PHANTOM DETAILS

The fluorescent beads incorporated in the surgical fluorescence phantoms were created by mixing an ICG solution with an epoxy resin (epoxy resin C, R&G Faserverbundwerkstoffe GmbH, Waldenbuch, Germany) using the following ratio: 10:6:1 for epoxy resin, epoxy hardener, and ICG solution, respectively. The ICG

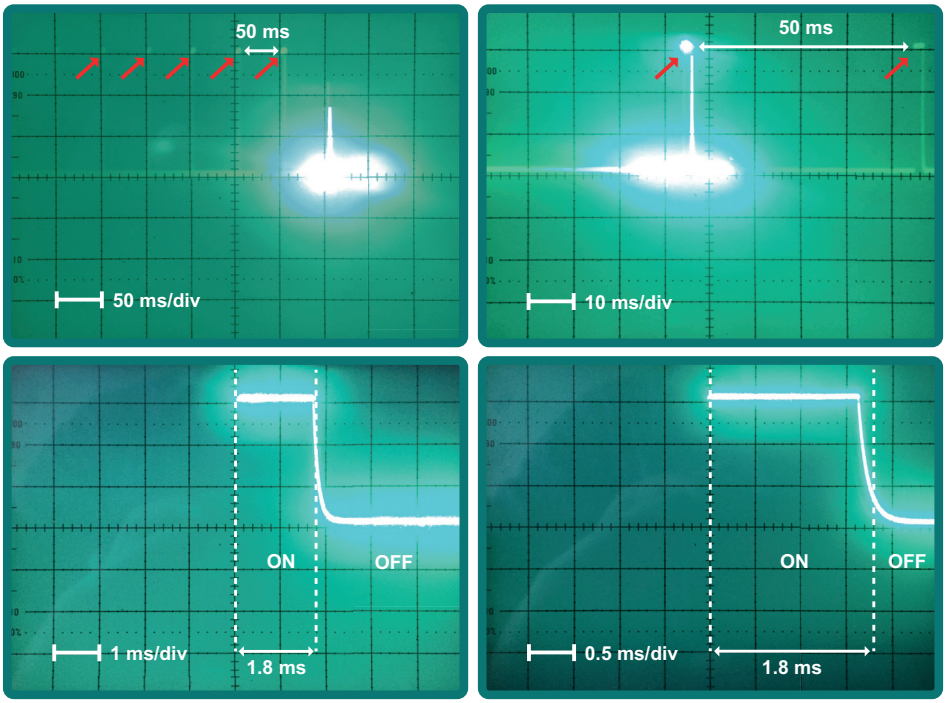

Figure 9. Temporal characterization OTS^{vicra} light pulse. *Oscilloscope screens are shown at different magnifications.*

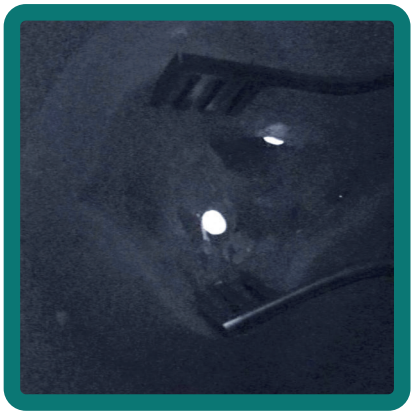

Figure 10. Video example of OTS^{vicra}-induced interference in the surgical fluorescence phantom navigation of PDE fluorescence camera *(Video 3 [URL: https://doi.org/10.1117/1.JBO.23.5.056003.3]).*

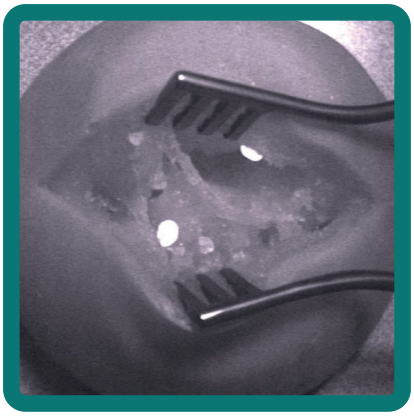

Figure 11. Video example of OTS^{orthos}-induced interference in the surgical fluorescence phantom navigation of PDE fluorescence camera *(Video 4 [URL: https://doi.org/10.1117/1.JBO.23.5.056003.4]).*

solution comprised of 1 mg/mL ICG dissolved in methanol. The effective ICG concentration in the beads was therefore 60 µg/mL, which roughly presents a clinically relevant and detectable ICG concentration [8].

APPENDIX C: VISUALIZATION OF OTS-INDUCED INTERFERENCE DURING THE IN VIVO AND PHANTOM APPLICATION

An example of the OTS-induced interference during in vivo application of the navigated PDE fluorescence camera is shown in Figures 1 and 2. This is based on data published by KleinJan et al., where the navigated PDE camera was demonstrated during sentinel lymph node biopsy in five penile cancer patients [4]. Interference observed in the surgical fluorescence phantoms is illustrated for the OTS^{vicra} in Figures 10 and 12, and for the OTS^{orthos} in Figures 11 and 13.

APPENDIX D: DETAILED OVERVIEW OF THE MPI MEASUREMENTS FOR A MODULAR TRACKING FREQUENCY AND DUTY CYCLE

A detailed overview of the MPI measurements obtained at different tracking frequency and duty cycle settings for the LED setup are shown for both the PDE and VITOM camera in Figure 14.

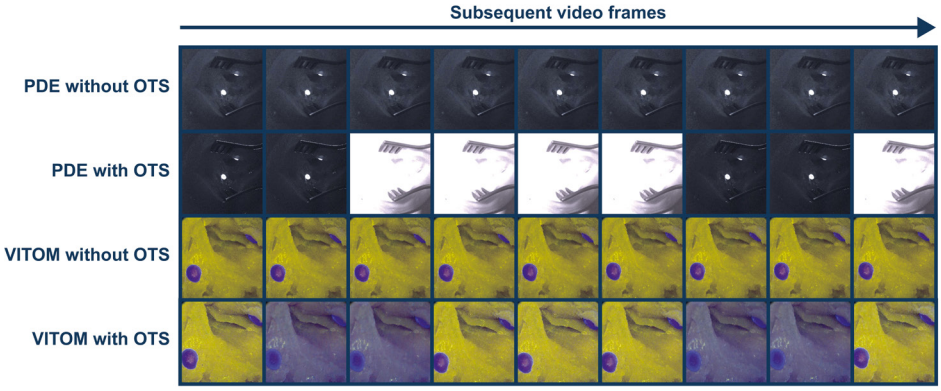

Figure 12. Video images of OTS^{vicra}-induced interference during fluorescence imaging in the open surgical phantom. *Top to bottom shows video image sequences of the surgical fluorescence phantom for the PDE without the OTS^{vicra}, PDE with the OTS^{vicra}, VITOM without the OTS^{vicra}, and VITOM with the OTS^{vicra}. The OTS^{vicra} was positioned at a distance of 130 cm.*

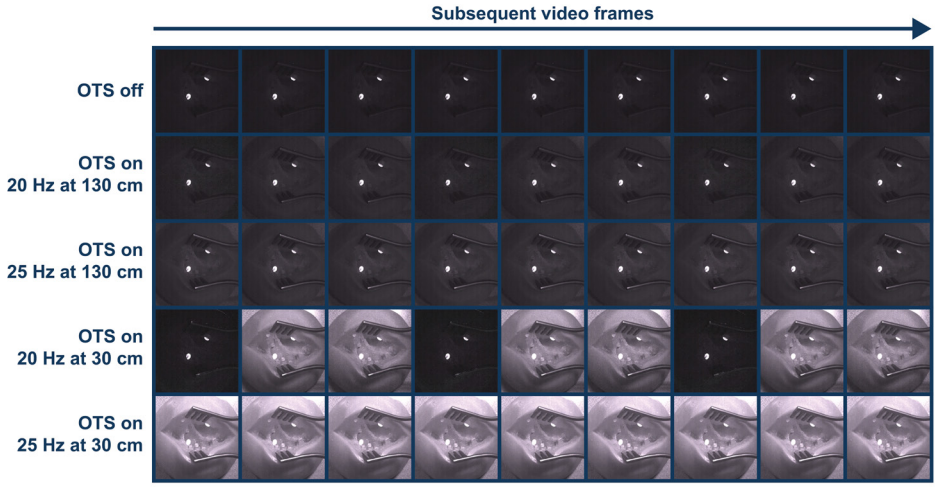

Figure 13. Video images of OTS^{orthos}-induced interference during fluorescence imaging in the open surgical phantom. *Top to bottom shows video image sequences of the surgical fluorescence phantom for the PDE without the OTS^{orthos} and with the OTS^{orthos} at different settings and distances.*

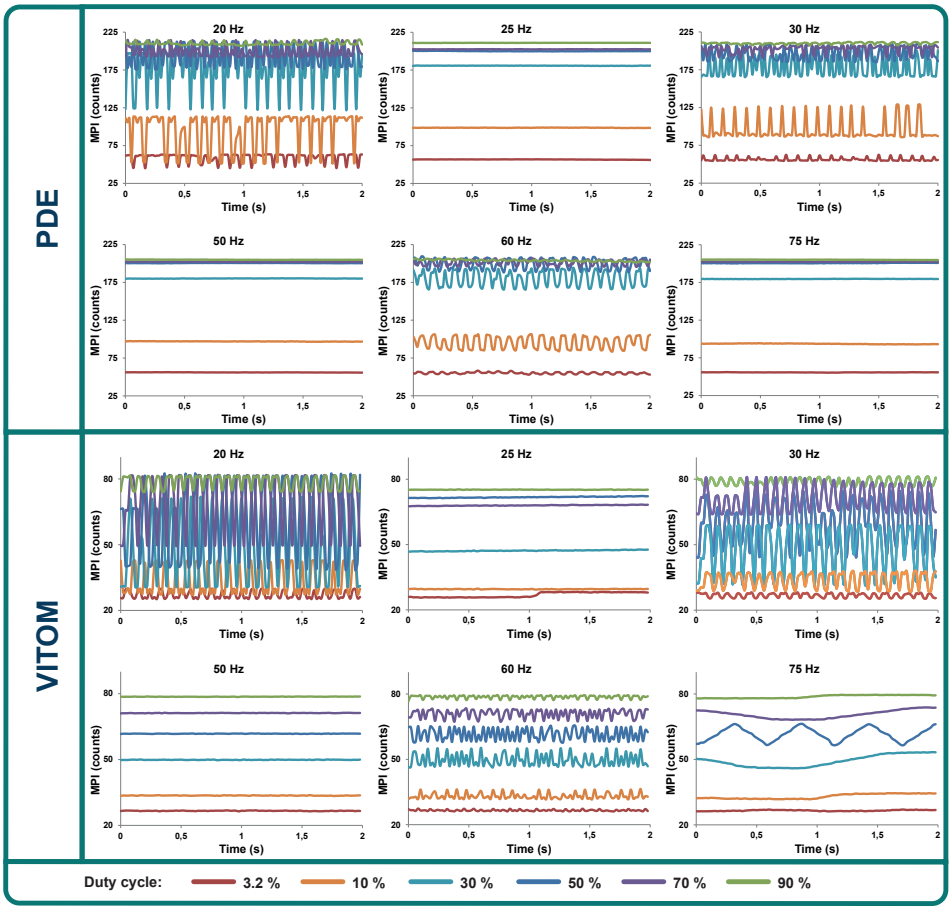

Figure 14. Mean pixel intensity for interference induced by the LED setup at various pulse frequency and duty cycle settings using both the PDE and VITOM.

REFERENCES

1. *F. W. B. van Leeuwen, J. C. Hardwick, and A. R. van Erkel, "Luminescence-based imaging approaches in the field of interventional molecular imaging," Radiology 276(1), 12–29 (2015).*
2. *I. Stoffels et al., "Intraoperative fluorescence imaging for sentinel lymph node detection: prospective clinical trial to compare the usefulness of indocyanine green vs technetium Tc 99m for identification of sentinel lymph nodes," JAMA Surg. 150(7), 617–623 (2015).*
3. *O. R. Brouwer et al., "Comparing the hybrid fluorescent-radioactive tracer indocyanine green-99mTc-nanocolloid with 99mTc-nanocolloid for sentinel node identification: a validation study using lymphoscintigraphy and SPECT/CT," J. Nucl. Med. 53(7), 1034–1040 (2012).*
4. *G. H. KleinJan et al., "Toward (hybrid) navigation of a fluorescence camera in an open surgery setting," J. Nucl. Med. 57(10), 1650–1653 (2016).*
5. *M. N. van Oosterom et al., "Navigation of fluorescence cameras during soft-tissue surgery—is it possible to use a single navigation setup for various open and laparoscopic urological surgery applications?" J. Urol. 199, 1061–1068 (2018).*
6. *M. N. van Oosterom et al., "Computer-assisted surgery: virtual-and augmented-reality displays for navigation during urological interventions," Curr. Opin. Urol. 28(2), 205–213 (2018).*

7. *O. R. Brouwer et al., "Image navigation as a means to expand the boundaries of fluorescence-guided surgery," Phys. Med. Biol. 57(10), 3123–3136 (2012).*
8. *M. N. van Oosterom et al., "Navigation of a robot-integrated fluorescence laparoscope in preoperative SPECT/CT and intraoperative freehand SPECT imaging data: a phantom study," J. Biomed. Opt. 21(8), 086008 (2016).*
9. *P.Waelkens et al., "Surgical navigation: an overview of the state-of-theart clinical applications," in Radioguided Surgery, K. Herrmann, O. E. Nieweg, and S. P. Povoski, Eds., pp. 57–73, Springer International Publishing, Switzerland (2016).*
10. *B. Zhu and E. Sevick-Muraca, "A review of performance of near-infrared fluorescence imaging devices used in clinical studies," Br. J. Radiol. 88(1045), 20140547 (2015).*
11. *G. H. KleinJan et al., "Optimisation of fluorescence guidance during robot-assisted laparoscopic sentinel node biopsy for prostate cancer," Eur. Urol. 66(6), 991–998 (2014).*
12. *D. M. van Willigen et al., "Multispectral fluorescence guided surgery; a feasibility study in a phantom using a clinical-grade laparoscopic camera system," Am. J. Nucl. Med. Mol. Imaging 7(3), 138–147 (2017).*
13. *G. H. KleinJan et al., "Fluorescence guided surgery and tracer-dose, fact or fiction?" Eur. J. Nucl. Med. Mol. Imaging 43(10), 1857–1867 (2016).*
14. *A. V. DSouza et al., "Review of fluorescence guided surgery systems: identification of key performance capabilities beyond indocyanine green imaging," J. Biomed. Opt. 21(8), 080901 (2016).*
15. *S. van derWal et al., "Synthesis and systematic evaluation of symmetric sulfonated centrally C-C bonded cyanine near-infrared dyes for protein labelling," Dyes Pigm. 132, 7–19 (2016).*
16. *F. Acerbi et al., "Fluorescein-guided surgery for malignant gliomas: a review," Neurosurg. Rev. 37(4), 547–557 (2014).*
17. *S. E. Craig et al., "Fluorescent-guided surgical resection of glioma with targeted molecular imaging agents: a literature review," World Neurosurg. 90, 154–163 (2016).*
18. *N. S. van den Berg, F. W. B. van Leeuwen, and H. G. van der Poel, "Fluorescence guidance in urologic surgery," Curr. Opin. Urol. 22(2), 109–120 (2012).*
19. *J. Burggraaf et al., "Detection of colorectal polyps in humans using an intravenously administered fluorescent peptide targeted against c-Met," Nat. Med. 21(8), 955–961 (2015).*
20. *R. Yang et al., "Design of an accurate near infrared optical tracking system in surgical navigation," J. Lightwave Technol. 31(2), 223–231 (2013).*
21. *S. Bernhardt et al., "The status of augmented reality in laparoscopic surgery as of 2016," Med. Image Anal. 37, 66–90 (2017).*
22. *W. Birkfellner et al., "Tracking devices," in Image-Guided Interventions, T. Peters and K. Cleary, Eds., pp. 23–44, Springer, Boston, Massachusetts (2008).*
23. *E. Wild et al., "Robust augmented reality guidance with fluorescent markers in laparoscopic surgery," Int. J. Comput. Assisted Radiol. Surg. 11(6), 899–907 (2016).*
24. *B. Fuerst et al., "First robotic SPECT for minimally invasive sentinel lymph node mapping," IEEE Trans. Med. Imaging 35(3), 830–838 (2016).*
25. *A. Hughes-Hallett et al., "Augmented reality partial nephrectomy: examining the current status and future perspectives," Urology 83(2), 266–273 (2014).*
26. *S. B. Mondal et al., "Optical see-through cancer vision goggles enable direct patient visualization and real-time fluorescence-guided oncologic surgery," Ann. Surg. Oncol. 24, 1897–1903 (2017).*

PART TWO

ENGINEERING NOVEL DETECTION MODALITIES FOR TRACER-BASED SURGICAL GUIDANCE

CHAPTER 6

U-SPECT-BIOFLUO: AN INTEGRATED RADIONUCLIDE, BIOLUMINESCENCE, AND FLUORESCENCE IMAGING PLATFORM

Adapted from: van Oosterom MN, Kreuger R, Buckle T, Mahn WA, Bunschoten A, Josephson L, van Leeuwen FWB, Beekman FJ

The European Journal of Nuclear Medicine and Molecular Imaging Research, 2014, 4(1): 56

ABSTRACT

In vivo bioluminescence, fluorescence, and single-photon emission computed tomography (SPECT) imaging provide complementary information about biological processes. However, to date these signatures are evaluated separately on individual preclinical systems. In this paper, we introduce a fully integrated bioluminescence-fluorescence-SPECT platform. Next to an optimization in logistics and image fusion, this integration can help improve understanding of the optical imaging (OI) results. For this purpose, an OI module was developed for a preclinical SPECT system (U-SPECT, MILabs, Utrecht, the Netherlands). The applicability of the module for bioluminescence and fluorescence imaging was evaluated in both a phantom and in an in vivo setting using mice implanted with a 4T1-luc+ tumor. A combination of a fluorescent dye and radioactive moiety was used to directly relate the optical images of the module to the SPECT findings. Bioluminescence imaging (BLI) was compared to the localization of the fluorescence signal in the tumors. Both the phantom and in vivo mouse studies showed that superficial fluorescence signals could be imaged accurately. The SPECT and bioluminescence images could be used to place the fluorescence findings in perspective, e.g. by showing tracer accumulation in non-target organs such as the liver and kidneys (SPECT) and giving a semi-quantitative read-out for tumor spread (bioluminescence). With that, the fully integrated multimodal platform developed provided complementary registered imaging of bioluminescent, fluorescent, and SPECT signatures in a single scanning session with a single dose of anesthesia. In our view, integration of these modalities helps to improve data interpretation of optical findings in relation to radionuclide images.

INTRODUCTION

Studies of human disease in animal models often provide an essential link between chemistry, fundamental research at the molecular level, and the development/evaluation of new diagnostic and therapeutic methods. Molecular imaging modalities such as single-photon emission computed tomography (SPECT), positron emission tomography (PET), bioluminescence, and fluorescence provide a means to generate a view into the in vivo situation [1,2].

SPECT and optical technologies are complementary in terms of resolution, speed, quantitative accuracy, and tracer availability [3-5]. Independent of the source depth, modern small animal SPECT systems can be used for longitudinal and quantitative imaging studies of dynamic processes in small structures (resolution <0.25 mm) [6]. Alternatively, optical imaging provides rapid and low-cost non-radioactive imaging and enables longitudinal studies of superficial lesions. The resolution of fluorescence imaging also enables the (ex vivo) microscopic visualization of molecular/cellular processes [7]. Potentially, a vast amount of optical tracers from molecular cell biology can be translated to in vivo use. Alternative to a use in combination with dedicated tracers, optical imaging can also be used to detect transfected (tumor) cell lines that contain e.g. luciferase or one of the fluorescent proteins [8], enabling the (longitudinal) monitoring of disease spread and progression in animal models. The main disadvantages for optical techniques are the significant scatter and absorption of photons by tissue/structures in the animal body. Fluorescence techniques additionally suffer from tissue autofluorescence, resulting in an unwanted background signal. These negative features can be partly overcome by using emissions in the near-infrared (NIR) spectrum, but unfortunately optical imaging cannot equal the detailed view and quantitative accuracy that SPECT provides at larger depths. One of the great challenges today is to place these two modalities in perspective and to determine the added value of optical imaging within the field of nuclear medicine [9].

When multimodal tracers with both a radioactive and fluorescent signature are used, a single tracer can provide 'best of both worlds'. Such tracers are reported with a peptide, monoclonal antibody, or nanoparticle basis [10-12]. Combined radioactive and fluorescence imaging has already provided added value in clinical surgical guidance studies [13,14].

Next to the development of multimodal tracers that combine two signatures, SPECT and optical modalities can also be combined on a single device with a single user interface. In this way, logistics, including anesthesia, are simplified and may improve animal welfare. Because animal positioning is no longer an issue with respect to co-registration of the imaging results, the complementary value of the different modalities can be exploited to its full extent; e.g. bioluminescent tumor cell localization combined with tracer distribution imaging (fluorescence and/or nuclear).

While other groups mainly focus on integrating nuclear imaging with three-dimensional (3D) fluorescence optical tomography (FOT) imaging [15-18] or fluorescence-mediated tomography (FMT) [19], we consider optical imaging, both bioluminescence and fluorescence, as intrinsically superficial technology, currently most suitable for planar imaging. Today, planar imaging is applied in the far majority of optical imaging studies in preclinical research since optical tomography is still highly challenging due to the ill-posed nature of optical data caused by strong light absorption and diffusion [20]. Therefore, we pursued integration of planar optical imaging with SPECT. We developed and tested a low-cost prototype system consisting of an add-on planar bioluminescence/fluorescence optical module for a dedicated small animal SPECT device (U-SPECTII, MILabs B.V., Utrecht, the Netherlands) [21-24].

METHODS

Optical module for small animal SPECT

The prototype optical imaging (OI) module was fitted onto the U-SPECT-II [21,22] installed at the LUMC (Leiden, the Netherlands) as is shown in Figure 1. The optical module consists of three main components: 1) a light tight 'dark box' (Figure 1.5), 2) a very sensitive CCD camera (Figure 1.3), and 3) a bright light source (Figure 1.6). Details about these components will be given in later paragraphs. The dark box was designed in such a way that when the module is in 'open' position, the handling of the animals in the bed of the U-SPECT is not hampered. When the module is 'closed', the CCD camera on top of the box is shielded from ambient light and can produce a total-body topview bioluminescent image of the animal via a mirror (Figure 1.11). For photographic and fluorescence imaging, the animal is illuminated by the light source via two optic fibers (Figure 1.4) entering the box and small mirrors (Figure 1.10) reflecting the light onto the bed (Figure 1.1). Excitation and emission light filters, well adapted to the spectral profile of the fluorescent dye under study, can be added to the system.

For SPECT scans, the animal bed is moved by an XYZ stage into the U-SPECT (Figure 1.9) collimator. For the OI position, the bed is held in the same position as used for placing an animal in the bed (U-SPECT 'bed eject position'). Alternatively, by mounting the OI module on a separate 'docking station', it can also be used as an independent optical imaging device. The docking station allows for parallel use of the SPECT and OI module.

Dark box

The dark box uses a rail system to slide over the table, enabling animal placement. The sliding mechanism consists of a U-profile mounted on the box and rails (Figure 1.8) mounted on the table that contains the XYZ stage to move the bed mounted at the front side of the USPECT. When the box slides to its closed position, it is lowered by about 1 cm. In this way, the U profiles lock over the rails.

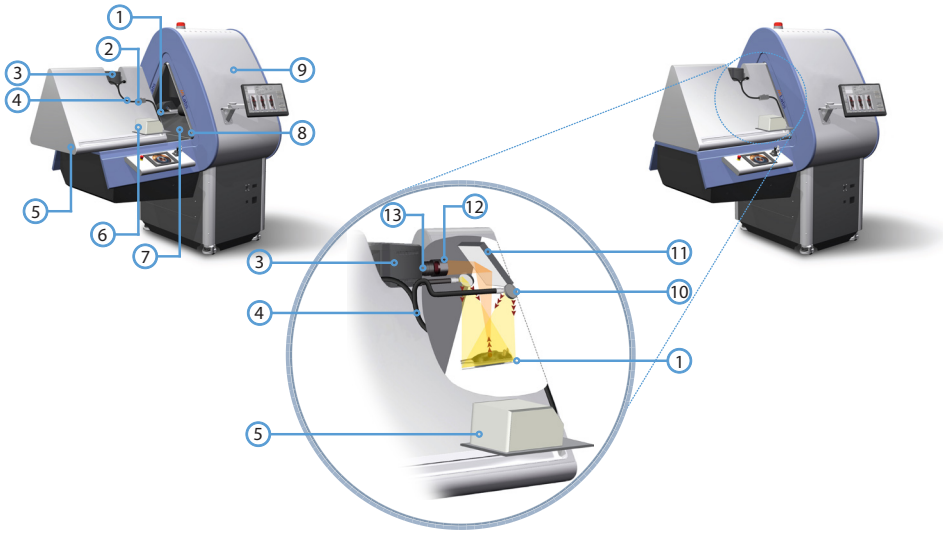

Figure 1. Overview of the U-SPECT-BioFluo platform. (1) *Animal bed.* ***(2)*** *Excitation filter box.* ***(3)*** *Camera.* ***(4)*** *Optical fiber bundle.* ***(5)*** *Dark box.* ***(6)*** *Light source.* ***(7)*** *Black ABS-plastic insert.* ***(8)*** *U-profile light lock.* ***(9)*** *U-SPECT.* ***(10)*** *Mirrors for excitation light.* ***(11)*** *Mirror directing light from the bed to the camera.* ***(12)*** *Lens hood and emission filter holder.* ***(13)*** *Camera lens.*

Blackboard paint has been applied on the rails and the U-profile to ensure the light tightness in locked position.

To further block ambient light, all joints on the box have been sealed with Sikaflex-221 (Sika AG, Baar, Zug, Switzerland) sealant. Blackboard paint is applied to the inside of the box to avoid light reflections. A black ABS-plastic insert (Figure 1.7) has been fitted to cover the entrance of the U-SPECT to prevent leakage of ambient light into the dark box and to avoid reflections from the metallic SPECT entrance. This insert was made with a tight fit to the entrance of the existing scanner, leaving maximum space to handle the animals on the bed. With the insert in place, the U-SPECT vision cameras can still be used to select the region of interest (ROI) in the U-SPECT acquisition software [21,22]. Remaining light leaks measured inside the closed black box were closed using tape sealants.

Camera, lens, and mirror

To allow for the detection of weak bioluminescence and fluorescence signals, an Andor iKon-M 912BV scientific CCD camera (Andor Technology plc., Belfast, UK) with a very low dark current level was used for recording OI images. This camera is based on a CCD77-00 (e2v Technologies Ltd., Essex, UK) with 512 × 512 pixels (24 × 24 µm) and has a quantum efficiency between ~50% and ~95% in the wavelength region of 400-900 nm. With the 16-bit camera read-out at a rate of 50 kHz, the read noise was below 2 counts/pixel. By means of an air-cooled Peltier element, the CCD operating temperature was set to −65°C, reducing the dark current to ~0.006 elec/pix/s. The camera was fully controlled by

the accompanying Andor Solis software.

The CCD camera was equipped with a Fujinon (Fujifilm Corp., Tokyo, Japan) CF25HA-1 lens (Figure 1.13). This lens has a fixed focal length (F) of 25 mm. To collect as much of the emitted luminescence as possible, we selected a lens whose diaphragm could be set as large as F/1.4. An emission filter holder (50 mm diameter; Figure 1.12) was mounted in front of the lens. A lens hood was integrated with the filter holder to avoid stray light entering the lens/filter combination.

A mirror was placed above the animal bed (Figure 1) to direct the emitted light to the CCD camera and generate a top-view image of an entire mouse. The selected Edmund Optics enhanced aluminum mirror (Edmund Optics Inc., Barrington, NJ, USA) has a high reflective index in the wavelength region of interest: between ~85% and ~98% for wavelengths larger than 450 nm.

Fluorescence excitation light

To excite fluorescent dyes, an illumination setup was constructed to expose the whole animal (bed in OI position) with a relatively high intensity of (excitation) light at the appropriate wavelength.

An MI-150 fiber optic illuminator (Edmund Optics Inc., Barrington, NJ, USA) with a 150-W EKE halogen light bulb produced a high intensity bundle of light (450 to 800 nm), covering our wavelength range of interest for fluorescence imaging. Light from the illuminator was guided to an excitation filter box (Figure 1.2) using a 0.25 inch glass fiber bundle guide. In the filter box, the spectrum of the excitation light can be tailored to a particular dye using a 12.5-mm diameter filter. After the filter, the light was split into two fiber bundles that enter the dark box next to the camera. The light from the fibers was reflected by two small mirrors above the bed to illuminate the mouse from two directions. Light leakage at the fiber bundle entrance points was prevented by applying cable glands.

Imaging with U-SPECT-BioFluo

With the U-SPECT-BioFluo device bioluminescence, fluorescence, and SPECT scans of a mouse can be made in a sequential fashion. The SPECT measurement settings are setup as described earlier for the U-SPECT [21,22]. To perform the optical measurements, the OI module is closed and the animal bed is moved to the OI position. After positioning, grayscale photographs and bioluminescent and/or fluorescent images can be recorded by the CCD camera and stored with the Solis software for further offline analysis with Matlab (MathWorks Inc., Natick, MA, USA).

Grayscale photograph

Grayscale images are recorded by the CCD camera to provide an anatomical context for the bioluminescence, fluorescence, and SPECT images. The grayscale images are recorded under white light illumination without the use of emission

and excitation filters. To avoid saturation of the CCD image for our minimal exposure time (50 ms), the lens diaphragm is set to F/22 and the iris of the light source is set to a minimum. The F/22 diaphragm allows for sharp photographs of the animal in OI position.

Bioluminescence imaging

The bioluminescence images are recorded without the use of excitation light and an emission filter. To provide total darkness in the module, the fiber optic illuminator is switched off and a light stop is put in the excitation filter box to block light entering the module via leaks in the illuminator. To collect a maximum of bioluminescent photons in a reasonable exposure time (<90 s), the largest possible lens diaphragm (F/1.4) is used.

Fluorescence imaging

During fluorescence imaging, the object or animal is continuously illuminated using an appropriate excitation filter for the dye under study. With a specific emission filter in front of the CCD camera lens, only the emitted fluorescent signal is recorded by the camera.

The CCD exposure time was kept to a minimum by using the largest possible lens diaphragm (F/1.4) and fully opening the iris of the illuminator. During imaging, the exposure time was adjusted to obtain images in which the brightest fluorescence spots have pixel values larger than half the full pixel ADC range.

Illumination calibration

The measured images are corrected for the non-uniform illumination pattern at the mouse bed by making calibration measurements. This is done by making an image (without emission filter) of the illumination pattern using a flat sheet of white paper in the OI position. The corresponding iris, diaphragm, and excitation filter are used for the grayscale or fluorescence calibration. The exposure time has to be adjusted to avoid CCD saturation. Since the bioluminescent images do not require illumination, they do not require such a calibration.

Image processing

The optical images from the CCD camera are processed offline with Matlab. Both the fluorescence and photographic calibration images are blurred with a Gaussian filter of 7.30 mm full width at half maximum (FWHM) to suppress small scale non-uniformities of the calibration paper sheet itself. The resulting calibration images are subsequently normalized by scaling their maximum pixel value to 1. The photographic and fluorescent images are corrected for the non-uniform illumination by dividing them by the corresponding normalized calibration image.

3D SPECT images are reconstructed from the SPECT list-mode data with MILabs reconstruction software version 2.38. Proper energy and background windows are set and data is reconstructed to an isotropic voxel grid of 0.2 mm

using a pixel-based ordered subset expectation maximization (POSEM) algorithm [25] which includes compensation for distance-depending blurring [26]. No attenuation correction is applied. For comparison to the optical images, a (2D) SPECT sum image is made by summing the voxel values along the vertical direction. For anatomical reference, the bioluminescence, fluorescence, and SPECT sum images are shown in color on top of the grayscale photographic image for pixel values above an adjustable threshold. For bioluminescence and fluorescence, this is straightforward as the same CCD camera is used to record these images. Overlay of the SPECT sum image was done by matching the mouse contours to the grayscale images of the mouse.

Performance characterization

To evaluate the multimodal imaging capabilities of the U-SPECT-BioFluo setup, pilot experiments were performed using a phantom and tumor-bearing mice injected with a multimodal tracer. Optical images were also acquired and processed on an IVIS Spectrum with Living Image software (Caliper Life Sciences Inc., Hopkinton, MA, USA). Bioluminescence imaging on the IVIS was done with open filter settings.

The fluorescent dye CyAL-5.5$_b$ ($\lambda_{ex,max}$ = 674 nm; $\lambda_{em,max}$ = 693 nm) [27] was used for the phantom and the multimodal tracer. For the fluorescence measurements on the IVIS, the (built-in) 640-nm excitation and 680-nm emission filters were selected. Their bandwidths were respectively 30 nm and 20 nm. However, for the OI module we selected a commercial filter (Edmund Optics TechSpec Fluorescence Bandpass, Barrington, NJ, USA) with a center wavelength of 692 nm and wider bandwidth of ~40 nm to match the dye's emission peak and to detect a larger part of the emission spectrum. From the same filter series another filter with ~40 nm bandwidth was used to excite this dye. To minimize the spectral overlap of the excitation and emission filters, an excitation center wavelength of 624 nm was selected. The excitation light spectrum of the filter was largely overlapping the dye's absorption spectrum. Both commercial filters have a 93% transmission within their passbands and a blocking factor >10^6 for wavelengths outside their passbands. This blocking factor is lower for non-perpendicular incident light. So, some excitation light reflected by the object and incident on the emission filter might still pass that filter causing the so-called excitation light leakage background in fluorescence images.

Phantom measurements

A phantom was generated, via a slightly modified procedure as described by Pleijhuis et al. [28], to evaluate the attenuation and resolution for the fluorescence and SPECT signals as function of tissue depth. This phantom (Figure 2) consisted of a cylinder of tissue simulating gel, in which a capillary, uniformly filled with a fluorescence/SPECT compound, was inserted under an oblique angle.

The gel consisted of a 1% (w/w) agarose solution that was prepared by

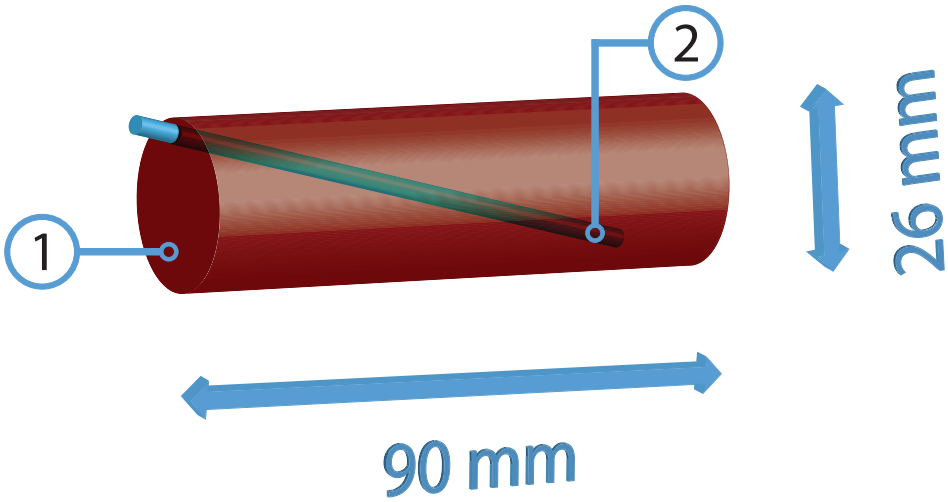

Figure 2. Schematic diagram of the tissue simulating gel phantom. (1) *Phantom.* ***(2)*** *Fluorescent and radioactive capillary.*

dissolving agarose (Roche, Basel, Switzerland) in 50 mL water under continuous heating and stirring. After cooling down to 40°C, 170 µM hemoglobin from bovine blood (Sigma Aldrich, St. Louis, MO, USA) was added to the solution to obtain an optically tissue equivalent gel [28]. The solution was poured into a 50-mL tube (Falcon, BD Biosciences, San Jose, CA, USA). After further cooling and solidification, the tube was removed and the gel was given blunt ends using a scalpel.

A 200-µM CyAL-5.5b solution was mixed 3:1 with a ^{99m}Tc-eluate (~1.3 GBq/mL). A glass capillary (inner diameter 0.9 mm) containing 50 µL of this mixture and closed by epoxy glue [29] was inserted into the gel. Prior to inserting the capillary in the phantom, we used the blue coloration to visually confirm that the fluorescent dye (CyAL-5.5b) was uniformly distributed in the capillary.

The phantom was placed in the U-SPECT-BioFluo bed, and a grayscale and a fluorescence image were recorded. Subsequently, a 20-min SPECT scan was made with the ROI containing the entire phantom. At last, fluorescence measurements were made on the IVIS for control.

In vivo measurements

Mouse scans were performed to interpret the different bioluminescent, fluorescent, and SPECT images for a practical preclinical case series of four animals. Tumor lesions were generated in Balb/c nude mice (6 to 8 weeks of age) by transplanting 4 T1-luc + tumor cells ($0.25 \cdot 10^5$), with firefly luciferase gene expression, into the fourth mammary fatpad [30].

For fluorescence and SPECT imaging, the previously reported multimodal tracer ^{111}In-MSAP-RGD [30], containing the above mentioned CyAL-5.5$_b$ dye, was used. Twenty-four hours prior to imaging, the mice were injected intravenously with this tracer (40 µg, 18 nmol, 10 MBq).

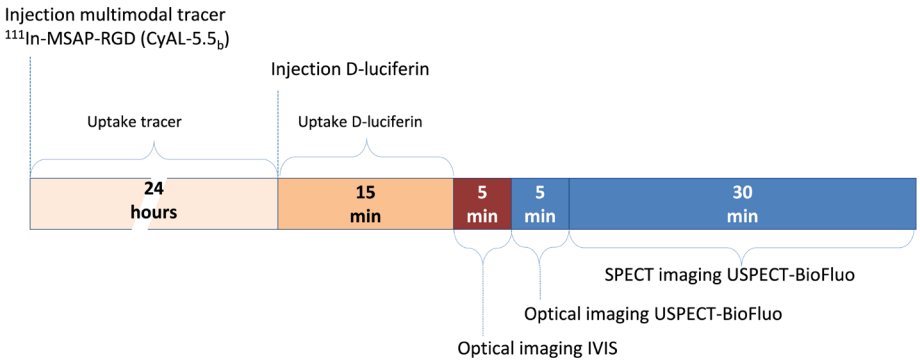

Figure 3. Protocol timeline for in vivo measurements. *The injection moments of ^{111}In-MSAP-RGD (CyAL-5.5$_b$ dye), D-Luciferin, and subsequent imaging periods are indicated.*

For bioluminescence imaging, the mice were injected intraperitoneally with 150 mg/kg D-Luciferin (Xenogen Corp., Alameda, CA, USA) in PBS. Ten to twenty minutes after this injection, the mice were placed in the transparent U-SPECT-BioFluo bed and first imaged on the IVIS. Afterwards, the bed with the mouse was immediately clicked on the stage of the U-SPECT-BioFluo for optical imaging followed by 30 min of SPECT imaging. The mice were anesthetized by means of Hypnorm/Dormicum/water (1:1:2; 5 µL/g i.p.). The protocol timeline is shown in Figure 3. These animal experiments were performed in accordance with Dutch welfare regulations and approved by the ethics committee of the Leiden University Medical Center under reference 2013/12189.

RESULTS

After installing the optical module on the U-SPECT, the optical image pixel size for the top-view image of the bed was found to be 0.36 mm. We verified the light tightness of the closed dark box by recording an image with a large lens diaphragm and an exposure time of 60 s, but without any optical filters or light source. This measurement resulted in a zero mean ambient light background level (standard deviation: 1.3 counts/pixel).

Phantom measurements

In Figure 4, the fluorescence and SPECT imaging results of the cylindrical phantom with the thin capillary source are shown both for the U-SPECT-BioFluo (500 ms exposure time) and the IVIS (1 s exposure time). Optical images obtained with U-SPECT-BioFluo and with IVIS are very similar. For SPECT reconstruction from list mode data, a 20% wide energy window has been set around the 140 keV ^{99m}Tc photopeak. The background windows for triple window scatter correction [31] were set to 124 to 136 keV and 166 to 184 keV. POSEM with 16 subsets and 6 iterations was performed for reconstructing 3D SPECT images. The SPECT images were subsequently blurred with a 3D Gaussian low pass filter (FWHM 0.47 mm).

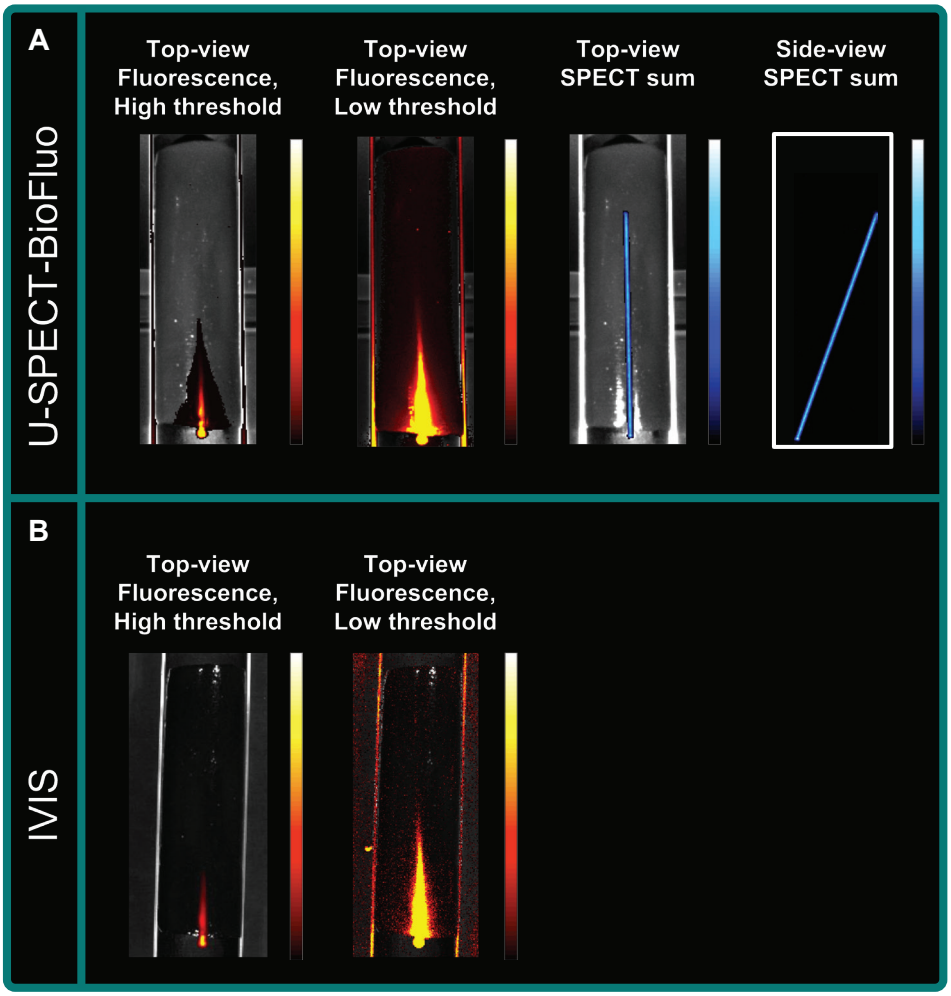

Figure 4. Phantom imaging results. (a) *Fluorescence (500 ms exposure time) and SPECT imaging on the U-SPECT-BioFluo.* ***(b)*** *Fluorescence imaging on the IVIS (1s exposure time).*

By adjusting the color scale threshold of the fluorescence image, sharp identification of the most superficial part of the capillary can be exchanged for a slight increase in the in-depth visibility. For the low threshold image, the threshold has been set at about the background level of the phantom which is due to e.g. excitation light leakage through the emission filter, fluorescence emission light scatter, and autofluorescence of the phantom [32].

In Figure 4a, the SPECT signal is also shown. In the top-view image, the 3D reconstructed SPECT data are vertically summed for 1:1 comparison with the fluorescence measurement. In the side view, the SPECT data are summed horizontally. In Figure 5a, the fluorescence and SPECT signal strength as a function of the capillary depth are shown. Line profiles (~1 mm wide) along the axial direction of the capillary were made from the topview images for both

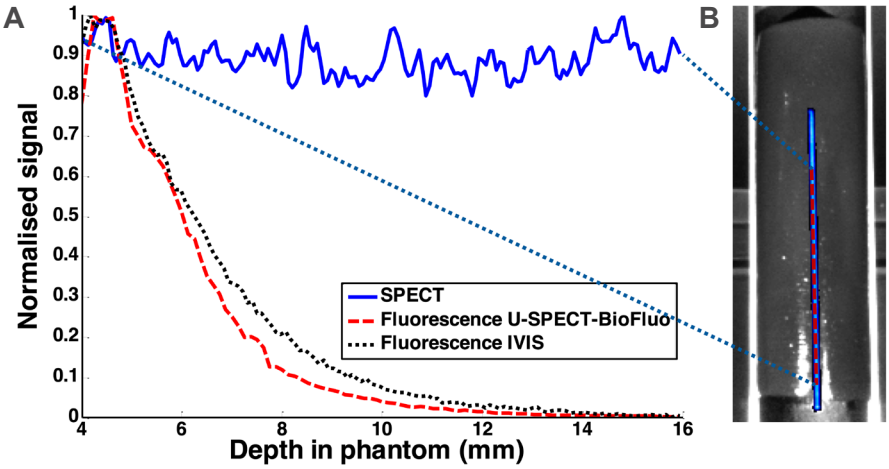

Figure 5. Effects of depth-dependent attenuation. (a) *Fluorescence signal (phantom background level subtracted) and SPECT signal of capillary versus depth in gel phantom. The maximum SPECT and fluorescence signals have been normalized to 1.* ***(b)*** *The positions of the axial line profiles are indicated in the top-view image of the phantom.*

modalities (Figure 5a). The axial position along these line profiles was converted into the capillary depth by using the inclination angle of the capillary determined from the SPECT side-view image Figure 4a. Both Figures 4a and 5 clearly demonstrate that while the SPECT signal barely suffers from attenuation in this phantom, the fluorescence signal of the uniformly distributed dye (CyAL-5.5$_b$) is decreasing with depth. The IVIS and our OI module show a similar attenuation behavior; at 7 mm the signal has already dropped by ~30%, and at 14 mm it is close to the fluorescence background level of the phantom. This decrease can be attributed to the light attenuation and scatter by hemoglobin and water in the phantom. A similar attenuation is observed in tissue [33].

The resolution curves of the fluorescence and SPECT signals (Figure 6a-c) were obtained by making ~1-mm wide line profiles in the top-view images orthogonal to the capillary corresponding to different depths (Figure 6d). Again, the depths have been obtained from the capillary inclination angle. For comparison, these curves have been normalized to their maximum signal. Like the signal strength, the resolution of the fluorescence images also shows severe depth dependence. At 6 mm depth, the width of the fluorescence profile was still close to that of the SPECT profile, namely ~1.2 mm (FWHM). At 14 mm depth, the resolution decreased to ~1.7 mm (FWHM) and the peak value was just 2.5 times the background. Both widths are largely determined by the 0.9 mm diameter of the capillary itself. Around 22 mm depth, the fluorescence signal can no longer be distinguished from the background.

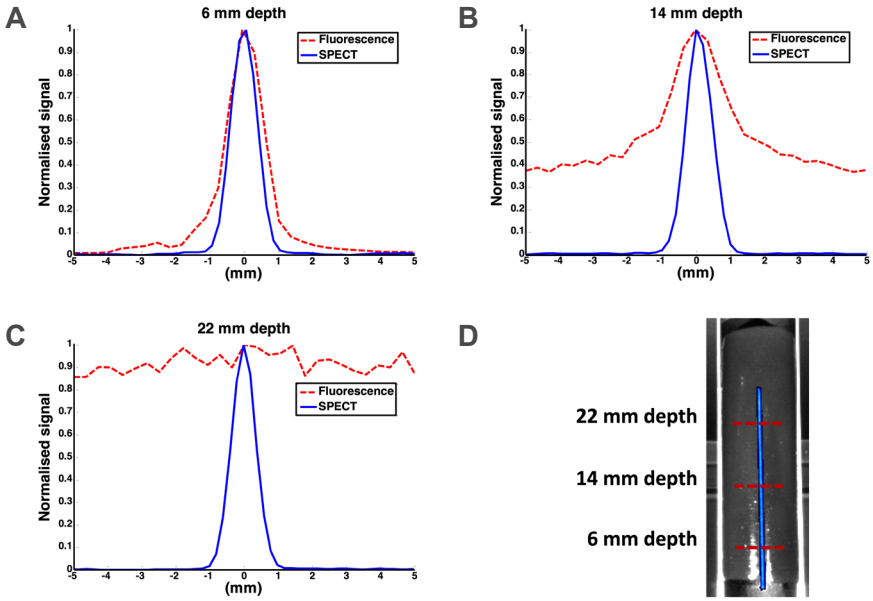

Figure 6. Comparison of image blurring for SPECT and fluorescence. (a,b,c) *SPECT and fluorescence line profiles orthogonal to the capillary at different depths in the phantom. The maximum signal of each profile has been normalized to 1.* ***(d)*** *The positions of the line profiles are indicated in the top-view image.*

In vivo measurements

Figure 7 presents the imaging results obtained from the different modalities in both U-SPECT-BioFluo and IVIS. Figure 7a shows respectively the bioluminescence, fluorescence, and SPECT sum images recorded with U-SPECT-BioFluo. The exposure time for the bioluminescence measurement was 60 s and for the fluorescence measurement 300 ms, as the fluorescent signal was much stronger. On the IVIS (Figure 7b), the exposure times were respectively 30 s and 1 s. The IVIS images are similar to those of the in-house developed OI. The bioluminescence images clearly show the viable tumor component, where luciferase converts D-Luciferin in bioluminescent light.

In the U-SPECT-BioFluo bioluminescence images in Figure 7a, one can notice some hot pixels that may be caused by absorption of ^{111}In-based gamma radiation in the CCD chip. This radiation was emitted by the radioactive component of the multimodal tracer ^{111}In-MSAP-RGD. A median filter of 4 × 4 pixels has been applied to remove these hot pixels. For the POSEM reconstruction (16 subsets and 6 iterations) of the SPECT scan, a 20% wide energy window has been set around the 171 keV ^{111}In photopeak. Background windows of 151 to 167 keV and 205 to 226 keV were chosen for the scatter correction. A 3D Gaussian filter (FWHM 1.18 mm) has been applied after reconstruction.

Looking at the figures, it becomes clear that the signal-depth related effects severely limit the diagnostic utility of the optical images. Nevertheless, the superficially located mammary tumors could be depicted using both optical technologies. Other than in the phantom setup, here the effect of fluorescence threshold changes was minimal. However, in the image representing the summed SPECT slices, the threshold was set at such a level that a tiny part of tumor seems to be 'missing' with respect to the optical images. We believe that the intensity of the signal of deeper located cells in SPECT can cause slightly different locations of the tumor compared to the tumor as is visualized by optical imaging: Optical imaging mainly displays the surface of the tracer distribution, while the SPECT shows deeper structures in the mouse very clear as well which affects also the sum image. On the other hand, the SPECT images revealed a substantial uptake of ^{111}In-MSAP-RGD in other regions of the mouse, e.g. the liver and kidneys, a finding that correlates with previously reported biodistribution studies [30]. The difference in detectability between the different modalities also becomes apparent when one zooms in on the tumor itself: SPECT images in Figure 7c show heterogeneity of tracer uptake (e.g. an area with less accumulated tracer) that can not be seen in fluorescence images. Earlier studies confirm that microSPECT enables to visualize and quantify tracer heterogeneity in tumors [24,34].

DISCUSSION

The rise of optical techniques for molecular imaging purposes has resulted in a demand for dedicated modalities. One of today's challenges lies in placing optical findings in perspective to nuclear medicine technologies. There is a trend to combine nuclear medicine with supplementary read-outs provided by other modalities. One very practical solution is to integrate multiple modalities on a single platform to prevent deformation issues. For this reason, we developed an optical module that can be provided as an add-on to the U-SPECT-II modality for preclinical nuclear medicine. Using luciferase-gene-modified tumor cells and multimodal tracers that combine radionuclear and optical properties [10-12], we incorporated bioluminescence and fluorescence imaging in a 3D SPECT imaging setting.

This initial pilot study underlined that the prototype design (see Figure 1) provided such a small CCD image background that both bioluminescence and fluorescence imaging could be successfully achieved. We used commercially available 40 nm wide bandpass filters specifically tailored to the excitation and emission spectra of the CyAL-5.5$_b$ dye with wavelengths only slightly different from the ones used on the IVIS. This small difference may explain the difference in the fluorescence attenuation profiles shown in Figure 5: Since the absorption coefficient for hemoglobin is higher at 624 nm than at 640 nm, the excitation light is somewhat more attenuated in the phantom on our setup than on the

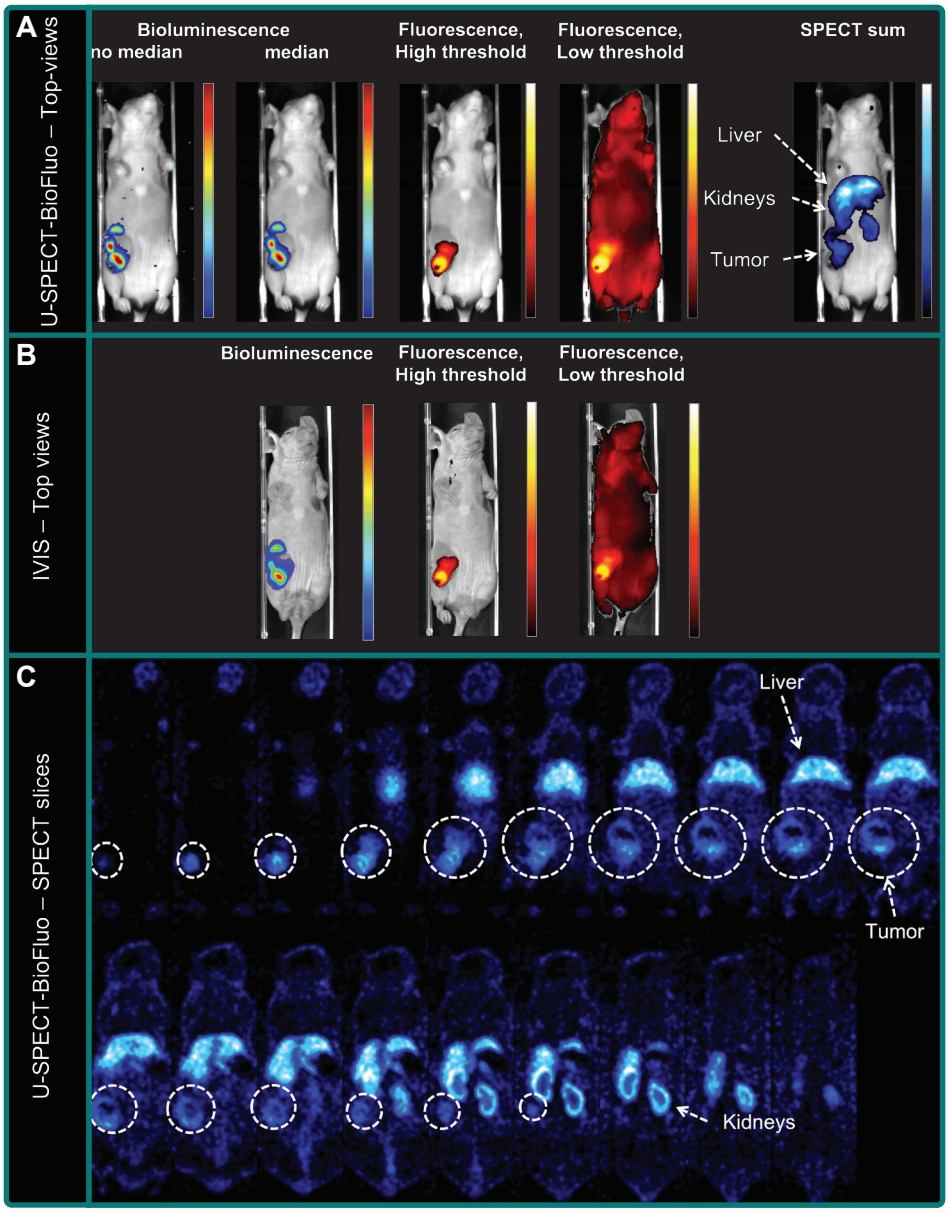

Figure 7. Imaging results for a mouse with a 4T1-luc+ tumor. Bioluminescence images are obtained by D-Luciferin injection. *Fluorescence and SPECT images are obtained by injection of multimodal tracer ^{111}In-MSAP-RGD.* ***(a)*** *U-SPECT-BioFluo. Bioluminescent images both with and without median filter applied.* ***(b)*** *IVIS.* ***(c)*** *U-SPECT-BioFluo: 1-mm thick horizontal SPECT slices (anterior to posterior). Organs have been indicated in the SPECT images. White circles indicate the tumor location in the slices.*

IVIS. For future studies with different dyes other commercial filters can be incorporated. The current halogen excitation lamp and CCD camera of the prototype already allow for excitation across the 450- to 800-nm spectrum.

Reasoning that accurate evaluation of the pharmacokinetics and distribution of a new (optical) imaging tracer is of paramount importance for any form of future clinical translation, we have used the in-depth information provided by SPECT to place the optical findings in perspective. In the present study we illustrate that, using a phantom setup and a multimodal angiogenesis tracer (^{111}In-MSAP-RGD) in an orthotopic mouse mammary tumor model, the SPECT/bioluminescence/fluorescence combination proposed in this paper may help prevent misconceptions of the tracer's specificity that could otherwise have resulted from using an optical evaluation only. The genetically engineered bioluminescent signal was confined to the tumor spread, while the fluorescent and radioactive emissions were used to define the distribution of the multimodal tracer used in this study. While the SPECT images show the complete distribution profile of the tracer used [30], the fluorescence images of both our in-house developed OI module as well as the IVIS images, only detected superficial emissions originating from the tumor. SPECT images clearly show tracer uptake e.g. in the liver (see Figure 7). In this case, possible toxicity issues due to unwanted uptake and retention in organs would have been missed with fluorescence imaging.

Where the preclinical SPECT findings are constant with depth, both the optical detectability and resolution degrade as functions of depth (see Figures 5 and 6). Factors contributing to the degradation of optical signals are signal attenuation and scattering - both increase with depth and occur for both the excitation light and emitted signal. In the case of fluorescence imaging, 'leakage' of excitation light through the filters and autofluorescence (depends on the tissue type) may raise the background signal. Even with NIR fluorescent dyes such as indocyanine green (ICG), these effects have shown to limit the use of fluorescence to superficial applications [32]. This said, the added value of optical imaging in superficial surgical guidance and/or pathological imaging situations is obvious and is driving the development of optical imaging tracers or multimodal tracers that contain an optical component [11,12].

In a future version of the OI module, the filter placement could be automated to enable fast switching between different fluorescent emissions, e.g. for multispectral imaging. This could then be combined directly with multi-isotope capabilities of SPECT, to allow for simultaneous evaluation of even multiple multimodal tracers. With UV transparent and more sensitive optics (e.g. larger aperture or deeper CCD cooling), it may become possible to detect much weaker signals such as the Cerenkov luminescence emitted by PET tracers [32]. As the U-SPECT-II can be adapted to perform collimated imaging of PET tracers (VECTor, [35,36]), this might even enable combined Cerenkov and PET imaging studies, which may help in the interpretation of Cerenkov findings. In addition, the used SPECT can be equipped with CT, further expanding the integration of imaging to a triple or quadruple imaging platform [37].

CONCLUSION

We evaluated a prototype optical add-on module that integrates optical imaging with a dedicated small animal SPECT system. This combination allows for complementary and registered imaging of bioluminescent, fluorescent, and SPECT signatures in a single scan session. The high-resolution and highly quantitative (3D) SPECT information about tracer kinetics and/or biodistribution can improve the interpretation of the fluorescence and bioluminescence images.

REFERENCES

1. *Weissleder R, Mahmood U: Molecular imaging. Radiology 2001, 219:316–333.*
2. *Ramaswamy AK, Hamilton M, Joshi RV, Kline BP, Li R, Wang P, Goergen CJ: Molecular imaging of experimental abdominal aortic aneurysms. Scientific World Journal 2013, 2013:973150.*
3. *Culver J, Akers W, Achilefu S: Multimodality molecular imaging with combined optical and SPECT/PET modalities. J Nucl Med 2008, 49:169–172.*
4. *Deroose CM, De A, Loening AM, Chow PL, Ray P, Chatziioannou AF, Gambhir SS: Multimodality imaging of tumor xenografts and metastases in mice with combined small-animal PET, small-animal CT, and bioluminescence imaging. J Nucl Med 2007, 48:295–303.*
5. *Park JM, Gambhir SS: Multimodality radionuclide, fluorescence, and bioluminescence small-animal imaging. Proc IEEE 2005, 93:771–783.*
6. *Ivashchenko O, Van der Have F, Villena J, Groen H, Ramakers RM, Weinans HH, Beekman FJ: Quarter-mm resolution molecular mouse imaging with U-SPECT$^{\alpha}$. Mol Imaging 2015, 14(1):7290-2014.*
7. *Kuil J, Buckle T, Oldenburg J, Yuan HS, Borowsky AD, Josephson L, van Leeuwen FWB: Hybrid peptide dendrimers for imaging of chemokine receptor 4 (CXCR4) expression. Mol Pharm 2011, 8:2444–2453.*
8. *Luker KE, Gupta M, Luker GD: Bioluminescent CXCL12 fusion protein for cellular studies of CXCR4 and CXCR7. Biotechniques 2009, 47:625–632.*
9. *Van Leeuwen FWB, de Jong M, Lahoutte T, Evangelista L, Barbet J, Del Vecchio S, Schibli R: Molecular imaging: the emerging role of optical imaging in nuclear medicine. Eur J Nucl Med Mol Imaging 2014, 41:2150–2153.*
10. *Kuil J, Velders AH, van Leeuwen FWB: Multimodal tumor-targeting peptides functionalized with both a radio- and a fluorescent label. Bioconjug Chem 2010, 21:1709–1719.*
11. *Buckle T, Chin PTK, van Leeuwen FWB: (Non-targeted) radioactive/fluorescent nanoparticles and their potential in combined pre- and intraoperative imaging during sentinel lymph node resection. Nanotechnology 2010, 21:482001.*
12. *Azhdarinia A, Ghosh P, Ghosh S, Wilganowski N, Sevick-Muraca EM: Dual-labeling strategies for nuclear and fluorescence molecular imaging: a review and analysis. Mol Imaging Biol 2012, 14:261–276.*
13. *van den Berg NS, Valdes-Olmos RA, van der Poel HG, van Leeuwen FWB: Sentinel lymph node biopsy for prostate cancer: a hybrid approach. J Nucl Med 2013, 54:493–496.*
14. *Brouwer OR, Buckle T, Vermeeren L, Klop WMC, Balm AJM, van der Poel HG, van Rhijn BW, Horenblas S, Nieweg OE, van Leeuwen FWB, Olmos RAV: Comparing the hybrid fluorescent-radioactive tracer indocyanine green-Tc-99 m-nanocolloid with Tc-99 m-nanocolloid for sentinel node identification: a validation study using lymphoscintigraphy and SPECT/CT. J Nucl Med 2012, 53:1034–1040.*
15. *Cao L, Peter J: Investigating line- versus point-laser excitation for three-dimensional fluorescence imaging and tomography employing a trimodal imaging system. J Biomed Opt 2013, 18:066015.*

16. *Li CQ, Yang YF, Mitchell GS, Cherry SR: Simultaneous PET and multispectral 3-dimensional fluorescence optical tomography imagingsystem. J Nucl Med 2011, 52:1268–1275.*
17. *Tan IC, Lu YJ, Darne C, Rasmussen JC, Zhu BH, Azhdarinia A, Yan SK, Smith AM, Sevick-Muraca EM: Fluorescence-enhanced optical tomography and nuclear imaging system for small animals. Multimodal Biomed Imag VII, Proc SPIE 2012, 8216:1.*
18. *Lu Y, Yang K, Zhou K, Pang B, Wang G, Ding Y, Zhang Q, Han H, Tian J, Li C, Ren Q: An integrated quad-modality molecular imaging system for small animals. J Nucl Med 2014, 55:1375–1379.*
19. *Solomon M, Nothdruft RE, Akers W, Edwards WB, Liang KX, Xu BG, Suddlow GP, Deghani H, Tai YC, Eggebrecht AT, Achilefu S, Culver JP: Multimodal fluorescence-mediated tomography and SPECT/CT for small-animal imaging. J Nucl Med 2013, 54:639–646.*
20. *Darne C, Lu YJ, Sevick-Muraca EM: Small animal fluorescence and bioluminescence tomography: a review of approaches, algorithms and technology update. Phys Med Biol 2014, 59:R1–R64.*
21. *van der Have F, Vastenhouw B, Ramakers RM, Branderhorst W, Krah JO, Ji CG, Staelens SG, Beekman FJ: U-SPECT-II: an ultra-high-resolution device for molecular small-animal imaging. J Nucl Med 2009, 50:599–605.*
22. *Branderhorst W, Vastenhouw B, van der Have F, Blezer ELA, Bleeker WK, Beekman FJ: Targeted multi-pinhole SPECT. Eur J Nucl Med Mol Imaging 2011, 38:552–561.*
23. *Befera NT, Badea CT, Johnson GA: Comparison of 4D-MicroSPECT and MicroCT for murine cardiac function. Mol Imaging Biol 2014, 16:235–245.*
24. *Zhou Y, Shao GQ, Liu S: Monitoring breast tumor lung metastasis by U-SPECT-II/CT with an integrin alpha(v)beta(3)-targeted radiotracer Tc-99m-3P-RGD(2). Theranostics 2012, 2:577–588.*
25. *Branderhorst W, Vastenhouw B, Beekman FJ: Pixel-based subsets for rapid multi-pinhole SPECT reconstruction. Phys Med Biol 2010, 55:2023–2034.*
26. *van der Have F, Vastenhouw B, Rentmeester M, Beekman FJ: System calibration and statistical image reconstruction for ultra-high resolution stationary pinhole SPECT. IEEE Trans Med Imaging 2008, 27:960–971.*
27. *Shao FW, Yuan HS, Josephson L, Weissleder R, Hilderbrand SA: Facile synthesis of monofunctional pentamethine carbocyanine fluorophores.Dyes Pigm 2011, 90:119–122.*
28. *Pleijhuis RG, Langhout GC, Helfrich W, Themelis G, Sarantopoulos A, Crane LMA, Harlaar NJ, de Jong JS, Ntziachristos V, van Dam GM: Near-infrared fluorescence (NIRF) imaging in breast-conserving surgery: assessing intraoperative techniques in tissue-simulating breast phantoms. Eur J Surg Oncol 2011, 37:32–39.*
29. *Buckle T, Chin PTK, van den Berg NS, Loo CE, Koops W, Gilhuijs KGA, van Leeuwen FWB: Tumor bracketing and safety margin estimation using multimodal marker seeds: a proof of concept. J Biomed Opt 2010, 15:056021.*
30. *Bunschoten A, Buckle T, Visser NL, Kuil J, Yuan HS, Josephson L, Vahrmeijer AL, van Leeuwen FWB: Multimodal interventional molecular imaging of tumor margins and distant metastases by targeting alpha v beta 3 Integrin. Chembiochem 2012, 13:1039–1045.*
31. *Ogawa K, Harata Y, Ichihara T, Kubo A, Hashimoto S: A practical method for position-dependent compton-scatter correction in single photon-emission Ct. IEEE Trans Med Imaging 1991, 10:408–412.*
32. *Chin PTK, Welling MM, Meskers SCJ, Olmos RAV, Tanke H, van Leeuwen FWB: Optical imaging as an expansion of nuclear medicine: cerenkov-based luminescence vs fluorescence-based luminescence. Eur J Nucl Med Mol Imaging 2013, 40:1283–1291.*
33. *Chin PT, Beekman CA, Buckle T, Josephson L, van Leeuwen FW: Multispectral visualization of surgical safety-margins using fluorescent marker seeds. Am J Nucl Med Mol Imaging 2012, 2:151–162.*

34. *Branderhorst W, Blezer EL, Houtkamp M, Ramakers RM, van den Brakel JH, Witteveen H, van der Have F, van Andel HAG, Vastenhouw B, Wu C, Stigter-van Walsum M, van Dongen GAMS, Viergever MA, Bleeker WK, Beekman FJ: Three-dimensional histologic validation of high-resolution SPECT of antibody distributions within xenografts. J Nucl Med 2014, 55:830–837.*
35. *Goorden MC, van der Have F, Kreuger R, Ramakers RM, Vastenhouw B, Burbach JPH, Booij J, Molthoff CFM, Beekman FJ: VECTor: a preclinical imaging system for simultaneous submillimeter SPECT and PET. J Nucl Med 2013, 54:306–312.*
36. *Walker MD, Goorden MC, Dinelle K, Ramakers RM, Blinder S, Shirmohammad M, van der Have F, Beekman FJ, Sossi V: Performance assessment of a preclinical PET scanner with pinhole collimation by comparison to a coincidence-based small-animal PET scanner. J Nucl Med 2014, 55:1368–1374.*
37. *Vaissier PEB, Wu C, Beekman FJ: Integration of small animal SPECT and PET with other imaging modalities. Tijdschrift voor Nucleaire Geneeskunde 2012, 35:961–967.*

CHAPTER 7

EXTENDING THE HYBRID SURGICAL GUIDANCE CONCEPT WITH FREEHAND FLUORESCENCE TOMOGRAPHY

Adapted from: van Oosterom MN, Meershoek P, Welling MM, Pinto F, Matthies P, Simon H, Wendler T, Navab N, van de Velde CJH, van der Poel HG, van Leeuwen FWB

IEEE Transactions On Medical Imaging, 2020, 39(1): 226-235

ABSTRACT

Within image-guided surgery, 'hybrid' guidance technologies have been used to integrate the complementary features of radioactive guidance and fluorescence guidance. Here, we explore how the generation of a novel freehand fluorescence (fhFluo) imaging approach complements freehand SPECT (fhSPECT) in a hybrid setup. Near-infrared optical tracking was used to register the position and the orientation of a hybrid opto-nuclear detection probe while recording its readings. Dedicated look-up table models were used for 3D reconstruction. In phantom and excised tissue settings (i.e., flat-surface human skin explants), fhSPECT and fhFluo were investigated for image resolution and in-tissue signal penetration. Finally, the combined potential of these freehand technologies was evaluated on prostate and lymph node specimens of prostate cancer patients receiving prostatectomy and sentinel lymph node dissection (tracers: indocyanine green (ICG) + ^{99m}Tc-nanocolloid or ICG-^{99m}Tc-nanocolloid). After hardware and software integration, the hybrid setup created 3D nuclear and fluorescence tomography scans. The imaging resolution of fhFluo (1 mm) was superior to that of fhSPECT (6 mm). Fluorescence modalities were confined to a maximum depth of 0.5 cm, while nuclear modalities were usable at all evaluated depths (<2 cm). Both fhSPECT and fhFluo enabled augmented- and virtual-reality navigation toward segmented image hotspots, including relative hotspot quantification with an accuracy of 3.9% and 4.1%. Imaging in surgical specimens confirmed these trends (fhSPECT: in-depth detectability, low resolution, and fhFluo: superior resolution, superficial detectability). Overall, when radioactive and fluorescent tracer signatures are used, fhFluo has complementary value to fhSPECT. Combined the freehand technologies render a unique hybrid imaging and navigation modality.

INTRODUCTION

Intraoperative tissue identification is often of paramount importance to achieve an effective and minimal invasive surgical procedure. One of the most frequently used surgical guidance methods encompasses the use of radioactive tracers that specifically accumulate in targeted tissues (e.g. tumorous tissue [1]), facilitating complete resection of the targeted tissue (e.g. clear tumor boundaries [2,3]) and sparing of healthy tissue (e.g. lymphatics [4]). Since the high penetration depth of gamma rays allow for sensitive detection of the tracer-targeted tissues deep within the patient anatomy, radioguided surgery can be considered the 'gold standard' for interventional molecular imaging [5]. These nuclear medicine qualities enable surgical planning via 3D preoperative imaging (e.g. single-photon emission computed tomography/X-ray computed tomography (SPECT/CT)) and intraoperative in-depth guidance via handheld gamma ray detection probes or mobile gamma cameras [6]. The latter can even be extended to 3D intraoperative tomographic imaging via freehand SPECT (fhSPECT) imaging [7,8]. Surgical guidance has a large visual component, a feature that is lacking in traditional radioguidance procedures.

Fluorescence guidance has emerged as an optical alternative for surgical guidance and is rapidly being adopted in many different interventional settings [9]. Unfortunately, fluorescence guidance can only be used for superficially located lesions, since light suffers from severe attenuation, scatter and reflection in tissue. This restricts fluorescent penetration to a maximum of roughly 1 cm deep in tissue [10]. This limits in-depth visibility, but prevents shine-through of underlying tracer distributions and as such facilitates the identification of superficial lesions located in close proximity to high background signals [11,12]. Moreover, when used superficially, fluorescence imaging can be performed with a superior spatial resolution when compared to gamma ray detection [11], even enabling (real-time) microscopic investigation [13,14]. Although 3D fluorescence imaging in the form of a fluorescence tomography setting has been reported for pre-interventional breast cancer diagnosis [15], to our knowledge, 3D or pseudo 3D fluorescence imaging has not yet been attempted in an image-guided surgery setting.

To further improve the accuracy of image-guided surgery, it seems logical to make use of hybrid strategies that combine radioactive and fluorescent signatures [16], thereby creating a best-of-both-worlds scenario. Multiplexing of the complementary signatures allows for surgical guidance concepts that harbor the advantages of the individual technologies, e.g. 3D preoperative radionuclide imaging and intraoperative optical guidance [16,17]. Acquiring both radioactive and fluorescent signals for (intraoperative) tissue identification can be achieved by applying two separate tracers, but more ideally is achieved using a single tracer that contains both the complementary emission types, yielding a so-called 'dual-modality' or 'hybrid' tracer. Extensive use of free indocyanine

green (ICG) in combination with ^{99m}Tc-nanocolloid [10,18–20] or the hybrid tracer ICG-^{99m}Tc-nanocolloid in clinical sentinel lymph node (SN) biopsy trials [11, 12,21–23], has underlined the value of the hybrid surgical guidance concept.

This successful clinical exploration of the hybrid surgical guidance concept has provided the basis for the development and clinical evaluation of a range of intraoperative hybrid detection modalities [24], [25]. The first reported clinically applied hybrid modality, which is now also commercially available, is the so-called opto-nuclear probe (Eurorad S.A., Eckbolsheim, France) [26–28]. In this device, numeric and acoustic gamma tracing is combined with numeric and acoustic tracing of the fluorescent dye ICG with a one channel optical detector. To our knowledge, fully integrated image-based hybrid gamma and fluorescence cameras have only been reported in the preclinical setting so far [29–31]. However, to study the potential of such an image-based hybrid modality during surgery, clinical studies have been performed in a setting wherein a tailored bracket was used to physically connect a gamma probe or a portable gamma camera to a fluorescence exoscope [32]. Key advantages of the hybrid modalities appeared to be: 1) the ability to use in-depth radioguidance to guide positioning of fluorescence imaging; 2) logistical simplification in the operating room.

Alternative to hybrid imaging devices, hybrid surgical navigation concepts have been used to successfully integrate the nuclear guidance as provided by preoperative SPECT or intraoperative fhSPECT images with fluorescence guidance [33–36]. Key advantages of the hybrid navigation approach appeared to be: 1) the ability to provide augmented reality displays of radioactive findings in a fluorescence video display; 2) virtual- or augmented-reality “video-game like” guidance of the fluorescence camera to the lesions (with numerical feedback of the distance to the lesion). While a complete hardware integration can also provide value when separate tracers are used for the radioactive and fluorescent signatures, e.g. separating targeted tissue from healthy tissue [37], success of this navigated fluorescence camera approach relies on a direct link between SPECT and fluorescence findings, thus requiring a single hybrid tracer.

Based on the assumption that radioactive and fluorescence guidance provide complementary information during surgery, we have now studied the integrated use of ICG-^{99m}Tc-nanocolloid, the opto-nuclear hybrid detection modality and a modified fhSPECT navigation platform (see Figure 1). To allow for hybrid imaging and navigation, fhSPECT was complemented by a new form of (pseudo-) 3D intraoperative fluorescence tomography that we call freehand fluorescence (fhFluo). To investigate if and how fhFluo imaging adds complementary information during surgical guidance, both fhSPECT and fhFluo technologies were evaluated in a phantom setup and initial clinical validation was performed on surgical specimens.

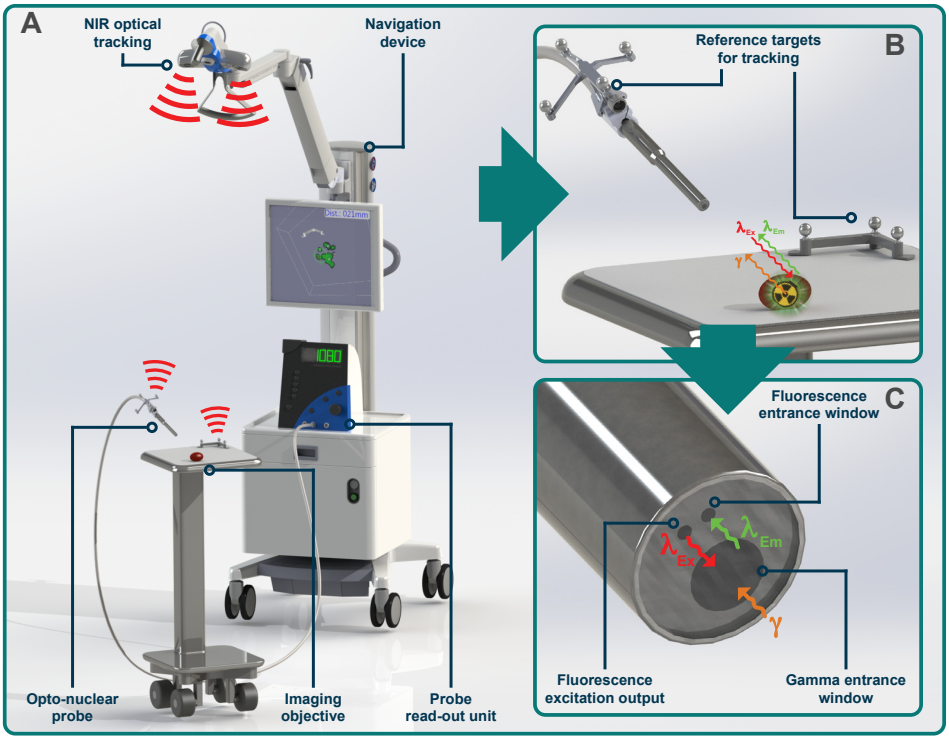

Figure 1. Schematic overview of the hybrid imaging and navigation modality. (a) *Overview of the total setup, showing near-infrared (NIR) tracking of both the opto-nuclear probe and the imaging objective.* ***(b)*** *Zoom-in of the opto-nuclear probe and imaging objective, displaying the presence of both a radioactive (γ) and fluorescent ($\lambda_{Excitation}$ and $\lambda_{Emission}$) tracer signature in the imaging bjective.* ***(c)*** *Zoom-in of the probe entrance windows for nuclear and fluorescence detection.*

METHODS

Integration of the Opto-Nuclear Probe With the DeclipseSPECT Navigation Device

The hybrid fhSPECT and fhFluo setup depicted in Figure 1 was realized using the declipseSPECT navigation device (SurgicEye GmbH, Munich, Germany) [7,8] and the opto-nuclear probe [27], capable of both gamma and fluorescence measurements in counts/s. As described by Van den Berg et al., the fluorescence measurements are acquired with two acrylic optical fibers, each containing a numerical aperture of 0.51 and a diameter of 1 mm. The first fiber is coupled to a 785 nm laser for excitation of the fluorescence dye ICG, providing a typical optical power of 3.7 mW/cm^2 at the fiber output. The second fiber is coupled to a > 810 nm optical filter and an infrared-extended photomultiplier tube (H10721-20, Hamamatsu Photonics kk., Hamamatsu, Japan) to collect the fluorescence emission signals. The resulting system sensitivity for ICG, in terms of minimum detectable ICG concentration, was previously reported as < 0.061 ng/mL [27]. To

enable position- and orientation-tracking of the opto-nuclear probe, the navigation system applies near-infrared (NIR) optical tracking (Polaris Vicra, Northern Digital Inc.,Waterloo, Canada) of a four-fiducial reference target, specifically designed to attach at the distal end of the probe (see Figure 1b). To geometrically calibrate the position of the gamma- or fluorescence-entrance windows with respect to this reference target, thereby tracking both gamma and fluorescence detection locations, individual geometrical calibrators were designed using SolidWorks computer-aided design software (Dassault Systèmes SA, Vélizy-Villacoublay, France), similar as previously described by Van Oosterom et al. [35]. These were 3D printed (acrylonitrile butadiene styrene plastics; Dimension Elite 3D printer, Stratasys Ltd., Eden Prairie, MN, USA) and used to calibrate the position of the respective detectors relative to the fiducials at the distal end of the opto-nuclear probe [35]. An oscilloscope (PicoScope, Pico Technology Ltd., Cambridgeshire, UK) housed within the declipseSPECT was used to transfer the probe-read-out signals to the declipseSPECT, either via an analogue signal (nuclear read-out of the gamma signal) or a digital transistor-transistor-logic signal (optical read-out of the fluorescence signal).

By simultaneously recording the position and orientation of the opto-nuclear probe and its 1D probe readings (sample rate of 0.5 s), software algorithms could be used to extrapolate the geometrical source location of the readings. A modified version of the declipse 6.0 software (SurgicEye GmbH) was used to reconstruct a tomographic 3D volume based on the gamma readings (i.e. an fhSPECT scan as previously described [8,38,40]). A tomographic 3D reconstruction of the fluorescence readings (i.e. a fhFluo scan) was realized in analogy to the well validated fhSPECT technology. The underlying mathematical models used were based on previously validated look-up table (LUT) methods [38,39,41]; The LUT model provides an estimate of which voxels in the scanning volume could have contributed, and with what kind of weight, to the individual probe measurements. In line with previous reports, a maximum likelihood expectation maximization algorithm was used to approximate the actual tracer distribution within the volume [39,42]. For the fhSPECT part, the reconstruction model was configured, as previously described, by using a dedicated LUT model based on nuclear Monte-Carlo simulations [39]. For fhFluo imaging, however, the real-measurements fluorescence LUT model was implemented [39]. This fluorescence LUT was obtained by measuring the response of a point source (6 µg/mL ICG dissolved in epoxy resin with a total volume of about 1.5 µL [43]) in air using a sample volume of 11x11x10 mm and a resolution of 1 mm. Subsequently, the acquired LUT model was filtered with a Gaussian filter (size: 1 mm standard deviation) in order to compensate for measurement and calibration inaccuracies, and subsequently normalized.

During both fhSPECT and fhFluo scan acquisition, the optonuclear probe was manually moved over and around the subject (no-tissue contact), thereby measuring at as many different positions and orientations as possible within

Table 1. Most important differences in freehand SPECT and freehand fluorescence reconstruction and navigation settings.

Reconstruction parameter	fhSPECT	fhFluo
Number of voxels	392000	392000
Voxel size (mm)	2x2x2	1x1x1
VOI size (voxels)	70x70x80	140x140x20
VOI size (mm)	140x140x160	140x140x20
Filter size (standard deviation, mm)	2	1
Acquisition + reconstruction time (typical range in min)	1-3	1-3
Navigation parameter	**fhSPECT**	**fhFluo**
Minimal scan hotspot size (mm)	1.2	0.6
Scan colormap	Green-blue-purple	Green-white
Augmented navigation targe size (mm)	4	4
Augmented navigation target color	Red (when targeted) Gray (when not targeted)	Red (when targeted) Gray (when not targeted)

a < 5 min acquisition time [8]; Previous clinical experience with fhSPECT during surgery suggests total scanning time should be kept roughly below 5 min [8,44,45] (see Table 1).

To geometrically link the position and orientation of the resulting scan to the imaged objective, thereby allowing for augmented reality overlay or subsequent navigation, a three-fiducial reference target, also tracked by the aforementioned tracking system, was attached nearby the specimen under study (see Figure 1b). When the fhSPECT and fhFluo scans were deployed for 3D surgical navigation, the intensity hotspots in the reconstructed tracer distribution functioned as the navigation targets (e.g. SN locations within the specimen). These navigation targets were segmented automatically, which occurred based on the weighted center of gravity of the intensity hotspots. Subsequent augmented and/or virtual reality visualizations where shown from the perspective as approached by the navigated instrument using the modified declipse 6.0 software.

Patients

Ex vivo human skin explants were obtained from an abdominal skin reduction procedure. SN and prostate samples were acquired from five prostate cancer patients receiving a combination of robot-assisted laparoscopic SN biopsy, extended pelvic lymph node dissection (ePLND) and prostatectomy. The prostate and dissected SN's contained either the hybrid tracer ICG-^{99m}Tc-nanocolloid or a combination of 'free' ICG and ^{99m}Tc-nanocolloid [19]. All procedures performed

were in accordance with the ethical approval of our institutions (B18-009, NL46580.031.13 and NL57838.031.16) and the Helsinki Declaration.

Reference Modalities

As reference to the hybrid 3D fhSPECT and 3D fhFluo imaging setup, all measurements were also performed with more traditional image-guided surgery modalities [24,25]. This included a handheld gamma camera (CrystalCam with low energy high resolution collimator and 30 s exposure time; Crystal Photonics GmbH, Berlin, Germany) and an open surgery fluorescence camera (FIS-00, Hamamatsu Photonics kk., Hamamatsu, Japan). This fluorescence camera is based on the previously reported m-PDE prototype system, harboring a CCD camera with > 820 nm optical longpass filter and a ring of LEDs for ICG excitation (755 nm center wavelength; 10 nm full-width-at-half-maximum) [43], [46]. In terms of minimum detectable ICG concentration, the sensitivity is reported as < 0.0093 ng/mL [46].

Image Resolvability and Quantification

To demonstrate the differences in imaging resolvability and resolution characteristics, a resolvability phantom was created. This phantom consisted of a 10 mm thick polymethylmethacrylate transparent plastic plate, where 12 well pairs were drilled with decreasing distances between the edges, ranging from 18 to 0.25 mm edge-to-edge. Each well was filled with a 170 µL solution of the hybrid tracer ICG-^{99m}Tc-nanocolloid containing 1.03 x 10^{-2} mg/mL ICG and 2 MBq ^{99m}Tc. These values are in the range of a typical SN size and tracer concentration as reported for prostate cancer [47]. All well pairs were repeatedly scanned with the fhSPECT, fhFluo, CrystalCam and FIS-00 imaging modalities. The whole experiment was performed in duplicate, resulting in 48 different wells, imaged within 12 scans per imaging modality (i.e. 4 wells per image). To determine the significance in differences between relative image-hotspot quantification, a paired samples t-test with confidence interval of 95% was used in IBM SPSS statistics 22 software (International Business Machines Corp., New York, USA).

Signal Penetration in Tissue

The influence of tissue attenuation was determined using human skin tissue (roughly a flat surface of 20 x 15 cm with a depth of 5 cm). To allow these investigations, an Eppendorf tube (Eppendorf AG, Hamburg, Germany) was filled with ICG-^{99m}Tc-nanocolloid (according to the above-mentioned volume and concentration), positioned at different depths from the skin surface (0, 0.5, 1 and 1.5 cm) and analyzed with the available imaging modalities.

Surgical Specimen Evaluation

In the operating room, excised specimens of the SNs and the prostate (i.e. the

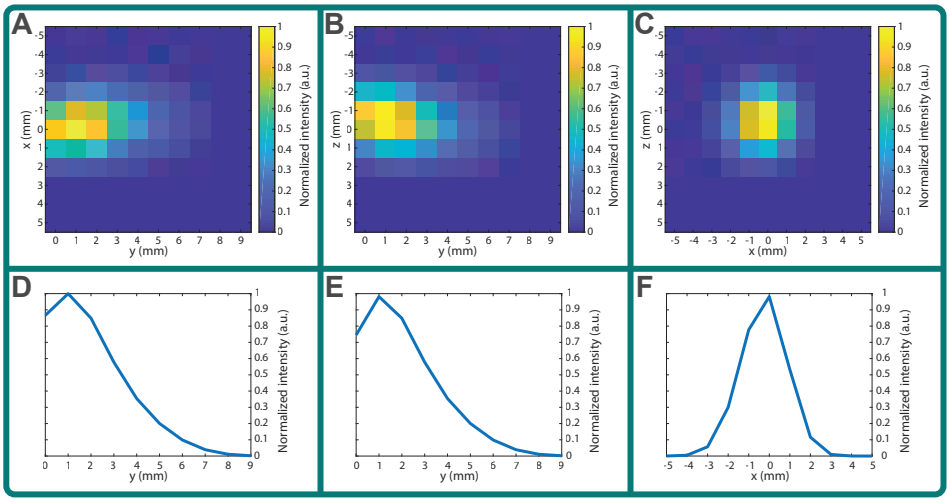

Figure 2. Overview of the ICG fluorescence look-up table. (a-c) *Maximum intensity projections of the look-up table, shown from three different directions, where the y-axis depicts the longitudinal axis of the optonuclear probe.* ***(d-f)*** *Horizontal line profiles taken at the middle of the maximum intensity projections as shown above.*

injection site of the tracer) were subjected to imaging with the fhSPECT, fhFluo, CrystalCam and FIS-00 modalities.

RESULTS

Integration of the Opto-Nuclear Probe With the DeclipseSPECT Navigation Device

Figure 2 shows a maximum intensity projection of the filtered fluorescence LUT model from different sides. The y-axis is depicted as the longitudinal axis of the probe. Interestingly, most likely due to the two-fiber setup (i.e. emitting and receiving), the acquired LUT model was not symmetrical and the maximum response was slightly in front of the probe (y = 1 mm). A curve along the longitudinal axis of the probe revealed a quick detection fall-off (100% at 1 mm, 50% at 3.3 mm, 10% at 6 mm and 5% at 6.8 mm). These findings are contrary to a typical LUT for gamma ray detection (^{99m}Tc) [39], which is symmetrical, has maximal response at the edge of the probe (y = 0 mm) and displays a more extended detection fall-off (100% at 0 mm, 50% at 5 mm, 10% at 19 mm and 5% at 33 mm).

Due to the above-mentioned detection differences, the customized fhFluo software was configured different to that of the fhSPECT (settings are shown in Table 1). To accommodate for the quick detection fall-off and typical tissue attenuation of fluorescent signals [9,48], the volume of interest (VOI) used for the fhFluo scans was limited to a depth of 20 mm, while the fhSPECT VOI depth was configured at 160 mm. For both fhSPECT and fhFluo imaging options,

scan reconstruction was performed 'on-the-fly' (i.e. during the 1-3 min scan acquisition). To ensure similar software performance, the number of voxels (392000) used was equal for both modalities. As a result, the reduced scan volume of the fhFluo yielded two-fold smaller voxel dimensions as compared to the fhSPECT scans.

Imaging Resolvability and Quantification

Figure 3a depicts the distinct differences in the resolvability outcomes obtained using the different modalities. The FIS-00 displayed the highest resolution: allowing separation at an edge-to-edge distance of 0.5 mm. The newly introduced fhFluo was second best, discriminating sources at 1 mm edge-to-edge. The CrystalCam came third with a resolvability of 2 mm, while the fhSPECT came last with a resolvability of 6 mm.

For the freehand imaging options the declipse 6.0 software was able to segment separate navigation targets for the tracer sources (depicted as virtual red and gray targets within the image hotspots; see Figure 3). Because of this segmentation, navigation and relative hotspot quantification became possible (see Figure 3b). For the latter, analysis of the fhSPECT images of the resolvability phantom yielded an average absolute inaccuracy of 3.9 $\pm$ 3.3%. The average absolute inaccuracy for the hotspot quantification found in fhFluo was 4.1 $\pm$ 2.7%. A paired-samples t-test revealed no significant difference between the quantification inaccuracies of both imaging modalities (p-value of 0.371).

Signal Penetration in Tissue

To study how the different modalities cope with the differences in tissue attenuation between radioactive and fluorescent signatures, in-depth detectability ($\leq$ 2 cm) was studied in human skin (see Figure 4). Again, the imaging modalities revealed distinct differences. The sources could be detected at all evaluated depths using the two nuclear imaging options (i.e. handheld gamma camera and fhSPECT). However, the shapes best seem to match that of the actual source at a 0 cm depth. In line with the resolvability experiments, the shape of the source was displayed with more detail (i.e. a higher resolution) using the fluorescence modalities. This advantage, however, disappeared at a > 0.5 cm depth due to clear signs of signal attenuation and diffusion. The FIS-00 camera did show a very diffuse fluorescence signal at 1 cm depth, though one could question if such a signal would provide valuable guidance during surgery. The observed attenuation and diffusion trends are in line with previous studies reporting the head-to-head comparison of signal penetrations in a phantom model [48].

Surgical Specimen Evaluation

Studies in surgical specimens containing ICG-^{99m}Tc-nanocolloid (see Figures 5 and 6), demonstrated that the fluorescence imaging modalities (i.e. FIS-00 and fhFluo) created a more detailed image of the (superficial) tracer distribution than

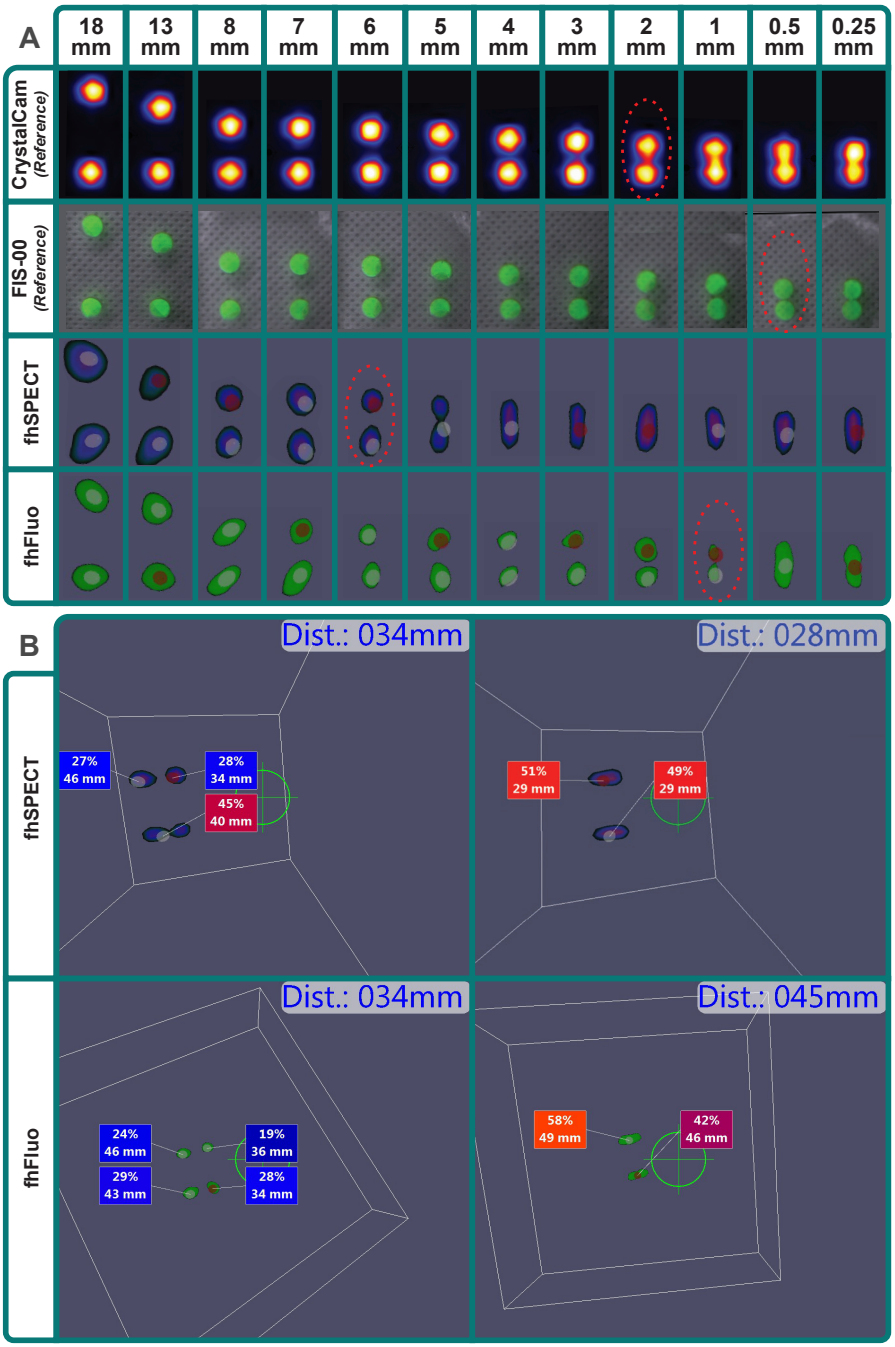

Figure 3. Freehand SPECT and freehand Fluorescence imaging resolvability, navigation and relative hotspot quantification. (a) *Results for image resolvability, based on two tracer sources located at varying distances with respect to each other, including the CrystalCam and FIS-00 reference modalities. A red dotted oval indicates the resolvability limit.* ***(b)*** *Example images of the virtual navigation and relative tracer quantification found for the segmented hotspots. The distance displayed is the distance estimated between the opto-nuclear probe tip and center of the navigation target aimed at.*

the nuclear imaging options (i.e. CrystalCam and fhSPECT). Especially in the larger tissues, multiple small foci became visible with fluorescence modalities, while the nuclear modalities only showed a low number of large hotspots. When ICG and ^{99m}Tc-nanocolloid were administered separately, a clear difference in signal distribution was observed in the SN and prostate specimens (see Figure 5). This is in line with the reported differences in tracer distribution kinetics [49].

Both fhSPECT and fhFluo allowed for navigation towards the middle of the segmented hotspots in augmented- and virtual-reality views (see Figure 6). During navigation the numerical distance to the tip of the navigated opto-nuclear probe was displayed in real-time. When used for navigation on the larger prostate samples, fhSPECT allowed for in-depth navigation towards the large hotspot(s) ("tomographic imaging"), while fhFluo allowed for navigation towards multiple superficial hotspots ("pseudo-tomographic imaging"). Combined the two technologies provided superior superficial and in-depth tomographic imaging.

DISCUSSION

In this study we have evaluated the integrated use of fhSPECT and fhFluo with a hybrid navigation concept for application in image-guided surgery. In such a setting, the complementary advantages of both nuclear and fluorescence imaging could be harnessed in a single setup. Hybrid freehand imaging offered a couple of additional features, not provided by more traditional hybrid systems: 1) 3D insight in to the tracer distribution (see Figures 3b, 4 and 6); 2) AR overlay of the reconstructed scan, including guidance features (see Figures 4, 5 and 6); 3) navigation towards the imaged lesions (see Figures 3b and 6); and 4) hotspot quantification within the image (see Figure 3b). Current fhSPECT and fhFluo acquisition times (~1-5 min) are long when compared to 2D handheld gamma cameras (~5-60 sec) or 2D fluorescence cameras (real time). However, by increasing both computing power and device sensitivity, future technical refinements (e.g. higher sample rates) are likely to reduce these scan times. Furthermore, tissue deformation in between the freehand scan acquisition and actual surgical targeting can influence the actual navigation accuracy [50]. The true extend of these limitations, however, only becomes apparent during clinical implementation of the technology. Luckily, the real-time audible and numerical feedback delivered by the opto-nuclear probe [27] will help make sure the procedural accuracy is not at risk [51].

Phantom measurements indicated that the surface resolution of the prototype fhFluo option was superior to that of fhSPECT (see Figure 3a) and hotspot quantification showed an equal accuracy (see Figure 3b). NIR optical tracking can obstruct NIR fluorescence imaging setups [34,43]. Interestingly, obstruction of the opto-nuclear probe detection only occurred when the detector was positioned within an unrealistic 15 cm from the optical tracking light source; the

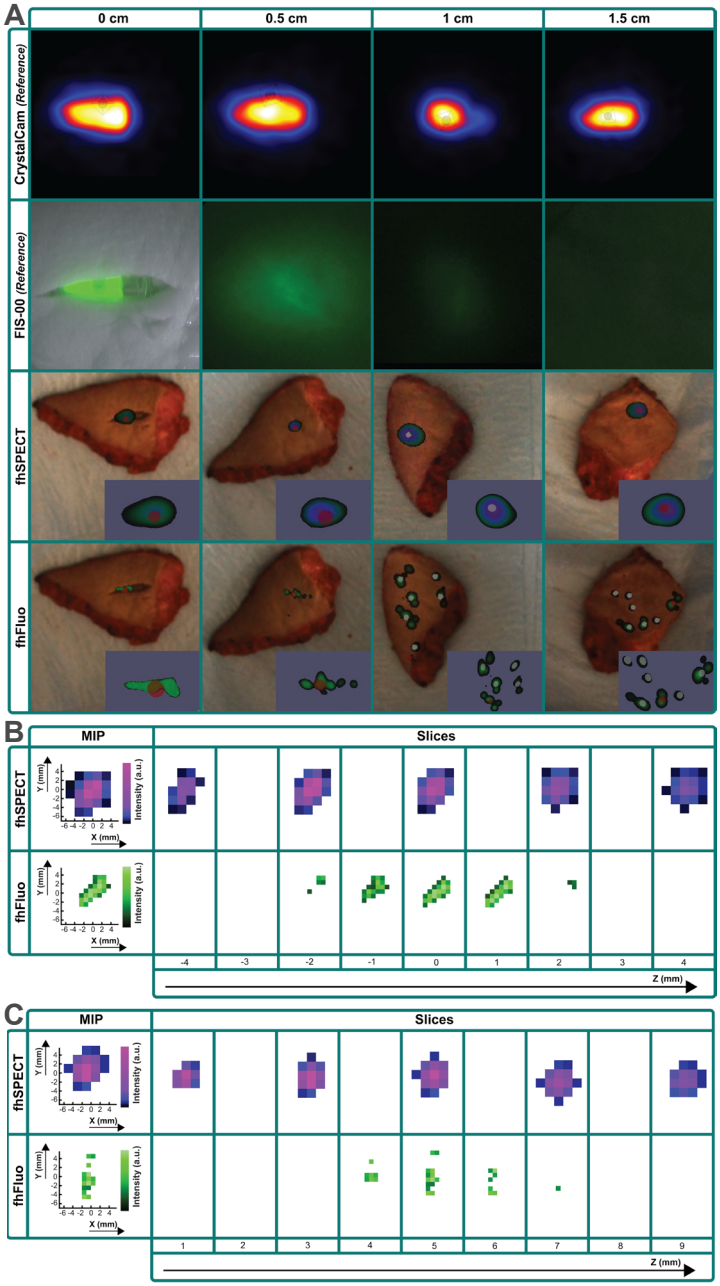

Figure 4. Signal penetration in tissue for freehand SPECT and freehand fluorescence imaging, including CrystalCam and FIS-00 reference modalities. (a) *Overview of all modalities. With a tracer source located at different depths in human skin, nuclear imaging (CrystalCam and fhSPECT) was useable at all depths, fluorescence imaging (FIS-00 and fhFluo) only up to 0.5 cm. However, source delineation (i.e. image resolution) was highest with fluorescence imaging at these superficial depths.* ***(b)*** *Zoomed-in look at the raw tomographic slices (using Matlab, MathWorks Inc.) of the freehand SPECT and freehand fluorescence 3D reconstructions with the tracer source at a depth of 0 cm, where MIP stands for maximum intensity projection.* ***(c)*** *Similar tomographic slices at 0.5 cm depth.*

opto-nuclear probe is typically used at a working distance of 100-250 cm with respect to the tracking device. Further optimization of the underlying physical detection models is likely to refine future fhFluo reconstructions. For example, recently introduced Monte Carlo based software for simulating fluorescence imaging setups [52,53] opens the door for high resolution ICG LUTs that even simulate tissue interaction effects. To prevent tissue deformations the opto-nuclear probe is not used in direct tissue contact. Consequently, the simulated LUTs will have to rely on a dynamic ratio of air and skin contributions, rendering this approach a challenging and computationally demanding task.

Despite the reduced resolution of fhSPECT, this freehand technology supports navigation towards deeper lying tracer deposits, a feature that could accommodate radical surgical excision through the use of safety margins (commonly ~0.5-2 cm [54–57]). In agreement with previous reports on freehand beta+ probe imaging (fhBeta^{+}) [58], fhFluo underlines the limitations of using imaging signatures that suffer from severe tissue attenuation to establish in-depth safety margins. On the bright side, the superficial nature of fhBeta$^{+/-}$ and fhFluo does provide a means to study surgical resection planes in detail with limited 'shine-through' effect from background signals [2,41]. In such applications, the superior resolution of fhFluo provides valuable detail. As such, fhFluo imaging might provide a valuable method for in vivo 3D mapping of surgical resection margins, preventing positive margins and disease recurrence. By facilitating in vivo application during surgery, possibly in a navigation workflow, resection details could be provided before excision of the tumor mass. When fhFluo is adapted for other wavelengths, it may help provide an optical alternative for such indications where superficial tissue detection is in demand; e.g. glioblastoma surgery using 5-aminolevolinic acid fluorescence [59], or nerve sparing during prostatectomy using fluorescein and Cy5 [60]. Even after surgery, such fhFluo scans might also provide useful insight and confirmation, allowing for macroscopic tomographic depictions of the tracer distribution in targeted structures (e.g. tumor location and margins or nerve density), thereby extending what is possible using 3D pathology [61].

Globally, radioguidance is routinely applied during SN procedures, radioguided occult lesion localization and radioguided seed localization [6]. With the increasing use of the hybrid tracer ICG-^{99m}Tc-nanocolloid during SN procedures, the proposed hybrid image-guided surgery approach should be directly implementable in a broad range of indications: prostate cancer [62], penile cancer [63], breast cancer [22], various head and neck cancers [11,23] and cervical cancer [21]. While the currently proposed fhFluo system is only applicable during open surgery procedures, the recently introduced laparoscopic opto-nuclear probe [28] indicates a translation towards laparoscopic procedures as well, similar as laparoscopic freehand SPECT [36,64,65]. In addition, radioguided surgery is also increasingly finding its way into receptor targeted tumor resections, such as the targeting of somatostatin [66] and prostate specific membrane

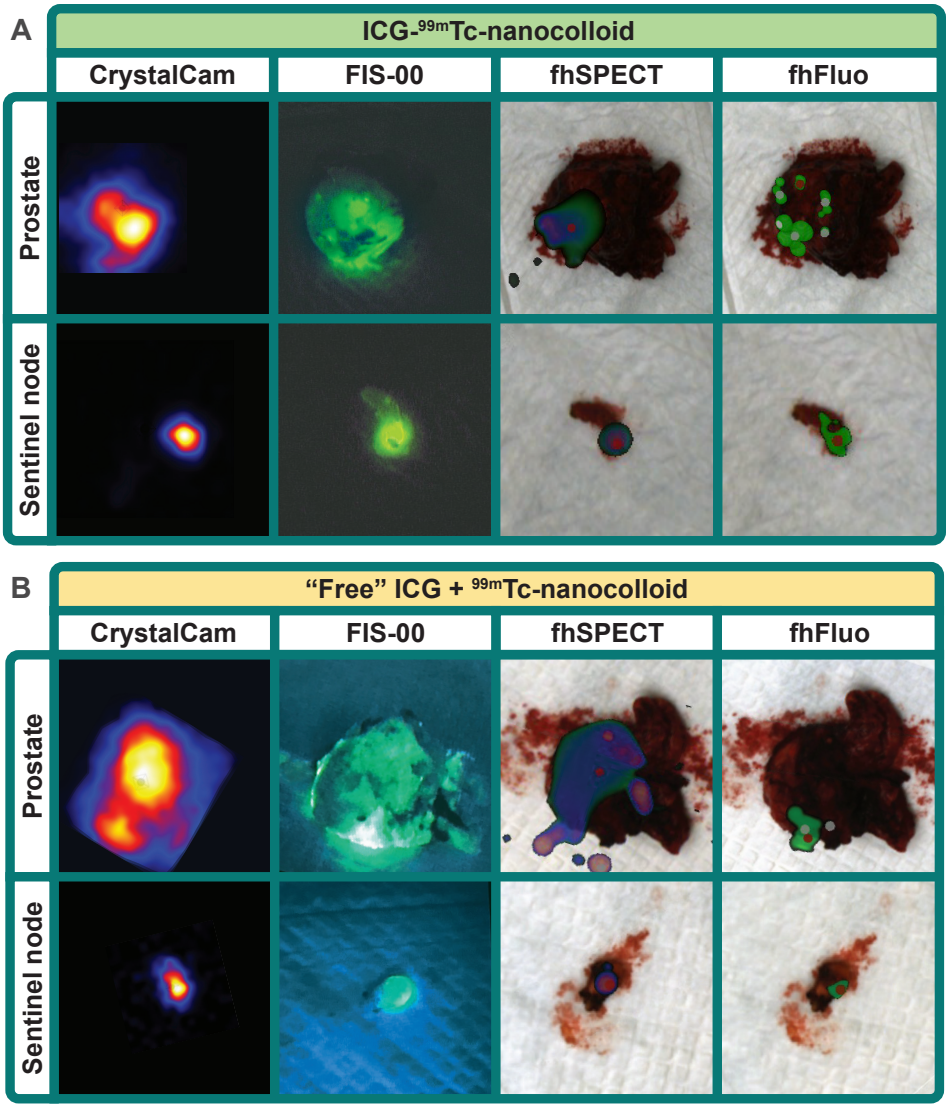

Figure 5. Imaging of prostate and sentinel lymph node specimens using freehand SPECT and freehand fluorescence, including CrystalCam and FIS-00 reference modalities. (a) *Examples of imaging when a single hybrid tracer (ICG-^{99m}Tc-nanocolloid) is used.* ***(b)*** *Examples of imaging when two separate tracers are used ("free" ICG + ^{99m}Tc-nanocolloid). A small difference in color is visible between the FIS-00 images due to a difference in recording facilities available.*

antigen [1] positive tumors. Continuous preclinical developments in to tumor-receptor targeted hybrid tracers [67,68] indicates that future use of the introduced technology can be envisioned when using e.g. PSMA I&F in prostate cancer [69], Cy5-^{111}In-DTPA-Tyr3-octreotate for neuroendocrine tumors [70], [^{111}In]-DTPA-trastuzumab-IRDye800 in breast cancer [71] or ^{111}In-girentuximab-IRDye-800CW in renal cancer [17]. As shown in the current study, next to complementing

fhSPECT imaging of hybrid tracers, fhFluo can also be used to independently visualize fluorescence tracers such as ICG. Multiplexing to discriminate between two tracers may be used to e.g. intraoperatively differentiate between healthy and diseased lymphatic structures [37].

Analogous as to how we use our smartphones with global positioning system (GPS) navigation to direct ourselves through a map of the city in every-day life, surgical navigation based on preoperative patient images (e.g. SPECT/CT) is increasingly used to guide lesion localization in the operating room [50]. However, when we do not use GPS-navigation in combination with dynamic data, live updates such as road construction and traffic jams, can render the guidance outdated. To this end, navigation extensions based on dynamic intraoperative fhSPECT and fhFluo imaging, provide a means to introduce the concept of "live updates" in the surgical navigation process. Just as a combination of satellite and local internet signals can drastically increase the precision of urban navigation due to their complementary natures [72], we reasoned the high resolution superficial nature of fluorescence can help refine the surgical navigation accuracy [33–36], a concept that is now extended with the fhFluo modality. Clinical studies are needed to determine if the proposed hybrid navigation setup should be pursued in a fully integrated fashion (i.e. fusion of fhSPECT and fhFluo visualizations) or in a sequential fashion where fhSPECT and fhFluo scans are acquired during different stages of the surgical procedure.

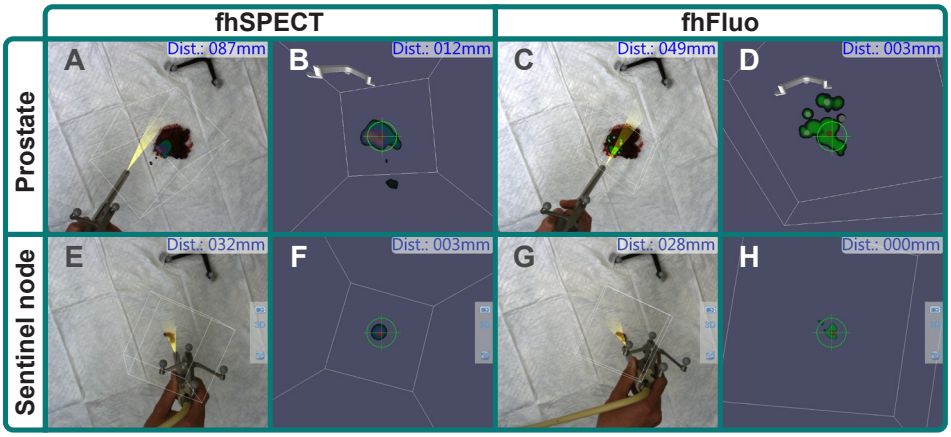

Figure 6. Navigation on prostate and sentinel lymph node samples, based on freehand SPECT and freehand fluorescence imaging. (a, c, e and g) *Examples of navigation in an augmented reality view.* ***(b, d, f and h)*** *Examples of navigation in a virtual reality view, where the tip of the opto-nuclear probe is positioned against the tissue surface. All distances shown are the estimated distances between the probe tip and the center of the navigated target.*

CONCLUSION

In this study, we introduced a novel method of fluorescence imaging (fhFluo), which can be applied during image-guided surgery. We demonstrated that the fhFluo approach ("pseudotomographic imaging") could complement fhSPECT ("tomographic imaging") during hybrid imaging and navigation studies. Having both fhSPECT and fhFluo available in a hybrid navigation setup: 1) combined the in-depth guidance of nuclear imaging with the high resolution of fluorescence imaging, 2) supported the differentiation between tissue attenuation of the different signals, 3) allowed multiplexing of different tracers, and 4) supported augmented and virtual reality multimodal visualization and guidance concepts.

REFERENCES

1. *T. Maurer et al., "99mTechnetium-based prostate-specific membrane antigen–radioguided surgery in recurrent prostate cancer," Eur. Urol., vol. 75, no. 4, pp. 659–666, Apr. 2018.*
2. *E. S. Camillocci et al., "A novel radioguided surgery technique exploiting beta− decays," Sci. Rep., vol. 4, Mar. 2014, Art. no. 4401.*
3. *S. Vidal-Sicart, M. Rioja, P. Paredes, M. Keshtgar, and R. Valdés Olmos, "Contribution of perioperative imaging to radioguided surgery," Quart. J. Nucl. Med. Mol. Imag., vol. 58, no. 2, pp. 140–160, Jun. 2014.*
4. *V. M. Moncayo, A. L. Alazraki, N. P. Alazraki, and J. N. Aarsvold, "Sentinel lymph node biopsy procedures," Seminars Nucl. Med., vol. 47, no. 6, pp. 595–617, Nov. 2017.*
5. *R. A. V. Olmos, D. D. D. Rietbergen, and S. Vidal-Sicart, "SPECT/CT and sentinel node lymphoscintigraphy," Clin. Transl. Imag., vol. 2, no. 6, pp. 491–504, Dec. 2014.*
6. *K. Herrmann, O. Nieweg, and S. P. Povoski, Radioguided Surgery: Current Applications and Innovative Directions in Clinical Practice. Cham, Switzerland: Springer, 2016.*
7. *C. Bluemel, P. Matthies, K. Herrmann, and S. P. Povoski, "3D scintigraphic imaging and navigation in radioguided surgery: Freehand SPECT technology and its clinical applications," Expert Rev. Med. Devices, vol. 13, no. 4, pp. 339–351, 2016.*
8. *T. Wendler et al., "First demonstration of 3-D lymphatic mapping in breast cancer using freehand SPECT," Eur. J. Nucl. Med. Mol. Imag., vol. 37, no. 8, pp. 1452–1461, Aug. 2010.*
9. *F. W. van Leeuwen, J. C. Hardwick, and A. R. van Erkel, "Luminescence-based imaging approaches in the field of interventional molecular imaging," Radiology, vol. 276, no. 1, pp. 12–29, Jul. 2015.*
10. *I. Stoffels, J. Dissemond, T. Pöppel, D. Schadendorf, and J. Klode, "Intraoperative fluorescence imaging for sentinel lymph node detection: Prospective clinical trial to compare the usefulness of indocyanine green vs technetium Tc 99m for identification of sentinel lymph nodes," JAMA Surg., vol. 150, no. 7, pp. 617–623, Jul. 2015.*
11. *A. Christensen et al., "Feasibility of real-time near-infrared fluorescence tracer imaging in sentinel node biopsy for oral cavity cancer patients," Ann. Surgical Oncol., vol. 23, no. 2, pp. 565–572, Feb. 2016.*
12. *G. KleinJan et al., "The best of both worlds: A hybrid approach for optimal pre- and intraoperative identification of sentinel lymph nodes," Eur. J. Nucl. Med. Mol. Imag., vol. 45, no. 11, pp. 1915–1925, Oct. 2018.*
13. *A. Bennàssar, A. Vilata, S. Puig, and J. Malvehy, "Ex vivo fluorescence confocal microscopy for fast evaluation of tumour margins during Mohs surgery," Brit. J. Dermatology, vol. 170, no. 2, pp. 360–365, Feb. 2014.*

14. G. Widhalm et al., "5-Aminolevulinic acid induced fluorescence is a powerful intraoperative marker for precise histopathological grading of gliomas with non-significant contrast-enhancement," PLoS ONE, vol. 8, no. 10, Oct. 2013, Art. no. e76988.
15. A. Corlu et al., "Three-dimensional in vivo fluorescence diffuse optical tomography of breast cancer in humans," Opt. Express, vol. 15, no. 11, pp. 6696–6716, May 2007.
16. F. W. van Leeuwen, R. Valdés-Olmos, T. Buckle, and S. Vidal-Sicart, "Hybrid surgical guidance based on the integration of radionuclear and optical technologies," Brit. J. Radiol., vol. 89, Jun. 2016, Art. no. 20150797.
17. M. C. Hekman et al., "Tumor-targeted dual-modality imaging to improve intraoperative visualization of clear cell renal cell carcinoma: A first in man study," Theranostics, vol. 8, no. 8, pp. 2161–2170, Mar. 2018.
18. M. Markuszewski, W. Polom, W. Cytawa, P. Czapiewski, P. Lass, and M. Matuszewski, "Comparison of real-time fluorescent indocyanine green and (99m)Tc-nanocolloid radiotracer navigation in sentinel lymph node biopsy of penile cancer," Clin. Genitourinary Cancer, vol. 13, no. 6, pp. 574–580, Dec. 2015.
19. P. Meershoek et al., "Robot-assisted laparoscopic surgery using DROP-IN radioguidance: First-in-human translation," Eur. J. Nucl. Med. Mol. Imag., vol. 46, no. 1, pp. 49–53, Jan. 2018.
20. B. E. Schaafsma et al., "Near-infrared fluorescence sentinel lymph node biopsy in vulvar cancer: A randomised comparison of lymphatic tracers," BJOG: An Int. J. Obstetrics Gynaecology, vol. 120, no. 6, pp. 758–764, May 2013.
21. P. Paredes et al., "Role of ICG-99mTc-nanocolloid for sentinel lymph node detection in cervical cancer, a pilot study," Eur. J. Nucl. Med. Mol. Imag., vol. 44, no. 11, pp. 1853–1861, Oct. 2017.
22. B. E. Schaafsma et al., "Clinical trial of combined radio- and fluorescence-guided sentinel lymph node biopsy in breast cancer," Brit. J. Surg., vol. 100, no. 8, pp. 1037–1044, Jul. 2013.
23. I. Stoffels, J. Leyh, T. Pöppel, D. Schadendorf, and J. Klode, "Evaluation of a radioactive and fluorescent hybrid tracer for sentinel lymph node biopsy in head and neck malignancies: Prospective randomized clinical trial to compare ICG-99m Tc-nanocolloid hybrid tracer versus 99mTc-nanocolloid," Eur. J. Nucl. Med. Mol. Imag., vol. 42, no. 11, pp. 1631–1638, Oct. 2015.
24. S. L. Bugby, J. Lees, and A. Perkins, "Hybrid intraoperative imaging techniques in radioguided surgery: Present clinical applications and future outlook," Clin. Transl. Imag., vol. 5, no. 4, pp. 323–341, Aug. 2017.
25. J. P. Gambini and T. P. Quinn, "Hybrid tracers and devices for intraoperative imaging: The future for radioguided surgery?" Clin. Transl. Imag., vol. 4, no. 5, pp. 343–351, Oct. 2016.
26. M.-A. Poumellec et al., "Détection du ganglion sentinelle dans le cancer du sein par sonde opto-nucléaire après injection de vert indocyanine et de technétium 99m," Gynécologie Obstétrique Fertilité, vol. 44, no. 4, pp. 207–210, Apr. 2016.
27. N. S. van den Berg et al., "First-in-human evaluation of a hybrid modality that allows combined radio- and (near-infrared) fluorescence tracing during surgery," Eur. J. Nucl. Med. Mol. Imag., vol. 42, no. 11, pp. 1639–1647, Oct. 2015.
28. S. Vidal-Sicart et al., "Clinical use of an opto-nuclear probe for hybrid sentinel node biopsy guidance: First results," Int. J. Comput. Assist. Radiol. Surg., vol. 14, no. 2, pp. 409–416, Feb. 2018.
29. H. G. Kang, S. H. Song, Y. B. Han, H.-Y. Lee, K. M. Kim, and S. J. Hong, "Proof-of-concept of a multimodal laparoscope for simultaneous NIR/gamma/visible imaging using wavelength division multiplexing," Opt. Express, vol. 26, pp. 8325–8339, 2018.
30. J. E. Lees et al., "A multimodality hybrid gamma-optical camera for intraoperative imaging," Sensors, vol. 17, no. 7, p. 554, 2017.
31. K. Popovic, Intraoperative Multimodal Imaging System for Surgical Guidance. Charlottesville, VA, USA: Univ. Virginia, 2013.
32. G. H. KleinJan et al., "Hybrid surgical guidance: Does hardware integration of - and fluorescence imaging modalities make sense?" J. Nucl. Med., vol. 58, no. 4, pp. 646–650, Apr. 2017.

33. O. R. Brouwer et al., "Image navigation as a means to expand the boundaries of fluorescence-guided surgery," Phys. Med. Biol., vol. 57, no. 10, pp. 3123–3126, May 2012.
34. G. H. KleinJan et al., "Toward (Hybrid) navigation of a fluorescence camera in an open surgery setting," J. Nucl. Med., vol. 57, no. 10, pp. 1650–1653, Oct. 2016.
35. M. N. van Oosterom et al., "Navigation of a robot-integrated fluorescence laparoscope in preoperative SPECT/CT and intraoperative freehand SPECT imaging data: A phantom study," Proc. SPIE, vol. 21, no. 8, 2016, Art. no. 086008.
36. M. N. van Oosterom et al., "Navigation of fluorescence cameras during soft tissue surgery-is it possible to use a single navigation setup for various open and laparoscopic urological surgery applications?" J. Urol., vol. 199, no. 4, pp. 1061–1068, Apr. 2017.
37. P. Meershoek et al., "Multispectral-fluorescence imaging as a tool to separate healthy from disease-related lymphatic anatomy during robotassisted laparoscopy," J. Nucl. Med., vol. 59, no. 11, pp. 1757–1760, Nov. 2018.
38. A. Hartl, D. I. Shakir, R. Kojchev, N. Navab, S. I. Ziegler, and T. Lasser, "Freehand SPECT reconstructions using look up tables," Proc. SPIE, vol. 8316, Feb. 2012, Art. no. 83162H.
39. A. Hartl, D. I. Shakir, T. Lasser, S. I. Ziegler, and N. Navab, "Detection models for freehand SPECT reconstruction," Phys. Med. Biol., vol. 60, no. 3, pp. 1031–1046, Feb. 2015.
40. T. Wendler et al., "Towards intra-operative 3D nuclear imaging: Reconstruction of 3D radioactive distributions using tracked gamma probes," in Proc. Int. Conf. Med. Image Comput. Comput.-Assist. Intervent., 2007, pp. 909–917.
41. F. Monge, D. I. Shakir, F. Lejeune, X. Morandi, N. Navab, and P. Jannin, "Acquisition models in intraoperative positron surface imaging," Int. J. Comput. Assist. Radiol. Surg., vol. 12, no. 4, pp. 691–703, Apr. 2017.
42. L. A. Shepp and Y. Vardi, "Maximum likelihood reconstruction for emission tomography," IEEE Trans. Med. Imag., vol. 1, no. 2, pp. 113–122, Oct. 1982.
43. M. N. van Oosterom, D. A. den Houting, C. J. van de Velde, and F. W. van Leeuwen, "Navigating surgical fluorescence cameras using near-infrared optical tracking," J. Biomed. Opt., vol. 23, May 2018, Art. no. 056003.
44. T. Engelen et al., "The next evolution in radioguided surgery: Breast cancer related sentinel node localization using a freehandSPECT-mobile gamma camera combination," Amer. J. Nucl. Med. Mol. Imag., vol. 5, no. 3, pp. 233–245, Feb. 2015.
45. G. H. KleinJan, B. Karakullukçu, W. M. C. Klop, T. Engelen, N. S. van den Berg, and F. W. van Leeuwen, "Introducing navigation during melanoma-related sentinel lymph node procedures in the head-and-neck region," EJNMMI Res., vol. 7, no. 1, p. 65, Aug. 2017.
46. N. S. van den Berg et al., "(Near-Infrared) fluorescence-guided surgery under ambient light conditions: A next step to embedment of the technology in clinical routine," Ann. Surgical Oncol., vol. 23, no. 8, pp. 2586–2595, Aug. 2016.
47. G. H. KleinJan et al., "Fluorescence guided surgery and tracer-dose, fact or fiction?" Eur. J. Nucl. Med. Mol. Imag., vol. 43, no. 10, pp. 1857–1867, Sep. 2016.
48. M. N. van Oosterom et al., "U-SPECT-BioFluo: An integrated radionuclide, bioluminescence, and fluorescence imaging platform," EJNMMI Res., vol. 4, p. 56, Oct. 2014.
49. N. Van Den Berg et al., "Hybrid tracers for sentinel node biopsy," Quart. J. Nucl. Med. Mol. Imag., vol. 58, no. 2, pp. 193–206, Jun. 2014.
50. M. N. van Oosterom, H. G. van der Poel, N. Navab, C. J. H. van de Velde, and F. W. B. van Leeuwen, "Computer-assisted surgery: Virtual- and augmented-reality displays for navigation during urological interventions," Current Opinion Urol., vol. 28, no. 2, pp. 205–213, Mar. 2018.
51. O. R. Brouwer et al., "Feasibility of intraoperative navigation to the sentinel node in the groin using preoperatively acquired single photon emission computerized tomography data: Transferring functional imaging to the operating room," J. Urol., vol. 192, no. 6, pp. 1810–1816, Dec. 2014.

52. *V. Cuplov, I. Buvat, F. Pain, and S. Jan, "Extension of the GATE Monte–Carlo simulation package to model bioluminescence and fluorescence imaging," Proc. SPIE, vol. 19, no. 2, Feb. 2014, Art. no. 026004.*
53. *H. G. Kang, S. H. Song, Y. B. Han, K. M. Kim, and S. J. Hong, "Lens implementation on the GATE Monte Carlo toolkit for optical imaging simulation," J. Biomed. Opt., vol. 23, no. 2, Feb. 2018, Art. no. 026003.*
54. *C. G. Ethun and K. A. Delman, "The importance of surgical margins in melanoma," J. Surgical Oncol., vol. 113, no. 3, pp. 339–345, Mar. 2016.*
55. *S. B. Ravi and S. Annavajjula, "Surgical margins and its evaluation in oral cancer: A review," J. Clin. Diagnostic Res., vol. 8, no. 9, pp. ZE01–ZE05, Sep. 2014.*
56. *E. Sadot et al., "Resection margin and survival in 2368 patients undergoing hepatic resection for metastatic colorectal cancer: Surgical technique or biologic surrogate?" Ann. Surg., vol. 262, no. 3, pp. 476–485, Sep. 2015.*
57. *S. Yamada et al., "Estimation of the width of free margin with a significant impact on local recurrence in surgical resection of oral squamous cell carcinoma," Int. J. Oral Maxillofacial Surg., vol. 45, no. 2, pp. 147–152, Feb. 2016.*
58. *T. Wendler, J. Traub, S. I. Ziegler, and N. Navab, "Navigated three dimensional beta probe for optimal cancer resection," in Medical Image Computing and Computer-Assisted Intervention, vol. 9. Berlin, Germany: Springer, 2006, pp. 561–569.*
59. *K. Roessler, A. Becherer, M. Donat, M. Cejna, and I. Zachenhofer, "Intraoperative tissue fluorescence using 5-aminolevolinic acid (5-ALA) is more sensitive than contrast MRI or amino acid positron emission tomography ((18)F-FET PET) in glioblastoma surgery," Neurological Res., vol. 34, no. 3, pp. 314–317, Apr. 2012.*
60. *D. M. van Willigen et al., "Multispectral fluorescence guided surgery; A feasibility study in a phantom using a clinical-grade laparoscopic camera system," Amer. J. Nucl. Med. Mol. Imag., vol. 7, no. 3, pp. 138–147, Jul. 2017.*
61. *A. K. Glaser et al., "Light-sheet microscopy for slide-free nondestructive pathology of large clinical specimens," Nature Biomed. Eng., vol. 1, no. 7, p. 0084, Jul. 2017.*
62. *G. H. KleinJan et al., "Optimisation of fluorescence guidance during robot-assisted laparoscopic sentinel node biopsy for prostate cancer," Eur. Urol., vol. 66, no. 6, pp. 991–998, Dec. 2014.*
63. *O. R. Brouwer et al., "A hybrid radioactive and fluorescent tracer for sentinel node biopsy in penile carcinoma as a potential replacement for blue dye," Eur. Urol., vol. 65, no. 3, pp. 600–609, Mar. 2014.*
64. *A. Markus et al., "Sentinel lymph node biopsy in endometrial and cervical cancers using freehand SPECT–first experiences," Gynecological Surg., vol. 13, no. 4, pp. 499–506, Nov. 2016.*
65. *J. Müller et al., "Handheld single photon emission computed tomography (handheld SPECT) navigated video-assisted thoracoscopic surgery of computer tomography-guided radioactively marked pulmonary lesions," Interact. Cardiovascular Thoracic Surg., vol. 23, no. 3, pp. 345–350, May 2016.*
66. *N. C. Hall et al., "Intraoperative use of a portable large field of view gamma camera and handheld gamma detection probe for radioguided localization and prediction of complete surgical resection of gastrinoma: Proof of concept," J. Amer. College Surgeons, vol. 221, no. 2, pp. 300–308, Aug. 2015.*
67. *A. Azhdarinia, P. Ghosh, S. Ghosh, N. Wilganowski, and E. M. Sevick-Muraca, "Dual-labeling strategies for nuclear and fluorescence molecular imaging: A review and analysis," Mol. Imag. Biol., vol. 14, no. 3, pp. 261–276, Jun. 2012.*
68. *J. Kuil, A. H. Velders, and F. W. van Leeuwen, "Multimodal tumortargeting peptides functionalized with both a radio- and a fluorescent label," Bioconjug Chem., vol. 21, no. 10, pp. 1709–1719,Oct. 2010.*

69. *M. Schottelius et al., "Synthesis and preclinical characterization of the PSMA-targeted hybrid tracer PSMA-I&F for nuclear and fluorescence imaging of prostate cancer," J. Nucl. Med., vol. 60, no. 1, pp. 71–78, Jan. 2019.*
70. *C. Santini et al., "Evaluation of a fluorescent and radiolabeled hybrid somatostatin analog in vitro and in mice bearing H69 neuroendocrine xenografts," J. Nucl. Med., vol. 57, no. 8, pp. 1289–1295, Aug. 2016.*
71. *X. Wang, M. B. Aldrich, M. V. Marshall, and E. M. Sevick-Muraca, "Preclinical characterization and validation of a dual-labeled trastuzumab-based imaging agent for diagnosing breast cancer," Chin. J. cancer Res., vol. 27, no. 1, pp. 74–82, Feb. 2015.*
72. *K. Nur, S. Feng, C. Ling, and W. Ochieng, "Integration of GPS with a WiFi high accuracy ranging functionality," Geo-Spatial Inf. Sci., vol. 16, no. 3, pp. 155–168, 2013.*

CHAPTER 8

REVOLUTIONIZING (ROBOT-ASSISTED) LAPAROSCOPIC GAMMA TRACING USING A DROP-IN GAMMA PROBE TECHNOLOGY

Adapted from: van Oosterom MN, Simon H, Mengus L, Welling MM, van der Poel HG, van den Berg NS, van Leeuwen FWB

American Journal of Nuclear Medicine and Molecular Imaging, 2016, 6(1):1-17

ABSTRACT

In complex (robot-assisted) laparoscopic radioguided surgery procedures, or when low activity lesions are located nearby a high activity background, the limited maneuverability of a laparoscopic gamma probe (LGP; 4 degrees of freedom (DOF)) may hinder lesion identification. We investigated a DROP-IN gamma probe (DIGP) technology to be inserted via a trocar, after which the laparoscopic surgical tool at hand can pick it up and maneuver it. Phantom experiments showed that distinguishing a low objective from a high background source (1:100 ratio) was only possible with the detector faced >90° from the high background source. Signal-low-objective-to-background ratios of 3.77, 2.01 and 1.84 were found for detector angles of 90°, 135° and 180°, respectively, whereas detector angles of 0° and 45° were unable to distinguish the sources. This underlines the critical role probe positioning plays. We then focused on engineering of the gripping part for optimal DIGP pick-up with a conventional laparoscopic forceps (4 DOF) or a robotic forceps (6 DOF). DIGPs with 0°, 45°, 90°, and 135°-grip orientations were designed, and their maneuverability- and scanning direction were evaluated and compared to a conventional LGP. The maneuverability- and scanning direction of the DIGP was found highest when using the robotic forceps, with the largest effective scanning direction range obtained with the 90°-grip design (0-180° versus 0-111°, 0-140°, and 37-180° for 0°, 45° and 135°-grip designs, respectively). For the laparoscopic forceps, the scan direction directly translated from the angle of the grip design with the advantage that the 135°-gripped DIGP could be faced backwards (not possible with the conventional LGP). In the ex vivo clinical setup, the surgeon rated DIGP pick-up most convenient for the 45°-grip design. Concluding, the DIGP technology was successfully introduced. Optimization of the grip design and grasping angle of the DIGP increased its utility for (robot-assisted) laparoscopic gamma tracing.

INTRODUCTION

A core development in healthcare has been the integration of medical imaging technologies into diagnostic- and therapeutic workflows. Here, the (detailed) information gathered with these imaging technologies can provide preoperative insight into both anatomical (e.g. using computed tomography (CT), magnetic resonance (MR) imaging, or ultrasound (US)) and functional (e.g. using single photon emission computed tomography (SPECT), positron emission tomography (PET), (lympho)scintigraphy, or optical imaging (OI)) patient aspects. Aside from their preoperative use, some imaging modalities can also be used in an interventional setting (e.g. CT, US, gamma tracing and -imaging, or OI) where they can provide the surgeon with (real-time) information during the procedure.

To date, one of the key surgical guidance tools is the handheld gamma probe. The gamma probe is frequently used in radioguided surgery procedures where it provides the surgeon with feedback with respect to the localization of radioactive isotopes in the surgical field [1, 2]. Using the handheld gamma probe, the intraoperative situation can be directly correlated to preoperative imaging findings (SPECT or (lympho) scintigraphy) [3, 4]. Gamma probes have been mainly used for procedures such as sentinel node biopsy (isotope: ^{99m}Tc), radioguided intraoperative margin evaluation (isotopes: ^{99m}Tc and ^{111}In), radioguided seed localization (isotope: ^{125}I) and radioguided occult lesion localization (isotope: ^{99m}Tc) [1, 5-11].

Using different detector materials and different collimator geometries, gamma probes can be tailored to the procedure specific needs like field of view, sensitivity and energy window [1, 2]. The two main types of gamma probe detectors are: 1) scintillation detectors (e.g. (thallium-doped) sodium iodine (NaI(Tl)), (thallium-doped) cesium iodine (CsI(Tl)) or cerium-doped lutetium oxyorthosilicate (LSO)); and 2) semiconductor detectors (e.g. cadmium telluride (CdTe) or cadmium zinc telluride (CdZnTe)). Both types of detectors convert incoming gamma photons into an analog voltage signal that is eventually presented as an acoustic and numerical read-out. The attenuation properties of the collimation materials (e.g. lead, tungsten, gold or platinum), and the collimation thickness and -length can be used to fine-tune the directional specificity of gamma detection [1, 2].

Tissue attenuation of gamma signals like the 140 keV emission of ^{99m}Tc is limited and since there is no native background signal the readout module provides a very good signal-to-noise ratio. This feature generates a powerful tool enabling the non-invasive identification of small nodules, like sentinel nodes, using imaging technologies such as scintigraphy, SPECT(/CT) and gamma tracing. However, there also is a downside to this sensitivity, namely that the signal coming from small (diseased) nodules can be obscured by background signals coming

from the injection site or nearby anatomies harboring non-specific tracer accumulation (e.g. bladder, kidneys or liver). When these signals reside within the field of view of the detector, it may render the weaker nodules undistinguishable from the background. This effect is particularly limiting in an intraoperative setting when using a gamma probe. Attempts have been made to lower this radiation background, for example by temporary shielding the injection site [12]. Yet the most practical solution to this problem would be to focus the field of view of the detector of the gamma probe on the object of interest solely, whereby the detector is facing the object of interest, but shielded from the background signal. In open surgery procedures this can be accomplished for a great variety of anatomical locations as placement of the gamma probe can occur with six degrees of freedom (DOF; Figure 1a and 1d).

In an attempt to minimize the invasive nature of surgery, there has been a move from open to laparoscopic and, more recently, robot-assisted laparoscopic procedures [13]. To maintain radioguidance for e.g. the sentinel node biopsy procedure under these changed circumstances, extended laparoscopic versions of the traditional gamma probe have been created (Figure 1b) and introduced into the clinic [6, 14, 15]. Requirements for this type of laparoscopic gamma probes are that they can be inserted through a single trocar, that their length is sufficient to reach the lesion of interest (distance insertion point-lesion of interest is typically 0-20 cm), and that the resulting maneuverability covers an area with a radius of roughly 15-20 cm. Combined this means that the DOF of the laparoscopic gamma probe is much more restricted than those of its parental version for open surgery (Figure 1d and 1e). More specifically, applying the gamma probe technology in a laparoscopic setting reduces the DOF from six (three translational and three rotational), to four (one translational and three rotational) thereby limiting the detectability of small nodules close to large radioactive background sources [16, 17].

One way to compensate for the reduced maneuverability is to alter the angle of the detector relative to the tip from 0° to 90° [6]. Unfortunately, different anatomical locations may require different angles of detector placement, essentially meaning that in a single procedure with radioactive hotspots at different locations, which is common during sentinel node biopsy procedures in prostate cancer patients [18], detectors with different angles would be required. Another practical disadvantage of a laparoscopic gamma probe is that it temporarily blocks the trocar that could otherwise be used to insert surgical tools that are of value during the resection of these lesions of interest. As a consequence the laparoscopic gamma probe has to be moved in and out of the patient multiple times during the procedure, thereby limiting logistics [6, 7].

In case of robot-assisted laparoscopic procedures, the surgeon is sitting at a distant robot control console, rather than standing beside the patient in the sterile field. This means that a bedside assistant has to perform laparoscopic gamma tracing under verbal guidance of the surgeon. Next to the above-described

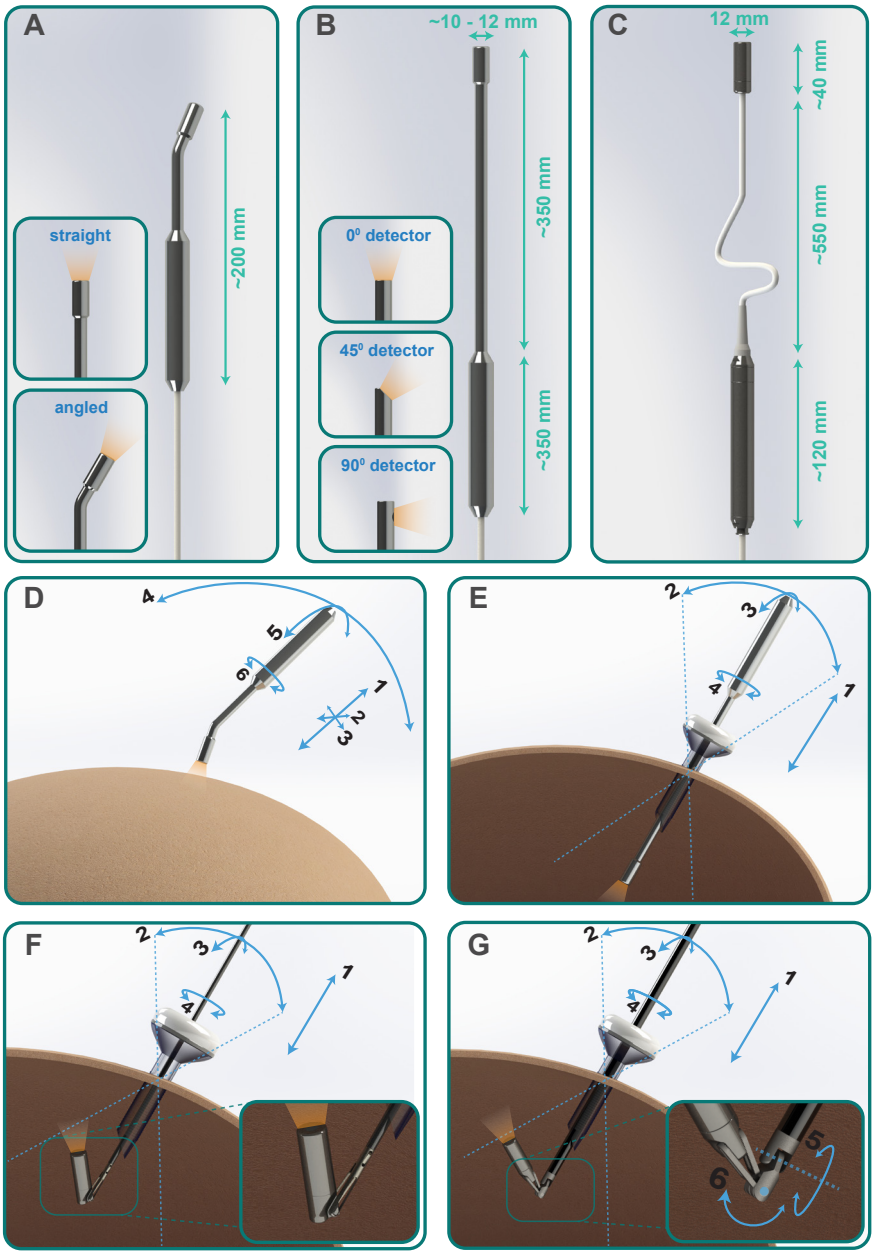

Figure 1. Degrees of freedom (DOF) of the various gamma probe setups. (a) *Typical gamma probe for open surgery.* ***(b)*** *Typical laparoscopic gamma probe with different detector angles available.* ***(c)*** *Novel DROP-IN gamma probe.* ***(d)*** *The open surgery gamma probe is placed in the wound area and provides movement with six unrestricted DOF.* ***(e)*** *The laparoscopic gamma probe is inserted via a trocar and is restricted to four DOF.* ***(f)*** *The DROP-IN gamma probe in combination with a non-articulated laparoscopic forceps. After insertion and picked-up, possible over different angles, the probe provides four DOF, inherent to the non-articulated forceps.* ***(g)*** *The DROP-IN gamma probe in combination with an articulated forceps. After insertion and picked-up, possible over different angles, the probe provides six DOF, inherent to the articulated forceps.*

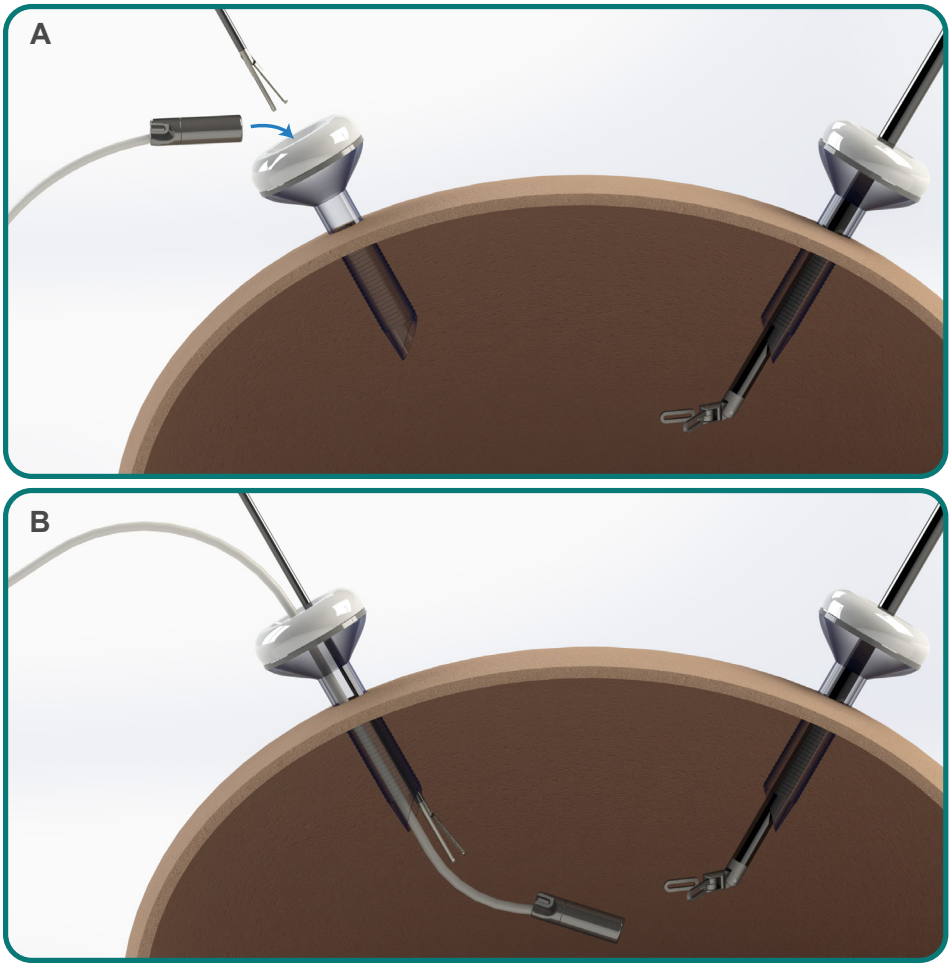

Figure 2. Insertion of the DROP-IN gamma probe through a trocar. (a) *The DROP-IN gamma probe is introduced into the abdominal cavity by the bedside assistant.* ***(b)*** *After insertion the operating surgeon grabs the DROP-IN probe with the available surgical tool.*

limitations for the laparoscopic surgical procedures, this aspect obviously limits the degree of control for the surgeon on the detection process during robot-assisted procedures. This may lead to confusing feedback, especially when using a laparoscopic gamma probe with an angled detector.

Using the DROP-IN ultrasound technology as an example [19], we reasoned that the use of a small-sized wired gamma probe that can be inserted ("dropped-in") through a trocar would provide a flexible mode of gamma tracing during (robot-assisted) laparoscopic procedures. Such a modality can be directly manipulated using the available surgical tools (Figures 1c, 1f, 1g, 2). Taking general engineering restrictions such as detector surface, shielding, trocar-diameter compatibility, cable thickness, and patient safety into account, we specifically focused on the engineering of the gripping technology for the DROP-IN gamma

probe. Of special interest were the modus of gripping and, in an attempt to reduce the influence of background signals within the probe field of view, the angle of gripping. Subsequently, we evaluated these different approaches in a phantom-, ex vivo clinical- and in vivo animal setting.

METHODS

DROP-IN gamma probe

A schematic outline of the DROP-IN gamma probe is given in Figure 1c. The detection and electronic principles of the DROP-IN gamma probe are similar to the standard open- and laparoscopic gamma probes of Eurorad S.A. (Eckbolsheim, France).

The engineering process focused mostly on the mechanical aspects of the DROP-IN gamma probe. Essentially, with the design of the DROP-IN gamma probe the standard gamma probe was split in two parts: the general setup remained very similar, though the fixation of the detector section to the rest of the gamma probe was changed from a rigid metal tube to a flexible cable. The head section of the DROP-IN gamma probe was designed with a diameter of 12.0 mm and a length of 39.8 mm. The detector in the head of the DROP-IN gamma probe consists of a 5.0 mm × 10.0 mm (diameter × length) CsI scintillation crystal coupled to a 25.0 mm^2 silicon photodiode. The circular collimation applied around the crystal was fabricated out of densimet 176, a tungsten-nickel-iron alloy. A 4.3 mm diameter biocompatible cable was used to connect the head of the DROP-IN gamma probe to the rest of the probe housing and to connect the total DROP-IN gamma probe to the control unit Europrobe 3 (Eurorad S.A.). The outer shells of the DROP-IN gamma probe were constructed of medical grade 316L stainless steel.

Design DROP-IN gamma probe prototypes

Surgical tool of choice

To ensure accurate, reproducible and intuitive gripping of the DROP-IN gamma probe, the grip structure was specifically designed to match a surgical tool of choice. From the tools frequently used in (robot-assisted) laparoscopic surgery, it was believed that, for this initial proof-of-concept study, the two below-described models would be most suitable for grasping larger objects like the DROP-IN gamma probe: 1) An articulated forceps used in robot-assisted laparoscopic surgery procedures, the da Vinci ProGrasp® forceps from the EndoWrist Graspers series (Intuitive Surgical Inc., Sunnyvale, CA, USA). This tool features a double wrist joint that contributes to a total of six DOF available for maneuverability of the DROP-IN gamma probe (Figure 1g); and 2) A non-articulated forceps that is used during laparoscopic surgical procedures (KARL STORZ Endoskope forceps, #33133 metal handle, #33300 metal outer sheath and #33310 ON forceps insert; KARL STORZ Endoskope GmbH & Co. KG, Tuttlingen, Germany). This laparoscopic

tool delivers four DOF for maneuverability of the DROP-IN gamma probe (Figure 1f).

DROP-IN gamma probe gripping part design

3D mechanical computer-aided design (CAD) software SolidWorks (Dassault Systèmes SA, Vélizy-Villacoublay, France) was used to design and optimize the geometries for the gripping process. Limiting these designs were: 1) *The 12 mm trocar inner diameter:* Every structure on top of, or attached to the DROP-IN gamma probe was bound to a maximal outer diameter of 12 mm; 2) *The <5 mm cable diameter:* Based on availability, we were constrained to a specific biocompatible cable with a 4.3 mm diameter. Since the maximal diameter of the gripping piece is 12 mm, the current cable occupies approximately 36% (4.3/12 mm) of the total grip diameter. In the future this cable diameter may become smaller; 3) *Cable placement:* Due to the attachment to the electronics inside the DROP-IN gamma probe, the cable had to originate from the central probe axis, preventing a direct off-center connection; 4) *Matching forceps designs*: The grip design had to be specifically tailored to the two forceps of interest. The grip design had to ensure a reproducible pickup with an accurate and stable grip with limited translational and rotational movement of the probe with respect to the forceps; 5) *Intuitive and facile probe pick-up by the operating surgeon:* The grip structure had to be designed in such a way that the intraoperative application time was short and the surgeon user-experience was positive for both probe pick-up and control; 6) *Stainless steel processing compatibility:* The grip design had to be fabricated form medical grade 316L stainless steel; 7) *Patient safety:* The grip design has to have a smooth surface without any sharp edges or structures that can potentially lead to unintentional tissue damage during the surgical procedure or when retracting the DROP-IN gamma probe after its use; 8) *Sterilization procedure:* Both the DROP-IN gamma probe geometry and the fabrication process used should allow for sufficient probe sterilization and decontamination; 9) *Maneuverability:* The gripping position should allow for flexible detector head placement during surgery covering a scanning range as large as possible.

During the design process we followed specific development steps taking into account the above-mentioned limitations (a schematic overview is shown in Figure 3): 1) An off-center gripper position, where the probe cable is directed from an internal center point to an offcenter exit, was developed. This allows for an on-center cable attachment to the electronics inside, while providing clearance around the gripping structure facilitating convenient probe pick up (Figure 3a); 2) The shape of the gripper was optimized with oblique angles to allow for a stable, reproducible, and conveniently grasped grip (Figure 3b); 3) To get a more robust design without any sharp angles, and to promote better probe extraction through the trocar, the optimized gripper conformation was integrated in a solid block (Figure 3c and 3d); 4) To further improve the ease and reproducibility of gripping, the walls surrounding the grip were modified so that the forceps would

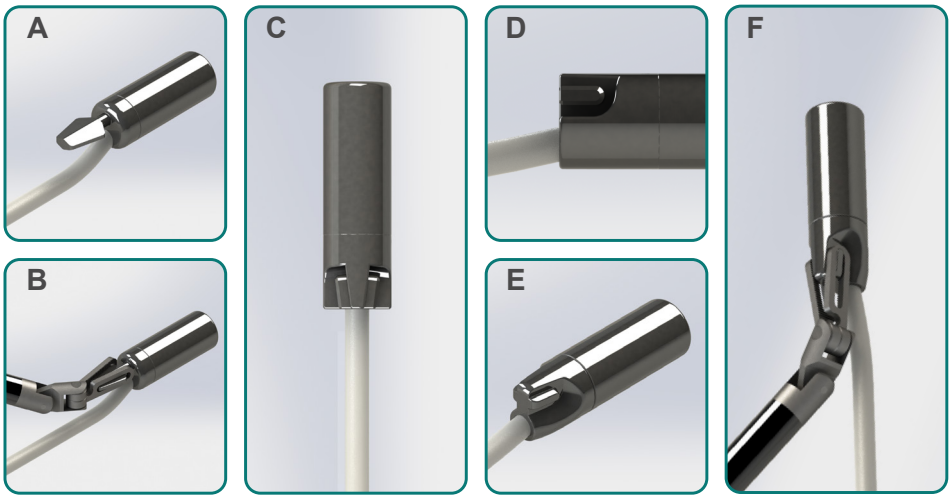

Figure 3. Grip design development steps. (a) *Off-center gripper and off-center cable exit, facilitating convenient probe pick-up, while maintaining on-center cable origin inside.* ***(b)*** *Optimizing the shape of the gripper to the forceps, providing a convenient and reproducible probe pick-up.* ***(c)*** *Integration of the design in robust solid block design without sharp edges (view 1).* ***(d)*** *Integration of the design in solid block (view 2).* ***(e)*** *Modification to the walls surrounding the grip structure, promoting ease and reproducibility of gripping.* ***(f)*** *0° grip structure displayed when grasped by the forceps.*

lock itself onto the central gripping structure (Figure 3e). In addition, these rounded geometries should facilitate probe extraction through the trocar even further; and 5) The grip design was modified so that it could be applied in angles ranging between 0° and 135° with respect to the detector in the head of the DROP-IN gamma probe.

DROP-IN gamma probe gripping part generation

For initial tests of the grip structure, prototypes were 3D printed in either polylactic acid (PLA) or acrylonitrile butadiene styrene (ABS) plastics. The choice of material was simply a matter of 3D printer availability and did not impact the designed structures.

PLA prototypes were printed with a slightly modified 3D Touch 3D printer (Bits from Bytes, 3D Systems Inc., Rock Hill, USA) and the accompanying Axon 2 slicer software (Bits from Bytes, 3D Systems Inc., Rock Hill, USA). Extruder temperatures were set ranging from 195-200°C with print resolution at 0.125 mm for the grip designs.

ABS prototypes were printed on the Dimension Elite 3D printer (Stratasys Ltd., Eden Prairie, MN, USA), with accompanying CatalystEX 4.4 slicer software (Stratasys Ltd., Eden Prairie, MN, USA). Designs were printed at temperatures of 260°C and a print resolution of 0.017 mm. The plastic prototypes were printed in two parts: 1) A generic hollow base, used for all prototypes, where the

collimation and detector are normally located; and 2) The specifically designed gripping part.

To further approximate the functioning of a working DROP-IN gamma probe, the probe cable was put into place and the weight was increased by filling the hollow base with lead. The resulting plastic prototypes weighed approximately 11 g. Note that these plastic prototypes did not house the detection electronics.

After initial plastic prototype evaluation, the most promising designs were fabricated out of stainless steel by Eurorad S.A. to test if the design allowed for metal powder sintering techniques. The real functioning DROP-IN gamma probe prototypes weighed about 36 g each.

Evaluation process

Gamma probe detection angle evaluation

To evaluate the effect of gamma probe maneuverability on the resolvability of two radioactive sources in close proximity to each other, a "1 cm-grid-phantom" setup was used [20].

Two ^{99m}Tc based radioactive sources were made to resemble a typical injection site and nearby lymph node for a case of prostate cancer for which a 100:1 ratio in tracer uptake was chosen. The background source (resembling the injection site) was prepared in an entirely and homogenously filled 500 µL Eppendorf tube containing ~200 MBq of radioactivity calibrated for the time of study. The low intensity objective (resembling the lymph node) was prepared with ~2 MBq of radioactivity in a 200 µL Eppendorf tube calibrated for the time of study. To immobilize the height of the radioactivity of this low intensity objective in the tube, the tube was filled 67% with a green colored resin (AG® Anion Exchange Resin, Life Science, Bio-Rad Laboratories B.V. Veenendaal, The Netherlands) and subsequently topped with a fitting piece of tissue paper containing the required radioactivity after which a final layer of resin filled the remaining space.

Two different setups were used to investigate the effect of different gamma-ray detection angles. In the first setup both the ~2 MBq source and the gamma detector were fixed on the grid with a 1 cm distance between the source and the front of the probe (Figure 4a1). The ~200 MBq source was then moved in half a circle (0-180 degrees) with a fixed radius of 5 cm with respect to the ~2 MBq source. This setup simulated the movement of the gamma probe around a hot nodule hindered by a background signal and is referred to as the "background-angle-setup".

In the second setup the gamma detector head was fixed at five different angles (0°, 45°, 90°, 135° and 180°) while both radioactive sources were moved passing the detector with the same 5 cm distance between both sources (Figure 4b1). The distance from the gamma probe head to the source path was 1 cm.

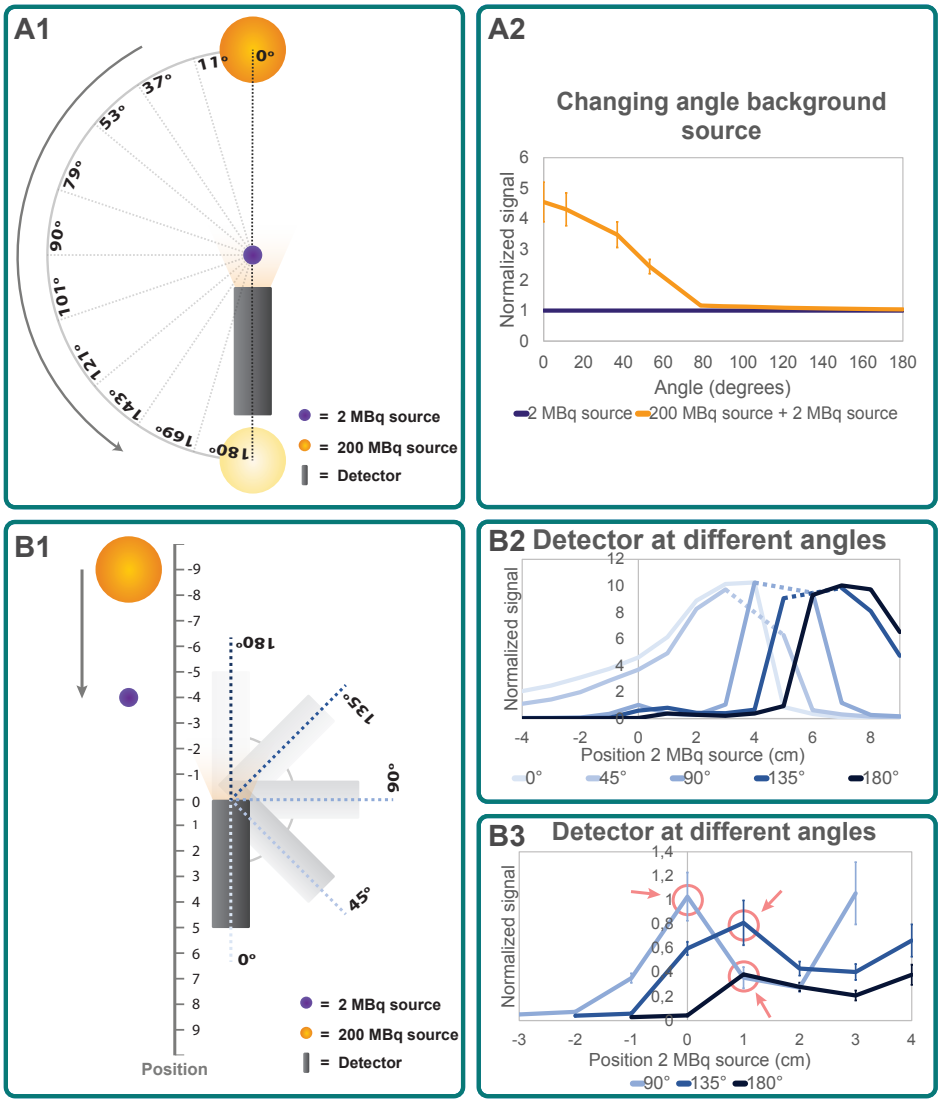

Figure 4. Gamma detector angle evaluation in the background-angle-setup (a) and the detector-angle-setup (b). (a1) *Schematic image of phantom measurements setup. The ~2 MBq source is at a fixed distance of 1 cm with respect to the front of the detector. The ~200 MBq source is at a fixed distance of 5 cm with respect to the ~2 MBq source.* ***(a2)*** *Resulting gamma probe signal plotted versus the angle of the ~200 MBq source. Error bars plotted with the orange curve indicate ±1 standard deviation.* ***(b1)*** *Schematic image of phantom measurements setup. The ~200 MBq and ~2 MBq sources have a fixed distance of 5 cm. The fixed distance from the detector to the source path is 1 cm.* ***(b2)*** *Resulting gamma probe signal plotted for five different detector angles (0°, 45°, 90°, 135° and 180°) when the two sources move along the position-axis.* ***(b3)*** *Zoom-in on the additional peak detected (indicated with red circle and arrow) when the detector is placed at 90°, 135° and 180°. Error bars indicate ±1 standard deviation.*

This setup provided a quantifiable form of feedback on the relation between the angle of detector placement and the influence of a background signal, and what influence this effect has on the resolvability of the two separate sources and is referred to as the "detector-angle-setup".

The readout for both setups was based on the count rates reported by the Europrobe 3 control unit. For every measurement the count scale was set to 10,000 and a counting time of 1 s was selected. For every evaluated point, the mean was taken of three consecutive 1 s measurements. Every complete measurement session was performed in triplicate with three different radioactive source pairs. All signals measured were corrected for radioactive decay with respect to the initial activity. For presenting the data, every separate session was normalized to the signal measured with only the low intensity object present at a 1 cm distance in front of the gamma probe detector head. These resulting signals were used to calculate the mean and standard deviation as shown in the graphs.

DROP-IN gamma probe prototype evaluation

A basic laparoscopic phantom was fabricated to simulate the setup of a (robot-assisted) laparoscopic prostatectomy procedure (Figure 5a). The phantom consisted of a 38.7 cm diameter, 46.0 cm long PVC tube with a wall thickness of 1.1 cm. The bottom was removed to create a level surface inside the phantom, resulting in a phantom height of 31.0 cm. Five pieces of ~3 mm thick rubber were fitted to mimic the stretch nature of skin and subsequently, holes were punctured and five 12 mm trocars were put in to place.

Initial evaluation of the designed and printed plastic DROP-IN gamma probe prototypes was performed with the laparoscopic phantom using a motorized articulated forceps (Figure 5). The generated motorized forceps setup was similar as described before (Integration of force feedback into minimally invasive robotic surgery 2007, *https://www.youtube.com/watch?-v=OtFy1AF8SbQ*) and consisted of: 1) A Pro-Grasp® forceps (Intuitive Surgical Inc.); 2) Four 12 V direct current (DC) transmission electro motors (20G-150, Igarashi Motoren GmbH, Burgthann-Ezelsdorf, Germany); 3) Four 3D printed coupling rings to couple the torque of the motor shaft to the four forceps wheels; 4) An acrylic plastic housing to mount all components together; and 5) A small electric circuit build to control all four forceps wheels in two directions.

After the phantom evaluation, the plastic prototypes were evaluated by a surgeon (HGvdP) who is specialized in (robot-assisted) laparoscopic radioguided surgery procedures. Evaluation of the designed prototypes was performed ex vivo with the Prograsp® forceps in combination with the da Vinci Si surgical robot system (Intuitive Surgical Inc.) and the KARL STORZ Endoskope laparoscopic forceps (KARL STORZ Endoskope GmbH & Co KG) in a typical operation room setup.

In both the phantom and ex vivo surgical setting, the grip structure of

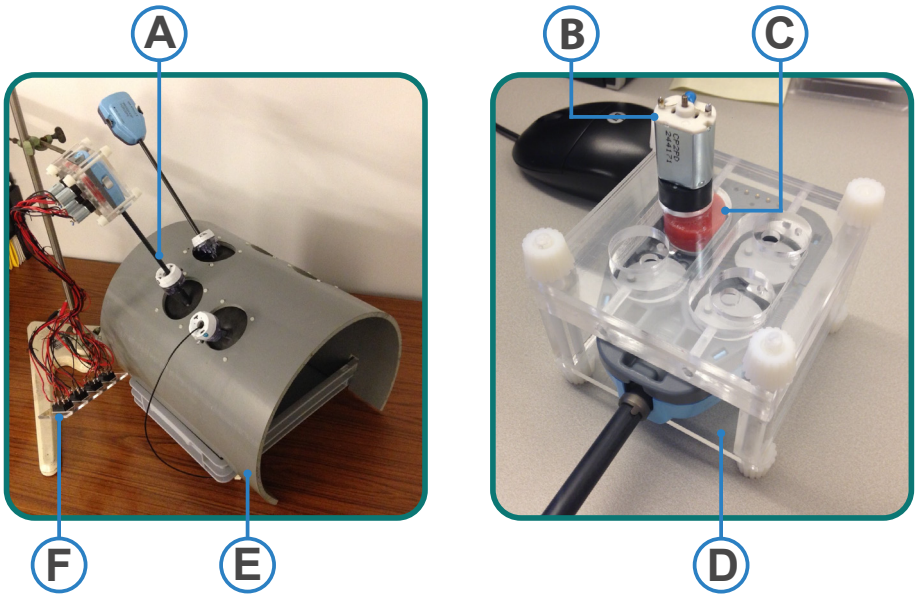

Figure 5. Laparoscopic phantom with motorized articulated forceps. (a) *Articulated forceps.* ***(b)*** *Electro motors.* ***(c)*** *Red PLA coupling rings.* ***(d)*** *Acrylic housing.* ***(e)*** *Laparoscopic phantom.* ***(f)*** *Electric control circuit.*

every designed prototype-in combination with the respective forceps-was evaluated for: 1) *Convenience of the probe pick-up:* This was rated from 'very poor' (--), to 'poor' (-), to 'medium' (o), to 'convenient' (+), to 'very convenient' (++); 2) *Scanning range available for gamma ray detection:* Multiple orientations of probe pick-up were evaluated. The axial axis, in-line with the gamma probe scanning direction, was defined as the 0° axis (see also Figure 4a1). The orthogonal axis, perpendicular with the gamma probe scanning direction, was defined as the 90° axis (see also Figure 4a1). The orientation of pick-up influences the resulting scanning range available for gamma ray detection. This was measured in degrees with respect to the axial axis; and 3) *Probe fixation in forceps grip:* Both the fixation of the grasped DROP-IN probe in the forceps and the reproducibility of this grip was evaluated.

8

First ex vivo and in vivo evaluation of a fully functioning DROP-IN gamma probe prototype

In addition to the evaluations as described above, a functioning DROP-IN gamma probe prototype was fabricated and used for a first ex vivo human tissue- and in vivo animal model evaluation. This DROP-IN gamma probe incorporated the first grip design prototype and was labeled as design 0 (Table 1).

Design 0 was firstly evaluated in an ex vivo clinical setup (Figures 6 and 7a). This setup consisted of a radioactive prostate and a radioactive sentinel node at an approximate distance of 2 cm (approximate radioactivity ratio: 100:1).

These human tissue samples were obtained from a patient that underwent a robot-assisted radical prostatectomy combined with sentinel node biopsy and an extended lymph node dissection as previously described [13]. Next to a gamma tracing evaluation in this setup, the surgeon evaluated the above-described three criteria (convenience of probe pick-up, scanning range, and probe fixation in the forceps grip).

Secondly, design 0 was evaluated in an in vivo porcine animal model (Figure 7b). Due to the facility-restricted use of radioactive sources in animals, evaluation of the DROP-IN gamma probe purely focused on evaluation of the convenience of probe pick-up, probe maneuverability and probe fixation in the forceps.

RESULTS

Gamma probe detection angle evaluation

In Figure 4a2 the results are shown for the measurements of the background-angle-setup, where a high-background source was moved around a fixed detector head-objective setup. The orange line was obtained when both the background and the objective sources were present in the setup. These measurements clearly underline how background signal positions in a <75° angle relative to the gamma probe detector head can lead to background counts that significantly exceed those emitted by the objective alone (blue line). In Figure 4b2 the measurements performed in the detector-angle-setup are presented. In the areas presented by the dashed line the detector was saturated. Only with the >90° positioning of the detector (90°, 135°, and 180°) a distinct peak of the ~2 MBq objective could be differentiated from the background signal (Figure 4b3). Calculating the ratio between the low objective peak and the lowest signal in-between the low objective peak and high background peak, the signal-low-objective-to-background ratio, resulted in 3.77, 2.01 and 1.84 for detector angles of 90°, 135° and 180°, respectively. This result further underlines the influence the angle of the detector-placement has on the diagnostic accuracy of gamma detection. Combined these results suggest that being able to turn the gamma probe detector head away from a high activity background source in an angle exceeding 90° improves the detection of a low activity objective.

DROP-IN gamma probe prototype evaluation

Table 1 provides an overview of the evaluated DROP-IN gamma probe prototype designs. During the evaluation process a 0° laparoscopic gamma probe served as reference.

Since the gamma photon scanning section is located at the front end of the probe head, and the most commonly used (laparoscopic) gamma probes have a 0° scanning configuration, we designed and fabricated the initial DROP-IN gamma probe with an axial grip design: design number 0. From the ex vivo and

Table 1. Overview of DROP-IN gamma probe grip design evaluation.

	Reference	Prototype					
	Rigid laparoscopic gamma probe	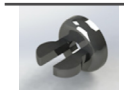 DROP-IN grip design 0	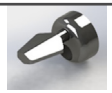 DROP-IN grip design 1	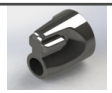 DROP-IN grip design 2	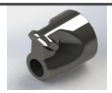 DROP-IN grip design 3	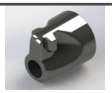 DROP-IN grip design 4	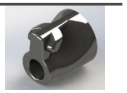 DROP-IN grip design 5
Cable exit	Center	Center	Off-center	Off-center	Off-center	Off-center	Off-center
Rounded edges	Yes	Yes	No	Yes	Yes	Yes	Yes
Grip location	N/A	Center	Off-center	Off-center	Off-center	Off-center	Off-center
Grip orientation (degrees)	N/A	0	0	0	45	90	135 (*potential for additional 45*)
Convenience of pick-up with forceps	N/A	-	+	+	++	+	+
Scanning direction with rigid probe (degrees)	0, 45 or 90	N/A	N/A	N/A	N/A	N/A	N/A
Scanning direction with non-articulated forceps (degrees)	N/A	0	0	0	45	90	135 (*potential for additional 45*)
Scanning direction with articulated forceps (range, degrees)	N/A	0-125	0-111	0-111	0-140	0-186 (*effective range: 0-180*)	37-235 (*effective range: 37-180*)

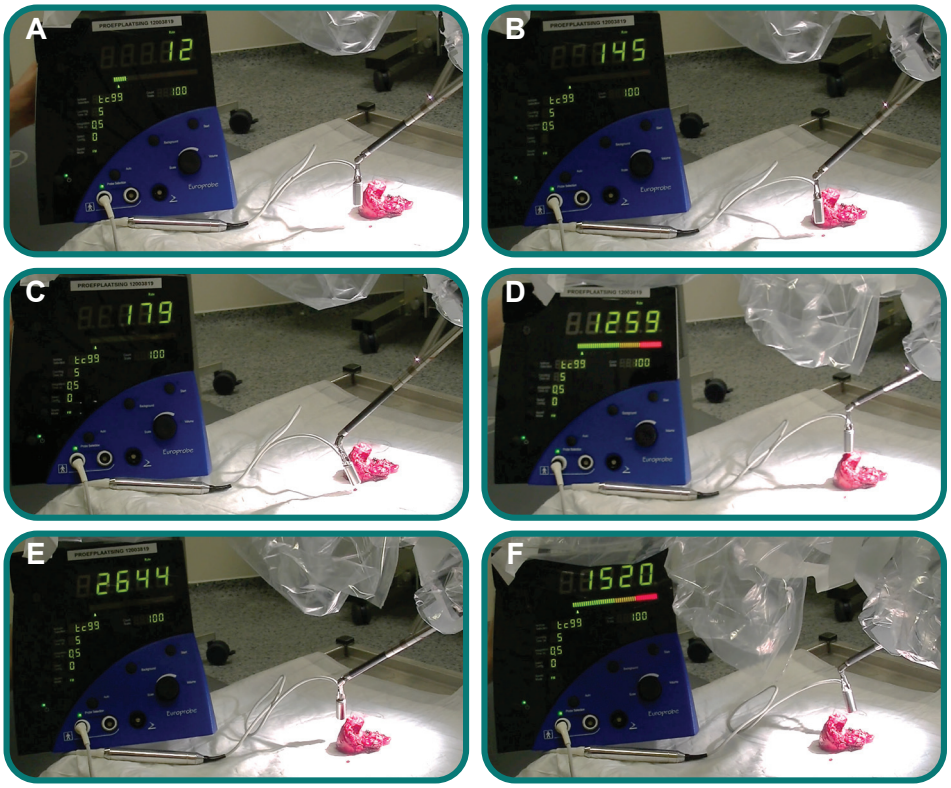

Figure 6. Maneuvrability of the DROP-IN gamma probe evaluated in ex vivo tissue setup with prototype design 0. (a-c) *DROP-IN gamma probe gamma tracing of a tiny sentinel node that is lying directly next to the prostate. (**d-f)** DROP-IN gamma probe gamma tracing of the prostate. By changing the angle under which the DROP-IN gamma probe looks at the radioactive sources, these can be discriminated from each other.*

in vivo experiments of this DROP-IN gamma probe, we found that gripping could be challenging. As can be seen in Figure 7, this was due to the central location of the connector cable, partly obstructing facile forceps placement over the grip design. Therefore, the resulting DROP-IN gamma probe prototype was rated 'poor' (-) for probe pick-up. When picked-up with the nonarticulated forceps, this DROP-IN probe design gave the same maneuverability as the rigid laparoscopic gamma probe. However, in combination with the articulated forceps, maneuverability was largely extended due to the extra DOFs available (see Figure 6). While both the rigid laparoscopic gamma probe and the nonarticulated forceps DROP-IN probe combination had a fixed scanning direction of 0°, the extra DOF with the articulated forceps allowed for a variable scanning direction of 0-125° with respect to the axial axis. Moreover, the fixation and reproducible gripping of this DROP-IN gamma probe were found challenging due to the round shapes of the grip design. The fixation and reproducibility errors were found to be ~8° and ~1 mm, respectively.

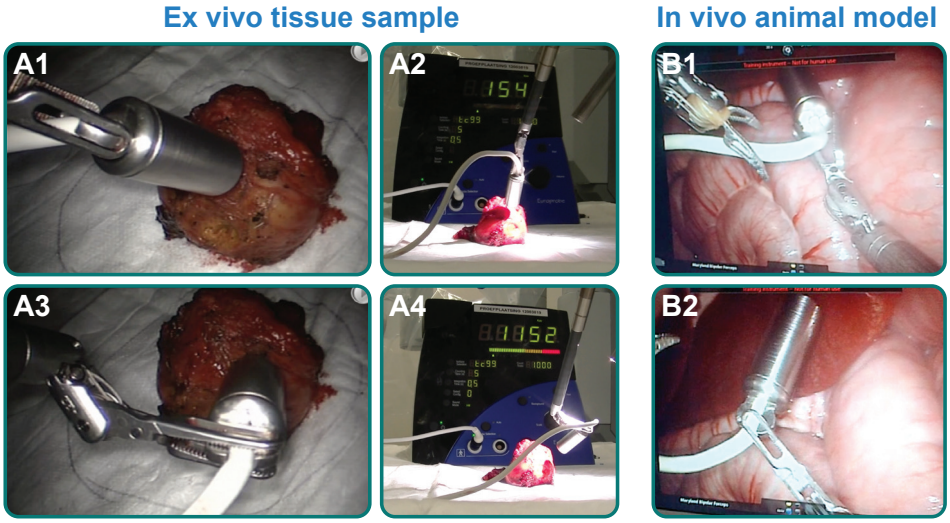

Figure 7. Ex vivo and in vivo gripping of DROP-IN gamma probe design 0. (a1-a2) *0° grip facing the radioactive prostate using the articulated forceps as seen when looking through the surgical goggles (surgeon view; a1) or when looked at from the side (filmed by camera; a2).* ***(a3-a4)*** *90° grip facing the radioactive prostate using the articulated forceps as seen when looking through the surgical goggles (surgeon view; a3) or when looked at from the side (filmed by camera; a4).* ***(b1-b2)*** *In vivo (porcine model), gripping and maneuverability of prototype design 0 were evaluated using an articulated forceps (surgeon view).*

The main focus of grip design 1, compared to design 0, was to optimize the central gripping structure for convenience of probe pick-up (see Figure 3a-b). This was done using a (double sided) pyramid shaped geometry that allowed the forceps to slide to a fixed end-position. To maintain a diameter <12 mm the cable had to be directed from the central probe axis to an off-center exit point at the probe back end. The resulting DROP-IN gamma probe prototype was rated 'convenient' (+) for probe pickup. The scanning range delivered with the nonarticulated forceps setup was equal to that of design number 0 (0° with respect to the axial axis). The scanning range delivered with the articulated forceps setup was found to be 0-111° with respect to the axial axis. The fixation and reproducibility errors were found to be ~5° and ~1.5 mm, respectively. During probe retraction through the trocar, this grip design could act as a small hook on the trocar, hindering the extraction process.

Grip number 2 was designed to further reduce the fixation and reproducibility errors, while improving the retraction process and maintaining usability (see Figure 3c-e). This was achieved using tightly fitted oblique walls surrounding the grip structure, which allowed the forceps to always slide back to a fixed end-position. To better place these oblique walls, and at the same time increase the mechanical durability of the grip structure, the design was integrated into a solid block. The resulting DROP-IN gamma probe prototype was still rated 'convenient' (+) for probe pick-up by the surgeon. The scanning range delivered

with both the nonarticulated forceps and the articulated forceps setup was equal to that of design number 1 (0° and 0-111° with respect to the axial axis, respectively; Figure 8b1 and 8b1). With this design the fixation and reproducibility errors were reduced to a negligible amount of ~0° and ~0 mm respectively. Probe retraction through the trocar was found to be more convenient compared to design number 1.

After optimization of the grip convenience, fixation and reproducibility, the goal of design number 3, 4, and 5 was to optimize the scanning range obtained with the DROP-IN gamma probe. By changing the grip orientation with respect to the axial axis, the three designs delivered 45° (design 3), 90° (design 4) and 135° (design 5) versions of the DROP-IN gamma probe. For all three designs the grip structure and the oblique walls had to be tailored to the specific forceps orientation and openings-angle, resulting in minor variations of the design. Prototype number 3 was rated 'very convenient' (++) for probe pick-up, due to the easiest approach. Prototypes 4 and 5 were rated 'convenient' (+) for probe pick-up. Grasped with the non-articulated forceps, design number 3 and 4 showed a scan direction of 45° and 90°, respectively. Design number 5 allowed for a 135° scan direction, allowing to position the gamma probe detector head in a backwards direction (Figure 8b4). Although the grip structure of design number 5 was not specifically designed for two-way grasping, it was also possible to grasp this DROP-IN gamma probe prototype in a second direction of 45°. If further developed, this may add an extra functionality to this design: The ability to look in both a forward and backwards direction. In combination with the articulated forceps, the scanning range for these three designs was found to cover 0-140°, 0-186°, and 37-235° with respect to the axial axis (Figure 8c2-c4), respectively. With the 135° grip orientation it was thus no longer possible to scan in a straight forward 0° direction. Figure 8a displays the obtained scanning ranges made possible with the different rigid laparoscopic gamma probe versions.

As designed, all DROP-IN gamma probe prototypes fitted through the 12 mm trocar. The use of the biocompatible cable and the medical grade stainless steel housing allowed the DROP-IN probe to be sterilized with ethylene oxide (ETO) sterilization methods. Complete sterilization results in overcoming the need for e.g. sterile draping which can interfere with reproducible and facile gripping of the probe.

DISCUSSION

The application of the current rigid laparoscopic gamma probes has proven to be challenging during complex surgical procedures such as sentinel node biopsy for prostate cancer [13] and gastrointestinal cancer [16,17] or radioguided localization of ^{111}In-prostate specific membrane antigen (PSMA) positive lesions [21]. One of the main limitations are the limited DOF that the current laparoscopic gamma probe setup has, rendering it difficult to accurately place the gamma

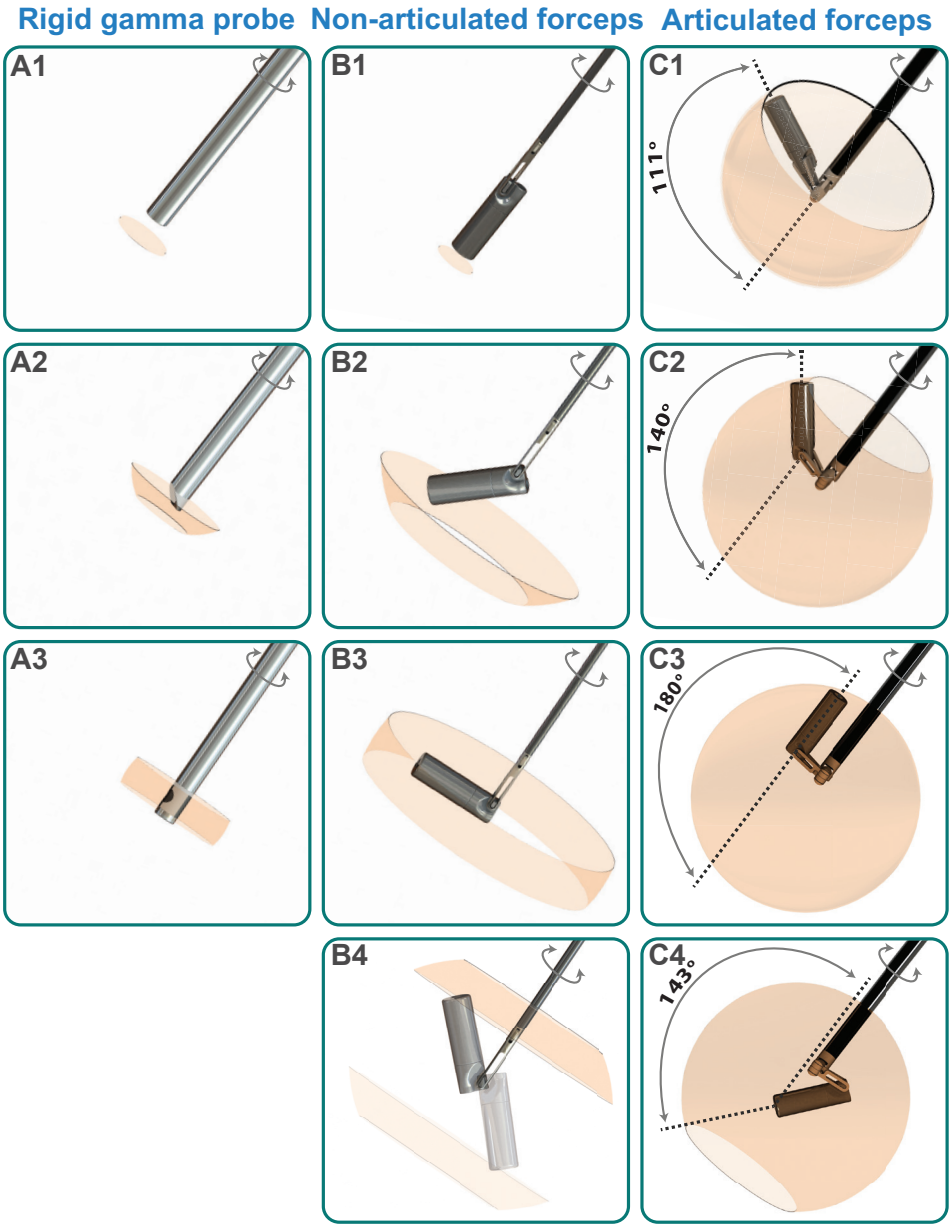

Figure 8. Effective scanning range available with the rigid laparoscopic gamma probe versions (a) and the different DROP-IN gamma probe designs in combination with the laparoscopic non--articulated forceps (b) and the robotic articulated forceps (c). (a1-a3) *Illustrate the 0°, 45° and 90° laparoscopic gamma probe versions respectively.* ***(b1-b4)*** *Illustrate design number 2 (0° grip), 3 (45° grip), 4 (90° grip) and 5 (135° grip) in combination with the non-articulated forceps, respectively. For design number 5, an additional 45° application is shown in transparent.* ***(c1-c4)*** *Illustrate design number 2 (0° grip), 3 (45° grip), 4 (90° grip) and 5 (135° grip) in combination with the articulated forceps, respectively. In all these articulated forceps combinations the effective scanning range was found to comprise 0-111°, 0-140°, 0-180° and 37-180° respectively.*

detector. In this paper, the phantom experiments with the background-angle-setup and the detector-angle-setup clearly illustrate the diagnostic benefit of detector maneuverability with respect to a high and low radiation source. Being able to turn the detector away from the high activity background source (typically produced by the injection site) allowed us to distinguish the low activity objective. Based on these results we therefore hypothesize that a small sized DROP-IN gamma probe, in combination with the right laparoscopic surgical tools can have great benefits in laparoscopic radioguided surgery applications.

Similar to the small sized DROP-IN ultrasound probe presented in the field of intra-abdominal ultrasound [19], the DROP-IN gamma probe was designed to be inserted through a trocar, after which it can be picked-up and manipulated by the (robotic) tools of the operating surgeon, as was illustrated in the porcine animal model. The two laparoscopic tools used for this proof-of-concept showed a clear difference in the DROP-IN probe maneuverability. The greatest DOF, and therefore maneuverability, was found with the articulated ProGrasp® forceps, allowing to scan (with grip design number 4) in both a forward 0° direction (for scanning while approaching the surgical site) and a backwards 180° direction (for placing the DROP-IN gamma probe in between the high background objective and low objectives), while also allowing the directional scanning angles in between (1-179°).

Although instruments with more DOF will give higher flexibility, the DROP-IN gamma probe can also be of value in combination with more conventional non-articulated laparoscopic tools. For example, the combination of grip design number 5 and the non-articulated KARL STORZ Endoskope laparoscopic forceps allowed backwards directed scanning (135°), which is impossible with current rigid laparoscopic gamma probes. This 135° scanning direction facilitates the placement of the DROP-IN gamma probe in-between high activity background signals and low activity objectives, while possibly allowing forward facing detection (45°) when using the reversed gripping modus.

In the ideal situation gamma probes have no limitations on maneuverability, harboring the freedom to scan in every direction of the abdominal cavity, focusing on (low) objective radiation while avoiding (high) background radiation. In this study, only the angle of the grip was changed with respect to the DROP-IN gamma probe, grasping the entire probe over different angles and so creating an as-large-as-possible scan direction range. Just as with the rigid laparoscopic gamma probe, it would also be possible to place the detector itself at different angles in the gamma probe [1,2]. Adjusting this element of the probe could open up additional interesting possibilities; for example: if a 45° detector placement would be combined with the 135° probe grip, that could also be grasped over 45°, it would be possible with the nonarticulated laparoscopic forceps used in this study, to scan in a direction of 0° and 180° with the same DROP-IN gamma probe. The DROP-IN gamma probe technique as described in this study, is therefor not limited to the tools used in this study. Slight adaptations to the grasping

part will allow versions of the DROP-IN gamma probe to complement other dedicated surgical tools.

Because the DROP-IN gamma probe technology is controlled with the surgical tools the surgeon has at hand during the procedure, positioning should be intuitive directly following the movement of the surgical tools. The impact of this feature will be most prominent in robot-assisted laparoscopic procedures where the surgeon is positioned away from the operating table. Additionally, during robot-assisted laparoscopic procedures, the surgeon has often three robot arms available with which can be worked. With these three arms, the arm holding the DROP-IN gamma probe can be positioned in such a way that the surgeon can monitor the removal of the target lesion in real-time as performed by the two other arms. The latter is similar to that used during open surgery [22]. Contrary to the rigid laparoscopic gamma probe, with the <5 mm diameter cable of the DROP-IN probe it will be possible to share a trocar (typically 12-14 mm) with different laparoscopic tools (typical diameter: 6 mm). This avoids the need of an extra trocar, and allows the probe to stay in the abdominal cavity during the entire procedure. This particular feature helps to further minimize the impact on the surgical procedure.

Besides providing acoustic radioguidance, (laparoscopic) gamma probes have also been used to produce a freehand SPECT scan in the operating room for example during parathyroidectomy and sentinel node biopsy procedures for breast and head and neck cancer [23-27]. In this technique a surgical navigation or tracking system is used to record every position of the gamma probe (or small handheld gamma camera) during scanning, thereby linking the measurements found to the corresponding location in space. To perform a freehand SPECT scan, it is important that sufficient information is acquired from different positions and orientations with respect to the tissue of interest [28]. For this reason, we imagine that the availability of DROP-IN gamma probes may enable a superior form of intra-abdominal freehand SPECT [29].

The DROP-IN probe technology isn't restricted to gamma radiation only, but can possibly also be extended to other forms of molecular imaging. With the proper adjustments, DROP-IN probes might be applied to the fields of for example beta radiation [2, 30], Cherenkov [31], (lifetime) luminescence [32] and even optoacoustic imaging [33].

CONCLUSION

The DROP-IN gamma probe technology increases the degrees of freedom with which laparoscopic gamma tracing can be performed. Herein the angle of gripping has proven to be the most critical engineering feature. Tailoring the grip design and angle helped in improving reproducible and easy grasping, while increasing the detection range and reducing the negative influence that background signals can have during gamma tracing procedures.

REFERENCES

1. *Povoski SP, Neff RL, Mojzisik CM, O'Malley DM, Hinkle GH, Hall NC, Murrey DA, Knopp MV and Martin EW. A comprehensive overview of radioguided surgery using gamma detection probe technology. World J Surg Oncol 2009; 7: 11-74.*
2. *Heller S and Zanzonico P. Nuclear probes and intraoperative gamma cameras. Semin Nucl Med 2011; 41: 166-181.*
3. *Valdés Olmos RA, Vidal-Sicart S and Nieweg OE. SPECT-CT and real-time intraoperative imaging: new tools for sentinel node localization and radioguided surgery? Eur J Nucl Med Mol Imaging 2009; 36: 1-5.*
4. *Jeschke S, Beri A, Grull M, Ziegerhofer J, Prammer P, Leeb K, Sega W and Janetschek G. Laparoscopic radioisotope-guided sentinel lymph node dissection in staging of prostate cancer. Eur Urol 2008; 53: 126-132.*
5. *Alex JC, Weaver DL, Fairbank JT, Rankin BS and Krag DN. Gamma-probe-guided lymph node localization in malignant melanoma. Surg Oncol 1993; 2: 303-308.*
6. *Beri A and Janetschek G. Technology insight: radioguided sentinel lymph node dissection in the staging of prostate cancer. Nat Clin Pract Urol 2006; 3: 602-610.*
7. *Winter A and Wawroschek F. Lymphadenectomy in prostate cancer. Radio-guided lymph node mapping: an adequate staging method. Front Radiat Ther Oncol 2008; 41: 58-67.*
8. *van den Berg NS, Valdes-Olmos RA, van der Poel HG and van Leeuwen FW. Sentinel lymph node biopsy for prostate cancer: a hybrid approach. J Nucl Med 2013; 54: 493-496.*
9. *KleinJan GH, Bunschoten A, Brouwer OR, Van den Berg NS, Valdes-Olmos RA and Van Leeuwen FW. Multimodal imaging in radioguided surgery. Clin Transl Imaging 2013; 1: 433-444.*
10. *van der Poel HG, Buckle T, Brouwer OR, Olmos RAV and van Leeuwen FW. Intraoperative Laparoscopic Fluorescence Guidance to the Sentinel Lymph Node in Prostate Cancer Patients: Clinical Proof of Concept of an Integrated Functional Imaging Approach Using a Multimodal Tracer. Eur Urol 2011; 60: 826-833.*
11. *Bunschoten A, Van den Berg NS, Valdes-Olmos RA, Blokland JA and Van Leeuwen FW. Tracers applied in radioguided surgery. In: Herrmann K, Nieweg OE, Povoski SP, editors. Radioguided Surgery - Current Applications and Innovation Directions in Clinical Practice. Springer International Publishing Switzerland; 2016, Chapter 5, pp. 75-101.*
12. *Warncke SH, Mattei A, Fuechsel FG, Z'Brun S, Krause T and Studer UE. Detection rate and operating time required for gamma probeguided sentinel lymph node resection after injection of technetium-99m nanocolloid into the prostate with and without preoperative imaging. Eur Urol 2007; 52: 126-132.*
13. *KleinJan GH, van den Berg NS, Brouwer OR, de Jong J, Acar C, Wit EM, Vegt E, van der Noort V, Olmos RA, van Leeuwen FW and van der Poel HG. Optimisation of Fluorescence Guidance During Robot-assisted Laparoscopic Sentinel Node Biopsy for Prostate Cancer. Eur Urol 2014; 66: 991-998.*
14. *Meinhardt W, Valdes Olmos RA, van der Poel HG, Bex A and Horenblas S. Laparoscopic sentinel node dissection for prostate carcinoma: technical and anatomical observations. BJU Int 2008; 102: 714-717.*
15. *Pijpers R, Buist MR, van Lingen A, Dijkstra J, van Diest PJ, Teule GJ, Kenemans P and Verheijen RH. The sentinel node in cervical cancer: scintigraphy and laparoscopic gamma probe-guided biopsy. Eur J Nucl Med Mol Imaging 2004; 31: 1479-1486.*
16. *Kitagawa Y and Kitajima M. Gastrointestinal cancer and sentinel node navigation surgery. J Surg Oncol 2002; 79: 188-193.*
17. *Kitagawa Y, Kitano S, Kubota T, Kumai K, Otani Y, Saikawa Y, Yoshida M and Kitajima M. Minimally invasive surgery for gastric cancer--toward a confluence of two major streams: a review. Gastric Cancer 2005; 8: 103-110.*

18. *Meinhardt W, van der Poel HG, Valdes Olmos RA, Bex A, Brouwer OR and Horenblas S. Lap aroscopic sentinel lymph node biopsy for prostate cancer: the relevance of locations outside the extended dissection area. Prostate Cancer 2012; 2012: 751753.*
19. *Schneider C, Guerrero J, Nguan C, Rohling R and Salcudean S. Intra-operative "Pick-Up" Ultrasound for Robot Assisted Surgery with Vessel Extraction and Registration: A Feasibility Study. In: Taylor RH, Yang G, editors. Information Processing in Computer-Assisted Interventions - Second International Conference, IPCAI 2011, Berlin, Germany, June 22, 2011. Proceedings. Springer Berlin Heidelberg; 2011. pp. 122-132.*
20. *Engelen T, Winkel BM, Rietbergen DD, KleinJan GH, Vidal-Sicart S, Olmos RA, van den Berg NS and van Leeuwen FW. The next evolution in radioguided surgery: breast cancer related sentinel node localization using a freehand-SPECT-mobile gamma camera combination. Am J Nucl Med Mol Imaging 2015; 5: 233-245.*
21. *Maurer T, Weirich G, Schottelius M, Weineisen M, Frisch B, Okur A, Kubler H, Thalgott M, Navab N, Schwaiger M, Wester HJ, Gschwend JE and Eiber M. Prostate-specific Membrane Antigen-radioguided Surgery for Metastatic Lymph Nodes in Prostate Cancer. Eur Urol 2015; 68: 530-4.*
22. *Vermeeren L, Meinhardt W, Bex A, van der Poel HG, Vogel WV, Hoefnagel CA, Horenblas S and Olmos RA. Paraaortic Sentinel Lymph Nodes: Toward Optimal Detection and Intraoperative Localization Using SPECT/CT and Intraoperative Real-Time Imaging. J Nucl Med 2010; 51: 376-382.*
23. *Bluemel C, Schnelzer A, Okur A, Ehlerding A, Paepke S, Scheidhauer K and Kiechle M. Freehand SPECT for image-guided sentinel lymph node biopsy in breast cancer. Eur J Nucl Med Mol Imaging 2013; 40: 1656-1661.*
24. *Heuveling DA, van Weert S, Karagozoglu KH and de Bree R. Evaluation of the use of freehand SPECT for sentinel node biopsy in early stage oral carcinoma. Oral Oncol 2015; 51: 287-290.*
25. *Rahbar K, Colombo-Benkmann M, Haane C, Wenning C, Vrachimis A, Weckesser M and Schober O. Intraoperative 3-D mapping of parathyroid adenoma using freehand SPECT. EJNMMI Res 2012; 2: 51-54.*
26. *van den Berg NS, KleinJan GH, Brouwer OR, Wendler T, Valdes-Olmos RA, Van der Poel HG and Van Leeuwen FW. SPECT/CT mixed-reality combined with freehand SPECT augmentedreality for intraoperative navigation in sentinel node biopsy during laparoscopic procedures. Eur J Nucl Med Mol Imaging 2013; 40: S215.*
27. *Wendler T, Herrmann K, Schnelzer A, Lasser T, Traub J, Kutter O, Ehlerding A, Scheidhauer K, Schuster T, Kiechle M, Schwaiger M, Navab N, Ziegler SI and Buck AK. First demonstration of 3-D lymphatic mapping in breast cancer using freehand SPECT. Eur J Nucl Med Mol Imaging 2010; 37: 1452-1461.*
28. *Wendler T, Hartl A, Lasser T, Traub J, Daghighian F, Ziegler SI and Navab N. Towards intraoperative 3D nuclear imaging: reconstruction of 3D radioactive distributions using tracked gamma probes. Med Image Comput Comput Assist Interv 2007; 10: 909-917.*
29. *Fuerst B, Sprung J, Pinto F, Frisch B, Wendler T, Simon H, Mengus L, Van den Berg NS, Van der Poel HG, Van Leeuwen FWB and Navab N. First Robotic SPECT for Minimally Invasive Sentinel Lymph Node Mapping. IEEE Trans Med Imaging 2015; 35(3):830-8.*
30. *Wendler T, Traub J, Ziegler SI and Navab N. Navigated three dimensional beta probe for optimal cancer resection. Med Image Comput Comput Assist Interv 2006; 9: 561-569.*
31. *Chin PT, Welling MM, Meskers SC, Olmos RA, Tanke H and van Leeuwen FW. Optical imaging as an expansion of nuclear medicine: Cerenkov-based luminescence vs fluorescencebased luminescence. Eur J Nucl Med Mol Imaging 2013; 40: 1283-1291.*
32. *van Leeuwen FW, Hardwick JC and van Erkel AR. Luminescence-based Imaging Approaches in the Field of Interventional Molecular Imaging. Radiology 2015; 276: 12-29.*
33. *Garcia-Allende PB, Glatz J, Koch M and Ntziachristos V. Enriching the interventional vision of cancer with fluorescence and optoacoustic imaging. J Nucl Med 2013; 54: 664-667.*

OUTLOOK

CHAPTER 9

COMPUTER-ASSISTED SURGERY: VIRTUAL- AND AUGMENTED-REALITY DISPLAYS FOR NAVIGATION DURING UROLOGICAL INTERVENTIONS

Adapted from: van Oosterom MN, van der Poel HG, Navab N, van de Velde CJH, van Leeuwen FWB

Current Opinion in Urology, 2018, 28(2): 205–213

ABSTRACT

The purpose of this review is to provide an overview of the developments made for virtual- and augmented-reality navigation procedures in urological interventions/surgery. Recent findings show that navigation efforts have demonstrated potential in the field of urology by supporting guidance for various disorders. The navigation approaches differ between the individual indications, but seem interchangeable to a certain extent. An increasing number of pre- and intra-operative imaging modalities has been used to create detailed surgical roadmaps, namely: (cone-beam) computed tomography, MRI, ultrasound, and single-photon emission computed tomography. Registration of these surgical roadmaps with the real-life surgical view has occurred in different forms (e.g. electromagnetic, mechanical, vision, or near-infrared optical-based), whereby the combination of approaches was suggested to provide superior outcome. Soft-tissue deformations demand the use of confirmatory interventional (imaging) modalities. This has resulted in the introduction of new intraoperative modalities such as DROP-IN US, transurethral US, (DROP-IN) gamma probes and fluorescence cameras. These noninvasive modalities provide an alternative to invasive technologies that expose the patients to X-ray doses. Whereas some reports have indicated navigation setups provide equal or better results than conventional approaches, most trials have been performed in relatively small patient groups and clear follow-up data are missing. However, the reported computer-assisted surgery research concepts do provide a glimpse in to the future application of navigation technologies in the field of urology.

KEY POINTS

- At present, soft-tissue deformations demand the use of interventional imaging or tracing modalities that confirm the real-world surgical target location.
- Due to their dose exposure, intraoperative use of X-ray-based imaging devices is undesirable, and technologies that provide a noninvasive alternative (e.g. gamma probes, US, and fluorescence) are much in demand.
- Early clinical studies have demonstrated the potential of virtual reality and augmented reality models (2D and 3D) to improve the surgical (navigation) accuracy.
- To date, a plurality of surgical navigation approaches has become available, thereby covering a range of urological interventions.

INTRODUCTION

The impact of computer technologies on life in the western civilization is an undeniable fact. One of the many advancements that has been created is the availability of navigation systems. Using, for example, smartphones, we are now able to accurately determine our geographic location and navigate ourselves efficiently from point A to point B, while even dynamically responding to deviations from the plotted route (Figure 1). Such navigation is made possible using a combination of urban roadmaps and satellite-based tracking systems such as the global positioning system (GPS). We, and others, have reasoned that a similar navigation concept, when translated to surgical interventions, could greatly impact healthcare. Building on the advancements made in medical imaging technology, anatomy and/or disease-related images of individual patients can be created. Such images can, subsequently, be used to provide detailed and interactive surgical roadmaps [1]. This computer-assisted surgery (CAS) concept creates the potential to increase the accuracy of lesion identification, and with that improves the surgical accuracy, logistics, and decision-making (Figure 1) [2]. Herein, surgical roadmaps can be used in different forms: they can be presented separately in the operating room or next to the laparoscopic-feed to allow the operating urologist to study the targeted tissue in detail during the procedure; they can be presented via virtual reality displays that provide, for example,

Figure 1. Analogy comparing navigation in everyday life with navigation during surgery. *Similar to navigation approaches applied during everyday life* ***(a)****, a surgeon can use a combination of guidance technologies to guide himself or herself quickly and efficiently to the surgical target [e.g. tumor, (metastatic) lymph node or kidney stone]* ***(b)****. These technologies can follow each other in consecutive order: disease description ('Descriptive'), two-dimensional preoperative imaging ('2D map'), three-dimensional preoperative imaging ('3D map'), 'GPS-like' virtual reality navigation ('VR navigation'), 'GPS-like' augmented reality navigation displays ('AR navigation') and intraoperative imaging/tracing ('Confirmative imaging').*

distance-to-target estimations; they can be presented as augmented reality overlays onto the real-world environment using (laparoscopic) video-feeds (Figure 1).

While rough navigation on a general anatomic map was already attempted as early as 1889, 'modern patient-specific' navigation (that is navigation based on individual patient scans) has only been used since 1986 [2]. At present, the field of surgical navigation offers a plurality of navigation concepts and methods. Most of these have been applied in neurological and orthopedic surgery, where the rigidity of the surgical field supports the alignment between the surgical roadmap and the actual surgical field. Soft tissues are, however, subject to movement – a feature that inherently complicates the registration process [3]. Nevertheless, due to their high potential, soft-tissue related navigation efforts have been explored in a translational research setting, as discussed in a number of reviews relevant for the topic [1–7]. During the past years, navigation in the field of urology has rapidly expanded, including novel indications and first-in-human applications. To provide a structured report of these evolutionary progressions, we have classified them into navigation for disorders in the urinary system or reproductive organs.

URINARY SYSTEM

Navigation efforts for urinary disorders are mainly focused on nephrolithotomy (urolithiasis) and nephrectomy (renal cell carcinoma). For these applications, (cone-beam) computed tomography (CT) – the modality proposed for these indications in the European Association of Urology guidelines – is the main modality used for the creation of the roadmap that provides the basis for the navigation-process [8,9].

Navigation during percutaneous nephrolithotomy

Rassweiler et al. [10,11] has clinically applied navigation technologies during nephrolithotomy using a futuristic iPad tablet-assisted guidance approach (Figure 2a). Using CT-derived roadmaps, this approach provides a movable two-dimensional augmented reality 'window into the body,' thereby facilitating the optimal access site for needle puncture. Roadmap-to-patient registration was realized using a vision-based tracking setup, encompassing the two-dimensional camera of the iPad and radiopaque colored fiducial markers, placed on the patient's skin. During needle puncture, fluoroscopy allowed adjustments to be made from the plotted needle course. A comparison to traditional ultrasound-fluoroscopy combinations, yielded a similar outcome, but also revealed that significantly higher X-ray doses and longer puncture times occurred with the iPad approach [11]. Incorporation of electromagnetic needle tracking was proposed as a future refinement. In a porcine study, Rodrigues et al. demonstrated that the incorporation of an electromagnetic sensor at both the needle and catheter-tip allowed needle placement to be performed by relying on the electromagnetic tracking

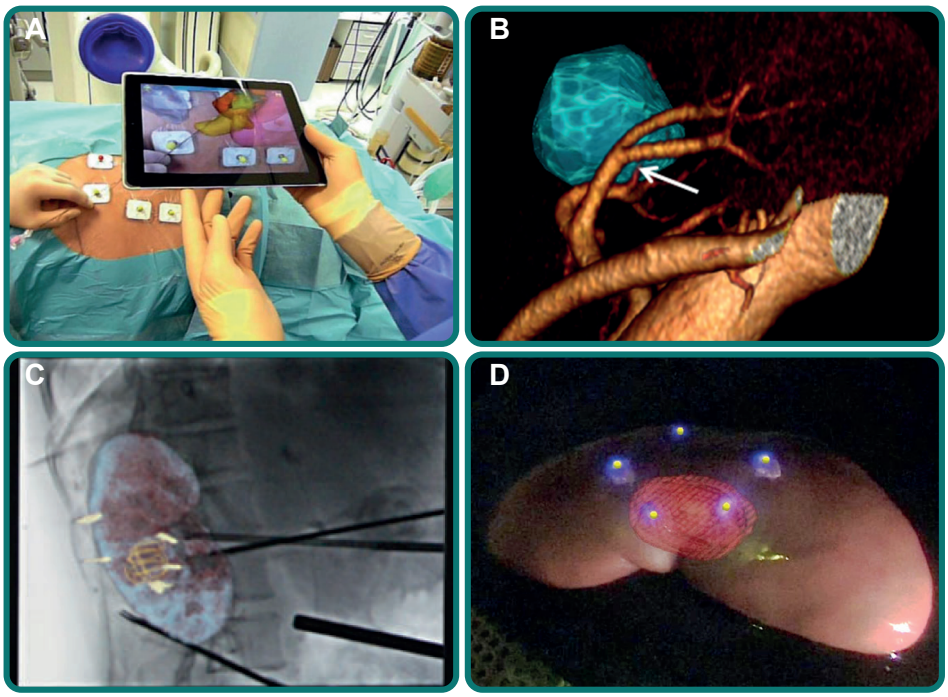

Figure 2. VR and AR technologies for navigation in the urinary system. (a) *iPad-assisted percutaneous access to the kidney during nephrolithotomy, providing CT-based AR 'window in to the body' [12].* ***(b)*** *CT-based VR model of renal cell carcinoma, to be used parallel to (RA)LPN, providing insight in the tumor-surrounding vasculature [13].* ***(c)*** *AR overlay of kidney and tumor models (including intra-abdominal fiducials) in the real-time fluoroscopy images for (RA)LPN [14].* ***(d)*** *AR overlay of tumor model in the real-time laparoscopic-feed using metabolizable and fluorescent fiducials [15].*

and vision of the ureteral fiberscope only [16]. After placement of the catheter tip next to the kidney or ureter stone via ureterorenoscopy, electromagnetic tracking supported real-time monitoring of the needle tip and stone relative to each other, abandoning the need for fluoroscopy. Integration of electromagnetic needle tracking and the iPad approach could thus help limit the X-ray dose while allowing visualization of the needle trajectory with respect to the organ models [17] (Figure 3a). In a similar percutaneous setup, interventional radiology (that is ablations of lesions in the kidney) indicated that electromagnetic-based navigation of ultrasound devices in preinterventionally acquired CT or MRI image planes improves the accuracy of needle placement [19–21]. Hence, the future use of US navigation could also help to further refine the needle-tracking technology.

Despite the potential advantages of electromagnetic tracking, fluoroscopy and (cone-beam) CT devices were shown to reduce the electromagnetic-tracking accuracy [22,23]. Research in to minimization and calibration efforts

has partially overcome this electromagnetic-tracking inaccuracy in static environments [22]. Unfortunately, such technologies do not (yet) apply for dynamic surgical environments [e.g. moving (robot-assisted) surgical tools] [1].

Navigation during nephrectomy

During (robot-assisted) laparoscopic partial nephrectomy [(RA)LPN], various forms of CAS have been applied. Furukawa et al. [13] used a CT-based three-dimensional virtual reality roadmap of the kidney, tumor, and vasculature that facilitates selective arterial clamping presented in the surgeon's console parallel to the laparoscopic feed using the TilePro function (Figure 2b). A comparison of this approach with traditional clamping procedures not only indicated virtual reality assistance was feasible, it was also shown to reduce the decrease in estimated glomerular filtration rates early after surgery [24]. Here, the use of an iPad can help facilitate the interaction with the virtual reality model, thereby improving the intraoperative appreciation of the hilar vascular anatomy [25]. Alternatively, Wang et al. [26] describe the use of a manually positioned two-dimensional augmented reality overlay, presenting a CT-model in the laparoscopic feed (i.e. static screenshots). Comparisons between patients receiving augmented reality guidance and those that went without, suggested the technology could help reduce the operating time and reduce blood loss values. For open liver surgery, similar manual two-dimensional augmented reality overlays have been helpful in localizing multiple tumor lesions within the organ [27]. Ukimura and Gill [21] used a near-infrared (NIR) optical tracking system (OTS) to support the automatic alignment of such augmented reality CT models in the two-dimensional laparoscopic feed, during (non-robotic) LPN. Although they indicate the navigation accuracy was sufficient for determination of the resection line, the need for a technology able to correct for tissue deformations was also mentioned.

For intra-abdominal vision-based tracking, colored and radiopaque needle-shaped fiducials were fixed in the kidney surface as to support the alignment of the cone-beam CT models with the two-dimensional real-time laparoscopic and two-dimensional fluoroscopy feed (Figure 2c) [14]. Though the navigated setup was successful, the increased X-ray dose was considered to be a limitation for wider implementation. Whereas the use of intra-abdominally placed fiducials did seem to support image registration, others have reported some limitations related to such an approach: fiducials could potentially physically hinder the tumor resection; visualization of the fiducials in the surgical environment could be challenging; and both placement (before navigation) and removal (after navigation) adds to the invasiveness of the procedure [1]. As alternative, metabolizable fiducials (CT-opaque and fluorescent) have been suggested (Figure 2d) [15]. Extension with fluorescence, however, does rely on the surgical procedures to be performed with a laparoscope capable of fluorescence imaging.

To increase the acceptance of US guidance during RALPN, an innovative DROP-IN US probe was designed [28,29] (Figure 4). This DROP-IN probe can be

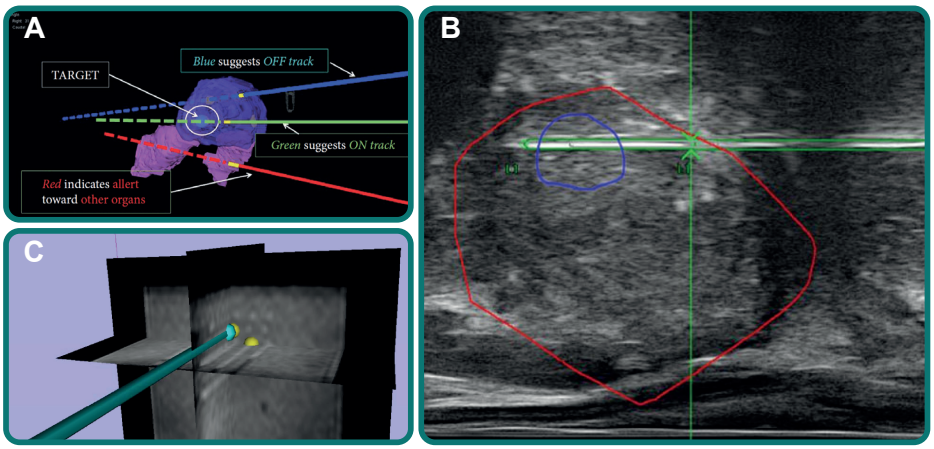

Figure 3. VR and AR technologies for needle-navigation to prostate lesions. (a) *CT-based VR model of the prostate displaying current needle track with respect to different organ models [17].* ***(b)*** *MRI-based navigation for targeted biopsy of the prostate displayed over the real-time TRUS images [12].* ***(c)*** *MRI-only-guided VR navigation for targeted biopsy in a phantom study [18].*

positioned with superior degrees of freedom, using laparoscopic tools. Via laparoscopic vision-based tracking of a chequered-pattern fiducial on the DROP-IN US (comparable to those used for crash test dummies), the two-dimensional US images could be directly projected as augmented reality overlay in the laparoscopic feed (Figure 4a). Combined with tracking of the robotic arms, this helped realize a three-dimensional navigation in a phantom setup (Figure 4b-c) [30,31].

REPRODUCTIVE ORGANS

For the reproductive organs, navigation efforts have been reported for the primary tumor and lymphatic involvement. In this application, next to ultrasound and MRI, also single-photon emission computed tomography (SPECT/CT), radiotracing, and fluorescence imaging have been used during the guidance process.

Navigation towards the primary tumor lesions

Transrectal US (TRUS)-guided biopsy in prostate cancer is commonly performed based on the lesion location defined by preoperative MRI images [32]. Recently, next to research systems, three-dimensional MRI-based navigation of TRUS has become commercially available (Figure 3) [33]. For registration, electromagnetic tracking, mechanical tracking, and image-based registrations have been used [33]. To enhance the insight into the relevant anatomy (e.g. prostate–bladder interface, seminal vesicles, distal prostate boundary, lesion location, biopsy tracks, neurovascular bundles, and urethra), TRUS-based navigation has also been applied in robot-assisted laparoscopic prostatectomy (RALP). Using US vision-based registration in combination with mechanical tracking, the two-dimensional TRUS

Figure 4. DROP-IN US technology. (a) *In-vivo application during (RA)LPN [28]. An AR overlay is shown directly in the laparoscopic-feed, displaying the real-time ultrasound imaging within the anatomical context.* ***(b)*** *Tracked DROP-IN ultrasound was used to generate a 3D model of the tumor* ***(c)*** *for navigation in a phantom (RA)LPN setup [30].*

automatically followed the position of the robotic tools, displaying the relevant US plane in the surgical console using the TilePro function [34]. Similar to such an automatic TRUS setup, robotic US acquisition has shown promising results for reproductive assistance and guidance for interventions in the abdomen [35]. The intraoperative use of three-dimensional virtual reality displays (based on preoperative TRUS and MRI) parallel to the laparoscopic-feed during RALP was said to further refine the resection accuracy in the vicinity of the cancer lesion, yielding 90% negative surgical margins [36] (Figure 5a). Such virtual reality models have also been suggested to facilitate nerve-sparing during pelvic surgery [38]. To enhance the urologist's preoperative appreciation of the patient anatomy (i.e. 'virtual therapy concept'), the virtual reality models were also three-dimensionally printed [39]. To further increase the information integration, for example, the neurovascular bundle and the biopsy proven cancer region, the use of direct augmented reality overlays in the two-dimensional laparoscopic feed have been studied (Figure 5b-c) [21,37]. The first study used a NIR OTS for the registration, thereby supporting the identification of an appropriate resection line. The second study used vision-based tracking of fiducial pins (colored and echogenic) placed in the prostate surface to realize the augmented reality alignment. In the latter setup, to prevent tumor spillage, the fiducial pins had to be removed together with the prostate itself. Unfortunately, both setups suffered from surgery-induced tissue deformations [21,37]. Lanchon et al. used transurethral US (TUUS) as alternative for TRUS [40]. In a phantom study using (US) vision-based tracking of fiducial pins, augmented reality models, formed using motorized TUUS, were displayed on the two-dimensional laparoscopic feed. Alternatively, the above mentioned DROP-IN US probe technology may in the future also support US navigation during prostatectomy [28,29]. In indications, where electromagnetic tracking is feasible, perhaps also commercially available US-navigation setups, as applied in interventional radiology, may find their way into prostate cancer surgery [19].

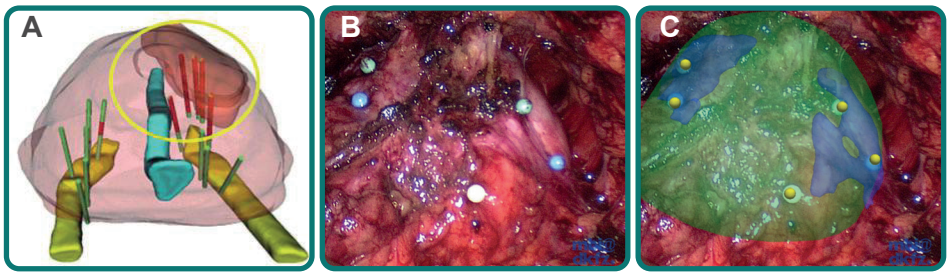

Figure 5. VR and AR technologies during prostatectomy. (a) *A TRUS/MRI-based VR model to be used in parallel to the laparoscopic view [36]. Different structures are shown: prostate (pink), ureter (blue), neurovascular bundles (yellow), biopsy-proven tumor lesion (red), and tumor biopsy cores (green (tumor negative) and red (tumor positive) cylinders).* ***(b)*** *After placement of intraabdominal fiducials (colored and echogenic pins in the prostate surface),* ***(c)*** *TRUS-based AR overlay of the prostate (green) and neurovascular bundles (blue) could be shown during (RA)LP [37].*

Navigation for the management of lymphatic disease

Navigated approaches have successfully been used to identify lymph nodes suspected to harbor metastases. Uniquely, in these procedures, nuclear molecular imaging approaches, namely preoperative SPECT/CT and intraoperatively acquired freehand (fh)SPECT [41], have provided the roadmaps for navigation.

The PSMA-specific tracer ^{111}In-PSMA-I&T has supported the radio-guided resection of metastasis-harboring lymph nodes during open salvage procedures [42]. Preoperative PET/CT or PET/MRI using ^{68}Ga-PSMA-HBED-CC supported patient selection and procedural planning. Intraopertively, fhSPECT was successfully applied to display the lesion location in two-dimensional augmented reality and support three-dimensional virtual reality navigation of a gamma probe (NIR OTS tracking) [42] (Figure 6). The acoustic readout of the gamma probe supported compensation of navigation inaccuracies when present. A similar navigation approach, using SPECT/CT, was used to identify (sentinel) lymph nodes that accumulated indocyanine green (ICG)-^{99m}Tc-nanocolloid [44]. In addition to acoustic gamma-tracing, non-integrated NIR fluorescence imaging was used as confirmatory modality. To integrate fluorescence imaging in the navigation workflow, SPECT/CT- or fhSPECT-based navigation of the fluorescence camera itself was applied in both prostate and penile cancer patients [43,45,46]. In these studies, an augmented-reality-SPECT(/CT) overlay was presented in the two-dimensional fluorescence camera feed and supported the detection of the injection site (primary tumor) and sentinel lymph nodes (Figure 6). Fluorescence imaging allowed for high-resolution real-time correction of deformation-induced navigation inaccuracies. Phantom studies indicated this same navigated fluorescence camera concept could become an integral part of robot-assisted procedures [47].

In an attempt to improve the radio-guidance during laparoscopic interventions, a DROP-IN gamma probe was developed, and evaluated during early

robot-assisted porcine surgery and on ex-vivo clinical specimens [48] (Figure 7a). To connect this technology to the CAS concept, in a phantom setup, a combination of chequered pattern vision-based, NIR OTS, and mechanical tracking, supported the generation of DROP-IN fhSPECT-images and the according navigation approaches (Figure 7b) [49].

DISCUSSION

During the past decade, a lot of exciting and promising CAS developments have opened the way for navigation setups to be used in urology.

Registration of (preoperative) imaging datasets with the surgical view helps to generate virtual reality and augmented reality environments that support the navigation process in two- or three-dimensions. The greatest limitation for these navigation setups so far is the registration accuracy and resulting navigation precision. This is also the area where further technical improvements are urgently needed. A consequence of the current inaccuracies is the requirement that virtual reality and augmented reality navigation approaches have to be benchmarked against the real-world surgical environment. This is especially critical when the surgical procedures are performed in soft-tissue structures that suffer from surgically induced deformations. In that sense, navigation procedures do not replace the surgeon's expertise, but rather improve the procedural accuracy and efficiency by increasing both insight in the anatomy/disease and the focus on the anatomies critical for surgery. In the end, the urologist is still required to make his/her expert call on the execution of the procedure. The quality of the virtual reality and augmented reality displays, however, can greatly influence the value of navigation approaches. Therefore, improved visualization methods that determine which virtual data are displayed during different phases of the surgical procedure (i.e. relevance-based virtual reality/augmented reality) [50], or visualization methods that facilitate improved augmented reality integration into the real-world surgical view (e.g. three-dimensional depth perception) [1] should be considered.

To link the navigation process to the real-world surgical environment, some form of real-time imaging feedback is instrumental. When the targets cannot be defined by eye, dedicated intraoperative imaging modalities provide outcome, for example, fluoroscopy, US, gamma tracing/imaging, or fluorescence imaging. The modality of choice, then, is predominantly defined by the characteristics of the target and the modality's neutrality with regard to enhanced patient burden. This means that invasive approaches, for example, X-ray modalities or the requirement of placing invasive fiducial markers, should ideally be replaced by the non-invasive alternatives that have become available during recent years.

The intraoperative imaging modality should also be able to accurately track the visualization of the targeted tissue with respect to a navigation reference

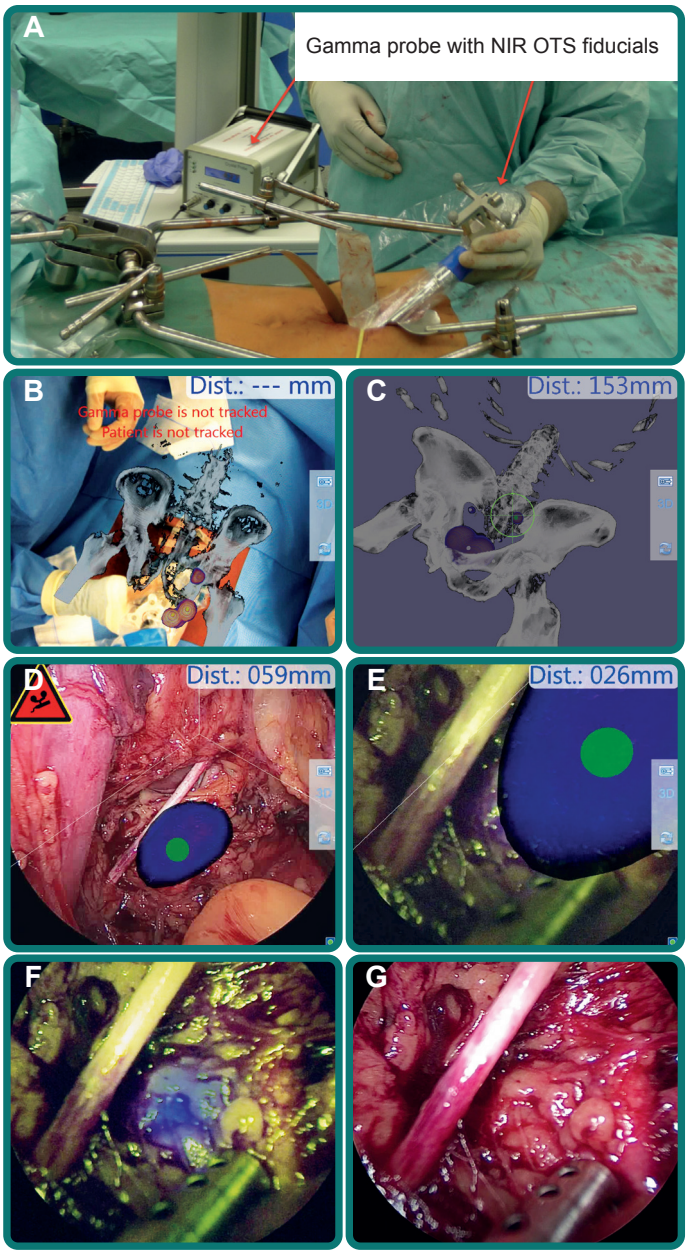

Figure 6. VR and AR technologies for navigation in the management of lymphatic disease. (a) *Intraoperative setup of navigated gamma probe (using NIR OTS tracking) towards metastatic LNs during open salvage prostatectomy (navigation based on fhSPECT) [42].* ***(b)*** *SPECT/CT-based navigation of a fluorescence camera towards sentinel LNs in penile cancer. AR SPECT/CT overlay was shown in the 2D camera-feed.* ***(c)*** *3D VR navigation of a gamma probe towards sentinel LNs in prostate cancer.* ***(d)*** *fhSPECT-based navigation of a fluorescence laparoscope towards sentinel LNs in prostate cancer, using an AR overlay directly shown in the 2D laparoscopic-feed [43].* ***(e)*** *AR overlays guided the fluorescence laparoscope to the vicinity of the LN.* ***(f)*** *Fluorescence imaging (fluorescence is shown in blue) confirmed the precise target location* ***(g)*** *not clearly visible by eye.*

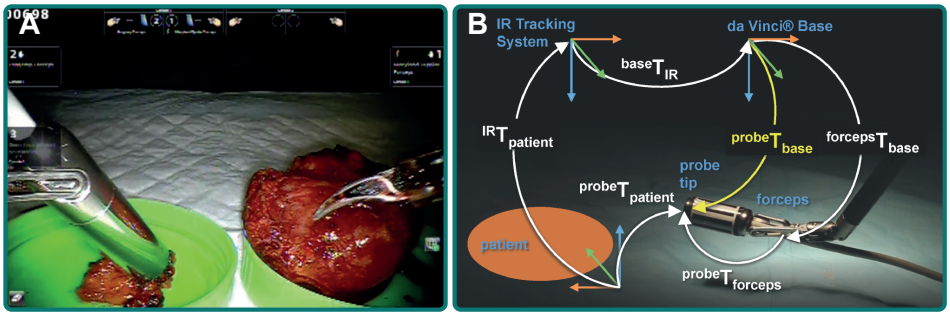

Figure 7. DROP-IN gamma probe technology. (a) *Ex-vivo application of the DROP-IN gamma probe, scanning LN package and prostate.* ***(b)*** *Tracked DROP-IN gamma probe (using a combination of tracking techniques) to create fhSPECT images for navigation purposes in a laparoscopic phantom LN setup [49].*

frame (i.e. the position of the target with respect to the navigated tools). Again, the indication and operating room setup define the most ideal tracking approach. That said, a combination of tracking techniques will most likely provide the highest accuracy [49,51]. For needle-based procedures, electromagnetic tracking and/or the more experimental fiber bragg grating tracking techniques will possibly work best [52]. Electromagnetic tracking, however, currently suffers from the use of metal equipment in the surgical environment. Hence, for surgical resections, a combination of NIR OTS, mechanical-tracking, and vision-based-tracking (e.g. using machine learning methods such as deep-learning) seems to hold most promise [53]. These preferences may, however, change when the individual technologies evolve.

CONCLUSION

Although there is still a lot of room for refinement, we believe the presented navigation efforts provide the first steps towards a promising future for computer-assisted urological surgery. This is strengthened by parallel developments in medical imaging devices, disease-specific tracers (e.g. ^{99m}Tc-PSMA-I&S) [42], and surgical tools. The up rise of robot-assisted procedures, thereby, provides a valuable platform for the integration of new modalities, for example, fluorescence imaging, DROP-IN modalities, and navigation setups.

REFERENCES

1. *Bernhardt S, Nicolau SA, Soler L, Doignon C. The status of augmented reality in laparoscopic surgery as of 2016. Med Image Anal 2017; 37:66–90.*
2. *Waelkens P, van Oosterom MN, van den Berg NS, Navab N, van Leeuwen FWB. Surgical navigation: an overview of the state-of-the-art clinical applications. In: Herrmann K, Nieweg OE, Povoski SP, editors. Radioguided Surgery. Cham: Springer; 2016. pp. 57–73.*
3. *Rassweiler J, Rassweiler M-C, Muller M, et al. Surgical navigation in urology: European perspective. Curr Opin Urol 2014; 24:81–97.*
4. *Greco F, Cadeddu JA, Gill IS, et al. Current perspectives in the use of molecular imaging to target surgical treatments for genitourinary cancers. Eur Urol 2014; 65:947–964.*
5. *Nakamoto M, Ukimura O, Faber K, Gill IS. Current progress on augmented reality visualization in endoscopic surgery. Curr Opin Urol 2012; 22: 121–126.*
6. *Navab N, Blum T, Wang L, et al. First deployments of augmented reality in operating rooms. Computer 2012; 45:48–55.*
7. *Nicolau S, Soler L, Mutter D, Marescaux J. Augmented reality in laparoscopic surgical oncology. Surg Oncol 2011; 20:189–201.*
8. *EAU. Urolithiasis guidelines; 2017. http://uroweb.org/guideline/urolithiasis/.*
9. *EAU. Renal cell carcinoma guidelines; 2017. http://uroweb.org/guideline/renal-cell-carcinoma/.*
10. *Rassweiler JJ, M€uller M, Fangerau M, et al. iPad-assisted percutaneous access to the kidney using marker-based navigation: initial clinical experience. Eur Urol 2012; 61:628–631.*
11. *Rassweiler M, Klein J, Mueller M, et al. 578 IPad assisted PCNL-clinical study to compare to the standard puncturing technique. Eur Urol Suppl 2016; 15:e578a.*
12. *Simpfendorfer T, Hatiboglu G, Hadaschik B, et al. Use of Surgical Navigation During Urologic Surgery. In: Rane´ A, Turna B, Autorino R, Rassweiler J, editors. Practical Tips in Urology. London: Springer; 2017. pp. 743–750.*
13. *Furukawa J, Miyake H, Tanaka K, et al. Console-integrated real-time threedimensional image overlay navigation for robot-assisted partial nephrectomy with selective arterial clamping: early single-centre experience with 17 cases. Int J Med Robot 2014; 10:385–390.*
14. *Simpfendorfer T, Gasch C, Hatiboglu G, et al. Intraoperative computed tomography imaging for navigated laparoscopic renal surgery: first clinical experience. J Endourol 2016; 30:1105–1111.*
15. *Wild E, Teber D, Schmid D, et al. Robust augmented reality guidance with fluorescent markers in laparoscopic surgery. Int J Comput Assist Radiol Surg 2016; 11:899–907.*
16. *Rodrigues PL, Vilac¸a JL, Oliveira C, et al. Collecting system percutaneous access using real-time tracking sensors: first pig model in vivo experience. J Urol 1932-; 190:7.*
17. *Marien A, Abreu L, Castro A, et al. Three-dimensional navigation system integrating position-tracking technology with a movable tablet display for percutaneous targeting. BJU Int 2015; 115:659–665.*
18. *Su H, Shang W, Cole G, et al. Piezoelectrically actuated robotic system for MRI-guided prostate percutaneous therapy. IEEE/ASME Trans Mechatron 2015; 20:1920–1932.*
19. *Burgmans MC, den Harder JM, Meershoek P, et al. Phantom study investigating the accuracy of manual and automatic image fusion with the GE Logiq E9: implications for use in percutaneous liver interventions. Cardiovasc Intervent Radiol 2017; 40:914–923.*
20. *Mauri G, Cova L, De Beni S, et al. Real-time US-CT/MRI image fusion for guidance of thermal ablation of liver tumors undetectable with US: results in 295 cases. Cardiovasc Intervent Radiol 2015; 38:143–151.*
21. *Ukimura O, Gill IS. Imaging-assisted endoscopic surgery: Cleveland Clinic experience. J Endourol 2008; 22:803–810.*

22. *Lugez E, Sadjadi H, Pichora DR, et al. Electromagnetic tracking in surgical and interventional environments: usability study. Int J Comput Assist Radiol Surg 2015; 10:253–262.*
23. *Wegner I, Teber D, Hadaschik B, et al. Pitfalls of electromagnetic tracking in clinical routine using multiple or adjacent sensors. Int J Med Robot 2013; 9:268–273.*
24. *Furukawa J, Nishikawa M, Terakawa T, et al. Renal function and perioperative outcomes of selective versus complete renal arterial clamping during robotassisted partial nephrectomy using console-integrated real-time three-dimensional image overlay navigation. J Urol 2016; 195:e566.*
25. *Hughes-Hallett A, Pratt P, Mayer E, et al. Image guidance for all: TilePro display of 3-dimensionally reconstructed images in robotic partial nephrectomy. Urology 2014; 84:237–243.*
26. *Wang D, Zhang B, Yuan X, et al. Preoperative planning and real-time assisted navigation by three-dimensional individual digital model in partial nephrectomy with three-dimensional laparoscopic system. Int J Comput Assist Radiol Surg 2015; 10:1461–1468.*
27. *Ntourakis D, Memeo R, Soler L, et al. Augmented reality guidance for the resection of missing colorectal liver metastases: an initial experience. World J Surg 2016; 40:419–426.*
28. *Hughes-Hallett A, Pratt P, Mayer E, et al. Intraoperative ultrasound overlay in robot-assisted partial nephrectomy: first clinical experience. Eur Urol 2014; 65:671–672.*
29. *Pratt P, Jaeger A, Hughes-Hallett A, et al. Robust ultrasound probe tracking: initial clinical experiences during robot-assisted partial nephrectomy. Int J Comput Assist Radiol Surg 2015; 10:1905–1913.*
30. *Singla R, Edgcumbe P, Pratt P, et al. Intra-operative ultrasound-based augmented reality guidance for laparoscopic surgery. Healthc Technol Lett 2017; 4:204–209.*
31. *Edgcumbe P, Singla R, Pratt P, et al. Augmented reality imaging for robotassisted partial nephrectomy surgery. International Conference on Medical Imaging and Virtual Reality: Springer; 2016.*
32. *Wegelin O, van Melick HH, Hooft L, et al. Comparing three different techniques for magnetic resonance imaging-targeted prostate biopsies: a systematic review of in-bore versus magnetic resonance imaging-transrectal ultrasound fusion versus cognitive registration. Is there a preferred technique? Eur Urol 2017; 71:517–531.*
33. *Kongnyuy M, George AK, Rastinehad AR, Pinto PA. Magnetic resonance imaging-ultrasound fusion-guided prostate biopsy: review of technology,techniques, and outcomes. Curr Urol Rep 2016; 17:32.*
34. *Mohareri O, Ischia J, Black PC, et al. Intraoperative registered transrectal ultrasound guidance for robot-assisted laparoscopic radical prostatectomy. J Urol 2015; 193:302–312.*
35. *Hennersperger C, Fuerst B, Virga S, et al. Towards MRI-based autonomous robotic US acquisitions: a first feasibility study. IEEE Trans Med Imaging 2017; 36:538–548.*
36. *Ukimura O, Aron M, Nakamoto M, et al. Three-dimensional surgical navigation model with TilePro display during robot-assisted radical prostatectomy. J Endourol 2014; 28:625–630.*
37. *Simpfendorfer T, Baumhauer M, Muller M, et al. Augmented reality visualization during laparoscopic radical prostatectomy. J Endourol 2011; 25:1841–1845.*
38. *Kraima AC, Derks M, Smit NN, et al. Careful dissection of the distal ureter is highly important in nerve-sparing radical pelvic surgery: a 3d reconstruction and immunohistochemical characterization of the vesical plexus. Int J Gynecol Cancer 2016; 26:959–966.*
39. *Shin T, Ukimura O, Gill IS. Three-dimensional printed model of prostate anatomy and targeted biopsy-proven index tumor to facilitate nerve-sparing prostatectomy. Eur Urol 2016; 69:377–379.*
40. *Lanchon C, Custillon G, Moreau-Gaudry A, et al. Augmented reality using transurethral ultrasound for laparoscopic radical prostatectomy: preclinical evaluation. J Urol 2016; 196:244–250.*
41. *Bluemel C, Matthies P, Herrmann K, Povoski SP. 3D scintigraphic imaging and navigation in radioguided surgery: freehand SPECT technology and its clinical applications. Expert Rev Med Devices 2016; 13:339–351.*

42. *Maurer T, Weirich G, Schottelius M, et al. Prostate-specific membrane antigen-radioguided surgery for metastatic lymph nodes in prostate cancer. Eur Urol 2015; 68:530–534.*
43. *Van Oosterom MN, Meershoek P, KleinJan GH, et al. Navigation of fluorescence cameras during soft-tissue surgery – is it possible to use a single navigation setup for various open and laparoscopic urological surgery applications? J Urol 2018; 199(4):1061-8.*
44. *Brouwer OR, van den Berg NS, Matheron HM, et al. Feasibility of intraoperative navigation to the sentinel node in the groin using preoperatively acquired single photon emission computerized tomography data: transferring functional imaging to the operating room. J Urol 2014; 192:1810–1816.*
45. *Brouwer OR, Buckle T, Bunschoten A, et al. Image navigation as a means to expand the boundaries of fluorescence-guided surgery. Phys Med Biol 2012; 57:3123.*
46. *KleinJan GH, van den Berg NS, van Oosterom MN, et al. Toward (Hybrid) navigation of a fluorescence camera in an open surgery setting. J Nucl Med 2016; 57:1650–1653.*
47. *van Oosterom MN, Engelen MA, van den Berg NS, et al. Navigation of a robot-integrated fluorescence laparoscope in preoperative SPECT/CT and intraoperative freehand SPECT imaging data: a phantom study. J Biomed Opt 2016; 21:86008.*
48. *van Oosterom MN, Simon H, Mengus L, et al. Revolutionizing (robot-assisted) laparoscopic gamma tracing using a DROP-IN gamma probe technology. Am J Nucl Med Mol Imaging 2016; 6:1–17.*
49. *Fuerst B, Sprung J, Pinto F, et al. First robotic SPECT for minimally invasive sentinel lymph node mapping. IEEE Trans Med Imaging 2016; 35:830–838.*
50. *Navab N, Hennersperger C, Frisch B, F€urst B. Personalized, Relevance-based Multimodal Robotic Imaging and Augmented Reality for Computer Assisted Interventions. Med Image Anal 2016; 33:64–71.*
51. *Hughes-Hallett A, Mayer EK, Marcus HJ, et al. Augmented reality partial nephrectomy: examining the current status and future perspectives. Urology 2014; 83:266–273.*
52. *Roesthuis RJ, van de Berg NJ, van den Dobbelsteen JJ, Misra S. Modeling and steering of a novel actuated-tip needle through a soft-tissue simulant using Fiber Bragg Grating sensors. Robotics and Automation (ICRA), 2015 IEEE International Conference on; 2015: IEEE.*
53. *Laina I, Rieke N, Rupprecht C, et al. Concurrent segmentation and localization for tracking of surgical instruments. Med Image Comput Assist Interv 2017; https://arxiv.org/abs/1703.10701.*

CHAPTER 10

SUMMARY
SAMENVATTING
CURRICULUM VITAE
LIST OF PUBLICATIONS

SUMMARY

In the quest to achieve precision surgery, the work described in this thesis introduces several novel (hybrid) detection and navigation modalities. All the presented engineering efforts focused on optimal detection and localization of cancer-related tissue using the complementary tracer signatures of either nuclear and fluorescence radiation, or a combination thereof, using so-called hybrid tracers. These newly developed image-guided surgery technologies were evaluated in different settings, ranging from phantom work to pre-clinical and even clinical studies.

Part one of this thesis covered several surgical navigation concepts. In **chapter 2** the general concepts for a typical surgical navigation workflow were introduced. Important requirements are: 1) some form of imaging, providing a 3D map of the disease; 2) computer-aided planning using the patient map; 3) registration of the patient map to the actual patient on the operating table; 4) position and orientation tracking of the patient and surgical tools in the operating room; and 5) navigation of the surgical tools towards the tissue of interest. This all constitutes to a workflow wherein the surgeon knows exactly where the surgical tools are on the patient map, relative to the targeted tissue. Apart from the fields of neurosurgery, radiotherapy and perhaps orthopedic surgery, the application of navigation remains experimental, mainly due to the inability to cope with, or compensate enough for, tissue-deformation-induced inaccuracy of the navigation workflow. Nevertheless, the studies shown, combined with the advances in the underlying technology, suggest that the use of surgical navigation will be much more widespread in the near future.

Chapter 3 demonstrated the concept of using nuclear-based navigation to position the robot integrated fluorescence laparoscope within the vicinity of the targeted lesion during robot-assisted laparoscopic surgery, using the hybrid tracer ICG-^{99m}Tc-nanocolloid, which is both radioactive and fluorescent. Phantom evaluations showed a navigation accuracy of 2.25 mm (coronal plane) and 2.08 mm (sagittal plane) when navigation was based on preoperative SPECT/CT scans. When navigation was based on freehand SPECT (fhSPECT) scans, these accuracies were 1.92 mm (coronal plane) and 2.83 mm (sagittal plane). In comparison to the <1 cm detection limit of fluorescence imaging, this would indicate that the navigation inaccuracies could be compensated using the real-time fluorescence feedback as provided by the fluorescence laparoscope. Therefore, these initial phantom experiments suggest that SPECT-based navigation of the robot-integrated fluorescence laparoscope has the potential to aid fluorescence-guided surgery procedures for lesions positioned deep within the patient anatomy.

In **chapter 4**, the navigated fluorescence camera concept was translated to a system applicable for both open and laparoscopic surgery, using a detachable exoscope and laparoscope respectively. Initial phantom evaluations revealed an overall tool-to-target distance accuracy of 2.1 mm for SPECT/CT-based and

3.2 mm for fhSPECT-based navigation. The augmented reality registration accuracy was found to be 1.1 and 2.2 mm, respectively. Evaluations in open (penile cancer) and laparoscopic (prostate cancer) navigation were successful and accurate enough to localize the fluorescence signals of the targeted tissues in vivo. This proof-of-concept study suggest that the single hybrid navigation setup studied is applicable in various open and laparoscopic surgical applications.

The studies evaluated in chapter 3 and 4, combined with the work of KleinJan et al. [1], revealed that using near-infrared optical tracking, obstructed fluorescence imaging of open surgery fluorescence cameras. **Chapter 5** thoroughly investigated the different components of this interference aspect and recommended possible solutions. The different measurements performed indicated that interference was caused by: (1) spectral overlap between the optical tracking system (OTS) light emitted and the fluorescence camera detection range, (2) OTS light intensity, (3) OTS duty cycle, (4) OTS emission frequency, (5) fluorescence camera measurement frequency, and (6) fluorescence camera sensitivity. Optimization of points 2-4 already indicated OTS and fluorescence camera compatibility can be used to support the navigated fluorescence guidance concept, even in open surgical procedures.

Part two of this thesis introduced several detection modalities, further supporting the translation of molecular imaging towards intraoperative guidance. **Chapter 6** described the engineering of a multimodal animal imaging platform, capable of imaging bioluminescence, fluorescence and SPECT emission signatures, optimally supporting preclinical hybrid tracer development. Phantom and in vivo mice evaluations indicated accurate imaging of all three signals (i.e. bioluminescence, fluorescence and SPECT). Hereby, the acquired SPECT and bioluminescence scans were used to place the fluorescence imaging results in to perspective: for example, by showing tracer accumulation in non-target organs such as the liver and kidneys (SPECT) and by giving a semi-quantitative read-out of the tumor spread (bioluminescence). This revealed the advantages of a fully integrated imaging platform, optimally using the complementary scans to improve data interpretation during research.

Chapter 7 explored how the generation of a novel freehand Fluorescence (fhFluo) imaging approach could complement fhSPECT in a hybrid setup. Next to the generation of fhSPECT scans, the conceived hybrid modality was capable of creating (pseudo-)3D fluorescence tomography scans. The imaging resolution of fhFluo (1 mm) was found to be superior to that of fhSPECT (6 mm), however, fhFluo was confined to a maximum depth of 0.5 cm, while fhSPECT imaging was usable at all depths (evaluated $\leq$2 cm). Both fhSPECT and fhFluo allowed for augmented- and virtual-reality navigation towards tracer hotspots, segmented in the image. Imaging in prostate and sentinel lymph node specimens confirmed these trends: fhSPECT has a lower resolution but a more in-depth detectability, while fhFluo harbors a superior resolution, but only supplies superficial detectability. Overall, using radioactive and fluorescent (hybrid) tracers, this

chapter showed that fhFluo has complementary value to fhSPECT, rendering a unique hybrid imaging/navigation modality.

Chapter 8 focused specifically on improving detection of the nuclear tracer emissions during robot-assisted laparoscopic surgery. To this end, a tethered and highly flexible DROP-IN gamma probe was developed which could optimally benefit from the flexible wrists of a (robot-assisted) laparoscopic forceps, increasing intra-abdominal maneuverability. In comparison to a conventional laparoscopic gamma probe (allowing for movements with 4 degrees of freedom (DOF)), a DROP-IN combination allowed for 6 DOF with a robotic forceps. Phantom experiments underlined the importance of this maneuverability, showing that distinguishing a low radioactive lesion (e.g. SN) from a high radioactive background (e.g. prostate) was only possible with the detector faced $\geq$90° away from the high background source. Further evaluation in phantom, ex vivo clinical (i.e. prostate and SN specimens) and in vivo porcine studies all influenced the different prototype designs of the DROP-IN geometry. After thorough investigation of the probe pick up grip design, the surgeon favored a 45°-grip at the distal end of the probe. Introduction and optimization of the first DROP-IN gamma probe prototypes indicated a better integration of using radioguidance during (robot-assisted) laparoscopic surgery. The clinical potential of this technology was recently demonstrated during prostate cancer related robot-assisted laparoscopic SN procedures [2].

In **chapter 9**, the **outlook** of this thesis, the introduced (hybrid) detection and navigation modalities were linked to an overview of the general research developments made for virtual- and augmented-reality computer-assisted procedures in urological interventions. Many different approaches were shown for both the urinary system (including nephrolithotomy and nephrectomy) and the reproductive organs (including primary tumor lesions and lymphatic spread). Within these fields, the detailed surgical roadmaps were created with pre- or intra-operative forms of (cone-beam) CT, MRI, ultrasound and SPECT imaging modalities. Registration of these surgical roadmaps with the real-life surgical view was performed using mainly electromagnetic, mechanical, vision or near-infrared optical-based tracking techniques, whereby the combination of approaches was suggested to provide superior outcome. Unfortunately, soft-tissue deformations remain one of the most challenging obstacles in this field of soft-tissue surgery, demanding the use of confirmatory interventional detection modalities. This has resulted in the introduction of new intraoperative detection modalities such as DROP-IN US, transurethral US, (DROP-IN) gamma probes and fluorescence cameras. Although most techniques are evaluated in small patient groups and there is still a lot of room for refinement, the presented navigation efforts might provide the first steps towards a promising future for computer-assisted surgery in urology, hopefully improving surgical accuracy and clinical outcome.

In conclusion, the different detection and navigation modalities engineered and investigated in this thesis, all used the complementary values of

nuclear and fluorescence tracer signatures to optimally guide the surgeon during the resection of cancer-related tissue. Hopefully, these image guided surgery approaches can all help to move the field towards a more precise, less invasive and more effective surgical procedure. While initial clinical evaluations were tailored towards SN procedures in urology (i.e. prostate and penile cancer), all presented techniques are of such a nature, that they could easily be applied in many different (hybrid) tracer-based surgical procedures. Such procedure already include hybrid SN procedures in head and neck cancer [3,4], SN in cervical cancer [5], SN in breast cancer [6] and radioguided occult lesion localization procedures [7]. Recent developments of tumor-receptor targeted hybrid tracers should open up many other applications in the (nearby) future, including localization of the primary tumor and metastatic spread in renal cancer (e.g. using an ^{111}In-girentuximab-IRDye800CW tracer) [8], neuroendocrine tumors (e.g. using a Cy5-^{111}In-DTPA-Tyr3-octreotate tracer) [9] and prostate cancer (e.g. using a PSMA I&F tracer) [10]. Alternatively, modalities like the introduced DROP-IN technology have also proven value during receptor targeted surgery, in specific PSMA guided resection of lymphatic metastases [11].

REFERENCES

1. *G. H. KleinJan et al., "Toward (Hybrid) Navigation of a Fluorescence Camera in an Open Surgery Setting", Journal of Nuclear Medicine 57(10), 1650-1653 (2016).*
2. *P. Meershoek et al., "Robot-assisted laparoscopic surgery using DROP-IN radioguidance: first-in-human translation", Eur J of Nucl Med and Mol Imaging 1-5 (2018).*
3. *A. Christensen et al., "Feasibility of real-time near-infrared fluorescence tracer imaging in sentinel node biopsy for oral cavity cancer patients", Ann Surg Oncol 23(2), 565-572 (2016).*
4. *I. Stoffels et al., "Evaluation of a radioactive and fluorescent hybrid tracer for sentinel lymph node biopsy in head and neck malignancies: prospective randomized clinical trial to compare ICG-^{99m}Tc-nanocolloid hybrid tracer versus ^{99m}Tc-nanocolloid", Eur J of Nucl Med and Mol Imaging 42(11), 1631-1638 (2015).*
5. *P. Paredes et al., "Role of ICG-99mTc-nanocolloid for sentinel lymph node detection in cervical cancer, a pilot study", Eur J of Nucl Med and Mol Imaging 44(11), 1853-1861 (2017).*
6. *B. E. Schaafsma et al., "Clinical trial of combined radio-and fluorescence-guided sentinel lymph node biopsy in breast cancer", Br J Surg 100(8), 1037-1044 (2013).*
7. *G. KleinJan et al., "Hybrid radioguided occult lesion localization (hybrid ROLL) of 18 F-FDG-avid lesions using the hybrid tracer indocyanine green-^{99m}Tc-nanocolloid", Rev Esp Med Nucl Imagen Mol 35(5), 292-297 (2016).*
8. *M. C. Hekman et al., "Targeted dual-modality imaging in renal cell carcinoma: an ex vivo kidney perfusion study", Clin Cancer Res 22(18), 4634-4642 (2016).*
9. *C. Santini et al., "Evaluation of a fluorescent and radiolabeled hybrid somatostatin analogue in vitro and in mice bearing H69 neuroendocrine xenografts", Journal of Nuclear Medicine jnumed.115.164970 (2016).*
10. *M. Schottelius et al., "Synthesis and preclinical characterization of the PSMA-targeted hybrid probe PSMA-I&F for nuclear and fluorescence imaging of prostate cancer", Journal of Nuclear Medicine 60(1):71-8 (2018).*
11. *F. W. B. v. Leeuwen et al., "Minimal-invasive robot-assisted image-guided resection of prostate-specific membrane antigen-positive lymph nodes in recurrent prostate cancer.", Clin Nucl Med. 44:580-1 (2019).*

SAMENVATTING

Strevend naar precieze chirurgie, beschrijft dit proefschrift de introductie van verschillende nieuwe (hybride) detectie- en navigatie-modaliteiten. Al de gepresenteerde technieken focussen op optimale detectie en lokalisatie van kanker-gerelateerd weefsel door gebruik te maken van tracers met complementaire radioactieve of fluorescente eigenschappen, of een combinatie daarvan in een hybride tracer-ontwerp. Deze nieuwe beeldgeleide chirurgie-technologieën zijn geëvalueerd in verschillende omgevingen, variërend van fantoomwerk tot preklinische en zelfs klinische studies.

Deel één van dit proefschrift omvat meerdere chirurgische navigatie-concepten. In **hoofdstuk 2** werden de algemene componenten voor een typisch chirurgisch-navigatie proces geïntroduceerd. De belangrijkste vereisten zijn: 1) een methode van beeldvorming voor het genereren van een 3D-kaart van de door de ziekte aangedane locaties; 2) computerondersteunde planning gebruikmakend van de patiëntenkaart; 3) registratie van de patiëntenkaart met de echte patiënt op de operatietafel; 4) positie- en oriëntatie-tracking van de patiënt en chirurgische instrumenten op de operatiekamer; en 5) navigatie van de chirurgische instrumenten naar de beoogde weefsels in de patiënt. Samengevoegd vormen deze stappen een proces waarbij de chirurg precies weet waar zijn instrumenten zijn op de patiëntenkaart, ten opzichte van de vooraf bepaalde weefsels. Naast het gebruik in neurochirurgie, radiotherapie en orthopedische chirurgie, is het gebruik van navigatie tijdens chirurgie nog van experimentele aard. Dit komt voornamelijk doordat huidige navigatiesystemen niet goed genoeg onnauwkeurigheden als gevolg van weefseldeformaties kunnen compenseren. Desondanks scheppen de genoemde studies, in combinatie met de ontwikkeling van de onderliggende technologie, goede hoop dat het gebruik van chirurgische navigatie wijdverspreid zal toenemen in de nabije toekomst.

Hoofdstuk 3 demonstreerde het concept om met behulp van nucleair-gebaseerde navigatie de fluorescentie-laparoscoop te geleiden naar vooraf bepaalde weefsels tijdens robot-geassisteerde laparoscopische chirurgie. Belangrijk onderdeel hierin is de hybride tracer ICG-^{99m}Tc-nanocolloid, welke zowel radioactief als fluorescent is. Fantoom-evaluaties van deze navigatie-opstelling lieten een nauwkeurigheid zien van 2.25 mm (coronaal vlak) en 2.08 mm (sagittaal vlak) wanneer navigatie was gebaseerd op preoperatieve SPECT/CT scans. Met navigatie gebaseerd op freehand SPECT (fhSPECT), waren deze nauwkeurigheden 1.92 mm (coronaal vlak) en 2.83 (sagittaal vlak). In vergelijking met de <1 cm detectie-grens voor fluorescentiebeeldvorming, zou dit betekenen dat de navigatie-onnauwkeurigheden gecompenseerd zouden kunnen worden door gebruik te maken van de nauwkeurige en rechtstreekse fluorescentiebeeldvorming. Daarmee wekt dit fantoom-onderzoek de verwachting dat SPECT-gebaseerde navigatie van de robotische fluorescentie-laparoscoop, fluorescentie-geleide chirurgie kan helpen wanneer laesies diep in de patiënt gepositioneerd zijn.

In **hoofdstuk 4** werd het concept van een genavigeerde fluorescentie-camera verder uitgewerkt naar een systeem dat bruikbaar is voor zowel open als laparoscopische chirurgie, door gebruik te maken van een verwisselbare exo- en laparoscoop. Ook hier werd eerst de navigatie-nauwkeurigheid onderzocht in een fantoom-opstelling, resulterend in een algemene instrument-tot-doel nauwkeurigheid van 2.1 mm (SPECT/CT navigatie) en 3.2 mm (fhSPECT navigatie). Registratie van de augmented reality navigatie-beelden toonde een nauwkeurigheid van 1.1 mm (SPECT/CT navigatie) en 2.2 mm (fhSPECT navigatie). De hierop volgende evaluatie tijdens open chirurgie (peniskanker) en laparoscopische chirurgie (prostaatkanker) was succesvol en accuraat genoeg om de fluorescente weefsels terug te vinden in de patiënten. Hiermee toont deze studie aan dat het hybride navigatie-concept mogelijk van waarde is in verschillende open en laparoscopische chirurgische toepassingen.

In combinatie met eerder gepubliceerd werk van KleinJan et al. [1], lieten hoofdstuk 3 en 4 zien dat dichtbij infrarode optische tracking interfereert met de fluorescentiebeeldvorming voor open chirurgie. In **hoofdstuk 5** werden de verschillende componenten van dit probleem grondig onderzocht en de mogelijke oplossingen hiervoor aangeboden. De verrichte metingen maakten duidelijk dat de interferentie wordt veroorzaakt door een samenspel van: (1) de spectrale overlap tussen het licht dat wordt gebruikt door het optische tracking systeem (OTS) en het detectie-bereik van de fluorescentie-camera, (2) de OTS lichtintensiteit, (3) de OTS arbeidscyclus, (4) de OTS emissie-frequentie, (5) de fluorescentie-camera meet frequentie, en (6) de fluorescentie camera gevoeligheid. Optimalisatie van punten 2-4 gaf al aan dat optische tracking weldegelijk gebruikt kan worden in het kader van de genavigeerde fluorescentie camera, ook voor open chirurgie.

Deel twee van dit proefschrift introduceerde verschillende detectie-modaliteiten, voortbouwend aan de translatie van moleculaire beeldvorming naar intra-operatieve begeleiding. **Hoofdstuk 6** beschreef het ontwerp en de constructie van een multimodale scanner voor moleculaire beeldvorming in dieren. Met de mogelijkheid tot het in beeld brengen van bioluminescentie, fluorescentie en SPECT straling, bood dit systeem een optimaal platform voor de preklinische ontwikkeling van hybride tracers. Fantoom-evaluaties en in vivo muizen-evaluaties onderschreven de kwaliteiten van de drie individuele technieken. Hierbij boden SPECT en bioluminescentie een manier om behaalde resultaten met fluorescente beeldvorming in perspectief te plaatsen, door bijvoorbeeld tracer-opname in achtergrondweefsel zoals de lever en nieren weer te geven (SPECT) en verspreiding van de tumor in kaart te brengen (bioluminescentie). Dit onderstreepte het voordeel van één compleet geïntegreerd systeem waar optimaal gebruik wordt gemaakt van de complementaire-scan eigenschappen om data-collectie en interpretatie te verbeteren in het onderzoek.

Hoofdstuk 7 onderzocht hoe de ontwikkeling van een nieuwe freehand Fluorescence (fhFluo) modaliteit complementair kan zijn aan fhSPECT in een

hybride opstelling. Naast het produceren van fhSPECT scans, gaf dit hybride systeem de mogelijkheid om (pseudo-)3D fluorescentie tomografie-scans te produceren. De beeldvormende resolutie van fhFluo (1 mm) bleek superieur aan die van fhSPECT (6 mm). Echter, de fhFluo beeldvorming was beperkt tot een diepte van 0.5 cm, terwijl fhSPECT beeldvorming bruikbaar was op alle geëvalueerde diepten ($\leq$2 cm). Zowel fhSPECT als fhFluo gaven de mogelijkheid tot augmented- en virtual-reality navigatie richting tracer hotspots, zoals gesegmenteerd in de beelden. Beeldvorming in prostaat- en schildwachtklier-weefsels bevestigde de trend: fhSPECT geeft een lagere resolutie met meer diepte-informatie, terwijl fhFluo een superieure resolutie levert voor oppervlakkige signalen. Daarmee liet dit hoofdstuk zien, gebruik makend van radioactieve en fluorescente (hybride) tracers, dat fhFluo complementaire waarde heeft ten opzichte van fhSPECT en een unieke beeldvorming- en navigatie-modaliteit levert.

Hoofdstuk 8 focust specifiek op het verbeteren van de detectie van radioactieve tracers tijdens robot-geassisteerde laparoscopische chirurgie. Voor dit doel is er een bekabelde, kleine en uiterst flexibele DROP-IN gamma probe ontwikkeld welke in de intra-abdominale ruimte opgepakt wordt en welke tijdens scannen optimaal gebruik maakt van de gewrichten in de bestaande (robotische) laparoscopische tangen. In vergelijking met de conventionele laparoscopische gamma probe (die beweging met 4 vrijheidsgraden biedt), bleek de manoeuvreerbaarheid van de DROP-IN gamma probe in combinatie met de robotische tangen veel groter (beweging met 6 vrijheidsgraden). Fantoom-experimenten onderstreepten het belang van deze manoeuvreerbaarheid door te laten zien dat het onderscheiden van een laagradioactieve laesie (bijv. schildwachtklier) ten opzichte van een hoogradioactieve achtergrond (bijv. prostaat) alleen mogelijk was als de detector $\geq 90^{\circ}$ weggedraaid kon worden van deze hoge achtergrond. Het ontwerp van verschillende prototype DROP-IN behuizingen werd verder beoordeeld in fantoom-studies, ex vivo klinische weefsel-studies (d.w.z. prostaat- en schildwachtklieren) en in vivo varkens studies. Na grondige evaluatie van het oppak-ontwerp, gaf de chirurg de voorkeur aan een grip over 45° distaal gepositioneerd op de probe. Introductie en optimalisatie van de eerste DROP-IN gamma probe prototypes gaf aan dat radiogeleide chirurgie op deze manier beter geïntegreerd wordt met (robot-geassisteerde) laparoscopische chirurgie. Recent heeft de eerste klinische studie inderdaad de potentie van deze vorm van radiogeleide chirurgie laten zien tijdens robotische schildwachtklier procedures in prostaatkanker [2].

In **hoofdstuk 9** van dit proefschrift, **het toekomstperspectief**, werden de geïntroduceerde (hybride) detectie- en navigatie-modaliteiten geplaatst in een overzicht van de algemene wetenschappelijke ontwikkelingen voor virtual- en augmented-reality computerondersteunde procedures binnen de urologie. Veel verschillende benaderingen werden aangehaald voor zowel het urinewegstelsel (inclusief nefrolithotomie en nefrectomie) als het voortplantingssysteem (inclusief primaire tumor laesies en lymfatische uitzaaiingen). Binnen deze verschillende

toepassingen werd de gedetailleerde patiëntenkaart gegenereerd met behulp van pre- of intra-operatieve beeldvorming, waaronder (cone-beam) CT-, MRI-, ultrasound- en SPECT-modaliteiten. Registratie van deze chirurgische 'road-map' en het intra-operatieve veld gebeurde over het algemeen met elektromagnetische-, mechanische-, beeldanalyse- of dichtbij infrarood optische-tracking technieken. Dit wekte de indruk dat een combinatie van deze technieken superieure resultaten geeft. Helaas is gebleken dat zachte-weefsel-deformaties nog steeds één van de grootste obstakels is in dit veld van zachte-weefsel chirurgie, waardoor validatie met intra-operatieve detectie-modaliteiten nodig blijft. Dit heeft echter wel geresulteerd in de introductie van nieuwe intra-operatieve detectie-modaliteiten, zoals de DROP-IN US, transurethraal US, (DROP-IN) gamma probes en fluorescentie camera's. Hoewel de meeste technieken alleen geëvalueerd zijn in kleine patiënten-groepen en er nog veel ruimte is voor verfijning, bieden de gepresenteerde navigatie-technieken wel een mogelijke eerste stap in de richting van een veelbelovende toekomst voor computerondersteunde chirurgie binnen de urologie, waarbij chirurgische precisie en medisch resultaten verbeterd worden.

De verschillende detectie en navigatie modaliteiten, zoals ontworpen en onderzocht in dit proefschrift, maakten allemaal gebruik van de complementaire eigenschappen van radioactieve en fluorescente tracers om de chirurg optimaal te begeleiden in het verwijderen van kanker-gerelateerd weefsel. Hopelijk kunnen deze beeldgeleide technieken bijdragen om het chirurgische veld vooruit te brengen richting preciezere, minder ingrijpende en meer effectieve procedures. Hoewel de eerste klinische evaluaties gericht waren op de schildwachtklierprocedure binnen de urologie (d.w.z. prostaat- en peniskanker), zijn al de gepresenteerde technieken van dien aard dat ze met relatief weinig moeite ook overgezet kunnen worden naar vele andere (hybride) tracer-gebaseerde chirurgische procedures. Voorbeelden hiervan binnen de huidige chirurgie zijn de hybride schildwachtklierprocedures in hoofd-halskanker [3,4], baarmoederhalskanker [5] en borstkanker [6] en de radiogeleide lokalisatie van verborgen laesies [7]. Daarnaast openen de recente ontwikkelingen op het gebied van tumor-receptor gerichte hybride tracers de weg naar nog veel meer toepassingen in de (nabije) toekomst, inclusief de lokalisatie van primaire tumor en uitzaaiingen in nierkanker (bijv. met de tracer ^{111}In-girentuximab-IRDye800CW tracer) [8], neuro-endocrine tumoren (bijv. met de tracer Cy5-^{111}In-DTPA-Tyr3-octreotate) [9] en prostaatkanker (bijv. met de tracer PSMA I&F) [10]. Daarnaast laten modaliteiten zoals de geïntroduceerde DROP-IN technologie nu al hun waarde zien binnen de tumor-receptor gerichte chirurgie, in het bijzonder met PSMA-gerichte resectie van lymfeklier-uitzaaiingen bij prostaat kanker [11].

REFERENTIES

1. *G. H. KleinJan et al., "Toward (Hybrid) Navigation of a Fluorescence Camera in an Open Surgery Setting", Journal of Nuclear Medicine 57(10), 1650-1653 (2016).*
2. *P. Meershoek et al., "Robot-assisted laparoscopic surgery using DROP-IN radioguidance: first-in-human translation", Eur J of Nucl Med and Mol Imaging 1-5 (2018).*
3. *A. Christensen et al., "Feasibility of real-time near-infrared fluorescence tracer imaging in sentinel node biopsy for oral cavity cancer patients", Ann Surg Oncol 23(2), 565-572 (2016).*
4. *I. Stoffels et al., "Evaluation of a radioactive and fluorescent hybrid tracer for sentinel lymph node biopsy in head and neck malignancies: prospective randomized clinical trial to compare ICG-^{99m}Tc-nanocolloid hybrid tracer versus ^{99m}Tc-nanocolloid", Eur J of Nucl Med and Mol Imaging 42(11), 1631-1638 (2015).*
5. *P. Paredes et al., "Role of ICG-99mTc-nanocolloid for sentinel lymph node detection in cervical cancer, a pilot study", Eur J of Nucl Med and Mol Imaging 44(11), 1853-1861 (2017).*
6. *B. E. Schaafsma et al., "Clinical trial of combined radio-and fluorescence-guided sentinel lymph node biopsy in breast cancer", Br J Surg 100(8), 1037-1044 (2013).*
7. *G. KleinJan et al., "Hybrid radioguided occult lesion localization (hybrid ROLL) of 18 F-FDG-avid lesions using the hybrid tracer indocyanine green-^{99m}Tc-nanocolloid", Rev Esp Med Nucl Imagen Mol 35(5), 292-297 (2016).*
8. *M. C. Hekman et al., "Targeted dual-modality imaging in renal cell carcinoma: an ex vivo kidney perfusion study", Clin Cancer Res 22(18), 4634-4642 (2016).*
9. *C. Santini et al., "Evaluation of a fluorescent and radiolabeled hybrid somatostatin analogue in vitro and in mice bearing H69 neuroendocrine xenografts", Journal of Nuclear Medicine jnumed.115.164970 (2016).*
10. *M. Schottelius et al., "Synthesis and preclinical characterization of the PSMA-targeted hybrid probe PSMA-I&F for nuclear and fluorescence imaging of prostate cancer", Journal of Nuclear Medicine 60(1):71-8 (2018).*
11. *F. W. B. v. Leeuwen et al., "Minimal-invasive robot-assisted image-guided resection of prostate-specific membrane antigen-positive lymph nodes in recurrent prostate cancer.", Clin Nucl Med. 44:580-1 (2019).*

10

CURRICULUM VITAE

Matthias van Oosterom was born in Rijswijk, the Netherlands on October 26th 1990. He graduated high school in 2008 (VWO; Christian Lyceum Delft, Delft, The Netherlands). In 2012 he finished his bachelor in Applied Physics (Delft University of Technology, Delft, The Netherlands) with a focus on biomedical engineering. His bachelor thesis investigated the generation of phantoms for intravascular ultrasound at the Laboratory of Acoustic Wavefield Imaging (Delft University of Technology). In 2014, Matthias obtained his master's degree in Applied Physics with a specialization in Research and Development in (Medical) Imaging Science & Technology and Medical Physics (Delft University of Technology). During his master internship, he worked on the design and development of a DROP-IN gamma probe for (robot-assisted) laparoscopic surgery (industrial partners: SurgicEye GmbH [Munich, Germany] and Eurorad S.A. [Eckbolsheim, France]). During his master thesis, he developed a hybrid bioluminescence, fluorescence and SPECT imaging system for small animals at the Delft University of Technology (Department of Radiation Science and Technology; Industrial partner: MI-Labs B.V. [Utrecht, The Netherlands]). In 2014, Matthias started his PhD at the Leiden University Medical Center (Leiden, The Netherlands) under supervision of prof. dr. C.J.H. van de Velde (Department of Surgery) and prof. dr. F.W.B. van Leeuwen (Department of Radiology). With an aim to advance precision surgery, he collaborated with various industrial partners on developing and translating engineering solutions for different surgical modalities (e.g. radioguided surgery, fluorescence-guided surgery and surgical navigation) into clinical studies. Since 2018, he holds a position as a post-doctoral researcher with the Interventional Molecular Imaging Laboratory (Department of Radiology, Leiden University Medical Center) and is a guest-researcher at the Department of Urology of the Netherlands Cancer Institute – Antoni van Leeuwenhoek Hospital.

LIST OF PUBLICATIONS

- Recent advances in nuclear and hybrid detection modalities for image-guided surgery; ***Matthias N van Oosterom****, Daphne DD Rietbergen, Mick M Welling, Henk G van der Poel, Tobias Maurer, Fijs WB van Leeuwen;* Expert Review of Medical Devices 2019, 16(8):711-34.
- Extending the hybrid surgical guidance concept with freehand fluorescence tomography; ***Matthias N van Oosterom****, Philippa Meershoek, Mick M Welling, Francisco Pinto, Philipp Matthies, Hervé Simon, Thomas Wendler, Nassir Navab, Cornelis JH van de Velde, Henk G van der Poel, Fijs WB van Leeuwen;* IEEE Transactions on Medical Imaging 2019, 39(1):226-35.
- Robot-assisted laparoscopic surgery using DROP-IN radioguidance: first-in-human translation; *Philippa Meershoek*,* ***Matthias N van Oosterom*****, Hervé Simon, Laurent Mengus, Tobias Maurer, Pim J van Leeuwen, Esther MK Wit, Henk G van der Poel, Fijs WB van Leeuwen;* European journal of nuclear medicine and molecular imaging 2019, 46(1): 49-53. *Shared first author
- Artificial intelligence and robotics: a combination that is changing the operating room; *Iulia Andras, Elio Mazzone, Fijs WB van Leeuwen, Geert De Naeyer,* ***Matthias N van Oosterom****, Sergi Beato, Tessa Buckle, Shane O'Sullivan, Pim J van Leeuwen, Alexander Beulens, Nicolae Crisan, Frederiek D'Hondt, Peter Schatteman, Henk van Der Poel, Paolo Dell'Oglio, Alexandre Mottrie;* World Journal of Urology 2019, World journal of urology. 2019, 27:1-8.
- Can fluorescence-guided surgery help identify all lesions in unknown locations or is the integrated use of a roadmap created by preoperative imaging mandatory? A blinded study in prostate cancer patients; *Phillipa Meershoek, Tessa Buckle,* ***Matthias N van Oosterom****, Gijs H KleinJan, Henk G van der Poel and Fijs WB van Leeuwen;* Journal of Nuclear Medicine, 2019, ePub ahead of print.
- Prostate-specific membrane antigen positron emission tomography/computed tomography combined with sentinel node biopsy for primary lymph node staging in prostate cancer; *Florentien J Hinsenveld, Esther MK Wit, Pim J van Leeuwen, Oscar R Brouwer, Maarten L Donswijk, Corinne N Tillier, Erik Vegt, Henricus AM van Muilekom,* ***Matthias N van Oosterom****, Fijs WB van Leeuwen and Henk G van der Poel;* Journal of Nuclear Medicine, 2019, ePub ahead of print.
- Quantification of wild-type and radiation attenuated Plasmodium falciparum sporozoite motility in human skin; *Béatrice MF Winkel, Clarize M de Korne,* ***Matthias N van Oosterom****, Diego Staphorst, Mark Meijhuis, Els Baalbergen, Munisha S Ganesh, Koen J Dechering, Martijn W Vos, Séverine C Chevalley-Maurel, Blandine Franke-Fayard, Fijs WB van Leeuwen, Meta Roestenberg;* Scientific reports 2019, 9(1): 1-11.
- Minimal-Invasive Robot-Assisted Image-Guided Resection of Prostate-Specific Membrane Antigen–Positive Lymph Nodes in Recurrent Prostate Cancer; *Fijs WB van Leeuwen,* ***Matthias N van Oosterom****, Philippa Meershoek, Pim J van Leeuwen, Christoph Berliner, Henk G van der Poel, Markus Graefen, Tobias Maurer;* Clinical Nuclear Medicine 2019, 44(7): 580-581.
- Freehand-SPECT with 99mTc-HDP as tool to guide percutaneous biopsy of skeletal lesions detected on bone scintigraphy; *Daphne DD Rietbergen, Philippa Meershoek,* ***Matthias N van Oosterom****, Meta Roestenberg, Arian R van Erkel, Frits Smit, Jos A van der Hage, Renato A Valdés Olmos, Fijs WB van Leeuwen;* Revista Española de Medicina Nuclear e Imagen Molecular 2019, 38(4): 218-223.
- Regulation of Plasmodium sporozoite motility by formulation components; *Clarize M de Korne, Luuk T Lageschaar,* ***Matthias N van Oosterom****, Els Baalbergen, Beatrice MF Winkel, Severine C Chevalley-Maurel, Aldrik H Velders, Blandine MD Franke-Fayard, Fijs WB van Leeuwen, Meta Roestenberg;* Malaria Journal 2019, 18(1): 155.
- Click Chemistry in the Design and Production of Hybrid Tracers; *Albertus W Hensbergen, Danny M van Willigen, Mick M Welling, Felicia A van der Wijk, Clarize M de Korne,* ***Matthias N van Oosterom****, Margret Schottelius, Hans-Jürgen Wester, Tessa Buckle, Fijs WB van Leeuwen;* ACS Omega 2019, 4, 12438–12448.

- A tracer-based method enables tracking of Plasmodium falciparum malaria parasites during human skin infection; *Béatrice MF Winkel, Clarize M de Korne, **Matthias N van Oosterom**, Diego Staphorst, Anton Bunschoten, Marijke CC Langenberg, Séverine C Chevalley-Maurel, Chris J Janse, Blandine Franke-Fayard, Fijs WB van Leeuwen, Meta Roestenberg;* Theranostics 2019, 9 (10): 2768.
- Synthesis and preclinical characterization of the PSMA-targeted hybrid tracer PSMA-I&F for nuclear and fluorescence imaging of prostate cancer; *Margret Schottelius, Alexander Wurzer, Katharina Wissmiller, Roswitha Beck, Maximilian Koch, Dimitrios Gorpas, Johannes Notni, Tessa Buckle, **Matthias N van Oosterom**, Katja Steiger, Vasilis Ntziachristos, Markus Schwaiger, Fijs WB van Leeuwen, Hans-Jürgen Wester;* Journal of Nuclear Medicine 2019, 60(1): 71-78
- Navigating surgical fluorescence cameras using near-infrared optical tracking; ***Matthias .N van Oosterom**, David A den Houting, Cornelis JH van de Velde, Fijs WB van Leeuwen*; Journal of Biomedical Optics 2018, 23(5): 056003.
- Navigation of Fluorescence Cameras during Soft Tissue Surgery—Is it Possible to Use a Single Navigation Setup for Various Open and Laparoscopic Urological Surgery Applications?; ***Matthias N van Oosterom**, Philippa Meershoek, Gijs H KleinJan, Kees Hendricksen, Nassir Navab, Cornelis JH van de Velde, Henk G van der Poel, Fijs WB van Leeuwen;* Journal of Urology 2018, 199(4): 1061-1068.
- Computer-assisted surgery: virtual-and augmented-reality displays for navigation during urological interventions; ***Matthias N van Oosterom**, Henk G van der Poel, Nassir Navab, Cornelis JH van de Velde, Fijs WB van Leeuwen;* Current Opinion in Urology 2018, 28(2): 205-213.
- Multispectral fluorescence imaging as a tool to separate healthy and disease related lymphatic anatomies during robot-assisted laparoscopic procedures; *Philippa Meershoek*, Gijs H KleinJan*, **Matthias N van Oosterom**, Esther MK Wit, Danny M van Willigen, Kevin P Bauwens, Erik J van Gennep, Alexandre M Mottrie, Henk G van der Poel, Fijs WB van Leeuwen;* Journal of Nuclear Medicine 2018, 59(11): 1757-1760. *Shared first author
- Nanoparticles reveal Extreme Size-Sorting and Morphologies in Complex Coacervate Superstructures; *Jan Bart ten Hove, **Matthias N van Oosterom**, Fijs WB van Leeuwen, Aldrik H Velders*; Scientific reports, 2018, 8.1: 13820.
- A supramolecular approach for liver radioembolization; *Silvia J Spa, Mick M Welling, **Matthias N van Oosterom**, Daphne DD Rietbergen, Mark C Burgmans, Willem Verboom, Jurriaan Huskens, Tessa Buckle, Fijs WB van Leeuwen*; Theranostics 2018, 8(9): 2377.
- Size-sorting and pattern formation of nanoparticle-loaded micellar superstructures in biconcave thin films; *Jan Bart ten Hove, Junyou Wang, **Matthias N van Oosterom**, Fijs WB Van Leeuwen, Aldrik H Velders*; ACS nano 2017, 11(11): 11225-11231.
- Hybrid surgical guidance: does hardware integration of γ-and fluorescence imaging modalities make sense?; *Gijs H KleinJan, Daan Hellingman, Nynke S van den Berg, **Matthias N van Oosterom**, Kees Hendricksen, Simon Horenblas, Renato A Valdes Olmos, Fijs WB van Leeuwen*; Journal of Nuclear Medicine 2017, 58(4): 646-650.
- Navigation of a robot-integrated fluorescence laparoscope in preoperative SPECT/CT and intraoperative freehand SPECT imaging data: a phantom study; ***Matthias N van Oosterom**, Myrthe A Engelen, Nynke S van den Berg, Gijs H KleinJan, Henk G van der Poel, Thomas Wendler, Cornelis JH van de Velde, Nassir Navab, Fijs WB van Leeuwen;* Journal of Biomedical Optics 2016, 21(8): 086008.
- Revolutionizing (robot-assisted) laparoscopic gamma tracing using a DROP-IN gamma probe technology; ***Matthias N van Oosterom**, Hervé Simon, Laurent Mengus, Mick M Welling, Henk G van der Poel, Nynke S van den Berg, Fijs WB van Leeuwen*; American Journal of Nuclear Medicine and Molecular Imaging 2016, 6(1): 1.
- Surgical Navigation: An Overview of the State-of-the-Art Clinical Applications; *Paulo Waelkens, **Matthias N van Oosterom**, Nynke S van den Berg, Nassir Navab, Fijs WB van Leeuwen*; In: Radioguided Surgery: Current Applications and Innovative Directions in Clinical Practice; Springer 2016 (editors: Ken Herrmann, Omgo E Nieweg, Stephen P Povoski).

- Toward (hybrid) navigation of a fluorescence camera in an open surgery setting; *Gijs H Klein-Jan, Nynke S van den Berg,* ***Matthias N van Oosterom****, Thomas Wendler, Mitsuharu Miwa, Axel Bex, Kees Hendricksen, Simon Horenblas, Fijs WB van Leeuwen*; Journal of Nuclear Medicine 2016, 57(10): 1650-1653.
- U-SPECT-BioFluo: an integrated radionuclide, bioluminescence, and fluorescence imaging platform; ***Matthias N van Oosterom****, Rob Kreuger, Tessa Buckle, Wendy A Mahn, Anton Bunschoten, Lee Josephson, Fijs WB van Leeuwen, Freek J Beekman*; EJNMMI research 2014, 4(1): 56.
- Fluorescent lectin-bionanoparticles for the in vivo visualization of peripheral nerves; *Gijs H KleinJan, Tessa Buckle, Danny M van Willigen,* ***Matthias N van Oosterom****, Silvia J Spa, Harmen E Kloosterboer, Fijs WB van Leeuwen*; Molecules 2014, 19(7):9876-92.